

UniversidadeVigo

UNIVERSITY OF VIGO  
DEPARTMENT OF ELECTRONICS TECHNOLOGY

DISSERTATION SUBMITTED FOR THE DEGREE OF  
DOCTOR OF PHILOSOPHY AT THE UNIVERSITY OF VIGO

“DOCTOR EUROPEUS” MENTION

DIGITAL RESONANT CURRENT CONTROLLERS FOR VOLTAGE  
SOURCE CONVERTERS

Author: Alejandro Gómez Yepes

Director: Jesús Doval Gandoy

Vigo, 14 December 2011



PH.D. COMMITTEE MEMBERS:

Fernando Briz

Emil Levi

Lennart Harnfors

Iustin Radu Bojoi

Francisco Daniel Freijedo

Josep María Guerrero

Ion Etxeberría Otadui

14 December 2011

University of Vigo

Vigo, Spain



# Vita

Alejandro Gómez Yepes was born in A Coruña, Spain, in November 1985. He received the M.Sc. degree from the University of Vigo, Spain in 2009.

From June 2008 he works in the Department of Electronics Technology of the University of Vigo. He is currently holder of an FPI grant related to the project “Multilevel Multiphase Power Electronics Conversion Techniques Applied to AC Drives and Renewable Energy” funded by the Spanish Ministry of Science and Innovation. From April 2011 to July 2011, he joined the RCEEE Electric Machines and Drives group of Liverpool John Moores University in the United Kingdom for a research stay. His research interests include digital control of power electronics converters, with special focus on power quality and ac drives.

He has authored more than 15 published technical papers in the field of power electronics [1–18]. Nine of them are published in JCR-indexed journals [1–9]. He is member of the Institute of Electrical and Electronic Engineers (IEEE), the IEEE Industrial Electronics Society and the IEEE Power Electronics Society.



# Digital Resonant Current Controllers For Voltage Source Converters

Alejandro Gómez Yepes

## (ABSTRACT)

Sinusoidal current regulation of voltage source converters is an aspect of paramount importance to achieve a high level of performance in a lot of different applications, such as ac motor drives, active power filters, wind turbines, static synchronous compensators, photovoltaic inverters or active rectifiers.

One of the most extended types of current regulators are resonant controllers, which achieve zero steady-state error at selected frequencies, while providing a good combination of simplicity and high performance. Nevertheless, there are certain aspects with regard to these controllers that have not been approached in the technical literature on the matter, and that should be investigated in order to take advantage of their actual potential.

Most studies devoted to resonant controllers have been carried out in the continuous domain; however, their observations and conclusions cannot be directly applied to digital devices, which work in the discrete-time domain. In nowadays scenarios, most current controllers are implemented in digital platforms, so the influence of the discretization process should not be ignored. Several discrete-time implementations of resonant controllers have been proposed, but a comparison among the performance obtained by a wide variety of discretization techniques applied to resonant controllers has not been presented at this point. One of the contributions of this thesis consists in an in-depth comparison among the effects of discretization strategies when applied to resonant controllers. The discretization process is proved to be of great importance in these regulators, mainly because of their resonant characteristics. The optimum discrete-time implementation alternatives are assessed, in terms of their influence on the resonant peak location and the phase versus frequency response.

The implementations of resonant controllers based on two interconnected integrators are widely employed due to their simplicity regarding frequency adaptation. However, it is proved in this thesis that these schemes require lower resource consumption, but at the expense of important inaccuracies that significantly worsen the performance, except for very low resonant frequencies and sampling periods. Alternative implementations based on two integrators are proposed in this dissertation, which achieve higher performance by means of more accurate resonant peak locations and delay compensation, while maintaining the advantage on low computational burden and good frequency adaptation of the original schemes.

The analysis and design of resonant controllers is also approached. The existing methods, which are mainly based on the phase margin criterion, present some limitations, specially when there are multiple 0 dB crossings in the gain versus frequency response. This situation arises in cases such as selective control and when relatively high resonant frequencies with respect to the

switching frequency are required (e.g., in high power converters, where the switching frequency should be low in order to reduce the commutation losses). In this thesis, resonant controllers are analyzed by means of Nyquist diagrams. It is proved that the minimization of the sensitivity peak permits to achieve a greater performance and stability rather than by maximizing the gain or phase margins. A systematic method, supported by closed-form analytical expressions, is proposed to obtain the highest stability and performance, even when there are multiple 0 dB crossings.

Contributions of this dissertation have been published in three JCR-indexed journal papers and presented at two international conferences.

# Acknowledgments

First of all, I sincerely thank my advisor, Dr. Jesús Doval Gandoy. He gave me the opportunity to devote myself to one of the most fascinating and rewarding tasks. I consider myself extremely lucky to have found such an enthusiastic and competent leader.

I wish to gratefully acknowledge Dr. Francisco D. Freijedo for all his patience and help during these years. A great part of this work would not have been possible without his support.

Also, I am very grateful to Dr. Óscar López for all his technical support, style suggestions and help with  $\text{\LaTeX}$ .

I express my gratitude to Prof. Emil Levi for allowing me to join to the RCEEE Electric Machines and Drives research group of the Liverpool John Moores University for a research stay.

I would also like to express my sincere gratitude to the members of the Ph.D. Committee for their unselfish collaboration in the evaluation of my work.

Many thanks to my colleagues of the Department of Electronics Technology of the University of Vigo, because of their continuous support and the good moments we have shared. Specially, I would like to mention Jano, Pablo, Ana, Ortiz, Alex, Felipe, Miguel and Javier.

To my family, for all their care and support, thanks. This dissertation is specially dedicated to you.



*A mi familia  
y amigos*



# Contents

<b>Contents</b>	<b>i</b>
<b>List of Figures</b>	<b>v</b>
<b>List of Tables</b>	<b>ix</b>
<b>List of Abbreviations and Acronyms</b>	<b>xi</b>
<b>Nomenclature</b>	<b>xiii</b>
<b>1 Introduction</b>	<b>1</b>
1.1 Motivation and Objectives . . . . .	1
1.2 Background and Review of Previous Research . . . . .	2
1.2.1 Stationary and Synchronous Frames . . . . .	2
1.2.2 Plant Model for Digitally Current-Controlled VSCs . . . . .	3
1.2.2.1 L Filters . . . . .	3
1.2.2.2 LCL Filters . . . . .	4
1.2.2.3 Discrete-Time Plant Model . . . . .	6
1.2.3 Hysteresis Control . . . . .	7
1.2.3.1 Conventional Two-Level Fixed-Band Hysteresis Control . . . . .	8
1.2.3.2 Minimization of Interference Between Phases . . . . .	9
1.2.3.3 Variable-Band Hysteresis Control . . . . .	9
1.2.3.4 Other Improvements and Proposals . . . . .	10
1.2.3.5 Digital Implementation . . . . .	10
1.2.4 Deadbeat Control . . . . .	11
1.2.5 PI Control in SRF . . . . .	12
1.2.5.1 Conventional PI . . . . .	13
1.2.5.2 PI with Cross-Coupling Decoupling . . . . .	15
1.2.5.3 Complex Vector PI . . . . .	15
1.2.6 Repetitive Control . . . . .	17
1.2.6.1 Repetitive Controllers in Recursive Form . . . . .	17
1.2.6.2 DFT-Based Repetitive Controllers . . . . .	22
1.2.7 Resonant Control . . . . .	24
1.2.7.1 Fundamentals of PR Controllers . . . . .	24
1.2.7.2 Fundamentals of VPI Controllers . . . . .	26
1.2.7.3 Considerations About Simultaneous Cross-Coupling Decoupling for Both Positive- and Negative-Sequences . . . . .	27

1.2.7.4	Resonant Controllers in Fundamental SRF . . . . .	29
1.2.7.5	Relation with Repetitive Controllers . . . . .	30
1.2.7.6	Analysis and Design . . . . .	32
1.3	Major Results . . . . .	36
<b>2</b>	<b>Effects of Discretization Methods on the Performance of Resonant Controllers</b>	<b>41</b>
2.1	Introduction . . . . .	41
2.2	Digital Implementations of Resonant Controllers without Delay Compensation	43
2.2.1	Implementations Based on the Continuous Transfer Function Discretization . . . . .	43
2.2.2	Implementations Based on Two Discrete Integrators . . . . .	43
2.3	Influence of Discretization on Roots Distribution . . . . .	45
2.3.1	Resonant Poles Displacement . . . . .	45
2.3.2	Effects on Zeros Distribution . . . . .	48
2.3.2.1	Displacement of $R_{1h}(s)$ Zeros by Group E Discretizations . . . . .	48
2.3.2.2	Displacement of $R_{2h}(s)$ Zeros by Group E Discretizations . . . . .	49
2.3.2.3	Displacement of Zeros by Group D Discretizations . . . . .	50
2.4	Influence of Discretization on Delay Compensation . . . . .	50
2.4.1	Delay Compensation in the Continuous Domain . . . . .	50
2.4.2	Discrete-Time Implementations of Delay Compensation Schemes . . . . .	53
2.4.3	Study of Discretization Effects on Delay Compensation . . . . .	54
2.5	Summary of Optimum Discrete-Time Implementations . . . . .	59
2.6	Experimental Setup Description . . . . .	60
2.6.1	Tuning of $G_{PR_h}$ Controllers . . . . .	63
2.6.2	Tuning of $G_{VPI_h}$ Controllers . . . . .	63
2.7	Experimental Results . . . . .	64
2.7.1	Comparison of Steady-State Error Provided by Discrete-Time Implementations . . . . .	64
2.7.1.1	Steady-State Error of $G_{PR_h}(s)$ Discretizations . . . . .	65
2.7.1.2	Steady-State Error of $G_{VPI_h}(s)$ Discretizations . . . . .	65
2.7.2	Test of Discrete-Time Delay Compensation . . . . .	67
2.7.2.1	Delay Compensation in PR controllers . . . . .	69
2.7.2.2	Delay Compensation in VPI controllers . . . . .	69
2.7.3	Comparison of Computational Burden . . . . .	70
2.8	Conclusions . . . . .	72
<b>3</b>	<b>High Performance Digital Resonant Current Controllers Implemented with Two Integrators</b>	<b>75</b>
3.1	Introduction . . . . .	75
3.2	Review of Resonant Controllers Implemented with Two Integrators . . . . .	76
3.2.1	Resonant Controllers in the Continuous Domain . . . . .	76
3.2.2	Discretization of Schemes Based on Two Integrators and Its Inaccuracies	78
3.3	Correction of Poles: Improvement in Resonant Frequency Accuracy . . . . .	79
3.4	Correction of Zeros: Improvement in Delay Compensation Accuracy . . . . .	82
3.4.1	Improvement in Target Leading Angle Expression . . . . .	83

3.4.2	Enhanced Discrete-Time Delay Compensation Schemes Based on Two Integrators . . . . .	87
3.4.2.1	Correction of Delay Compensation Technique . . . . .	87
3.4.2.2	Comparison of Leading Angle Accuracy of the Different Delay Compensation Techniques . . . . .	91
3.5	Experimental Results . . . . .	92
3.5.1	Experimental Setup . . . . .	92
3.5.2	Improvement in Resonant Frequency Accuracy . . . . .	92
3.5.3	Improvement in Delay Compensation Accuracy . . . . .	96
3.5.3.1	Nominal Conditions . . . . .	96
3.5.3.2	Frequency Deviations from Nominal . . . . .	97
3.5.3.3	Summary . . . . .	98
3.6	Conclusions . . . . .	98
<b>4</b>	<b>Analysis and Design of Resonant Current Controllers for Voltage Source Converters by Means of Nyquist Diagrams and Sensitivity Function</b>	<b>101</b>
4.1	Introduction . . . . .	101
4.2	Analysis of Stability Margins by Means of Nyquist Diagrams . . . . .	103
4.2.1	Nyquist diagrams of PR Controllers . . . . .	104
4.2.2	Nyquist Diagrams of VPI Controllers . . . . .	110
4.3	Relation Between Closed-Loop Anomalous Peaks and the Sensitivity Function	112
4.3.1	Relation Between the Closed-Loop Transfer Function and the Sensitivity Function . . . . .	112
4.3.2	Anomalous Closed-Loop Peaks . . . . .	114
4.4	Minimization of Sensitivity Function . . . . .	116
4.4.1	Sensitivity Minimization in PR Controllers . . . . .	117
4.4.2	Sensitivity Minimization in VPI Controllers . . . . .	118
4.5	Experimental Results . . . . .	119
4.5.1	Sensitivity Minimization by Means of Optimum Leading Angle . . . . .	119
4.5.1.1	Sensitivity Minimization in PR Controllers . . . . .	120
4.5.1.2	Sensitivity Minimization in VPI controllers . . . . .	121
4.5.2	Active Power Filter Operating at Low Switching Frequency . . . . .	123
4.5.2.1	APF with PR Controllers . . . . .	124
4.5.2.2	APF with VPI controllers . . . . .	126
4.6	Conclusions . . . . .	128
<b>5</b>	<b>Conclusions and Future Research</b>	<b>129</b>
5.1	Conclusions . . . . .	129
5.2	Publications . . . . .	130
5.3	Future Research . . . . .	130
	<b>References</b>	<b>131</b>
<b>A</b>	<b>Mathematical Development of Expressions for Chapter 2</b>	<b>159</b>
A.1	Discretization of Resonant Controllers without Delay Compensation . . . . .	159
A.1.1	Zero-Order Hold . . . . .	159
A.1.2	First-Order Hold . . . . .	160

A.1.3	Forward Euler . . . . .	160
A.1.4	Backward Euler . . . . .	160
A.1.5	Tustin . . . . .	161
A.1.6	Tustin with Prewarping . . . . .	161
A.1.7	Zero-Pole Matching . . . . .	162
A.1.8	Impulse Invariant . . . . .	162
A.1.9	Forward Euler & Backward Euler . . . . .	163
A.1.10	Backward Euler & Backward Euler + Delay . . . . .	163
A.1.11	Tustin & Tustin . . . . .	164
A.2	Discretization of Resonant Controllers with Delay Compensation . . . . .	164
A.2.1	Zero-Order Hold . . . . .	164
A.2.2	First-Order Hold . . . . .	165
A.2.3	Tustin with Prewarping . . . . .	166
A.2.4	Zero Pole Matching . . . . .	167
A.2.5	Impulse Invariant . . . . .	168
A.2.6	Forward Euler & Backward Euler . . . . .	168
<b>B</b>	<b>Mathematical Development of Expressions for Chapter 3</b>	<b>171</b>
B.1	Phase of Plant Model at a Given Frequency . . . . .	171
B.2	Slope of Plant Model Phase at a Given Frequency . . . . .	171
<b>C</b>	<b>Mathematical Development of Expressions for Chapter 4</b>	<b>173</b>
C.1	$K_{PT}$ Expression as a Function of $\eta_P$ . . . . .	173
C.2	$\phi'_h$ Expression for $\eta_h$ Maximization in PR Controllers . . . . .	175
<b>D</b>	<b>Further Information About Testing Facilities</b>	<b>177</b>
D.1	dSPACE Platform . . . . .	177
D.2	Voltage Source Converter . . . . .	178
D.3	Chroma Voltage Source . . . . .	179
D.4	Kepeco Bidirectional Power Supply . . . . .	179
D.5	HP Power Supply for DC-Link . . . . .	180
D.6	Programmable Load . . . . .	180
D.7	Measurements . . . . .	181
D.8	Inductors . . . . .	183

# List of Figures

1.1	Relation between the stationary and synchronous reference frames. . . . .	3
1.2	Current-controlled VSC supplying a voltage source (or equivalent) through a low-pass filter. . . . .	4
1.3	Bode diagrams of L and LCL filters, with equivalent parameters at low frequencies. . . . .	5
1.4	Block diagram of LCL filter. . . . .	6
1.5	Block diagram of current control closed-loop (stationary frame). . . . .	7
1.6	Basic hysteresis controller implementation, referred to one phase. . . . .	8
1.7	Closed-loop Bode diagram provided by $G_{DB}(z)$ controller. . . . .	12
1.8	Conventional PI control in SRF. . . . .	14
1.9	Conventional PI control in SRF, including a leading angle $\phi'_h$ . . . . .	14
1.10	Complex vector block diagrams of closed-loop with different PI controllers in SRF. . . . .	15
1.11	Generation of periodic signal with period $n_d T_s$ . . . . .	17
1.12	Implementation of repetitive controller, according to (1.23). Resonant peaks are placed at both odd and even harmonics. . . . .	18
1.13	Implementation of repetitive controller that leads to resonant peaks only at odd harmonics. . . . .	18
1.14	Open-loop Bode diagrams of the repetitive controllers shown in Figs. 1.12 and 1.13 with a proportional gain equal to one in parallel. . . . .	19
1.15	Repetitive controller proposed in [19], which presents notches (zeros) at the intermediate frequencies between the resonant peaks. Resonant peaks are placed at both odd and even harmonics. . . . .	19
1.16	Modification of the repetitive controller shown in Fig. 1.15 that places resonant peaks only at odd harmonics and notches at even harmonics. . . . .	20
1.17	Open-loop Bode diagrams of the repetitive controllers shown in Figs. 1.15 and 1.16. . . . .	20
1.18	Modification of the repetitive controller shown in Fig. 1.15 that places resonant peaks at $6k \pm 1$ harmonics and notches at $3k$ harmonics, with $k \in \mathbb{N}$ . . . . .	21
1.19	Open-loop Bode diagram of the repetitive controller shown in Fig. 1.18. . . . .	21
1.20	Repetitive controller based on the DFT . . . . .	22
1.21	Open-loop Bode diagram of the DFT-based repetitive controller with a proportional gain equal to one in parallel. . . . .	23
1.22	Block diagrams of frequency adaptive resonant controllers $G_{PR_h}(s)$ and $G_{PR_h}^d(s)$ based on two integrators. . . . .	25

1.23	Block diagram of PI controllers with cross-coupling decoupling schemes implemented in positive- and negative-sequence SRF simultaneously. . . . .	28
1.24	Open-loop Bode diagrams $G_C(z) G_{PL}(z)$ obtained with PR controllers without delay compensation, for different $K_{I_h}$ values. . . . .	34
1.25	Closed-loop Bode diagrams using PR controllers with and without delay compensation. . . . .	35
1.26	Closed-loop Bode diagrams using VPI controllers. . . . .	37
2.1	Block diagram of frequency adaptive $G_{VPI_h}(s)$ controller based on two integrators. . . . .	44
2.2	Pole locus of the discretized resonant controllers. . . . .	46
2.3	Deviation of the actual resonant frequency $f_a$ of the discretized controller from the resonant frequency $hf_1$ of the continuous controller. . . . .	47
2.4	Bode plot of $R_{1_h}(s)$ discretized with group E methods, tuned at $hf_1 = 350$ Hz and with $f_s = 10$ kHz. . . . .	49
2.5	Study of group E discretizations effect on $R_{2_h}(s)$ zeros. . . . .	51
2.6	Frequency response of $R_{1_h}(s)$ and $G_{VPI_h}(s)$ implemented with group D methods, tuned at $hf_1 = 350$ Hz and with $f_s = 10$ kHz. . . . .	52
2.7	Implementations of $R_{1_h}^d(s)$ and $R_{2_h}^d(s)$ based on two integrators. . . . .	53
2.8	Frequency response of $R_{1_h}^d(s)$ and $R_{2_h}^d(s)$ , for different values of $n_s$ . . . . .	54
2.9	Study of the error in degrees $\epsilon_{\phi_h}$ between the expected and the actual phase within a vicinity of the resonant frequency, for $R_{1_h}^d(s)$ and $R_{2_h}^d(s)$ discretized with group E methods. . . . .	57
2.10	Study of the error in degrees $\epsilon_{\phi_h}$ between the expected and the actual phase within a vicinity of the resonant frequency, for $R_{1_h}^d(s)$ and $R_{2_h}^d(s)$ discretized with group D methods. . . . .	58
2.11	Active power filter lab prototype circuit and controller . . . . .	62
2.12	Open-loop Bode diagram of $G_C(z) G_{PL}(z)$ , for PR controllers with $n_h = 15$ . . . . .	64
2.13	Spectrum of programmed load current $i_L$ to test the effect of resonant poles displacement, both for $G_{PR_h}(z)$ and $G_{VPI_h}(z)$ . . . . .	65
2.14	Steady-state currents and spectra of $i_S$ for different discrete implementations of $G_{PR_h}(s)$ , with $n_h = 15$ and $f_1 = 50$ Hz. . . . .	67
2.15	Steady-state currents and spectra of $i_S$ for different discrete implementations of $G_{VPI_h}(s)$ , with $n_h = 15$ and $f_1 = 50$ Hz. . . . .	68
2.16	Spectrum of programmed load current $i_L$ for the tests of discrete-time delay compensation. . . . .	69
2.17	Steady-state currents and spectra of $i_S$ when implementing digital compensation of the computational delay, with $n_s = 2$ , $n_h = 61$ and $f_1 = 50$ Hz. . . . .	70
2.18	Steady-state currents and spectra of $i_S$ for frequency adaptive implementations of Table 2.10, with $n_h = 15$ and $f_1 = 52$ Hz. . . . .	74
3.1	Block diagrams of continuous resonant controllers based on two integrators. . . . .	77
3.2	Open-loop Bode diagrams provided by PR controllers with different $\phi_h$ values. . . . .	78
3.3	Block diagrams of digital resonant controllers based on two integrators, including proposed correction (3.5) for the resonant poles. . . . .	80
3.4	Resonant frequency error with the proposed correction (3.5) for the implementations based on two discrete integrators, as a function of $hf_1$ and $f_s$ . . . . .	81

3.5	Resonant frequency error with the proposed correction (3.5) for the implementations based on two discrete integrators, as a function of the ratio $hf_1/f_s$ . . . . .	82
3.6	Comparison of $ \angle G_{\text{PL}}(z) $ and leading angle provided by different expressions. . . . .	84
3.7	Closed-loop Bode diagrams using PR controllers with phase lead of two samples and according to (3.14), for $hf_1 \in \{1050, 1150, \dots, 2250\}$ Hz. In both cases, $\phi_h = \phi'_h$ has been assured. . . . .	85
3.8	Open-loop Bode diagrams $G_{\text{C}}(z) G_{\text{PL}}(z)$ using PR controllers with phase lead of two samples and according to (3.14). . . . .	86
3.9	Open-loop Bode diagrams provided by $G_{\text{PR}_h}^{\text{dimp}}(z)$ and $G_{\text{PR}_h}^{\text{d}'}(z)$ . . . . .	88
3.10	High performance proposed implementations of PR controllers based on two integrators, including resonant poles correction (3.5) and with different delay compensation techniques. . . . .	89
3.11	Leading angle error $\phi_h - \phi'_h$ provided by different implementations in presence of $f_1$ deviations, with $\phi'_h$ according to (3.14), and for $h \in \{1, 3, 5, \dots, 45\}$ . . . . .	91
3.12	Spectrum of programmed load current $i_{\text{L}}$ . . . . .	93
3.13	Steady-state currents and spectra of source current $i_{\text{S}}$ for different values of $n_{\text{T}}$ , with $f_1 = f_{1\text{n}} = 50$ Hz. . . . .	95
3.14	Test of frequency adaptation provided by Fig. 3.10b proposed scheme. . . . .	97
4.1	Nyquist diagram of generic $[K_{\text{P}_\text{T}} + K_{\text{I}_h} R_{1_h}^{\text{d}}(z)] G_{\text{PL}}(z)$ . . . . .	105
4.2	Nyquist diagrams of $[K_{\text{P}_\text{T}} + K_{\text{I}_h} R_{1_h}^{\text{d}}(z)] G_{\text{PL}}(z)$ ( $\phi'_h = 0$ ) for different values of $K_{\text{P}_\text{T}}$ . . . . .	107
4.3	Examples of $[K_{\text{P}_\text{T}} + K_{\text{I}_h} R_{1_h}^{\text{d}}(z)] G_{\text{PL}}(z)$ with two different $R_{1_h}^{\text{d}}$ , which show that $\eta_h$ provides more information about the actual proximity to instability than $PM_h$ . . . . .	108
4.4	Examples of $[K_{\text{P}_\text{T}} + K_{\text{I}_h} R_{1_h}^{\text{d}}(z)] G_{\text{PL}}(z)$ with two different $\phi'_h$ , which show that $\phi'_h = \angle G_{\text{PL}}(e^{jh\omega_1 T_s})$ increases $PM_h$ at the expense of reducing $\eta_h$ with respect to other $\phi'_h$ values. . . . .	108
4.5	$K_{\text{P}_\text{T}}$ tuning to obtain a certain $\eta_{\text{P}}$ , according to (4.5). . . . .	109
4.6	Nyquist diagram of generic $G_{\text{VPI}_h}^{\text{d}}(z) G_{\text{PL}}(z)$ . . . . .	110
4.7	Effect of $K_h$ variation in $G_{\text{VPI}_h}^{\text{d}}(z)$ controller. . . . .	111
4.8	Relation between $C_{\text{L}}(z)$ and $S(z) = 1/D(z)$ , according to (4.9). . . . .	113
4.9	Examples of closed-loop anomalous peaks. Point A corresponds with the resonant frequency $hf_1$ , and B is the closest point to $(-1, 0j)$ . . . . .	116
4.10	Optimum asymptote at $h\omega_1$ in order to maximize $D(z)$ at frequencies around $h\omega_1$ , in $G_{\text{PR}_h}^{\text{d}}(z)$ controllers. . . . .	117
4.11	Optimum $\phi'_h$ values in order to maximize $D(z)$ around $hf_1$ , as a function of $hf_1$ and $K_{\text{P}_\text{T}}$ . . . . .	118
4.12	Experimental setup for the tests of section §4.5.1. . . . .	119
4.13	Experimental tests that compare the effect of a $i^*$ deviation from $f_1 = 50$ Hz to $f_1 = 50.46$ Hz on a $G_{\text{PR}_h}^{\text{d}}(z)$ controller tuned at $h = 13$ , when $\phi'_h = 0$ and $\phi'_h$ according to proposed expression (4.17) are employed. . . . .	121
4.14	Experimental tests that compare the effect of a $i^*$ deviation from $f_1 = 50$ Hz to $f_1 = 49.6$ Hz on a $G_{\text{PR}_h}^{\text{d}}(z)$ controller tuned at $h = 15$ , when $\phi'_h = 2.2698$ rad $\approx \angle G_{\text{PL}}(e^{jh\omega_1 T_s})$ and $\phi'_h$ according to proposed expression (4.17) are employed. . . . .	122

4.15	Experimental tests that compare the effect of a $i^*$ deviation from $f_1 = 50$ Hz to $f_1 = 50.12$ Hz on a $G_{\text{VPI}_h}^d(z)$ controller tuned at $h = 26$ , when $\phi'_h = 0$ and $\phi'_h$ according to proposed expression (4.17) are employed. . . . .	123
4.16	Spectrum of the current $i_L$ demanded by the load, in the active power filter tests. . . . .	124
4.17	Nyquist diagram of active power filter current control $G_C(z)G_{\text{PL}}(z)$ with PR controller. . . . .	125
4.18	Experimental captures of active power filter operating at low switching frequency and with PR current controller. . . . .	126
4.19	Active power filter transient performance with PR controller when the harmonic compensation is enabled. . . . .	126
4.20	Nyquist diagram of active power filter current control $G_C(z)G_{\text{PL}}(z)$ with VPI controllers. . . . .	127
4.21	Experimental captures of active power filter operating at low switching frequency and with VPI current controllers. . . . .	127
4.22	Active power filter transient performance with VPI controllers when the harmonic compensation is enabled. . . . .	128
C.1	Matlab script to obtain (C.6) and (C.9). . . . .	175
D.1	Block diagram of dSPACE DS1004 platform. . . . .	178
D.2	Voltage source converter. . . . .	179
D.3	Chroma 61501 voltage source. . . . .	180
D.4	Kepeco BOP100-4D bidirectional power supply. . . . .	180
D.5	HP 6035A power supply. . . . .	180
D.6	Hoherl & Hackl ZSAC426 programmable load. . . . .	181
D.7	Tektronix TPS2014 digital oscilloscope. . . . .	181
D.8	Box including voltage and current sensors, as well as their conditioner circuits. . . . .	182
D.9	Inductors. . . . .	182

# List of Tables

2.1	Relations for discretizing $R_{1_h}(s)$ and $R_{2_h}(s)$ by different methods . . . . .	43
2.2	$z$ -domain transfer functions obtained by discretization of $R_{1_h}(s)$ and $R_{2_h}(s)$ by different methods . . . . .	44
2.3	Discrete transfer functions $G_{PR_h}(s)$ and $G_{VPI_h}(s)$ obtained by two discretized integrators . . . . .	45
2.4	Groups of expressions with identical poles in the $z$ -domain . . . . .	46
2.5	$R_{1_h}^d(s)$ discretized by groups E and D . . . . .	55
2.6	$R_{2_h}^d(s)$ discretized by groups E and D . . . . .	55
2.7	Performance summary of the discrete-time implementations . . . . .	59
2.8	Optimum discrete-time implementations . . . . .	60
2.9	Power circuit values . . . . .	61
2.10	Implementation code for the tests of computational burden . . . . .	71
2.11	Execution time of the controllers in the tests of steady-state error . . . . .	72
3.1	Resonant frequency error (Hz) with $f_s = 10\text{kHz}$ . . . . .	81
3.2	Phase margin (deg) of individual resonant controllers . . . . .	87
3.3	Implementation code for the tests of section §3.5.2 . . . . .	93
3.4	Current control execution times . . . . .	96
4.1	Power circuit values for tests of section §4.5.1 . . . . .	119
4.2	Power circuit values for tests of section §4.5.2 . . . . .	124



# List of Abbreviations and Acronyms

<b>ADC</b>	analog to digital converter
<b>APF</b>	active power filter
<b>DCT</b>	discrete cosine transform
<b>DFT</b>	discrete Fourier transform
<b>DSP</b>	digital signal processor
<b>EMF</b>	electromotive force
<b>ESR</b>	equivalent series resistance
<b>FFT</b>	fast Fourier transform
<b>FIR</b>	finite impulse response
<b>FOH</b>	first-order hold
<b>FPGA</b>	field-programmable gate array
<b>IEEE</b>	Institute of Electrical and Electronic Engineers
<b>IGBT</b>	insulated-gate bipolar transistor
<b>PC</b>	personal computer
<b>PCC</b>	point of common coupling
<b>PCI</b>	peripheral component interconnect
<b>PI</b>	proportional-integral
<b>PICCD</b>	PI controller with cross-coupling decoupling
<b>PLL</b>	phase-locked loop
<b>PMSM</b>	permanent magnet synchronous motor
<b>PPC</b>	PowerPC
<b>PR</b>	proportional-resonant

<b>PWM</b>	pulsewidth modulation
<b>RMS</b>	root mean square
<b>RTI</b>	real-time interface
<b>SDRAM</b>	synchronous dynamic random memory
<b>SRF</b>	synchronous reference frame
<b>STATCOM</b>	static synchronous compensator
<b>THD</b>	total harmonic distortion
<b>UPS</b>	uninterruptible power supply
<b>VPI</b>	vector proportional-integral
<b>VSC</b>	voltage source converter
<b>ZOH</b>	zero-order hold
<b>ZPM</b>	zero-pole matching

# Nomenclature

$BPF_h$	Transfer function of band-pass filter centered at $hf_1$ .
$C$	Capacitance.
$\mathbf{C}$	Clarke transformation matrix.
$C_h$	Corrected input for resonant controllers implemented with two integrators that improves the resonant frequency accuracy.
$C_L$	Closed-loop transfer function.
$D$	Distance between the Nyquist plot and the critical point $(-1, 0j)$ .
$\delta$	Constant in the range $(0,1]$ that adds damping to the poles of a repetitive controller with feedforward path.
$e$	Tracking error $i^* - i$ .
$e_{\max}$	Upper bound of the band for a hysteresis controller.
$e_{\min}$	Lower bound of the band for a hysteresis controller.
$E$	$Z$ transform of $e$ .
$\varepsilon_d$	Difference between $ C_L(z) $ and its average value $1/ D(z) $ , when $\angle D(z)$ varies in the range $(-\pi, \pi)$ .
$\varepsilon_{\phi_h}$	Error in degrees between the expected and the actual phase within a vicinity of the resonant frequency of a resonant term with delay compensation.
$f_1$	Fundamental frequency in hertz.
$f_{1n}$	Nominal value of $f_1$ .
$f_{90}$	Frequency in hertz located a decade above the L filter pole.
$f_a$	Actual resonant frequency in hertz of a resonant controller in the $z$ -domain.
$f_c$	Crossover frequency of $K_{PT} G_{PL}(z)$ in hertz.
$f_{\text{res}}$	Resonant frequency in hertz of an LCL filter.

$f_s$	Sampling frequency in hertz.
$f_{sw}$	Switching frequency in hertz.
$F_1$	Expression to calculate which $K_{PT}$ should be employed in order to achieve a certain sensitivity peak $1/\eta_P$ when implementing PR controllers.
$F_2$	Expression for $\phi'_h$ to minimize $\eta_h$ in PR Controllers.
$\phi_h$	Difference between the actual phase provided by a given resonant controller at frequencies infinitely close to $h\omega_1$ and that provided by $G_{PR_h}(s)$ .
$\phi'_h$	Parameter to introduce delay compensation in a resonant controller transfer function. In the case of $G_{PR_h}^d$ controllers, it is also the target (design) value for $\phi_h$ .
$\phi'_{hm}$	Particular case of $\phi'_h$ , which represents the target $\phi_h$ for a $G_{PR_h}^d$ controller tuned at the harmonic $h$ of the nominal fundamental frequency $\omega_{1n}$ .
$\phi'_0$	Ordinate at the origin of $\phi'_h$ expression.
$G_C$	Transfer function of current controller.
$G_L$	Transfer function of L filter $[I(s)/V_C(s)]$ .
$G_{LCL}^C$	Transfer function of LCL filter, when control of $i_C$ is performed $[I_C(s)/V_C(s)]$ .
$G_{LCL}^G$	Transfer function of LCL filter, when control of $i_G$ is performed $[I_G(s)/V_C(s)]$ .
$G'_L$	$G_L$ transformed to fundamental SRF.
$G_{PI}$	Transfer function of conventional PI controller.
$G_{PI_h}$	Transfer function of conventional PI controller in a SRF rotating at $\omega_o = h\omega_1$ .
$G_{PI_h}^+$	Equivalent transfer function in stationary frame of a $G_{PI_h}$ controller implemented in a positive-sequence SRF.
$G_{PI_h}^-$	Equivalent transfer function in stationary frame of a $G_{PI_h}$ controller implemented in a negative-sequence SRF.
$G_{cPI_h}$	Transfer function of complex vector PI controller.
$G_{cPI_h}^+$	Equivalent transfer function in stationary frame of a $G_{cPI_h}$ controller implemented in a positive-sequence SRF.
$G_{cPI_h}^-$	Equivalent transfer function in stationary frame of a $G_{cPI_h}$ controller implemented in a negative-sequence SRF.
$G_{PL}$	Transfer function of plant model.
$G_{PR_h}$	Transfer function of PR controller tuned at harmonic order $h$ .

$G_{\text{PR}_h}^{\text{d}}$	Transfer function of PR controller with delay compensation and tuned at harmonic order $h$ .
$G_{\text{PR}_h}^{\text{d}'}$	Transfer function to obtain an accurate phase lead ( $\phi_h = \phi_h'$ ) in the discrete-time domain for a PR controller with delay compensation and tuned at harmonic order $h$ .
$G_{\text{VPI}_h}$	Transfer function of VPI controller tuned at harmonic order $h$ .
$G_{\text{cVPI}_h}$	Modification of $G_{\text{VPI}_h}$ to achieve full plant cross-coupling decoupling when implemented in fundamental SRF.
$G_{\text{VPI}_h}^{\text{d}}$	Transfer function of VPI controller with delay compensation and tuned at harmonic order $h$ .
$GM_h$	Gain margin of a resonant controller tuned at harmonic order $h$ : either $K_{\text{PT}} + K_{\text{I}_h} R_{1_h}(z)$ , $K_{\text{PT}} + K_{\text{I}_h} R_{1_h}^{\text{d}}(z)$ , $G_{\text{VPI}_h}(z)$ or $G_{\text{VPI}_h}^{\text{d}}(z)$ .
$GM_{\text{P}}$	Gain margin of $K_{\text{PT}} G_{\text{PL}}(z)$ .
$\gamma_h$	Angle between the asymptote of a Nyquist trajectory at $h\omega_1$ (limit from the left) and the real axis.
$\eta$	Modulus of the minimum distance between a Nyquist plot and the critical point $(-1, 0j)$ .
$\eta_h$	Modulus of the minimum distance between the critical point $(-1, 0j)$ and the Nyquist plot of a resonant controller tuned at harmonic order $h$ : either $K_{\text{PT}} + K_{\text{I}_h} R_{1_h}(z)$ , $K_{\text{PT}} + K_{\text{I}_h} R_{1_h}^{\text{d}}(z)$ , $G_{\text{VPI}_h}(z)$ or $G_{\text{VPI}_h}^{\text{d}}(z)$ .
$\eta_{\text{P}}$	Modulus of the minimum distance between the critical point $(-1, 0j)$ and the Nyquist plot of $K_{\text{PT}} G_{\text{PL}}(z)$ .
$i$	Generic current signal.
$i^*$	Generic current reference.
$i_{\text{a}}$	Phase a current in a three-phase system.
$i_{\alpha}$	Projection of the current onto the $\alpha$ axis of a stationary frame.
$i_{\alpha\beta}$	Current complex vector, expressed in stationary frame ( $i_{\alpha} + j i_{\beta}$ ).
$i_{\alpha\beta}^*$	Reference for $i_{\alpha\beta}$ .
$i_{\text{b}}$	Phase b current in a three-phase system.
$i_{\beta}$	Projection of the current onto the $\beta$ axis of a stationary frame.
$i_{\text{c}}$	Phase c current in a three-phase system.
$i_{\text{C}}$	Converter-side current in an LCL filter.

$i_d$	Projection of the current onto the d axis of a SRF.
$i_d^*$	Reference for $i_d$ .
$i_{dq}$	Current complex vector, expressed in SRF ( $i_d + j i_q$ ).
$i_{dq}^*$	Reference for $i_{dq}$ .
$i_F$	Current supplied by a VSC operating as a shunt APF.
$i_G$	Grid-side current in an LCL filter.
$i_F^*$	Reference for $i_F$ .
$i_{F1}^*$	Fundamental component of $i_F^*$ .
$i_L$	Current demanded by a nonlinear load.
$i_{L1}$	Fundamental component of $i_L$ .
$i_{Lh}$	Harmonic components of $i_L$ .
$i_S$	Current supplied by a voltage source.
$I$	Laplace or Z transform of $i$ .
$I^*$	Laplace or Z transform of $i^*$ .
$I_C$	Laplace transform of $i_C$ .
$I_G$	Laplace transform of $i_G$ .
$i_q$	Projection of the current onto the q axis of a SRF.
$i_q^*$	Reference for $i_q$ .
$k$	Generic natural value.
$K_d$	Degree of freedom in the zero-pole matching discretization method.
$k_h$	Gain of a $G_{cPI_h}$ controller, equal to $k_{P_h}/L_F$ .
$K_h$	Gain of a VPI controller, equal to $K_{P_h}/L_F$ .
$k_I$	Integral gain of a $G_{PI}$ controller.
$k_{I_h}$	Integral gain of a $G_{PI_h}$ or $G_{cPI_h}$ controller.
$K_{I_h}$	Integral gain of a resonant controller tuned at harmonic order $h$ .
$k_P$	Proportional gain of a $G_{PI}$ controller.

$k_{P_h}$	Proportional gain of a $G_{PI_h}$ or $G_{cPI_h}$ controller.
$K_{P_h}$	Proportional gain of a resonant controller tuned at harmonic order $h$ .
$K_{P_T}$	Sum of the $K_{P_h}$ gains of all PR controllers included in $G_C(z)$ .
$\mathcal{L}$	Laplace transform.
$\mathcal{L}^{-1}$	Inverse Laplace transform.
$L_C$	Converter-side inductance in an LCL filter.
$L_F$	Inductance of the L filter in series with the VSC.
$L_G$	Grid-side inductance in an LCL filter.
$L_S$	Output inductance of voltage source.
$\lambda$	Slope of $-\angle G_{PL}(z)$ with respect to frequency at a certain frequency $\omega_\lambda$ .
$\lambda_k$	Generic real value. The subindex $k \in \mathbb{N}$ is employed to distinguish among several real values.
$m$	Pulsewidth modulation duty cycle.
$n_d$	Number of samples delayed in order to implement a repetitive controller. It is selected so that $n_d T_s = 1/f_1$ .
$n_h$	Highest harmonic order to be controlled by means of resonant controllers.
$n_s$	Number of samples to compensate by delay compensation.
$n_T$	Taylor series order for the resonant poles correction $C_h$ .
$N_h$	Set of harmonic orders to be controlled.
<b>P</b>	Park transformation matrix.
$PM_h$	Phase margin of a resonant controller tuned at harmonic order $h$ : either $K_{P_T} + K_{I_h} R_{1_h}(z)$ , $K_{P_T} + K_{I_h} R_{1_h}^d(z)$ , $G_{VPI_h}(z)$ or $G_{VPI_h}^d(z)$ .
$PM_P$	Phase margin of $K_{P_T} G_{PL}(z)$ .
$R_{1_h}$	Resonant term of the form $s/(s^2 + h^2 \omega_1^2)$ .
$R_{2_h}$	Resonant term of the form $s^2/(s^2 + h^2 \omega_1^2)$ .
$R_{1_h}^d$	Resonant term $R_{1_h}$ including delay compensation.
$R_{2_h}^d$	Resonant term $R_{2_h}$ including delay compensation.
$R_F$	ESR of the L filter in series with the VSC.

$R_C$	ESR of the converter-side inductor, in an LCL filter.
$R_D$	Resistance in series with the capacitor, in an LCL filter, to passively damp its resonance.
$R_G$	ESR of the grid-side inductor, in an LCL filter.
$\rho$	Variable equal to $e^{R_F T_s / L_F}$ .
$S$	Sensitivity function.
$t$	Time.
$T_s$	Sampling period.
$\theta_1$	Phase of grid voltage fundamental component.
$\hat{\theta}_1$	Estimated $\theta_1$ .
$v_{ac}$	Generic alternating voltage, which acts as a perturbation of the current control.
$v_C$	Output voltage of the VSC.
$v_D$	Voltage drop in the capacitor and damping resistance of an LCL filter.
$v_{dc}$	Dc-link voltage of the VSC.
$v_{dc}^*$	Reference for $v_{dc}$ .
$v_{PCC}$	Voltage in the point of common coupling.
$v_S$	Output voltage of voltage source.
$V_{ac}$	Laplace transform of $v_{ac}$ .
$V_C$	Laplace transform of $v_C$ .
$V_D$	Laplace transform of $v_D$ .
$\omega$	Generic frequency in radians per second.
$\omega_0$	Synchronous frequency of a SRF in radians per second.
$\omega_1$	Fundamental frequency in radians per second.
$\omega_{1n}$	Nominal value of $\omega_1$ .
$\hat{\omega}_1$	Estimated $\omega_1$ .
$\omega_B$	Frequency that corresponds to point B, at which $ D(z) $ is minimum, in radians per second.

$\omega_c$	Crossover frequency of $K_{PT} G_{PL}(z)$ in radians per second.
$\omega_\eta$	Frequency at which $ D(z) $ has its global minimum $\eta_P$ , when PR controllers are employed, in radians per second.
$\omega_\lambda$	Frequency at which the slope of $-\angle G_{PL}(z)$ with respect to frequency is $\lambda$ , in radians per second.
$\xi_h$	Damping factor of $BPF_h(s)$ .
$Y^C$	Transfer function of converter-side inductor admittance in an LCL filter.
$Y^G$	Transfer function of grid-side inductor admittance in an LCL filter.
$\mathcal{Z}$	Z transform.
$Z^D$	Transfer function of capacitor and damping resistance impedance in an LCL filter.

### Superscripts Relative to Discretization Methods (Chapter 2)

$X$	Resonant term or resonant controller discretized with method $X$ , where $X \in \{\text{zoh, foh, f, b, t, tp, zpm, imp}\}$ .
$X\&Y$	Resonant term or resonant controller implemented with two discrete integrators, with the direct one discretized with method $X$ and the feedback one with method $Y$ , where $X, Y \in \{\text{zoh, foh, f, b, t, tp, zpm, imp}\}$ .
$X-Y$	Resonant controller $G_{VPI_h}(z)$ or $G_{VPI_h}^d(z)$ , in which $R_{1_h}(s)$ or $R_{1_h}^d(s)$ is discretized with method $X$ and $R_{2_h}(s)$ or $R_{2_h}^d(s)$ with method $Y$ , where $X, Y \in \{\text{zoh, foh, f, b, t, tp, zpm, imp}\}$ .



# Chapter 1

## Introduction

### 1.1 Motivation and Objectives

Sinusoidal current regulation of voltage source converters (VSCs) is an aspect of paramount importance to achieve a high level of performance in a lot of different applications, such as ac motor drives, active power filters (APFs), wind turbines, static synchronous compensators (STATCOMs), photovoltaic inverters and active rectifiers. In this manner, the research and development in the field of current controllers for VSCs has been a very active area in recent years.

Currently, one of the most extended types of current regulators are resonant controllers, which achieve zero steady-state error at selected frequencies, while providing a good combination of simplicity and high performance. Nevertheless, there are certain aspects with regard to these controllers that have not been approached in the technical literature on the matter, and that should be investigated in order to take advantage of their actual potential. This work provides an in-depth study of uncovered issues regarding digital resonant controllers for current regulation in VSCs.

Most studies devoted to resonant controllers have been carried out in the continuous domain; however, their observations and conclusions cannot be directly applied to digital devices, which work in the discrete-time domain. In nowadays scenarios, most current controllers are implemented in digital platforms, so the influence of the discretization process should not be ignored. One of the main objectives of this thesis is to provide an in-depth comparison among the effects of discretization strategies when applied to resonant controllers, and to develop optimized discrete-time implementations to achieve a high performance in combination with a suitable resource-consumption and complexity.

On the other hand, the existing approaches for analysis and design of digital resonant current controllers, which are mainly based on the phase margin criterion, are proved in this thesis to be very limited, specially in cases in which more than one cross-over frequency exists. This constraint excludes applications such as selective control (which is desirable because of reasons such as lowering of converter rating) and tracking of relatively high frequencies with respect to the switching frequency (e.g., in high power converters). Thus, another objective of this dissertation is to develop a systematic method to obtain the highest stability and performance, even when there are multiple 0 dB crossings.

## 1.2 Background and Review of Previous Research

In this section, several important background concepts are introduced, and a brief review of the state-of-the-art in current control for VSCs is presented. Special focus is devoted to proportional-integral (PI) regulators in synchronous reference frame (SRF) and to their equivalents in stationary frame: the repetitive and resonant controllers (with which most contributions of this thesis deal).

### 1.2.1 Stationary and Synchronous Frames

Given a three-phase system, with  $i_a$ ,  $i_b$  and  $i_c$  being the currents in each of the three phases, the Clarke transform  $\mathbf{C}$  can be expressed as

$$\begin{pmatrix} i_\alpha \\ i_\beta \end{pmatrix} = \underbrace{\frac{2}{3} \begin{pmatrix} 1 & -\frac{1}{2} & -\frac{1}{2} \\ 0 & \frac{\sqrt{3}}{2} & -\frac{\sqrt{3}}{2} \end{pmatrix}}_{\mathbf{C}} \cdot \begin{pmatrix} i_a \\ i_b \\ i_c \end{pmatrix} \quad (1.1)$$

where  $i_\alpha$  and  $i_\beta$  result from the projection of a vector  $i_{\alpha\beta} = i_\alpha + j i_\beta$  onto a stationary reference frame with two orthogonal axes:  $\alpha$  and  $\beta$  (see Fig. 1.1) [20]. These two variables (and, hence, also  $i_{\alpha\beta}$ ) include all information about both positive- and negative-sequences of the three-phase currents, and none about their zero-sequence. Hence, this transformation permits to control the three currents  $i_a$ ,  $i_b$  and  $i_c$  by means of just two controllers (one in each of the  $\alpha\beta$  axes), as long as there is no homopolar current (e.g., when there is no neutral wire).

The Park transformation  $\mathbf{P}$  can be expressed as

$$\begin{pmatrix} i_d \\ i_q \end{pmatrix} = \underbrace{\frac{2}{3} \begin{pmatrix} \cos(\theta) & \cos(\theta - \frac{2\pi}{3}) & \cos(\theta + \frac{2\pi}{3}) \\ -\sin(\theta) & -\sin(\theta - \frac{2\pi}{3}) & -\sin(\theta + \frac{2\pi}{3}) \end{pmatrix}}_{\mathbf{P}} \cdot \begin{pmatrix} i_a \\ i_b \\ i_c \end{pmatrix} \quad (1.2)$$

where  $\theta = \omega_0 t$  is an instantaneous phase angle at instant  $t$  and  $\omega_0$  is the synchronous frequency [21]. The variables  $i_d$  and  $i_q$  are the projections of  $i_{\alpha\beta}$  onto two orthogonal axes rotating with angular speed  $\omega_0$ . This rotating frame associated with the Park transformation and synchronized with the phase of the signals to control is known as SRFs. Fig. 1.1 illustrates the relation between the stationary and synchronous (dq axes) reference frames. The current can be expressed with respect to the SRF as  $i_{dq} = i_d + j i_q$ .

The constant  $2/3$  included in the Clarke and Park transforms assures that the rms and peak magnitudes of the signals are kept invariant. To maintain the power value,  $\sqrt{2/3}$  should be employed instead.

Transformation between stationary and synchronous frames can be performed by means of the following relations:

$$i_{\alpha\beta} = i_{dq} e^{j\omega_0 t} = i_{dq} [\cos(\omega_0 t) + j \sin(j\omega_0 t)] \quad (1.3)$$

$$i_{dq} = i_{\alpha\beta} e^{-j\omega_0 t} = i_{\alpha\beta} [\cos(\omega_0 t) - j \sin(j\omega_0 t)]. \quad (1.4)$$

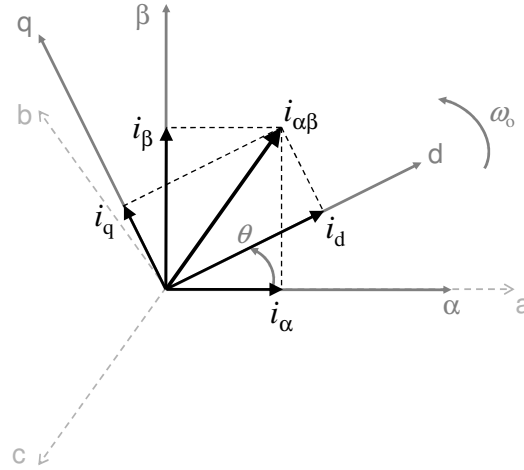


Figure 1.1: Relation between the stationary ( $\alpha\beta$  axes) and synchronous ( $dq$  axes) reference frames. The SRF rotates with  $\theta = \omega_o t$ .

From (1.4), it can be observed that the Park transformation introduces a  $-\omega_o$  frequency shift in the stationary frame variables. In this manner, the components that alternate at  $\omega_o$  with respect to the  $\alpha\beta$  axes become constants in the SRF, so it is easier to operate with their values and to control them.

## 1.2.2 Plant Model for Digitally Current-Controlled VSCs

The plant modeling is an essential step for the control analysis, so special care should be taken to assure its accuracy. The system under study is a VSC whose alternating current is controlled by means of a digital device. In these converters, usually a passive element filters the high-order harmonics that result from the commutation of their switches. They can be mainly classified into first-order inductive filters (L), second-order filters (LC) and third-order filters (LCL). Nevertheless, it should be noted that LC filters are just a particular case of LCL filters in which the third inductance is considered to be negligible. Hence, in this section we will focus on L and LCL ones.

### 1.2.2.1 L Filters

The generic situation depicted in Fig. 1.2a (single-phase representation) is valid for many applications, from adjustable speed drives to active filters or active rectifiers [22–24]. It is a digitally current-controlled VSC with pulsewidth modulation (PWM), connected in series with an L filter that attenuates the commutation harmonics and a voltage source (or equivalent).  $L_F$  and  $R_F$  are the filter inductance and equivalent series resistance (ESR), respectively (the output impedance of the source can be included). The signal  $v_C$  corresponds to the VSC output voltage. The source voltage  $v_{ac}$  may represent, for example, the grid voltage or the back electromotive force (EMF) of an electric machine. Note that any additional elements connected in parallel to the voltage source (such as nonlinear loads, in the case of a shunt APF) do not alter this model. Induction motors can be also transformed into an equivalent LR load as that in Fig. 1.2a by approximately decoupling the back EMF caused by the rotor flux [25], by means of a rotor flux estimation as in [26].

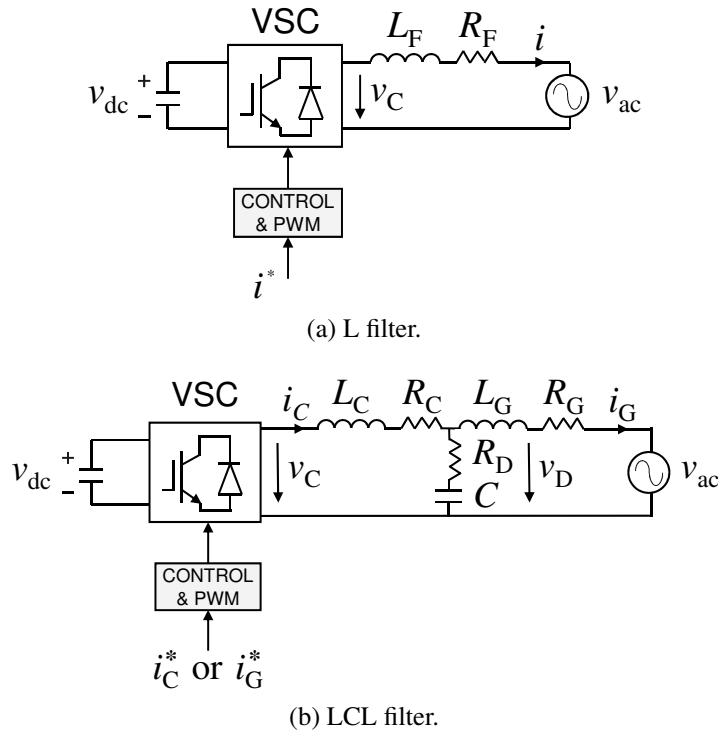


Figure 1.2: Current-controlled VSC supplying a voltage source (or equivalent) through a low-pass filter (single-phase representation). Other control inputs are omitted for clarity.

The behavior of the L filter can be modeled by the transfer function

$$G_L(s) = \frac{I(s)}{V_C(s)} = \frac{1}{sL_F + R_F}. \quad (1.5)$$

The dotted line in Fig. 1.3 represents the Bode diagram of  $G_L(s)$ , in which the filter low-pass behavior (20 dB per decade) can be appreciated.

### 1.2.2.2 LCL Filters

Alternatively to L filters, implementation of LCL filters is getting increasing attention in recent years for grid-connected converters [27], mainly because of its greater attenuation of commutation harmonics. Fig. 1.2b depicts the single-phase representation of a VSC connected through an LCL filter. In this case, the voltage source (which supplies  $v_{ac}$ ) usually corresponds to the grid voltage, since LCL filters are mainly employed for grid-connected converters (to meet the grid interconnection standards [28]).  $L_C$  and  $R_C$  represent the inductance and ESR of the converter-side inductor, respectively.  $L_G$  and  $R_G$  are the inductance and ESR of the grid-side inductor.  $C$  is the filter capacitance, and  $R_D$  is the addition of the capacitance ESR and a resistor that may be placed in series with it to perform passive damping of the LCL resonance [29, 30]. The currents  $i_C$  and  $i_G$  are the converter-side and grid-side ones, respectively. It should be remarked that control can be performed on any of these two currents, by means of the reference signals  $i_C^*$  or  $i_G^*$ .

The relations between the voltages and currents shown in Fig. 1.2b are described by the

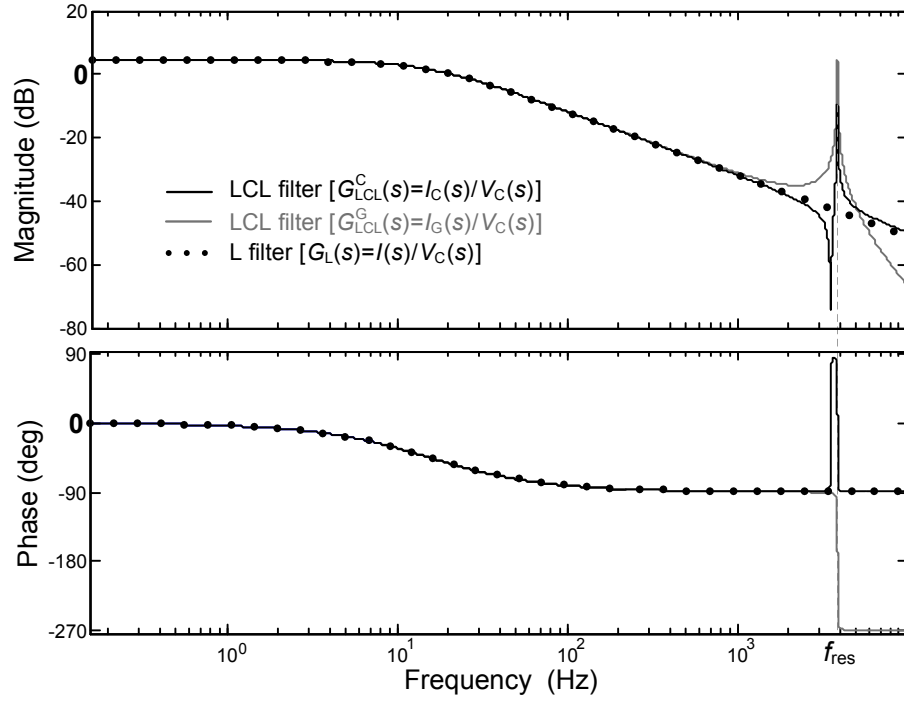


Figure 1.3: Bode diagrams of L and LCL filters, with equivalent parameters at low frequencies (i.e.,  $L_F = L_C + L_G$  and  $R_F = R_C + R_G$ ). Parameters:  $L_F = 6$  mH,  $R_F = 0.6 \Omega$ ,  $L_C = 5$  mH,  $R_C = 0.5 \Omega$ ,  $L_G = 1$  mH,  $R_G = 0.1 \Omega$ ,  $R_D = 0$ ,  $C = 2 \mu\text{F}$ .

transfer functions

$$\frac{I_C(s)}{V_C(s) - V_D(s)} = \frac{1}{sL_C + R_C} = Y^C(s) \quad (1.6)$$

$$\frac{I_G(s)}{V_D(s) - V_{ac}(s)} = \frac{1}{sL_G + R_G} = Y^G(s) \quad (1.7)$$

$$\frac{V_D(s)}{I_C(s) - I_G(s)} = \frac{1}{sC} + R_D = Z^D(s). \quad (1.8)$$

With these expressions, the LCL filter can be modeled by means of the block diagram shown in Fig. 1.4. Depending on whether  $i_C$  or  $i_G$  is considered, and according to the application of Mason's gain formula [31] to the LCL block diagram shown in Fig. 1.4, the transfer functions of the LCL filter can be expressed as

$$G_{LCL}^C(s) = \frac{I_C(s)}{V_C(s)} = \frac{Y^C(s) [1 + Y^G(s) Z^D(s)]}{1 + Y^C(s) Z^D(s) + Y^G(s) Z^D(s)} \quad (1.9)$$

$$G_{LCL}^G(s) = \frac{I_G(s)}{V_C(s)} = \frac{Y^C(s) Y^G(s) Z^D(s)}{1 + Y^C(s) Z^D(s) + Y^G(s) Z^D(s)}. \quad (1.10)$$

The main advantages of LCL filters over L filters are the following [27, 28, 30, 32–34].

- At high frequencies, the gain decays 60 dB per decade instead of 20 dB per decade, because of their third-order nature. Consequently, they provide better attenuation of switching harmonics. This can be checked in Fig. 1.3, which shows Bode diagrams of L and LCL filters.

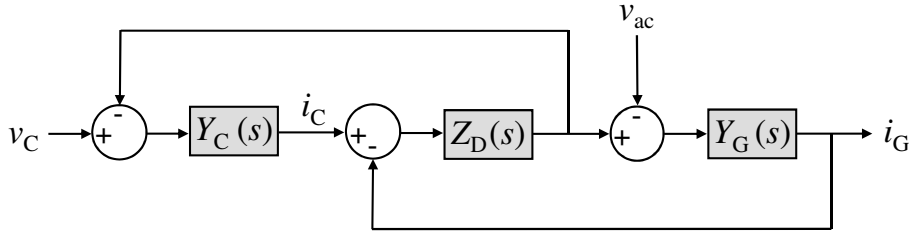


Figure 1.4: Block diagram of LCL filter.

- Smaller size and cost, to obtain the same attenuation of commutation harmonics. This is a consequence of the previous bullet.
- Reduction of electromagnetic interference.

On the other hand, they present the following drawbacks [27, 30, 33–36].

- More complex power circuit. In fact, a lot of works have been published regarding design issues of LCL filters [28, 29, 37–39].
- A resonance is introduced in the system (at resonant frequency  $f_{\text{res}}$  in Fig. 1.3), which may lead to undesired oscillations or instability. Active (by means of digital control) [30, 32–34, 36, 38, 40–48] and passive ( $R_D \neq 0$ ) [28, 29, 39, 42] damping techniques have been proposed to attenuate the resonant peak. The former is usually preferable, since the latter implies greater power losses [42].
- Uncertain resonant modes associated with grid and filter parameter variations. Specific controllers aimed at enhancing robustness to these uncertainties have been developed [27, 32, 49, 50].

Regarding the plant model of an LCL filter for the purpose of analysis and design of resonant controllers, it should be remarked that (1.9) and (1.10) can be usually simplified to (1.5). From Fig. 1.3, the frequency response of an LCL filter is approximately the same as that of an L filter at frequencies below the resonant frequency

$$f_{\text{res}} = \frac{1}{2\pi} \sqrt{\frac{L_F + L_G}{C L_F L_G}}. \quad (1.11)$$

In fact, LCL filters are usually modeled as L ones in the range of frequencies to be controlled [29, 37, 47, 51–59]. It should be also remarked that the damping of the LCL resonance does not affect the frequency response at lower frequencies [46], so this assumption is still valid once the damping technique is added.

### 1.2.2.3 Discrete-Time Plant Model

Fig. 1.5a represents the current control closed-loop scheme, where  $G_C(s)$  is the controller,  $i^*$  is the current reference,  $i$  is the actual current value (with respect to a stationary frame),  $e = i^* - i$  is the tracking error,  $T_s = 1/f_s$  is the sampling period and  $G_L(s)$  is described by (1.5). The computational delay can be modelled as  $e^{-sT_s}$  if the state variables are sampled and the

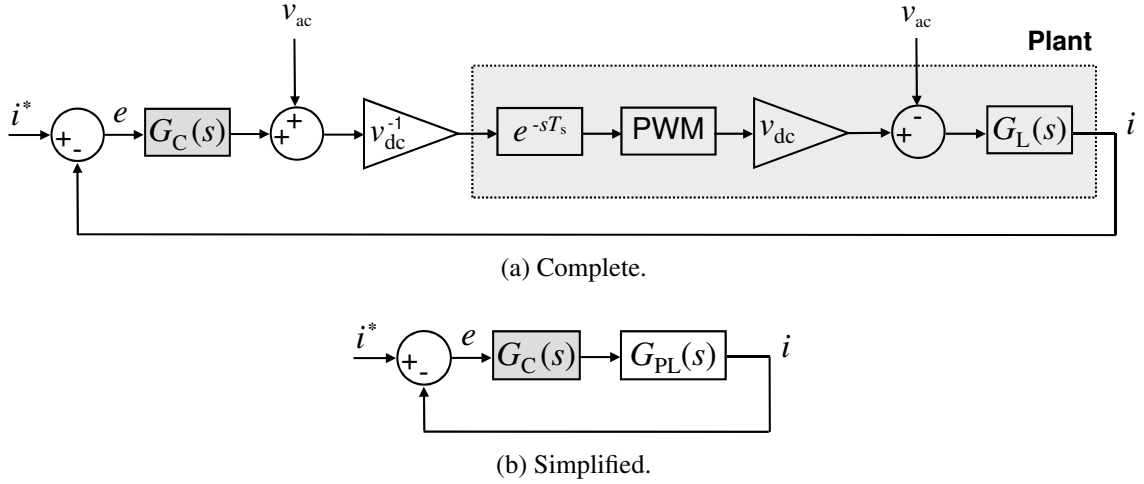


Figure 1.5: Block diagram of current control closed-loop (stationary frame).

duty cycle is updated once per switching period. This is actually the most common solution in digital signal processors (DSPs) and microcontroller-based control implementations [60].

The voltage source signal  $v_{ac}$  of Fig. 1.2a can be eliminated by sensing and adding its instantaneous value to the output of  $G_C(s)$  (feedforward signal) as shown in Fig. 1.5a. In any case, a controller with infinite open-loop gain at the frequency of  $v_{ac}$  is usually included in  $G_C(s)$  to assure perfect rejection of  $v_{ac}$  in steady-state. Thus, for simplicity, this perturbation may be ignored for the plant modeling [61]. The output of the controller is multiplied by  $v_{dc}^{-1}$  to make the parameters of  $G_C(s)$  independent of the bus voltage. Taking into consideration all these facts, the block diagram may be simplified as shown in Fig. 1.5b.

If the delay due to computation and modulation is neglected (it can be assumed for frequencies much lower than the sampling frequency  $f_s$ ), the plant model in stationary frame  $G_{PL}(s)$  can be considered to be approximately equal to  $G_L(s)$ . This simplification is actually assumed in many studies [25, 56, 57, 62–69].

To obtain the discrete-time transfer function equivalent to the plant in Fig. 1.5 without neglecting the delays, the computational delay  $e^{-sT_s}$  is substituted by  $z^{-1}$  and the PWM block is replaced by a zero-order hold (ZOH) [61, 70–72]. The ZOH model represents a very good approximation in the case of triangular carrier waveform [71]. Thus, by discretization of  $G_L(s)$  with the ZOH method, the plant model in the  $z$ -domain becomes

$$G_{PL}(z) = z^{-1} \mathcal{Z} \left\{ \mathcal{L}^{-1} \left[ \frac{1 - e^{-sT_s}}{s} G_L(s) \right] \Big|_{t=kT_s} \right\} = \frac{z^{-2}}{R_F} \frac{1 - \rho^{-1}}{1 - z^{-1}\rho^{-1}} \quad (1.12)$$

where  $\rho = e^{R_F T_s / L_F}$  [71].

### 1.2.3 Hysteresis Control

Hysteresis control is an old and popular approach to perform current control in power converters. Actually, some years ago, it has been often regarded as one of the techniques capable of providing the highest performance [73]. It has been employed with successful results in a lot of different fields, from its origin to our days [22, 71, 73–107].

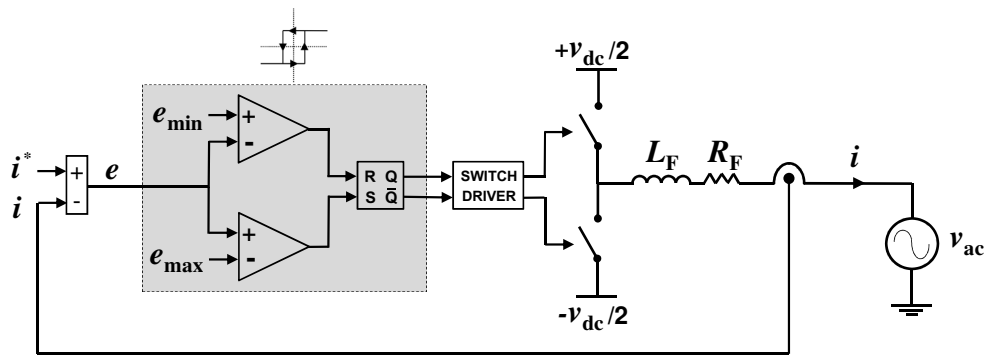


Figure 1.6: Basic hysteresis controller implementation, referred to one phase. Several phases may be controlled by independent regulators of this form.

### 1.2.3.1 Conventional Two-Level Fixed-Band Hysteresis Control

Fig. 1.6 depicts the implementation (in single-line representation) of a basic two-level hysteresis current controller. The firing signals for the transistors are obtained by comparison of the current error  $e$  with a hysteresis band. In this manner, when  $e$  is greater than  $e_{\max}$ , the upper switch is turned on until  $e$  becomes lower than  $e_{\min}$ . On the contrary, when  $e$  is lower than  $e_{\min}$ , the lower switch is turned on until  $e$  becomes greater than  $e_{\max}$ . In both cases, the other switch in the same line is fired by the complementary signal, taking into account the delays and dead-times (not shown in Fig. 1.6). The variables  $e_{\max}$  and  $e_{\min}$  are usually set to be equal in magnitude. When these parameters are constant, this scheme corresponds to the conventional hysteresis controller with fixed-band, also known as free-running hysteresis controller [74, 75].

The main advantages of the hysteresis current-control technique are simplicity, unconditioned stability, independence of load parameters, good accuracy and very fast response [22, 73, 75–91]. Actually, it is capable of providing the fastest dynamic response possible for a VSC, due to the fact that it does not require any modulator (the state of the switches is directly obtained by comparison of the actual current and its reference) [71]. On the other hand, PWM techniques present slower dynamics due to intrinsic modulation delay and current regulator response time [84].

The basic fixed-band hysteresis technique is affected by the drawbacks of heavy interference among the phases in the case of a three-phase system with isolated neutral (the instantaneous error may double the value of the hysteresis band), difficult protection of the converters due to the randomness in the duty cycle, continuously spread harmonic spectrum and variable switching frequency [22, 73, 75, 77–80, 82–85, 87–90, 92–97]. These variations in the switching frequency may become quite problematic, because of the risk of exciting resonant frequencies of other loads, increase of power losses and semiconductors stress when high switching frequencies are required, significant current ripple when the switching frequency is low and need for expensive and difficult to design filters [71, 73–75, 77, 79, 81, 96, 98]. The spread spectrum may cause, among other problems, torque ripple and machine heating [77, 78].

Additional drawbacks of these controllers are their inability to perform selective control (which would permit to reduce the converter rating and avoid undesired frequencies) and their great dependence on the converter topology: actually, specific hysteresis regulators have been proposed for particular topologies such as four-leg [108, 109] and multilevel VSCs [76, 91, 93, 99–102].

A lot of different solutions have been proposed to overcome these issues. A brief review of some of the most significant improvements is exposed in the following.

### 1.2.3.2 Minimization of Interference Between Phases

Several analytical expressions to suppress the coupling between phases, when one hysteresis controller per-phase is implemented, have been proposed [79–83]. They are based on decomposing the error  $e$  into two parts, one that depends only on the phase voltages and another one only due to phase interaction, and then performing the hysteresis control on the first part instead of on the whole  $e$  signal (the usual method).

Nevertheless, phase decoupling can be achieved more easily by means of the Clarke and Park transforms (see section §1.2.1), given that the homopolar component is not reflected in the  $\alpha\beta$  and dq axes. Thus, if a pair of hysteresis controllers is implemented in either of these two frames, no interference between phases occurs [85, 88, 110]. Furthermore, their use in SRF offers certain additional advantages in several applications, such as torque-ripple minimization in ac drives by means of a narrower band for the torque current component (q axis) than for the flux current component (d axis) [75, 110]

### 1.2.3.3 Variable-Band Hysteresis Control

The width of the hysteresis band may be modified (adaptive  $e_{\max}$  and  $e_{\min}$ ), according to different criteria, to reduce the problems derived from a fixed-band. In this manner, the range of the switching frequency fluctuations can be limited or fixed to a certain value [22, 77, 79, 81–84, 95, 98, 103–107, 111], and the harmonic spectrum becomes then quite similar to that of a PWM-based modulator (concentrated at high frequencies) [78, 84, 103, 107]. Some of the alternatives to adapt the hysteresis band are summarized in the following.

- Several algorithms calculate the variable band by means of system parameters [77, 103, 104]. The main problem is the sensitiveness to variation in the parameter values and estimation errors.
- The upper and lower limits may follow a sinusoid with the same frequency and phase as the reference  $i^*$  [78, 111], or with opposite phase [105]. The resulting current presents a better spectral behavior (more concentrated) at the expense of a higher average switching frequency. To avoid the elevated number of commutations when the band is narrower, mixed-band and equidistant-band hysteresis controllers were proposed [111]. The latter has been recently implemented with several improvements in [85, 112].
- Tekwani et al. implement parabolic bands to control an induction machine, and they were dynamically adjusted depending on the angular speed. This controller is implemented mainly by means of look-up tables [107].
- A phase-locked loop (PLL) synchronization can be employed to ensure constant switching frequency [79–83]. This technique may present stability and synchronization problems, specially during large transients [22, 77, 107].
- Buso et al. achieve a good synchronization (they manage to center the inverter voltage pulses in the modulation period) in a single switching period, by means of a deadbeat

controller in charge of the band adaptation [22]. Dead-times are also compensated. This method improves the ones based on PLLs in terms of synchronization and stability.

#### 1.2.3.4 Other Improvements and Proposals

Another possibility to achieve constant switching frequency consists in subtracting a triangular waveform before the hysteresis comparison [89, 96], which is known as ramp-comparison control [94]. However, this causes steady-state error both in magnitude and phase, and special care should be taken to assure that the slope of the triangular carrier is greater than that of  $e$  [74, 89].

The power losses may be reduced by performing modulations only in two inverter legs at any time, while keeping the third one with the upper or lower transistor connected for a longer time [80, 96].

The average switching frequency can be reduced by injection of zero voltage vectors, as done in [85, 86, 88, 90, 91, 94, 97, 98, 106, 110, 112–118].

It is possible to employ several levels of hysteresis bands to reduce the harmonic components, the switching frequency and the error region: three-level [97, 106, 110, 113, 115, 117, 118], four-level [85, 112] and five-levels [91] hysteresis controllers have been posed. At the same time, these bands may be either fixed or variable. For instance, a five-level hysteresis controller with equidistant bands is implemented in [112] to reduce the switching frequency fluctuations during transients, with respect to five-level fixed-bands.

#### 1.2.3.5 Digital Implementation

Hysteresis regulators were essentially analog in their origin. However, given the current advances in digital devices, and the advantages typical of digital solutions (in terms of interfacing, maintenance, reproducibility, flexibility, integration, etc.), it is desirable to seek for a fully digital implementation of hysteresis controllers.

To take advantage of these features, several works calculate the upper and lower limits by digital means, while the comparators are implemented analogically [22, 77, 81]. The main drawback of this approach with respect to other more recent digital controllers is the need for analog components apart from the digital device.

If the comparisons are also digitally performed to avoid external analog circuits, low harmonic components appear in the current due to the fact that the turn-on and turn-off times should be multiple of the sampling period [84, 85], and hence a very high sampling frequency would be required to achieve a good performance [119]. In fact, because of this reason, fully digital PWM linear controllers are most commonly used for current control [84]. A performance comparable to that of an analog hysteresis controller is achieved in [84] with a fully digital hysteresis controller (the comparators are also digitally implemented) by means of a predictive algorithm and a sampling frequency higher than the switching frequency. However, its control complexity, numerous concurrent operations and extensive signal processing requirements make it only suitable for very powerful digital devices with capability to run in parallel several tasks, such as field-programmable gate arrays (FPGAs) [58, 84, 85, 120].

It should be also taken into account that, even if the switching frequency is fixed by any of the existing methods, it is done at the cost of a lower accuracy. There is always a tradeoff between accuracy and switching frequency [85].

These reasons, together with the advances in reliability and reduced cost of digital devices such as DSPs, have currently pushed the use of hysteresis regulation into the background, in favor of linear digital controllers. In any case, hysteresis controllers may be still a good solution for cases in which their extremely fast transient response and stability are priority, such as traction applications in which fast-changing nonlinear load conditions prevail [91].

### 1.2.4 Deadbeat Control

The deadbeat controller, which belongs to the family of predictive regulators [119], is a popular control technique in many recent applications [23, 24, 52, 59, 61, 71, 119, 121–153]. It is obtained by isolation of  $G_C(z)$  in the closed-loop transfer function

$$C_L(z) = \frac{G_C(z) G_{PL}(z)}{1 + G_C(z) G_{PL}(z)} \quad (1.13)$$

when  $C_L(z)$  is assumed to be equal to the lowest possible delay at all frequencies, that is,  $C_L(z) = z^{-2}$  (one cycle due to computation, and another one due to modulation and other delays such as those caused by passive filters and dead-times.) [61, 71, 121–123]. Thus, when deadbeat control is well-tuned, it permits to achieve the fastest transient response among all digital current controllers [71, 121].

From (1.13) and (1.12), the resulting transfer function for the deadbeat controller is

$$G_{DB}(z) = \frac{R_F}{1 - \rho^{-1}} \frac{1 - z^{-1} \rho^{-1}}{1 - z^{-2}}. \quad (1.14)$$

Fig. 1.7 shows the closed-loop Bode diagram that results when  $G_C(z)$  takes the form of  $G_{DB}(z)$  in (1.13). As expected, unity gain is achieved for all frequencies, but the two samples delay prevents from achieving zero steady-state error except at 0 Hz (which is not desired in control of alternating currents).

The main drawbacks of this control technique are the sensitiveness to deviations in plant parameters from their estimated values, requirement of the  $v_{ac}$  feedforward [because of  $G_{DB}(z)$  low disturbance rejection capability], sensitiveness to measurement noise, need for dead-times compensation and the inability to achieve zero steady-state error at frequencies different from 0 Hz (a delay of two samples is always present) [71, 119, 121, 124, 153].

Several improvements have been proposed to address these issues. Most of them rely on the addition of observers or estimators to compensate the computational delay, as well as plant nonlinearities, to improve the perturbation rejection, or to reduce the sensitiveness to plant uncertainties and parameter mismatches [23, 24, 52, 71, 121, 122, 125–135]. In any case, these modifications usually imply a great complexity with respect to the simple transfer function in (1.14), and this fact restricts the implementation of deadbeat controllers in applications in which such a fast response is not required.

An interesting work that emphasizes the importance of adding additional structures to compensate the steady-state error left by a deadbeat controller is posed by Allmeling in [153], where the author proposes to add resonant controllers in parallel in order to assure perfect tracking of specific frequencies.

It should be also remarked that, due to the deadbeat large gain at high frequencies, special care should be taken when it is combined with LCL filters. Timbus et al. have proposed a

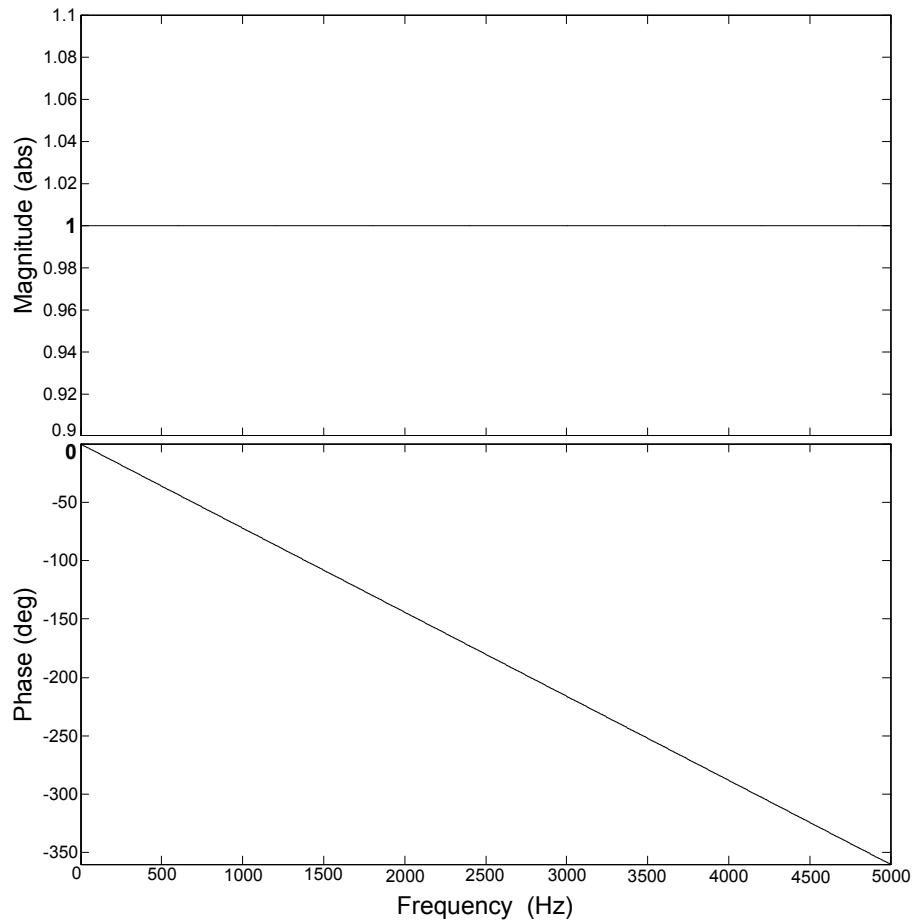


Figure 1.7: Closed-loop Bode diagram [i.e., of  $C_L(z)$ ] provided by  $G_{DB}(z)$  controller, with  $f_s = 10\text{kHz}$ .

technique to provide an enhanced robustness to grid impedance variation with LCL filters [119]. It is based on artificially reducing the gain of the obtained deadbeat transfer function, so that stability is improved at the expense of modifying  $C_L(z)$ .

### 1.2.5 PI Control in SRF

PI control is one of the most studied, well-known and established control techniques in many applications, in which a constant or slowly-varying reference should be tracked. Nevertheless, the application of PI regulators to control alternating signals (such as currents in the ac side of a VSC) is not straightforward.

Implementation of PI controllers in stationary frame gives rise to a significant steady-state error, because they only assure perfect tracking at 0Hz (they provide open-loop infinite gain at 0Hz). In order to achieve unit closed-loop gain for alternating signals, these should be firstly transformed into dc values. This can be achieved by means of the Park transform, as exposed in section §1.2.1. In this manner, the well-known PI regulators can be also employed to control alternating currents with zero steady-state error, by implementation of an independent PI controller in the d and q axes separately [154, 155].

Different structures to implement PI controllers in SRF can be found in the existing litera-

ture.

### 1.2.5.1 Conventional PI

A conventional PI controller is defined by the transfer function

$$G_{\text{PI}}(s) = k_{\text{P}} + \frac{k_{\text{I}}}{s} \quad (1.15)$$

where  $k_{\text{P}}$  and  $k_{\text{I}}$  are the proportional and integral gains, respectively. A controller with the form of (1.15) can be implemented in each of the two SRF axes to achieve zero steady-state error. The synchronous frequency  $\omega_0$  for the Park transformation [see (1.2)] should be adjusted to coincide with the frequency of the harmonic order  $h$  to control, that is,  $\omega_0 = h\omega_1$ , with  $\omega_1$  being the fundamental frequency. For negative-sequence components,  $\omega_0 = -h\omega_1$  should be considered. The PI controllers for each harmonic order  $h$  can be tuned with independent proportional and integral gains ( $k_{\text{P}_h}$  and  $k_{\text{I}_h}$ , respectively):

$$G_{\text{PI}_h}(s) = k_{\text{P}_h} + \frac{k_{\text{I}_h}}{s}. \quad (1.16)$$

The resulting scheme is shown in Fig. 1.8a. The superscript \* denotes reference signals, whereas its absence means actual values. The angle  $h\omega_1 t$  is usually obtained by estimation of  $v_{\text{ac}}$  phase with a synchronization algorithm, e.g. a PLL [156].

Given that

$$i_{\text{dq}}^* e^{\pm jh\omega_1 t} - i_{\text{dq}} e^{\pm jh\omega_1 t} = \left( i_{\text{dq}}^* - i_{\text{dq}} \right) e^{\pm jh\omega_1 t} \quad (1.17)$$

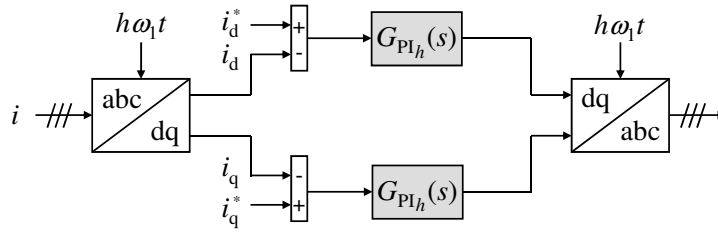
it can be concluded that there is no practical difference between calculating the error after (as in Fig. 1.8a) or before the Park transformation.

PI control in dq axes performed by means of the Park transform is only suitable for three-phase systems. An equivalent controller for single-phase systems, based on product demodulation instead of  $\mathbf{P}$ , is shown in Fig. 1.8b [65]. It is also interesting to note that the scheme shown in Fig. 1.8a is equivalent to implement that of Fig. 1.8b for the  $\alpha$  and  $\beta$  axes, separately [157, 158]. To also compensate homopolar component, Fig. 1.8b scheme can be implemented for each of the three-phases.

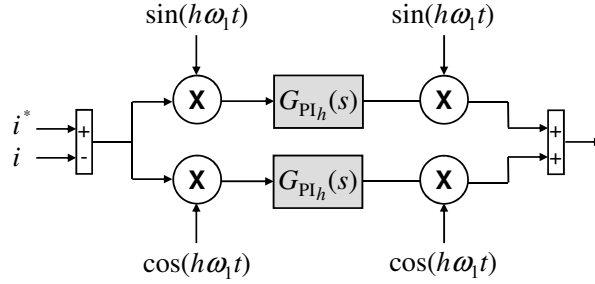
Given that  $k_{\text{P}_h}$  affects all the spectrum equally, it can be taken out of the SRF to stationary frame. Once the integral term is isolated in the SRF, it is possible to employ a different angle for the direct and inverse Park transformations (see Fig. 1.9), with the aim of introducing a leading angle  $\phi_h'$  at the vicinity of the synchronous frequency  $h\omega_1$  [71, 157, 158]. This leading angle can be useful for compensation of plant delays. From section §1.2.1, the variable  $i_{\alpha\beta}$  in Fig. 1.9a is the current in complex vector notation with respect to the  $\alpha\beta$  axes ( $i_{\alpha\beta} = i_{\alpha} + j i_{\beta}$ ), and  $i_{\alpha\beta}^*$  is its reference signal. It should be also noted that, when  $\phi_h' = 0$ , the block diagrams shown in Fig. 1.9 are equivalent to those shown in Fig. 1.8.

The plant model  $G_{\text{L}}(s)$  is transformed to a positive-sequence SRF rotating with angular speed  $\omega_0 = h\omega_1$  by application of the substitution  $s \rightarrow s + jh\omega_1$  to (1.5) [in accordance to (1.3), when  $\omega_0 = h\omega_1$ ; note that  $G_{\text{L}}(s)$  is placed after the inverse Park transformation, so (1.3) should be employed instead of (1.4)] [51, 58]:

$$G_{\text{L}}'(s) = G_{\text{L}}(s + jh\omega_1) = \frac{1}{sL_{\text{F}} + R_{\text{F}} + jh\omega_1 L_{\text{F}}}. \quad (1.18)$$

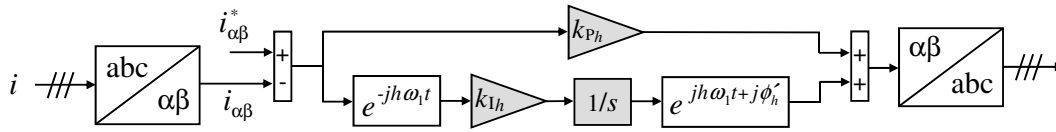


(a) Three-phase systems (based on the Park transform).

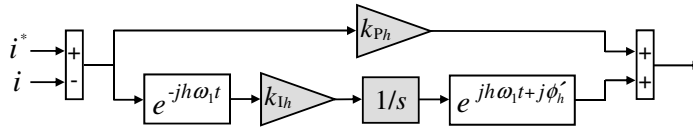


(b) Single-phase systems (based on product demodulation).

Figure 1.8: Conventional PI control in SRF.



(a) Three-phase systems.



(b) Single-phase systems.

Figure 1.9: Conventional PI control in SRF, including a leading angle  $\phi'_h$ . Note that, when  $\phi'_h = 0$ , these schemes are equivalent to those in Fig. 1.8.

For simplicity, the delay caused by computation and modulation and the techniques to compensate its effect ( $\phi'_h \neq 0$ ) are not taken into account for the analysis at this point (they will be analyzed later).

Fig. 1.10a represents the complex vector block diagram of a conventional PI controller in a positive-sequence SRF [25]. The plant model corresponds to the transfer function in (1.18). From section §1.2.1, the variable  $i_{dq}$  is the current in complex vector notation with respect to the dq axes ( $i_{dq} = i_d + j i_q$ ), and  $i_{dq}^*$  is its reference signal.

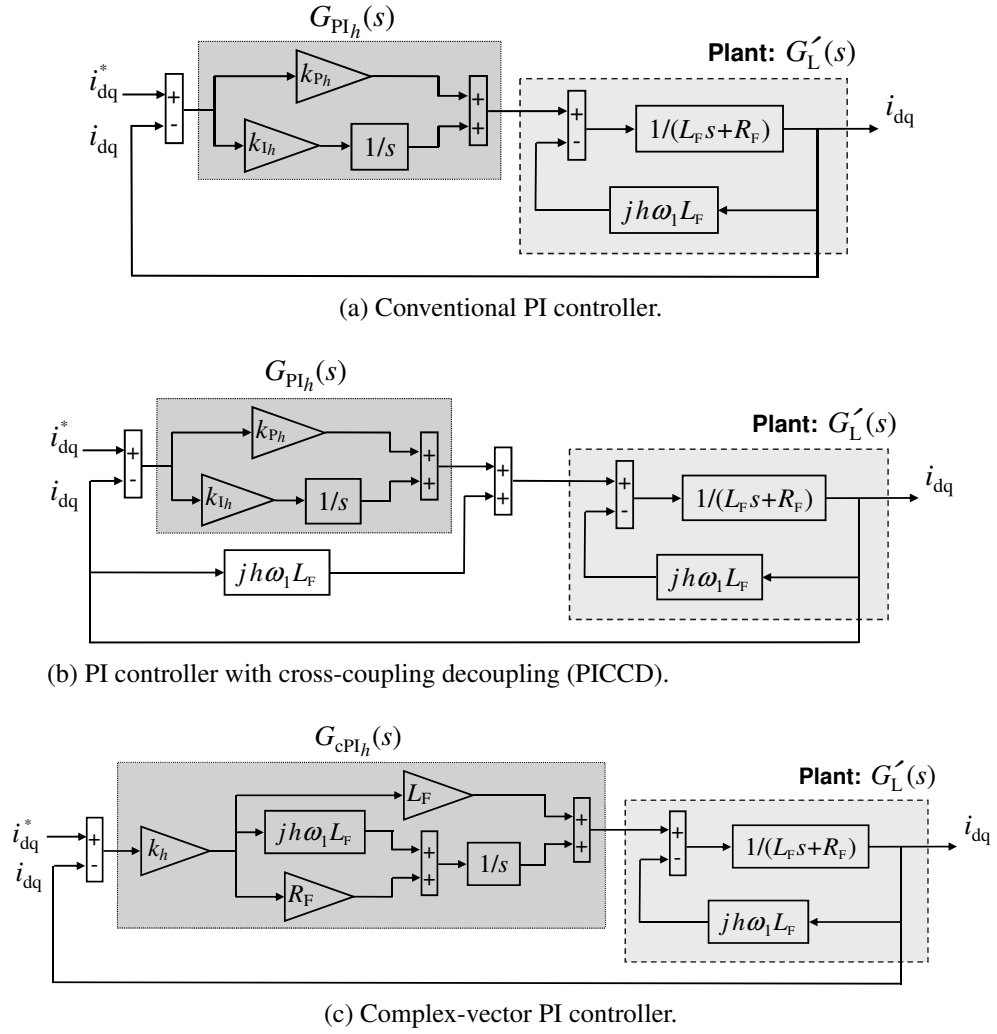


Figure 1.10: Complex vector block diagrams of closed-loop with different PI controllers in SRF.

### 1.2.5.2 PI with Cross-Coupling Decoupling

If the complex term in (1.18) and in Fig. 1.10a is not effectively decoupled, a significant performance degradation occurs. Particularly, stability margins are reduced, transient response is worsened, and anomalous gain peaks appear in the closed-loop frequency response near  $h\omega_1$  [25]. To avoid these problems, a PI controller with cross-coupling decoupling (PICCD), shown in Fig. 1.10b, may be implemented. The effect of the decoupling scheme may be understood as a displacement of the plant pole to the real axis, so that  $G'_L(s)$  is replaced by  $G_L(s)$  [25].

### 1.2.5.3 Complex Vector PI

An alternative PI controller, named complex vector PI, can be found in [25, 159, 160]:

$$G_{cPI_h}(s) = \frac{sk_{P_h} + k_{I_h} + jh\omega_1 k_{P_h}}{s} \quad (1.19)$$

where  $k_{P_h}$  and  $k_{I_h}$  should be adjusted to satisfy  $k_{I_h}/k_{P_h} = R_F/L_F$ . Thus, (1.19) can be rewritten as

$$G_{cPI_h}(s) = k_h \frac{sL_F + R_F + jh\omega_1 L_F}{s} \quad (1.20)$$

where  $k_h = k_{P_h}/L_F$ .

It can be clearly appreciated that the numerator in (1.20) is of the same form as the denominator in (1.18), and hence, the coupling of the latter will be effectively canceled if the enhanced PI controller  $G_{cPI_h}(s)$  is implemented in SRF, as shown in Fig. 1.10c.

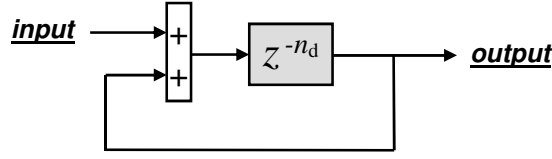
The essential difference between the PICCD (Fig. 1.10b) and the complex vector PI (Fig. 1.10c) lies in the fact that, while the former moves the plant pole to the real axis, the latter moves the controller zero so that it corresponds with the plant pole. This difference implies, in practice, that, if  $L_F$  is not well estimated, the frequency response and dynamics of the system at the vicinity of the frequency to be controlled ( $h\omega_1$  in stationary frame) will be more degraded in the case of the scheme including PICCD than in the case of the  $G_{cPI_h}(s)$ . In the former, the inexact displacement of the plant zero abruptly modifies the frequency response at the vicinity of the frequency to be controlled ( $h\omega_1$  in stationary frame), whereas in the case of the latter an inexact displacement of the pole is reflected as a variation of the frequency response mainly at frequencies (at 0 Hz in stationary frame) far from the one of interest [25].

Another advantage of the  $G_{cPI_h}(s)$  controller over the PICCD, which is not commented in [25, 159], is exposed in the following. Several  $G_{cPI_h}(s)$  regulators can be implemented in parallel (to simultaneously track several harmonics or sequences) while maintaining the pole-zero cancellation between the plant and controller in each SRF. On the other hand, a group of PICCDs in parallel SRFs would be able to achieve effective cross-coupling decoupling only in one of the SRFs. This limitation of the latter structure is a consequence of the fact that it is based on a displacement of the plant pole, which is present in all reference frames.

For example, if a structure as that shown in Fig. 1.10b is implemented for the fundamental frequency ( $h = 1$ ), the plant model in that reference frame  $G'_L(s)$  is transformed into  $G_L(s)$ . The resulting plant would be seen in a SRF tuned at the negative-sequence 5th harmonic ( $\omega_o = -5h\omega_1$ ) as

$$G_L(s - j6\omega_1) = \frac{1}{sL_F + R_F - j6\omega_1 L_F}. \quad (1.21)$$

Note that to decouple the cross-coupling in (1.21), now the decoupling branch in Fig. 1.10b should be  $-j6\omega_1 L_F$  instead of  $-j5\omega_1 L_F$ , since the decoupling scheme in the fundamental SRF has displaced the plant pole a quantity  $j\omega_1 L_F$  in the imaginary axis. However, if the cross-coupling in the 5th harmonic SRF was decoupled, the plant model seen in the fundamental SRF would present cross-coupling again (a decoupling branch with  $j6\omega_1 L_F$  would be required). In this manner, it can be concluded that it is not possible to decouple the axes by means of Fig. 1.10b scheme in more than one SRF at the same time. This is an important disadvantage when implementation of various SRFs in parallel (multiple reference frames) to track several harmonics or sequences at the same time (as in [155, 161–163]) is desired. In these situations, a complex vector PI would be more suitable, because it is not based on moving the plant pole, but on displacing each of the controllers' zeros independently.

Figure 1.11: Generation of periodic signal with period  $n_d T_s$ .

## 1.2.6 Repetitive Control

The repetitive control is based on the internal model principle [71, 164–168]. This principle states that a controller achieves zero steady-state error for a given reference if the model that generates a signal of the form of the reference is included in the closed-loop [169, 170]. For example, in order to provide perfect tracking of sinusoidal references, a digital model capable of generating sinusoidal signals should be included in  $G_C(z)$ . This sinusoidal generator could be either recursive or based on the discrete Fourier transform (DFT).

### 1.2.6.1 Repetitive Controllers in Recursive Form

The scheme depicted in Fig. 1.11 generates periodic signals with a period of  $n_d$  samples [167, 171–174]. Alternatively, it can be also understood as a generation of an infinite set of sinusoids with period  $n_d T_s$  and all its integer submultiples.

If the block diagram shown in Fig. 1.11 is included in  $G_C(z)$ , the positive feedback with the delay  $z^{-n_d}$  provides open-loop infinite gain for the frequency  $1/(n_d T_s)$  and all its harmonics. From (1.13),  $C_L(z) \rightarrow 1$  when  $G_C(z) \rightarrow \infty$ . Thus, once the loop is closed, unity gain (zero steady-state error) is assured for all those frequencies. Note that, to control  $f_1$  and its harmonics,  $n_d$  should be selected so that it satisfies  $n_d T_s = 1/f_1$ .

An ideal repetitive controller, that incorporates the scheme from Fig. 1.11, may be expressed by the transfer function

$$G_{\text{rep}}(z) = K_{\text{rep}} \frac{z^{-n_d}}{1 - z^{-n_d}} \quad (1.22)$$

where  $K_{\text{rep}}$  is an adjustable gain that defines the width of the open-loop gain peaks around each frequency multiple of  $1/(n_d T_s)$ , and hence, the transient response and stability margins.

However, the scheme of Fig. 1.11 usually leads to instability since it amplifies many high-order harmonics (theoretically up to the Nyquist frequency), while the system to be controlled [ $G_{\text{PL}}(z)$ ] introduces a large phase lag at high frequencies. To assure acceptable stability margins, a phase lead of  $n_s$  samples and filters  $F_1(z)$  and  $F_2(z)$  may be introduced [71, 175]:

$$G_{\text{rep}}^d(z) = K_{\text{rep}} F_1(z) \frac{z^{-n_d+n_s}}{1 - z^{-n_d} F_2(z)}, \quad (1.23)$$

which corresponds to the block diagram shown in Fig. 1.12.

$F_1(z)$  and  $F_2(z)$  are usually designed to behave as low-pass filters. In that manner, the gain peaks are attenuated as the frequency increases, and stability can be achieved at the cost of non-zero steady-state error [71].  $F_1(z)$  may also serve as a notch filter in order to avoid resonances introduced by the plant [176]. Often, only one of the two filters is implemented:  $F_1(z)$  in [171, 177–181], and  $F_2(z)$  in [71, 175, 182–186]. In other works, alternatively, a combination

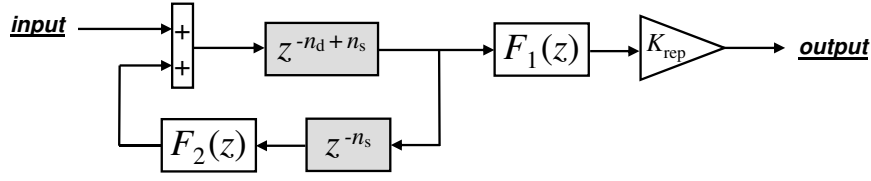


Figure 1.12: Implementation of repetitive controller, according to (1.23). Resonant peaks are placed at both odd and even harmonics.

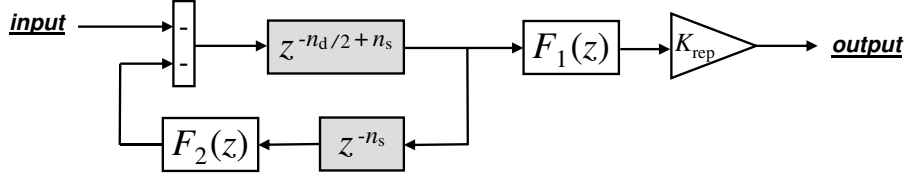


Figure 1.13: Implementation of repetitive controller that leads to resonant peaks only at odd harmonics.

of both filters is employed to achieve a more accurate tuning [147, 165, 166, 176, 187–192, 192–196].

If only the fundamental and the odd harmonics should be tracked, which is quite typical in most power conversion applications, a delay of just  $n_d/2$  samples can be implemented instead of one of  $n_d$  samples and the positive signs in the adder may be replaced with negative ones. On the contrary,  $n_s$  should not be modified. The resulting scheme is shown in Fig. 1.13. These changes lead to infinite gain peaks only at odd harmonics, whereas the original repetitive controller presents peaks also at even harmonics [166, 168, 172, 184, 191, 197, 198]. Note that this modification permits to halve the number of samples to be stored. An analog-circuit implementation of this approach is proposed in [185].

The Bode diagrams shown in Fig. 1.14 compare the frequency response of the repetitive controllers shown in Figs. 1.12 and 1.13.

A proportional or PI regulator can be implemented in parallel to repetitive controllers, so that the transient response is improved (the residual error is reduced as the bandwidth grows) [71]. In the works of Griñó et al. [168, 172, 197], the implemented controller can be understood as a repetitive controller in parallel with a proportional gain equal to one; then, the resulting signal is introduced in an additional filter to improve robustness.

Escobar et al. proposed in [19] to include in the repetitive scheme (the one with peaks at both even and odd harmonics) a feedforward line in addition to the feedback path. The resulting block diagram, expressed in the  $z$ -domain, is depicted in Fig. 1.15. In this case,  $F_1(z)$  is a low-pass filter and  $F_2(z)$  a high-pass filter, the latter of which serves to cancel the effect of a pole at the origin caused by the feedforward line. The filter  $F_1(z)$  may be avoided if  $T_s$  is low enough [199]. The constant  $\delta \in (0,1]$  introduces damping in the poles and zeros by moving them to the interior of the unit circle.

The main difference between the scheme shown in Fig. 1.15 and the conventional repetitive regulator lies in the fact that the former, apart from achieving infinite gain peaks (slightly attenuated by the filters) at the frequencies  $k/(n_d T_s) \forall k \in \mathbb{N}$ , also provides notches (also attenuated) at the intermediate frequencies  $0.5(2k+1)/(n_d T_s) \forall k \in \mathbb{N}$ . This has the advantage of making the compensators more selective, in the sense that the original overlapping or interac-

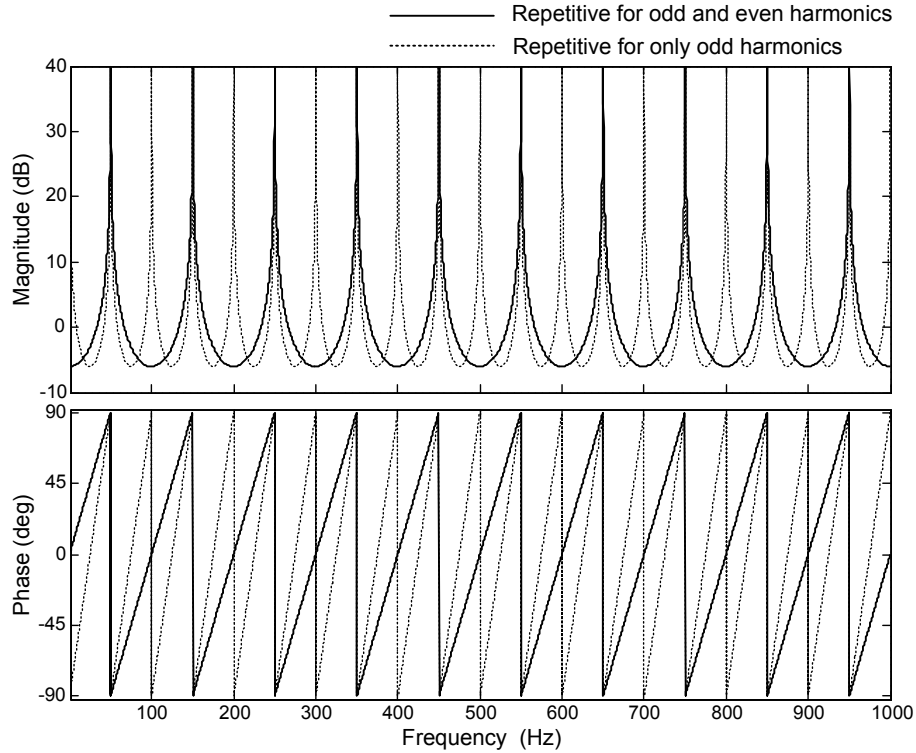


Figure 1.14: Open-loop Bode diagrams of the repetitive controllers shown in Figs. 1.12 and 1.13 with a proportional gain equal to one in parallel. The filters are ignored, because they should be selected depending on the plant. Parameters:  $K_{\text{rep}} = 1$ ,  $n_s = 0$ ,  $f_s = 10\text{kHz}$  and  $n_d = 200$ .

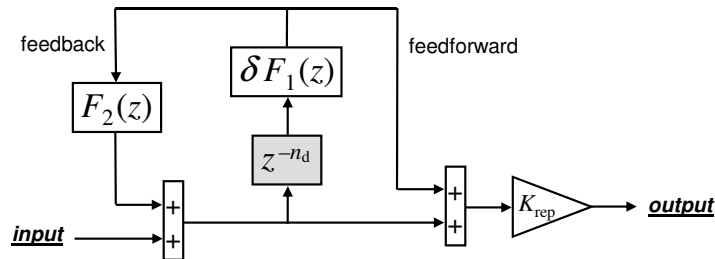


Figure 1.15: Repetitive controller proposed in [19], which presents notches (zeros) at the intermediate frequencies between the resonant peaks. Resonant peaks are placed at both odd and even harmonics.

tion between consecutive resonant peaks, appearing at the valleys, is removed by the notches. This would, in principle, allow peaks of bigger gains and slightly wider bandwidth, but without exciting harmonics located in between two consecutive peaks [19, 200].

As well as with the conventional repetitive controller without notches, it is also possible to replace  $n_d$  by  $n_d/2$  and to invert the sign of the feedback and feedforward signals, in order to have poles only at the odd harmonics. In this case, zeros are placed in the origin and at even harmonics [199–201]. As there is no longer a pole in the origin,  $F_2(z)$  may be removed. The resulting block diagram is depicted in Fig. 1.16.

The Bode diagrams shown in Fig. 1.17 compare the frequency response of the repetitive

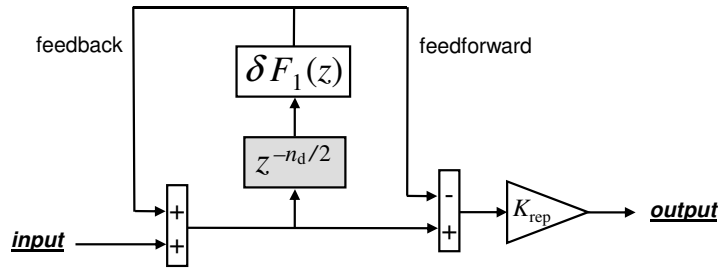


Figure 1.16: Modification of the repetitive controller shown in Fig. 1.15 that places resonant peaks only at odd harmonics and notches at even harmonics.

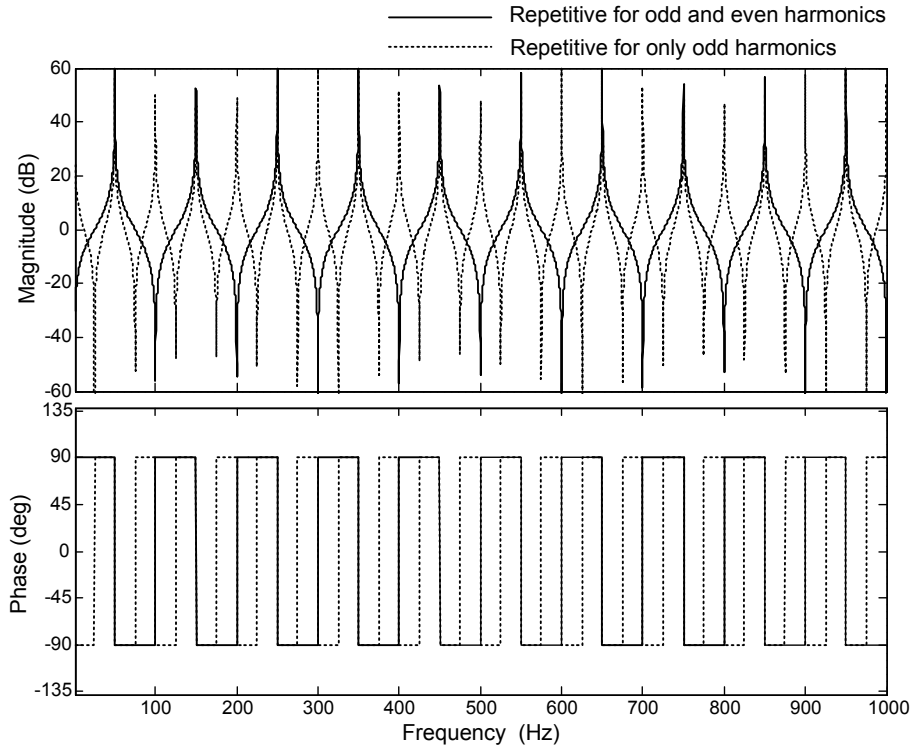


Figure 1.17: Open-loop Bode diagrams of the repetitive controllers shown in Figs. 1.15 and 1.16. The filters are ignored, because they should be selected depending on the plant. Parameters:  $K_{\text{rep}} = 1$ ,  $\delta = 1$ ,  $f_s = 10\text{kHz}$  and  $n_d = 200$ .

controllers shown in Figs. 1.15 and 1.16. In this case, the proportional gain in parallel with the repetitive scheme has not been included to obtain the Bode diagrams, so that the presence of the notches is emphasized. Once this proportional gain is added, the magnitude becomes 0 dB at the frequencies that corresponds to the notches, whereas in the repetitive controllers without the notches the gain would depend on  $K_{\text{rep}}$ .

An additional modification of the scheme shown in Fig. 1.16 has been proposed in [202]. In order to place poles only at the  $6k \pm 1$  harmonics of the fundamental frequency (with  $k \in \mathbb{N}$ ), which are actually the most common [18, 51, 56–58, 120, 202–205], the repetitive scheme shown in Fig. 1.18 was proposed. Furthermore, this implementation includes zeros at  $3k$  harmonic components, which offers an improved performance due to its potential to provide higher gains with enhanced selectivity [202]. It should be also remarked that this scheme requires only

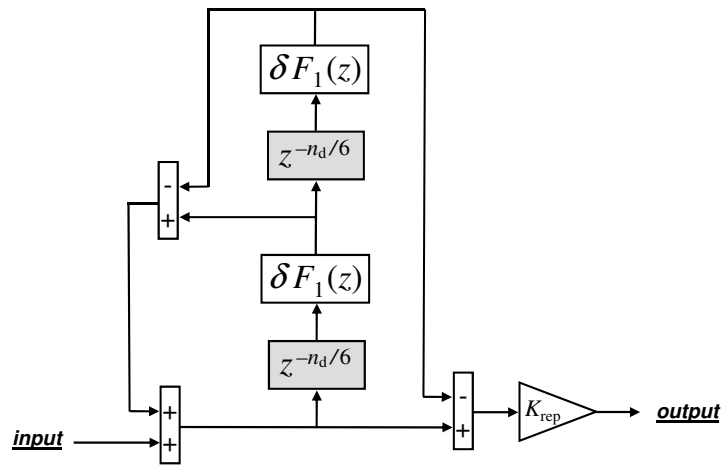


Figure 1.18: Modification of the repetitive controller shown in Fig. 1.15 that places resonant peaks at  $6k \pm 1$  harmonics and notches at  $3k$  harmonics, with  $k \in \mathbb{N}$ .

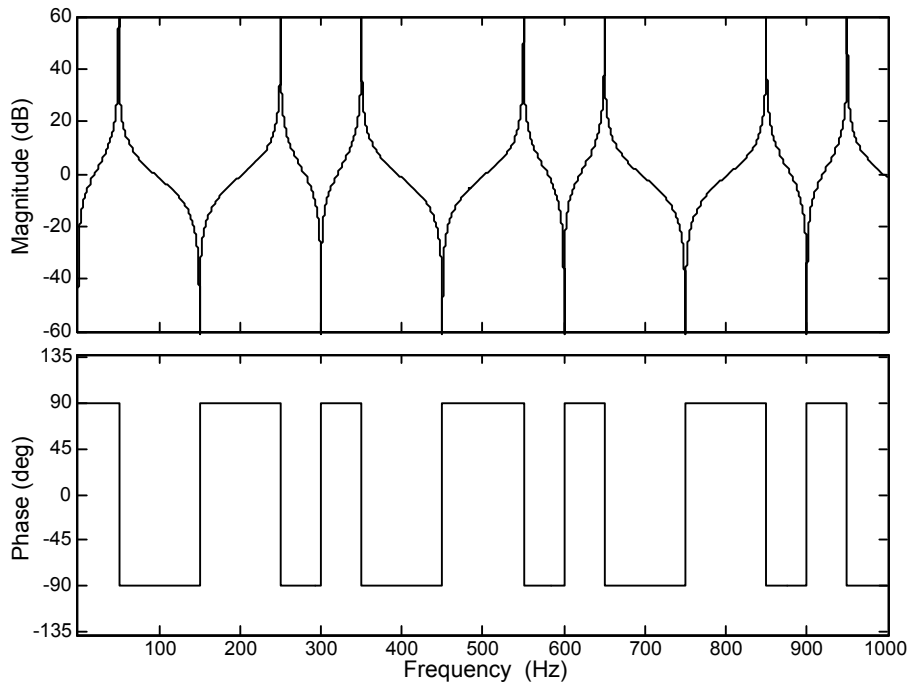


Figure 1.19: Open-loop Bode diagram of the repetitive controller shown in Fig. 1.18. The filters are ignored, because they should be selected depending on the plant. Parameters:  $K_{\text{rep}} = 1$ ,  $\delta = 1$ ,  $f_s = 9.9 \text{ kHz}$  and  $n_d = 198$ .

$n_d/3$  taps to be stored, as opposed to the original (see Fig. 1.12), in which at least  $n_d$  taps were needed.

Fig. 1.19 shows the Bode diagram of the repetitive controller depicted in Fig. 1.18. As expected, the resonant peaks are located at the  $6k \pm 1$  harmonics and zeros are placed at  $3k$  harmonic components of the fundamental frequency. Note that the sampling frequency has been modified to  $f_s = 9.9 \text{ kHz}$  so that  $n_d/3$  and  $n_d/6$  become integer numbers.

In summary, all these implementations of repetitive controllers in recursive form are capable

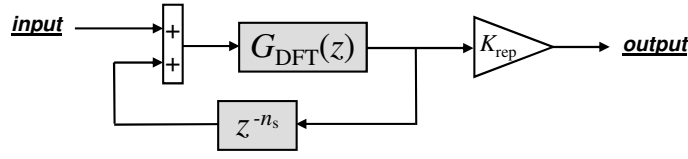


Figure 1.20: Repetitive controller based on the DFT.

of achieving a very satisfying performance. However, due to the fact that these controllers provide multiple resonant peaks at frequencies up to the Nyquist frequency, some important drawbacks arise that should be considered. To assure stability, additional filters or damping factors should be included to attenuate the gain of the peaks as the frequency increases. This degrades the performance, because the steady-state error is increased. Moreover, the tuning of the controller and filters becomes quite difficult [71].

### 1.2.6.2 DFT-Based Repetitive Controllers

Those drawbacks may be overcome by means of an alternative repetitive controller, based on a finite impulse response (FIR) filter that implements a running DFT with a window width of a fundamental period:

$$G_{\text{DFT}}(z) = \frac{2}{n_d} \sum_{k=0}^{n_d-1} \left\{ \sum_{h \in N_h} \cos \left[ \frac{2\pi h}{n_d} (k + n_s) \right] \right\} z^{-k} \quad (1.24)$$

where  $N_h$  is the set of the harmonic orders to be tracked [71, 158, 206–208]. It is also called discrete cosine transform (DCT) filter [1, 71, 206]. Equivalent properties can be achieved with half the number of taps by means of a slightly different implementation of  $G_{\text{DFT}}(z)$  [53, 120]:

$$G_{\text{DFT}}(z) = \frac{4}{n_d} \sum_{k=0}^{\frac{n_d}{2}-1} \left\{ \sum_{h \in N_h} \cos \left[ \frac{2\pi h}{n_d} (k + n_s) \right] \right\} z^{-k}. \quad (1.25)$$

The DFT-based repetitive controller can be obtained by a positive feedback of the  $G_{\text{DFT}}(z)$  output, as depicted in Fig. 1.20 [71, 120, 158, 206, 208]. Note that a delay of  $n_s$  samples is required in the feedback path in order to achieve infinite gain at the expected frequencies.

The main advantage of this DFT-based repetitive controller over the conventional repetitive controller implemented in recursive form, is that the former only provides resonant peaks at the selected harmonic frequencies (set by the  $h$  values). Consequently, the filters  $F_1(z)$  and  $F_2(z)$  are no longer required, so zero steady-state error can be achieved and the tuning process becomes much simpler. It may be also noted that compensation of more harmonics does not increase the computation complexity of (1.24), since the same number of coefficients is required for the FIR filter [71, 158, 206].

Fig. 1.21 shows the frequency response of the DFT-based repetitive controller (i.e., the scheme shown in Fig. 1.20), with  $G_{\text{DFT}}(z)$  according to (1.24), when it is implemented with a proportional gain equal to one in parallel. It can be appreciated that infinite gain is only achieved at the selected harmonic frequencies:  $h \in \{1, 5, 7, 11, 13, 17, 19\}$ . Thus, zero steady state-error can be achieved with a relatively simple design.

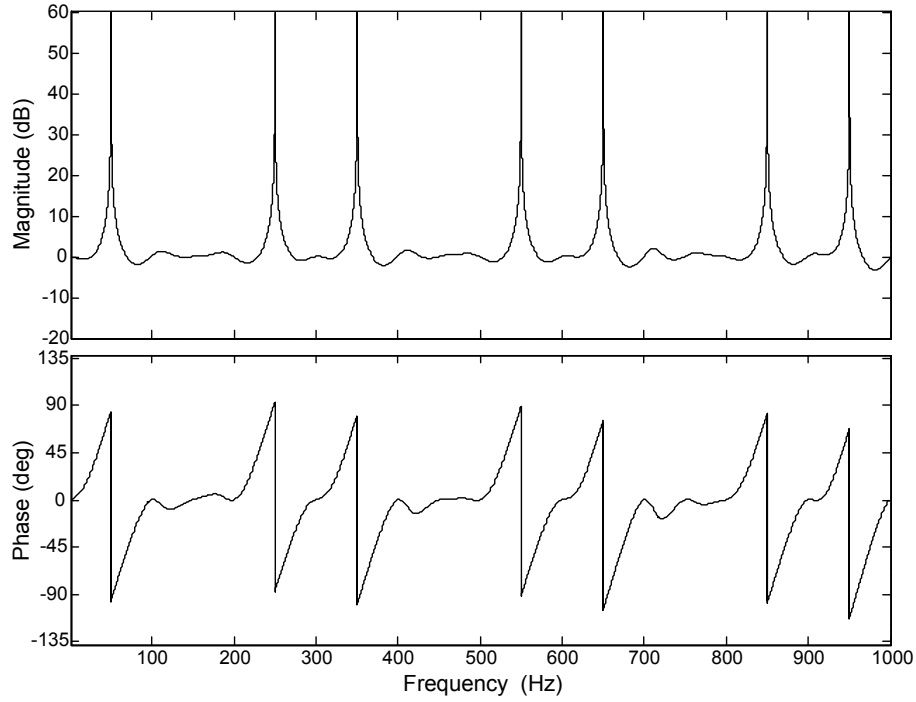


Figure 1.21: Open-loop Bode diagram of the DFT-based repetitive controller (see Fig. 1.20) with a proportional gain equal to one in parallel. Parameters:  $K_{\text{rep}} = 1$ ,  $n_s = 0$ ,  $f_s = 10\text{kHz}$ ,  $n_d = 200$  and  $h \in \{1, 5, 7, 11, 13, 17, 19\}$ .

Nevertheless, even though the DFT-based repetitive controller avoids some of the disadvantages of the one implemented in recursive form, it still presents certain limitations (inherited from the recursive one) that should be considered.

- $n_s$  should be the same for all harmonics, so that the feedback path with the  $z^{-n_s}$  term provides infinite gain. However, the phase response of the plant may not be proportional to frequency. That is the case of current-controlled VSCs (see section §1.2.2). Therefore, the phase lag caused by the plant cannot be effectively compensated by the controller at different frequencies. This fact implies a constraint to obtain the best stability margins and performance.
- $n_s$  should be an integer number, so that it is possible to implement the  $z^{-n_s}$  term in the feedback line. Analogously to the previous point, this also means a constraint to adjust the stability margins.
- Adaptation of the controller to variations in the frequency to be controlled is a complicated task. Several approaches are possible: to adapt the sampling period, to modify the number of samples  $n_d$ , or to change both simultaneously. If only adaptation of  $n_d$  is adopted, a low resolution in the resonant frequencies would be obtained, leading to large steady-state error. Thus, on-line variation of  $T_s$  is suggested, as done in [175, 209]. This approach has the following inconveniences [175].
  - Variable switching frequency.
  - Increased switching losses when high  $f_s$  values are required.

- Increased current ripple when low  $f_s$  values are needed.
- More complicated control design and stability analysis (nonlinear dynamics).

## 1.2.7 Resonant Control

Resonant controllers are equivalent to conventional PI regulators implemented in two SRFs at the same time: one positive-sequence SRF and one negative-sequence SRF [56, 57, 65, 71, 157, 158, 210]. Therefore, they are capable of tracking sinusoidal references of arbitrary frequencies of both positive- and negative-sequences with zero steady-state error, and they achieve virtually the same steady-state and transient performance as PI control in SRF [211].

Nevertheless, they provide several advantages over the latter, such as important saving of computational burden and complexity because of their lack of Park transformations, less sensitivity to noise and error in synchronization, direct application to single-phase systems, and compensation of unbalance with less number of regulators because of their ability to simultaneously track both sequences [58, 63–65, 120, 203, 205, 210, 212–217]. In this manner, resonant controllers have become a widely employed option in a lot of different applications, and also target of comprehensive research [1, 6, 27, 32, 43–49, 51, 54–58, 62–71, 119, 120, 153, 157, 158, 203–205, 207, 210? –298]. They have been employed with satisfactory results in many power converters applications, such as APFs [1, 6, 51, 56, 57, 63, 64, 70, 120, 153, 203, 205, 229–236], wind turbines [47, 68, 119, 215, 219, 237–243], water turbines [244], photovoltaic inverters [47, 119, 207, 219, 225, 245–248], STATCOMs [249–251], uninterruptible power supplies (UPSs) [224, 227, 229, 252, 253], dynamic voltage restorers [254–258], active rectifiers [48, 62, 69, 211, 213, 259, 260], boost converters [229, 261], induction drives [27, 65, 66, 210, 214, 262, 298? ], permanent magnet synchronous motors (PMSMs) [67, 263–269], fuel-cell inverters [45, 54, 55, 275] and microgrids [270–274].

Mainly two types of resonant regulators can be mentioned: proportional-resonant (PR) and vector proportional-integral (VPI) controllers.

### 1.2.7.1 Fundamentals of PR Controllers

The equivalent transfer function in stationary frame of a PI controller implemented in a positive-sequence SRF can be obtained by application of a frequency shift of  $-h\omega_1$  at all frequencies [in accordance to (1.4), when  $\omega_o = h\omega_1$ ], that is, by substitution of  $s \rightarrow s - jh\omega_1$  in (1.16) [57, 65, 71, 202, 210]:

$$G_{\text{PI}_h}^+(s) = G_{\text{PI}_h}(s - jh\omega_1) = k_{\text{P}_h} + \frac{k_{\text{I}_h}}{s - jh\omega_1}. \quad (1.26)$$

On the other hand, the substitution  $s \rightarrow s + jh\omega_1$  [in accordance to (1.4), when  $\omega_o = -h\omega_1$ ] should be applied to (1.16) in order to obtain the transfer function in stationary frame of a PI controller implemented in a negative-sequence SRF [57, 65, 71, 210]:

$$G_{\text{PI}_h}^-(s) = G_{\text{PI}_h}(s + jh\omega_1) = k_{\text{P}_h} + \frac{k_{\text{I}_h}}{s + jh\omega_1}. \quad (1.27)$$

Addition of (1.26) and (1.27) leads to

$$G_{\text{PR}_h}(s) = G_{\text{PI}_h}^+(s) + G_{\text{PI}_h}^-(s) = \underbrace{2k_{\text{P}_h}}_{K_{\text{P}_h}} + \underbrace{2k_{\text{I}_h}}_{K_{\text{I}_h}} \frac{s}{s^2 + h^2\omega_1^2} = K_{\text{P}_h} + K_{\text{I}_h} \overbrace{\frac{s}{s^2 + h^2\omega_1^2}}^{R_{1_h}(s)} \quad (1.28)$$

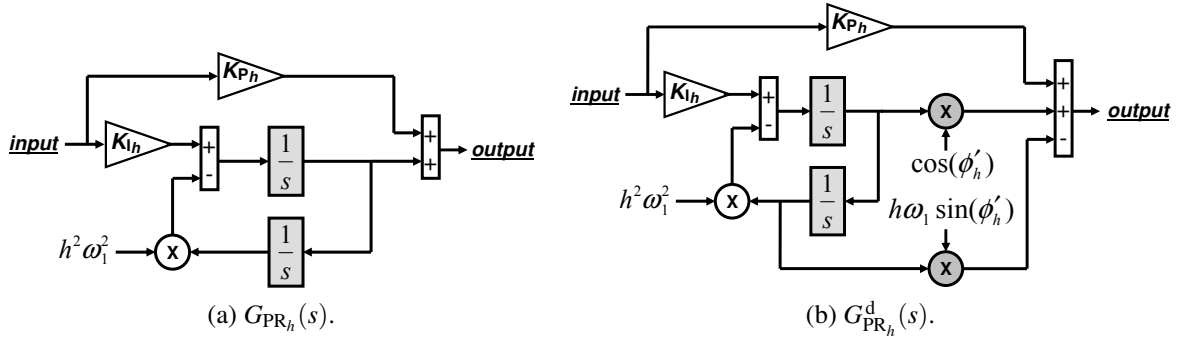


Figure 1.22: Block diagrams of frequency adaptive resonant controllers  $G_{PR_h}(s)$  and  $G_{PR_h}^d(s)$  based on two integrators.

which is the transfer function of a PR controller [65].  $G_{PR_h}(s)$  provides infinite gain in open-loop at the resonant frequency  $h\omega_1$ , so that unity gain and zero phase shift in closed-loop (zero steady-state error) is achieved at that frequency. It should be remarked that to implement (1.28) with additional damping terms should be avoided [65, 158]. The resonant term  $R_1(s)$  is the part of a  $G_{PR_h}(s)$  controller that provides infinite gain at the resonant frequency.  $R_{1_h}(s)$  is preferred to be the Laplace transform of a cosine function instead of that of a sine function, since the former provides better stability [63, 67].

It can be also noted that PR controllers, as well as repetitive ones (see section §1.2.6), also satisfy the internal model principle, because  $R_{1_h}(s)$  is of the same form as the Laplace transform of the signals (sinusoidal) to be tracked. Moreover, from the equivalence between PR controllers and PI control in SRF, it can be stated that the latter also satisfies the internal model principle.

The transfer function  $G_{PR_h}(s)$  can be implemented by decomposing  $R_{1_h}(s)$  into two simple integrators, as shown in Fig. 1.22a [63]. The input  $h\omega_1$  shown in Fig. 1.22a can be modified in real-time according to the actual value of the frequency to be controlled. In this manner, it is a common practice to implement this scheme due to the simplicity it permits for frequency adaptation [58, 63, 120, 203, 219–222, 228, 282, 298].

Several  $G_{PR_h}(s)$  controllers are often implemented in parallel to control several frequencies simultaneously, so the current controller takes the form

$$G_C(s) = \sum_h^{n_h} G_{PR_h}(s) \quad (1.29)$$

with  $n_h$  being the highest harmonic order to be controlled.

From (1.28), the proportional gain  $K_{P_h}$  does not affect any term with frequency-dependence, so it has the same effect over the whole spectrum. Thus, the individual gains  $K_{P_h}$  of each  $G_{PR_h}(s)$  controller may be added in a single parameter  $K_{P_T}$ , so that (1.29) is rewritten as

$$G_C(s) = \sum_h^{n_h} \overbrace{K_{P_h}}^{K_{P_T}} + \sum_h^{n_h} K_{I_h} \frac{\overbrace{R_{1_h}(s)}^{R_{1_h}(s)}}{s} = K_{P_T} + \sum_h^{n_h} K_{I_h} R_{1_h}(s). \quad (1.30)$$

Actually, the term ‘PR controller’ is often employed in the literature to make reference to the global structure in (1.30) and not to each individual  $G_{PR_h}(s)$  component.

To compensate system delays, the zero at the origin in (1.28) can be displaced, so that a phase lead  $\phi'_h$  is introduced at the vicinity of the synchronous frequency [158, 203]:

$$G_{\text{PR}_h}^{\text{d}}(s) = K_{\text{P}_h} + K_{\text{I}_h} \overbrace{\frac{s \cos(\phi'_h) - h\omega_1 \sin(\phi'_h)}{s^2 + h^2\omega_1^2}}^{R_{1_h}^{\text{d}}(s)}. \quad (1.31)$$

The superscript d makes reference to the fact that delay compensation is included. This transfer function is equivalent to transform a pair of schemes as those shown in Fig. 1.9a (one for each sequence) from synchronous to stationary frame [158]:

$$G_{\text{PR}_h}^{\text{d}}(s) = k_{\text{P}_h} + \frac{k_{\text{I}_h}}{s - jh\omega_1} e^{j\phi'_h} + k_{\text{P}_h} + \frac{k_{\text{I}_h}}{s + jh\omega_1} e^{-j\phi'_h}. \quad (1.32)$$

To compensate an integer number of samples  $n_s$ ,  $\phi'_h = h\omega_1 n_s T_s$  should be chosen. The optimum value is often considered to be of two samples ( $n_s = 2$ ) [58, 64, 120, 260, 276]. It should be also remarked that delay compensation becomes more important as the resonant frequency becomes larger with respect to  $f_s$ , that is, as the product  $h\omega_1 T_s$  is increased [51, 56–58, 120, 203].

The scheme shown in Fig. 1.22b was proposed by Bojoi et al. in [203] to implement  $G_{\text{PR}_h}^{\text{d}}(s)$  with two integrators.

### 1.2.7.2 Fundamentals of VPI Controllers

An alternative resonant regulator, known as VPI controller, was proposed by Lascu et al. in [56]. The difference between PR and VPI controllers is that the latter is not equivalent to conventional PI controllers in SRF, but to complex vector PI controllers in SRF:

$$\begin{aligned} G_{\text{VPI}_h}(s) &= \overbrace{\frac{(s - jh\omega_1)k_{\text{P}_h} + k_{\text{I}_h} + jh\omega_1 k_{\text{P}_h}}{s - jh\omega_1}}^{G_{\text{cPI}_h}^+} + \overbrace{\frac{(s + jh\omega_1)k_{\text{P}_h} + k_{\text{I}_h} - jh\omega_1 k_{\text{P}_h}}{s + jh\omega_1}}^{G_{\text{cPI}_h}^-} \\ &= \frac{s^2 \overbrace{2k_{\text{P}_h}}^{K_{\text{P}_h}} + s \overbrace{2k_{\text{I}_h}}^{K_{\text{I}_h}}}{s^2 + h^2\omega_1^2} = \frac{s^2 K_{\text{P}_h} + s K_{\text{I}_h}}{s^2 + h^2\omega_1^2} \end{aligned} \quad (1.33)$$

with  $G_{\text{cPI}_h}^+$  being the equivalent in the stationary frame of a complex vector PI controller implemented in a positive-sequence SRF and  $G_{\text{cPI}_h}^-$  being the equivalent in the stationary frame of a complex vector PI controller implemented in a negative-sequence SRF.

Equation (1.33) can be rewritten as

$$G_{\text{VPI}_h}(s) = K_{\text{P}_h} \overbrace{\frac{R_{2_h}}{s^2}} + K_{\text{I}_h} \overbrace{\frac{R_{1_h}}{s}}. \quad (1.34)$$

It can be noted that  $R_{1_h}$  coincides with the resonant term in (1.28), and a slightly different resonant term is defined as  $R_{2_h}$ . Expression (1.34) will be useful for the discretization analysis in chapter §2, because the decomposition of  $G_{\text{VPI}_h}(s)$  into two separated transfer functions  $R_{1_h}$

and  $R_{2h}$  permits to study a lot of different possibilities for discretization of  $G_{\text{VPI}_h}(s)$ . In that manner, a different discrete-time implementation can be employed for each resonant term. If both resonant terms are discretized with the same method, then the same transfer function as if that discretization method was directly applied to (1.33) is obtained.

To achieve cancellation of the plant zero,  $K_{P_h}$  and  $K_{I_h}$  gains in (1.33) should be adjusted so that  $K_{I_h}/K_{P_h} = R_F/L_F$  [56, 57], as done with the complex vector PI in section §1.2.5.3. Thus, the VPI controller can be also expressed as

$$G_{\text{VPI}_h}(s) = K_h \frac{s(sL_F + R_F)}{s^2 + h^2\omega_1^2} \quad (1.35)$$

where  $K_h = K_{P_h}/L_F$ .

From (1.5) and (1.35), the plant pole in stationary frame (neglecting the effect of computational delay and modulation) is canceled by one of the zeros of the VPI controller. After this cancellation, the open-loop transfer function results in

$$G_{\text{VPI}_h}(s) G_L(s) = K_h \frac{s}{s^2 + h^2\omega_1^2}. \quad (1.36)$$

Once the control loop is closed, a second-order band-pass filter centered at  $h\omega_1$  is obtained [56, 57]:

$$C_L(s) = \frac{I(s)}{I^*(s)} = \frac{G_{\text{VPI}_h}(s) G_L(s)}{1 + G_{\text{VPI}_h}(s) G_L(s)} = \frac{s K_h}{s^2 + s K_h + h^2\omega_1^2} \quad (1.37)$$

where  $I(s)$  and  $I^*(s)$  are the Laplace transforms of  $i$  and  $i^*$ , respectively.

A scheme for implementation of  $G_{\text{VPI}_h}(s)$  with two interconnected integrators is obtained in section §2.2.2 of this thesis, so frequency adaptation can be easily achieved.

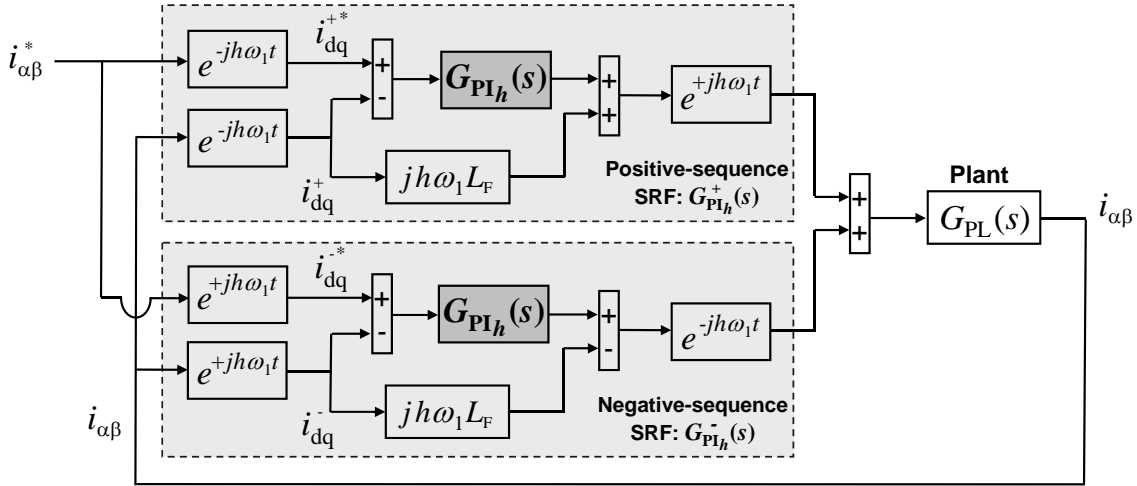
Analogously to PR controllers, it is also possible to implement several  $G_{\text{VPI}_h}(s)$  regulators in parallel to control multiple current harmonics:

$$G_C(s) = \sum_h^{n_h} G_{\text{VPI}_h}(s). \quad (1.38)$$

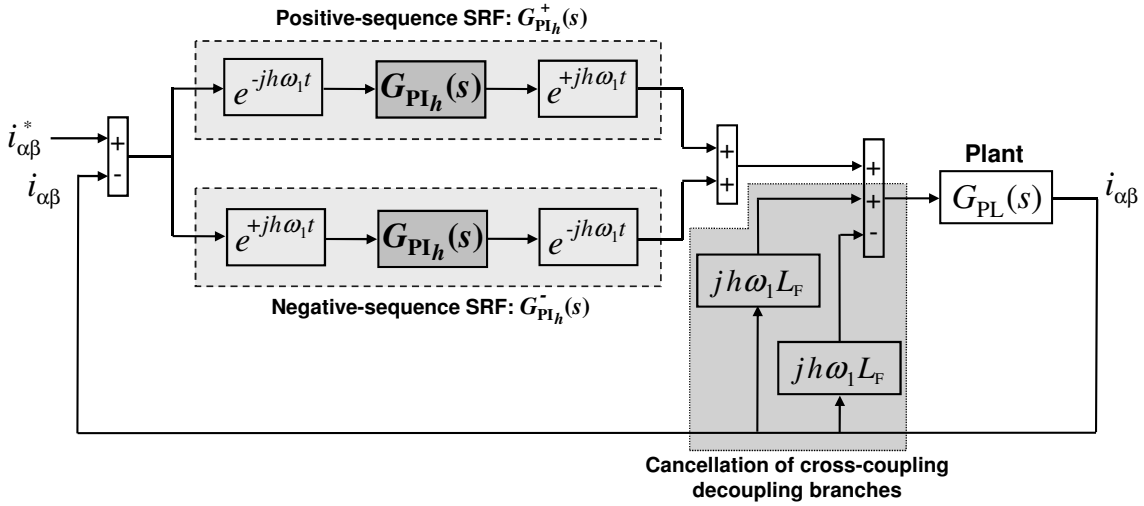
As well as with PR controllers, a delay compensation technique can be added to VPI controllers. This was actually done in several works [51, 57, 58]. Because of  $G_{\text{VPI}_h}(s)$  superior stability, it only requires delay compensation for much greater resonant frequencies than  $G_{\text{PR}_h}(s)$  [51, 56–58]. However, specific details about how to implement VPI controllers with delay compensation have not been presented. A closed-form transfer function to perform delay compensation in VPI controllers is proposed in section §2.4.1 of this thesis.

### 1.2.7.3 Considerations About Simultaneous Cross-Coupling Decoupling for Both Positive- and Negative-Sequences

It has been shown in sections §1.2.7.1 and §1.2.7.2 that PR and VPI controllers are equivalent to, respectively, conventional PI and complex-vector PI controllers implemented in two SRFs at the same time (positive- and negative-sequence). An interesting question to consider is the existence or not of an equivalent resonant controller to PICCDs scheme (described in section §1.2.5.2) in both SRFs. The resulting block diagram of the latter SRF-based structure is shown



(a) Usual implementation [217, 259, 299, 300].



(b) Equivalent scheme to that in Fig. 1.23a. Note the cancellation between the remnant cross-coupling decoupling branches.

Figure 1.23: Block diagram of PI controllers with cross-coupling decoupling schemes implemented in positive- and negative-sequence SRFs simultaneously.

in Fig. 1.23a. The signals  $i_{dq}^+$  and  $i_{dq}^-$  shown in Fig. 1.23a are the projections of the current  $i_{\alpha\beta}$  onto positive- and negative-sequence dq axes, respectively. The same applies to the current references (with superscript \*). Identical implementations to the one shown in Fig. 1.23a can be found, for instance, in Fig. 4 of [259], Fig. 5 of [299], Fig. 5 of [217] and Fig. 3 of [300].

From (1.17) and

$$e^{\pm jh\omega_1 t} jh\omega_1 L_F e^{\mp jh\omega_1 t} = jh\omega_1 L_F \quad (1.39)$$

the scheme shown in Fig. 1.23b is equivalent to the one in Fig. 1.23a. It can be appreciated in Fig. 1.23b that the cross-coupling decoupling branches can be taken unaltered from the SRFs to the stationary frame [in accordance to (1.39)]. In this manner, since they have opposite signs, they are canceled with each other. Therefore, it can be concluded that to implement PICCDs in two SRFs at the same time is in practice the same as to employ conventional PI controllers without decoupling. Both approaches are, hence, equivalent to PR controllers.

It should be noted that this reasoning is in agreement with section §1.2.5.3, where it was explained that effective decoupling cannot be achieved for several SRFs at the same time by means of PICCDs.

#### 1.2.7.4 Resonant Controllers in Fundamental SRF

In three-phase systems, the most common current harmonics are negative-sequence  $6k - 1$  harmonics and positive-sequence  $6k + 1$  harmonic components, with  $k \in \mathbb{N}$  [18, 51, 56–58, 120, 202–205]. To apply a Park transformation with  $\omega_0 = \omega_1$  is equivalent to a  $-\omega_1$  frequency shift at all frequencies [57, 65, 202, 210]. Therefore, each pair of positive-sequence  $6k + 1$  and negative-sequence  $6k - 1$  harmonics is combined into a single harmonic of order  $6k$  when expressed in fundamental (positive-sequence) SRF. In this manner, both harmonics can be tracked by a single resonant controller tuned at  $h = 6k$  in fundamental SRF [18, 49, 51, 56–58, 120, 203–205, 216, 234, 235, 238, 243].

##### A) PR Controllers in Fundamental SRF:

From (1.18) and (1.28), the open-loop transfer function of a PR controller tuned at harmonic  $h$  [i.e.,  $G_{\text{PR}_h}(s)$ ] and implemented in the fundamental SRF results in

$$G_{\text{PR}_h(s)} G'_L(s) = \left( K_{\text{P}_h} + K_{\text{I}_h} \frac{s}{s^2 + h^2 \omega_1^2} \right) \frac{1}{s L_F + R_F + j \omega_1 L_F}. \quad (1.40)$$

The presence of a complex term in (1.40) is due to the cross-coupling between the dq axes. As exposed in section §1.2.5, the imaginary terms can be compensated to avoid several undesired effects. This can be achieved by a simple cross-coupling decoupling scheme analogous to that of the PI controller in SRF shown in Fig 1.10b, that is, by addition of  $j \omega_1 L_F$  at the output of  $G_{\text{PR}_h}(s)$ . In practice, this would mean to replace  $G'_L(s)$  by  $G_L(s)$ , which has been defined in (1.5). In any case, due to the fact that  $G_{\text{PR}_h}(s)$  is equivalent to conventional PI control in SRF without cross-coupling decoupling (see section §1.2.7.1), the issues associated with the cross-coupling at resonant frequencies are still present when PR controllers are implemented in fundamental SRF.

##### B) VPI Controllers in Fundamental SRF:

In the case of a VPI controller in fundamental SRF, the open-loop transfer function is

$$G_{\text{VPI}_h(s)} G'_L(s) = K_h \frac{s(s L_F + R_F)}{s^2 + h^2 \omega_1^2} \frac{1}{s L_F + R_F + j \omega_1 L_F}. \quad (1.41)$$

As with PR controllers in fundamental SRF [see (1.40)], certain cross-coupling between the axes can be appreciated in (1.41).

However, the equivalence between the VPI controllers and complex vector PI regulators in SRF (see section §1.2.7.2) assures that no additional cross-coupling at high frequencies is introduced by the resonant controller, as opposed to PR controllers in fundamental SRF.

In this manner, the consequences of the whole cross-coupling in the case of VPI controllers, when implemented in SRF, are much less significant than with PR controllers. Actually, no noticeable magnitude peaks higher than one and no phase variations in the vicinity of the harmonic frequencies of interest occur [58]. Nevertheless, as exposed by Bojoi et al. in [58], the non-compensated  $j \omega_1 L_F$  term in (1.41) has the following negative effects: a closed-loop resonant peak at  $-50$  Hz in the d axis and another one at  $+50$  Hz in the q axis. As a consequence

of this fact, if the current sampling is not perfect and introduces some dc offset, a second-order harmonic would be injected by the current control [58].

A possible approach to overcome this problem would be to add a cross-coupling decoupling scheme as that employed in PI control in SRF (see Fig. 1.10b), so that  $G'_L(s)$  is replaced by  $G_L(s)$ .

Another option would be to implement the resonant controller proposed by Bojoi et al. in [51, 58] to overcome this issue, defined as

$$G_{\text{cVPI}_h}(s) = K_h \frac{s(sL_F + R_F + j\omega_1 L_F)}{s^2 + h^2\omega_1^2} \quad (1.42)$$

so that the resulting open-loop transfer function lacks any cross-coupling:

$$G_{\text{cVPI}_h}(s) G'_L(s) = K_h \frac{s}{s^2 + h^2\omega_1^2}. \quad (1.43)$$

Note that this result exactly coincides with the open-loop transfer function in (1.36), with the only difference that the former is expressed in fundamental SRF and the latter in stationary frame. Analogously, once the loop is closed, a second-order band-pass filter centered at  $h\omega_1$  [as that in (1.37)] is obtained

$$C_L(s) = \frac{G_{\text{cVPI}_h}(s) G'_L(s)}{1 + G_{\text{cVPI}_h}(s) G'_L(s)} = \frac{s K_h}{s^2 + s K_h + h^2\omega_1^2}. \quad (1.44)$$

This fact corroborates that the cross-coupling has been effectively decoupled by means of  $G_{\text{cVPI}_h}(s)$ .

The difference between the implementation of a conventional  $G_{\text{VPI}_h}(s)$  controller in fundamental SRF in combination with a cross-coupling decoupling scheme and the implementation of  $G_{\text{cVPI}_h}(s)$  is that the former moves the plant pole to the real axis, whereas the latter displaces the controller zero so that it coincides with  $G'_L(s)$  pole. This situation is analogous to the comparison of the conventional PI controller in SRF and the complex vector PI controller in SRF (see section §1.2.5.3). By means of a similar reasoning, it can be concluded that the approach with  $G_{\text{cVPI}_h}(s)$  is less sensitive to deviations in the plant parameters.

### 1.2.7.5 Relation with Repetitive Controllers

The analytical equivalences between a sum of infinite resonant terms of the  $R_{1_h}$  type and repetitive controllers as those in Figs. 1.15 and 1.16 have been developed in [19] and [199, 201], respectively. The similarity between the DFT-based repetitive control and resonant controllers tuned at only certain harmonics has been exposed in [158, 206]. These relations are briefly explained in the following.

#### A) Equivalence with Repetitive Controllers for Odd and Even Harmonics:

A sum of resonant terms of the  $R_{1_h}(s)$  type, multiplied by their corresponding  $K_{I_h}$  gains, is considered:

$$\sum_{h=1}^{\infty} K_{I_h} R_{1_h} = K_{I_1} \frac{s}{s^2 + \omega_1^2} + K_{I_2} \frac{s}{s^2 + (2\omega_1)^2} + K_{I_3} \frac{s}{s^2 + (3\omega_1)^2} + \dots \quad (1.45)$$

If we assume that all gains take the same value  $K_{\text{rep}}$ , from the properties of the exponential function it is obtained that

$$\frac{K_{\text{rep}}}{1 - e^{-s n_d T_s}} = \frac{K_{\text{rep}}}{n_d T_s} \left( \frac{1}{s} + \sum_{h=1}^{\infty} R_{1_h} \right) + \frac{1}{2} \quad (1.46)$$

where, from section §1.2.6,  $n_d T_s = 1/f_1$  [19]. Further development of (1.46) leads to

$$K_{\text{rep}} \frac{1 + e^{-s n_d T_s}}{1 - e^{-s n_d T_s}} = \frac{2 K_{\text{rep}}}{n_d T_s} \left( \frac{1}{s} + \sum_{h=1}^{\infty} R_{1_h} \right). \quad (1.47)$$

Addition of proportional gain  $K_{\text{PT}}$  to both members of (1.47) gives

$$K_{\text{PT}} + \overbrace{K_{\text{rep}} \frac{1 + e^{-s n_d T_s}}{1 - e^{-s n_d T_s}}}^{\text{Rep. controller (Fig. 1.15)}} = K_{\text{PT}} + \underbrace{\frac{2 K_{\text{rep}}}{n_d T_s} \sum_{h=1}^{\infty} R_{1_h}}_{K_{I_h}} + \frac{2 K_{\text{rep}}}{n_d T_s} \frac{1}{s} \quad (1.48)$$

which describes the relation between PR controllers and the repetitive controller shown in Fig. 1.15, when  $F_1(z)$ ,  $F_2(z)$  and  $\delta$  assume unit values. The equivalent in the  $s$ -domain has been obtained by means of the substitution  $z = e^{s T_s}$ . Note that, as expected from section §1.2.6.1, the repetitive scheme includes a pole at the origin if not compensated by  $F_2(z)$ .

*B) Equivalence with Repetitive Controllers for Only Odd Harmonics:*

Alternatively, if only resonant terms for odd harmonics are considered (i.e.,  $h = 2k - 1$   $\forall k \in \mathbb{N}$ ) and  $K_{I_{2k-1}} = 2 K_{\text{rep}} / (n_d T_s) \forall k \in \mathbb{N}$  is assumed, then it is obtained [199, 201]:

$$\frac{K_{\text{rep}}}{n_d T_s} \sum_{k=1}^{\infty} \frac{2s}{s^2 + (2k-1)^2 \omega_1^2} = K_{\text{rep}} \tanh \left( \frac{s}{n_d T_s} \right) = K_{\text{rep}} \frac{1 - e^{-s n_d T_s / 2}}{1 + e^{-s n_d T_s / 2}}. \quad (1.49)$$

Finally, the equivalence between the PR controller and the repetitive controller shown in Fig. 1.16 results in

$$K_{\text{PT}} + \overbrace{K_{\text{rep}} \frac{1 - e^{-s n_d T_s / 2}}{1 + e^{-s n_d T_s / 2}}}^{\text{Rep. controller (Fig. 1.16)}} = K_{\text{PT}} + \underbrace{\frac{2 K_{\text{rep}}}{n_d T_s} \sum_{k=1}^{\infty} R_{1_{2k-1}}}_{K_{I_{2k-1}}}. \quad (1.50)$$

*C) Equivalence with DFT-Based Repetitive Controllers:*

Given a sum of  $R_{1_h}(s)$  terms tuned at selected frequencies in  $N_h$  and with identical  $K_{I_h}$  gains, it verifies

$$K_{I_h} \sum_{h \in N_h} R_{1_h} = \frac{K_{I_h}}{\xi_h h \omega_1} \sum_{h \in N_h} \frac{BPF_h(s)}{1 - BPF_h(s)} \quad (1.51)$$

with  $BPF_h(s)$  being a band-pass filter of the form

$$BPF_h(s) = \frac{s \xi_h h \omega_1}{s^2 + s \xi_h h \omega_1 + h^2 \omega_1^2} \quad (1.52)$$

where  $\xi_h$  is a damping factor [158, 206]. If these pass-band filters are very selective, then (1.51) can be approximated (for frequencies around the selected harmonics) as

$$\frac{K_{I_h}}{\xi_h h \omega_1} \sum_{h \in N_h} \frac{BPF_h(s)}{1 - BPF_h(s)} \approx \frac{K_{I_h}}{\xi_h h \omega_1} \frac{\sum_{h \in N_h} BPF_h(s)}{1 - \sum_{h \in N_h} BPF_h(s)}. \quad (1.53)$$

These conditions are satisfied by means of a running DCT filter as (1.24) with  $n_s = 0$  [158, 206].

The same reasoning can be easily applied to  $R_{1_h}^d(s)$ , which gives (1.24) with  $n_s = \phi_h'/T_s$ , as long as  $\phi_h'/T_s$  is constant and assumes the same value for all harmonics [158, 206].

*D) Differences Between Resonant and Repetitive Controllers:*

From the previous analysis, it can be stated that a single repetitive controller is approximately equivalent to a bank of resonant controllers implemented in parallel and satisfying certain conditions. In any case, the following differences and clarifications can be pointed out.

- This equivalence is only satisfied in the case of the  $R_{1_h}$  type of resonant terms. Since the repetitive controllers are usually implemented with a proportional gain (often with unit value) in parallel, they become analogous to PR controllers. The behavior provided by VPI controllers is not achieved with repetitive regulators.
- Repetitive controllers are less sensitive to quantization and rounding errors, specially in fixed-point implementations [158, 206].
- To implement just a certain number of resonances avoids potential instability issues and steady-state error caused by additional filters. Among repetitive controllers, only the DFT-based one offers this possibility, whereas it is always possible with resonant controllers.
- As exposed in section §1.2.6.2, repetitive controllers impose two restrictive constraints on  $n_s$ : it should be an integer number, and it should take the same value for all resonant frequencies. On the contrary, resonant controllers permit to set a different  $\phi_h'/(h\omega_1 T_s)$  value for each harmonic, and to select any real number for the time step to be compensated. In current-controlled VSCs it is preferable to select a different  $n_s$  for each harmonic, mainly because the phase response of the plant is not proportional to frequency (further investigated in section §3.4.1).
- Regarding frequency adaptation, it can be achieved in resonant controllers by just recalculation of the transfer function coefficients, whereas repetitive regulators usually require on-line modification of the sampling and switching frequencies [175].
- Repetitive controllers do not allow for an independent adjustment of the bandwidth for each of the resonant peaks, but this is possible in resonant controllers by means of the separated  $K_{I_h}$  gains for each harmonic  $h$ .

### 1.2.7.6 Analysis and Design

*A) PR Controllers:*

As exposed in section §1.2.7.1, PR controllers can be divided into two main groups: the ones without delay compensation ( $G_{PR_h}$ ) and those including delay compensation ( $G_{PR_h}^d$ ). Most

studies that can be found regarding tuning of PR controllers are focused on the former type, while the analysis and design of the latter has been still scarcely approached.

The parameters of  $G_{PR_h}(z)$  are often tuned by means of Bode diagrams [44, 45, 47, 51, 55, 57, 58, 63–65, 67–69, 71, 119, 157, 158, 199, 205, 219, 225, 230, 241–243, 246, 251, 254, 255, 274, 279, 281, 282, 284, 286, 292, 293, 297, 298]. As an example, Fig. 1.24 shows the open-loop Bode diagrams [ $G_C(z) G_{PL}(z)$ ] obtained with  $G_{PR_h}(z)$  controllers tuned at three harmonics ( $h \in \{1, 3, 5\}$ ) and for three different values of  $K_{I_h}$  (with  $K_{I_1} = K_{I_3} = K_{I_5} = K_{I_h}$ ): 0, 500 and 2000.

At this point, the following indications can be found in the existing literature about the tuning of PR controllers without delay compensation for current control in VSCs, in those cases in which the plant can be modeled as for an L filter [i.e., with the form of (1.12)].

- The proportional gain  $K_{P_T}$  establishes the cross-over frequency  $f_c$ , at which the gain is 0 dB, if no resonant terms are considered (i.e.,  $K_{I_h} = 0$  in Fig. 1.24).
- Once the resonant terms  $R_{1_h}$  are added in parallel to  $K_{P_T}$ , the global frequency response is appreciably modified only in the vicinity of each resonant frequency  $hf_1$ . Hence, the bandwidth and phase margin  $PM_P$  are almost the same as without the resonant terms [47, 64, 68, 205, 207, 211, 217, 230, 246, 251, 255]. This fact can be also checked in Fig. 1.24.
- In accordance with Fig. 1.24, the integral gain  $K_{I_h}$  defines the resonance width around  $hf_1$ . As  $K_{I_h}$  is increased, the resonant peak becomes less selective (more sensitive to noise and unwanted frequencies), but more tolerant to frequency deviations, and the transient response for  $hf_1$  frequencies becomes faster [64, 70, 71, 203, 280].
- To assure stability, all resonant controllers should be tuned at resonant frequencies lower than  $f_c$  [47, 64, 70, 205, 246, 296].
- The effect of  $K_{I_h}$  on stability is usually neglected, due to its small influence on the global frequency response (second bullet).
- The stability of the system is mainly set by  $K_{P_T}$ . It is tuned to provide an adequate tradeoff between transient response, maximum resonant frequency  $hf_1$  (of resonant controllers) and phase margin [47, 64].

In this manner, the most common tuning procedure basically consists in adjusting  $K_{P_T}$  as for a simple proportional controller [ $K_{P_T} G_{PL}(z)$  is considered], by means of the phase margin criterion, and then resonant controllers [ $R_{1_h}(z)$  terms] are included so that their resonant frequencies are lower enough than  $f_c$ . In many practical situations, this approach is actually sufficient to achieve satisfying results.

Concerning PR controllers including delay compensation, these indications are no longer enough. Thanks to their leading angle,  $G_{PR_h}^d(z)$  controllers may be tuned at frequencies higher than  $f_c$  without violating the stability limits [51, 58, 70, 158]. In that situation, two additional 0 dB crossings (phase margins) appear around each of these resonant frequencies. These extra stability margins may be much lower than the phase margin at  $f_c$ . Consequently, the value of this phase margin is no longer representative of the whole system stability, so an alternative indicator of proximity to instability should be sought.

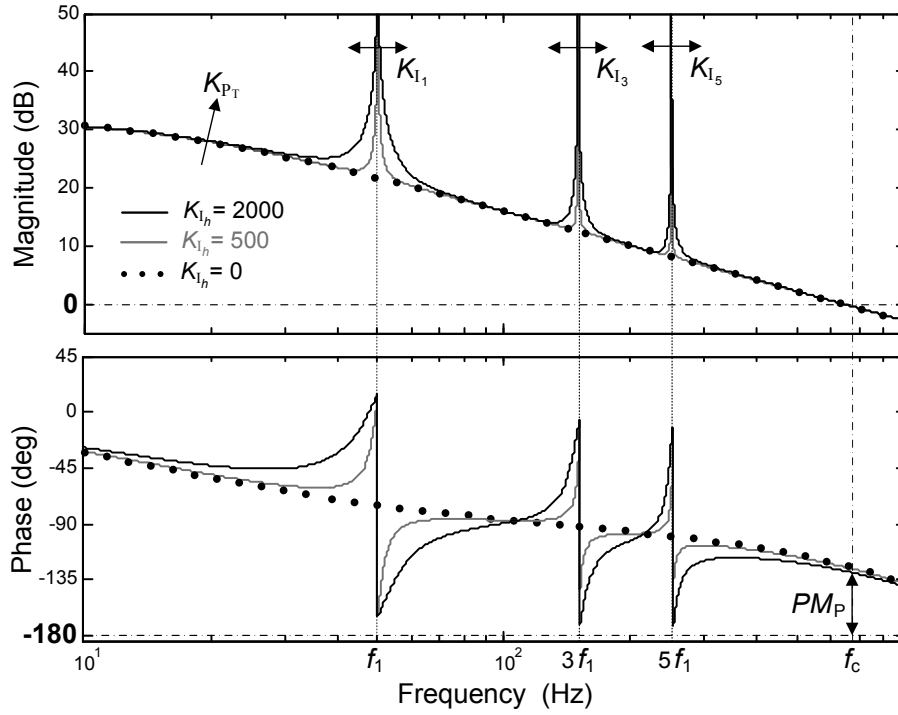


Figure 1.24: Open-loop Bode diagrams  $G_C(z)G_{PL}(z)$  obtained with PR controllers without delay compensation, for different  $K_{I_h}$  values. Note that the system phase margin  $PM_P$  and cross-over frequency  $f_c$  almost do not change with  $K_{I_h}$ . Parameters:  $L_F = 5$  mH,  $R_F = 0.5 \Omega$ ,  $f_s = 10$  kHz,  $h \in \{1, 3, 5\}$ ,  $f_1 = 50$  Hz,  $K_{I_1} = K_{I_3} = K_{I_5} = K_{I_h}$  and  $K_{P_T} = 20$ .

Furthermore, the additional degree of freedom  $\phi'_h$  can be employed, if appropriately adjusted, to reduce anomalous closed-loop gain peaks in the frequency response [51, 58]. Fig. 1.25 shows a closed-loop Bode diagram, in which this kind of undesired resonances can be appreciated near the resonant frequencies  $hf_1$ . The presence of anomalous closed-loop resonances caused by  $G_{PR_h}(z)$  is in agreement with the study presented by Briz et al. in [25], where it has been proved that PI controllers implemented in SRF without cross-coupling decoupling (equivalent to PR controllers, as exposed in section §1.2.7.1) also exhibit this kind of gain peaks in their closed-loop frequency response. It can be also appreciated in Fig. 1.25 that, when a leading angle of two samples (the most common choice [58, 64, 120, 260, 276]) is included (i.e.,  $\phi'_h = 2h\omega_1 T_s$ ), the closed-loop peaks are reduced. If not compensated, those gain peaks may cause magnification of inter-harmonics found in the vicinity of integer harmonics (e.g., in variable speed drives [301–305]), or even amplification of integer harmonics, instead of unity gain (perfect tracking), when small frequency deviations occur.

Most technical publications that investigate the implementation of  $G_{PR_h}^d(z)$  controllers assume that the leading angle  $\phi'_h$  should be equal to the system phase lag  $\angle G_{PL}(z)$  at the resonant frequency [51, 58, 64, 203, 260]. They introduce a leading angle proportional to the resonant frequency:  $\phi'_h \propto h\omega_1$  (typically, a phase lead of two samples, i.e.,  $\phi'_h = 2h\omega_1 T_s$ ). With these approaches, two objectives are pursued.

- Reduction of closed-loop anomalous gain peaks close to  $h\omega_1$  in the closed-loop frequency response.

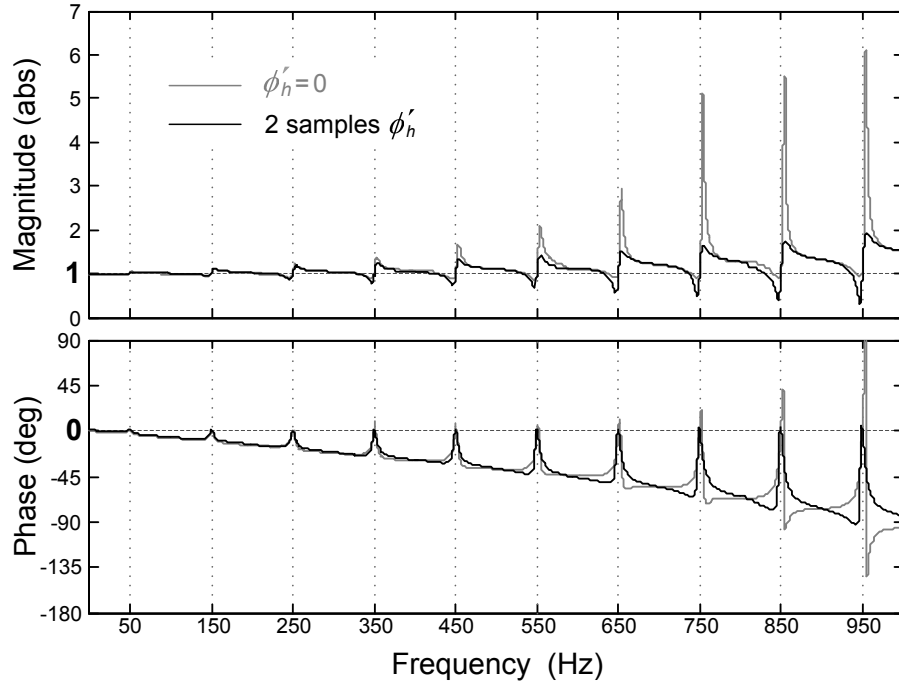


Figure 1.25: Closed-loop Bode diagrams using PR controllers with ( $\phi'_h = 2h\omega_1 T_s$ ) and without ( $\phi'_h = 0$ ) delay compensation. Note the anomalous gain peaks near the resonant frequencies  $hf_1$ . Parameters:  $L_F = 5$  mH,  $R_F = 0.5$   $\Omega$ ,  $f_s = 10$  kHz,  $h \in \{1, 3, 5, \dots, 19\}$ ,  $f_1 = 50$  Hz and  $K_{P_T} = 25$ .

- Improvement in stability, so that resonant controllers may be tuned at resonant frequencies higher than the cross-over frequency:  $hf_1 > f_c$ .

It has been proved in [51, 58] that both aspects are indeed enhanced with respect to PR controllers without delay compensation, when  $\phi'_h \propto h\omega_1$  is chosen. However, as proved in this thesis, these previous approaches for  $\phi'_h$  adjustment do not fully exploit its actual potential. In summary, two main points can be mentioned.

- The actual phase lag of the plant is not proportional to frequency. As proved in section §3.4.1, to assume  $\phi'_h \propto h\omega_1$  implies that the system phase lag is not effectively compensated; thus, the anomalous closed-loop resonances are not reduced as much as possible, and the phase margins are not optimized. An alternative  $\phi'_h$  expression, that compensates both the L filter phase lag and the delay introduced by computation and modulation [ $\phi'_h \approx -\angle G_{PL}(e^{jh\omega_1 T_s})$ ], is proposed in section §3.4.1. It is proved that this approach permits to obtain much higher phase margins and lower undesired closed-loop resonances than  $\phi'_h \propto h\omega_1$ .
- To seek for  $\phi'_h \approx -\angle G_{PL}(e^{jh\omega_1 T_s})$ , as exposed in the previous bullet, manages to maximize the phase margins that appear around  $hf_1$  when  $hf_1 > f_c$ . However, in certain conditions (specially when  $K_{P_T}$  is large, as it will be shown in section §4.4.1), these phase margins are not a reliable indicator of stability. It is proved in chapter §4 that to minimize the sensitivity peak leads to better results in resonant controllers than to maximize the gain or phase margins: it is a more reliable indicator of proximity to instability, and a closed-form relation is found between its value and the closed-loop resonances. A systematic method is proposed in chapter §4 to obtain the highest stability and avoidance

of closed-loop anomalous peaks, as well as an improved transient response, by means of minimization of the sensitivity function (inverse of the Nyquist trajectory to the critical point) and its peak value (the sensitivity peak).

*B) VPI Controllers:* Lascau et al. exposed in [56, 57] how to tune VPI controllers so that certain closed-loop bandwidth around each resonant frequency is obtained. From (1.37), there is a direct relation between  $K_h$  and the closed-loop pass-band width around  $hf_1$ , determining the selectivity and the transient time. This can be checked in the closed-loop Bode diagram shown in Fig. 1.26a.

However, the frequency response analysis of VPI controllers presented in [56, 57] does not take into account the delay introduced by computation and modulation. If it is not appropriately compensated, anomalous closed-loop resonances appear (see Fig. 1.26b) and stability may be compromised [51, 58]. However, an analysis about how to perform delay compensation in VPI controllers cannot be found in the technical literature; only assessments regarding the difference between including or not delay compensation have been published. These observations are summarized in the following.

- It is possible to achieve stability with  $G_{\text{VPI}_h}(z)$  controllers ( $\phi'_h = 0$ ) at higher resonant frequencies than with  $G_{\text{PR}_h}(z)$  ones ( $\phi'_h = 0$ ) [51, 57, 58, 120].
- VPI controllers with one sample phase lead are able to compensate up to the 61th harmonic (with sampling frequency  $f_s = 12.5$  kHz) without becoming unstable [57].
- When delay compensation is added to VPI controllers, even when tuned at very high resonant frequencies, the Nyquist trajectory does not encircle the critical point (the system is made stable) [51]. Note that the analysis presented in [51] is limited to check if the system is stable or not, but the stability margins are not studied. Furthermore, the value of  $\phi'_h$  chosen is not specified.
- A two samples phase lead is assumed in [58] to be the optimum leading angle for both PR and VPI controllers, but no proof is given.

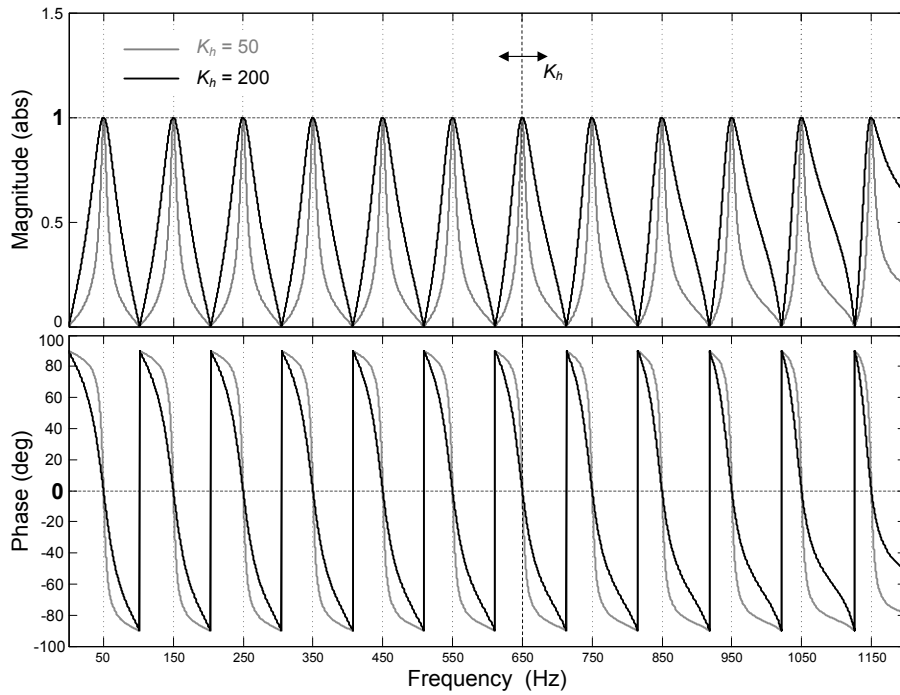
Therefore, a study focused on how to adjust the leading angle in VPI controllers to optimize stability margins and to minimize anomalous closed-loop peaks should be carried out.

Furthermore, a method to measure and optimize the proximity to instability of VPI controllers has not been proposed. Whereas PR controllers only present more than one 0 dB crossing when higher resonant frequencies than  $f_c$  are employed, the VPI controllers always exhibit this kind of complex open-loop frequency response. Thus, the tuning of VPI resonant controllers also requires to seek for a more adequate method than the usual approaches involving Bode plots and the phase margin criterion.

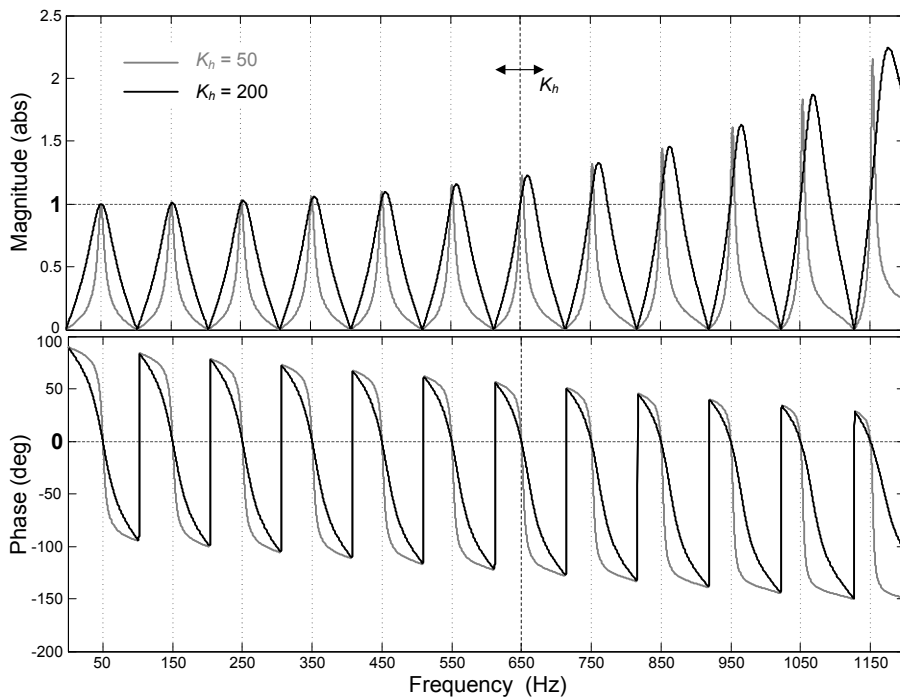
These uncovered issues are approached in chapter §4 by means of Nyquist diagrams and sensitivity function.

### 1.3 Major Results

The work in this dissertation is divided into the following major parts.



(a) Without taking into account the delay due to computation and modulation in the plant model, that is, the open-loop transfer function is  $G_{VPI_h}(s) G_L(s)$ . This corresponds with the frequency response analysis performed in [56, 57].



(b) Taking into account the delay due to computation and modulation in the plant model, that is, the open-loop transfer function is  $G_{VPI_h}(z) G_{PL}(z)$ . Sampling frequency:  $f_s = 10$  kHz.

Figure 1.26: Closed-loop Bode diagrams using VPI controllers without delay compensation. Parameters:  $L_F = 5$  mH,  $R_F = 0.5 \Omega$ ,  $h \in \{1, 3, 5, \dots, 23\}$  and  $f_1 = 50$  Hz.

**Chapter 2: “Effects of Discretization Methods on the Performance of Resonant Controllers”**

This chapter provides an exhaustive analysis and comparison regarding the performance obtained by a wide variety of discretization techniques applied to resonant controllers. The optimum discrete-time implementation alternatives are assessed, in terms of their influence on the resonant peak location (capability of achieving zero steady-state error) and phase versus frequency response (related to stability). Experimental results obtained with a single-phase shunt APF provide a real-time comparison among discretization strategies, which validate the theoretical analysis.

**Chapter 3: “High Performance Digital Resonant Current Controllers Implemented with Two Integrators”**

Alternative implementations based on two interconnected integrators are proposed in this chapter to overcome the issues associated to the original ones (exposed in the previous chapter): large steady-state error and low stability margins. This chapter proposes solutions for both problems without adding a significant resource consumption by correction of the roots placement. A simple expression to calculate the target leading angle, in delay compensation schemes, is also proposed to improve stability margins by means of a better accuracy than previous approaches. In this manner, these enhanced schemes achieve higher performance by means of more accurate resonant peak locations and delay compensation, while maintaining the advantage on low computational burden and good frequency adaptation of the original ones. Experimental results obtained with a laboratory prototype corroborate the theoretical analysis and the improvement achieved by the proposed discrete-time implementations.

**Chapter 4: “Analysis and Design of Resonant Current Controllers for Voltage Source Converters by Means of Nyquist Diagrams and Sensitivity Functions”**

In this chapter, resonant controllers for current-controlled VSCs are analyzed by means of Nyquist diagrams. Due to the fact that a resonant controller only affects the frequency response within a very narrow band of frequencies, the whole control is studied by separated analysis of the individual Nyquist plots that correspond to each of the resonant controllers. The effect of each freedom degree on the trajectories is studied, and their relation with the distance to the critical point (inverse of the sensitivity function) is established. It is proved that the minimization of the sensitivity peak permits to achieve a greater performance and stability rather than by maximizing the gain or phase margins, the latter of which is the most common approach. A systematic method is proposed to obtain the highest stability and avoidance of closed-loop anomalous peaks by means of minimization of the sensitivity function and its peak value. Finally, several experimental tests, including an APF operating at low switching frequency and compensating harmonics up to the Nyquist frequency, validate the theoretical approach.

**Chapter 5: “Conclusions and Future Research”**

The main conclusions of this dissertation are summarized in this chapter and some recommendations for future research topics are provided.

**Appendix A: “Mathematical Development of Expressions for Chapter 2”**

This appendix exposes the analytical development of several complex expressions required for chapter §2.

**Appendix B: “Mathematical Development of Expressions for Chapter 3”**

This appendix exposes the analytical development of several complex expressions required for chapter §3.

**Appendix C: “Mathematical Development of Expressions for Chapter 4”**

This appendix exposes the analytical development of several complex expressions required for chapter §4.

**Appendix D: “Further Information About Testing Facilities”**

Original research results, described in conjunction with chapters 2-4, have been verified using various laboratory prototypes. Each chapter contains brief description of the corresponding experimental facilities. Further information on laboratory prototypes is provided in this Appendix.



# Chapter 2

## Effects of Discretization Methods on the Performance of Resonant Controllers

***Abstract** —An exhaustive study about different discrete-time implementations is contributed in this chapter. Because of the high selectivity of resonant controllers, their performance is very dependent on the accuracy of the resonant frequency. Some discretization methods, such as the popular ones based on two integrators, cause that the frequency of the resonant peaks differ from expected. Such inaccuracies result in significant loss of performance, specially for tracking high frequency signals, since infinite gain at the expected frequency is not achieved, and therefore, zero steady-state error is not assured. Other discretization techniques are demonstrated to provide a more reliable mapping of the resonant poles. The effect on zeros is also analyzed, establishing the influence of each method on the stability. Finally, the study is extended to the discretization of the schemes with delay compensation, which is also proved to be of great importance in relation with their performance. A single-phase active power filter laboratory prototype has been implemented and tested. Experimental results provide a real-time comparison among discretization strategies, which validate the theoretical analysis. The optimum discrete-time implementation alternatives are assessed and summarized.*

### 2.1 Introduction

Most studies devoted to resonant controllers have been carried out in the continuous domain. However, their observations and conclusions cannot be directly applied to digital devices, which work in the discrete-time domain. In nowadays scenarios, most current controllers are implemented in digital platforms, so the influence of the discretization process should not be ignored.

Several discrete-time implementations of resonant controllers have been proposed, but a comparison among the performance obtained by a wide variety of discretization techniques applied to resonant controllers has not been presented at this point. In this chapter, an in-depth comparison among the effects of discretization strategies when applied to resonant controllers is provided.

Because of the narrow band and infinite gain of resonant controllers, they are specially sensitive to the discretization process. Actually, a slight displacement of the resonant poles causes a significant loss of performance, since it implies a large increase in the steady-state error. On the other hand, if selectivity was reduced (wider peaks) to increase robustness to frequency variations, undesired frequencies and noise might be amplified. Thus, an accurate

peak position is preferable to low selectivity. Therefore, it is of paramount importance to study the effectiveness of the different alternatives of discretization in providing an accurate resonant frequency.

As proved in this chapter, many of the existing discretization techniques cause a displacement of the poles. This fact results in a deviation of the frequency at which the infinite gain occurs with respect to the expected resonant frequency. This error becomes more significant as the sampling period and the desired resonant frequency increase. In practice, it can be stated that most of these discretization methods result in suitable implementations when tracking 50/60 Hz (fundamental) references and even for low order harmonics. However, as shown in this chapter, some of them do not perform so well in applications in which signals of higher frequencies should be tracked, such as active power filters (APFs) and ac motor drives. This error has special relevance in the case of implementations based on two interconnected integrators, since it is a widely employed option mainly due to its simplicity for frequency adaptation [58, 63, 120, 203, 219–222, 228, 282, 298].

Discretization also has an effect on zeros, modifying their distribution with respect to the continuous transfer function. These discrepancies should not be ignored, because they have a direct relation with stability. In fact, resonant controllers are often preferred to be based on the Laplace transform of a cosine function instead of that of a sine function because its zero improves stability [63, 67]. In a similar way, the zeros mapped by each technique will affect the stability in a different manner. Consequently, it is also convenient to establish which are the most adequate techniques from the point of view of phase versus frequency response.

Furthermore, for large values of the resonant frequency, the computational delay affects the system performance and may cause instability. Therefore, a delay compensation scheme should be implemented [57, 64, 120, 203]. It can be performed in the continuous domain as proposed in [158, 203]. However, the discretization of that structure leads to several different expressions. A possible implementation in the  $z$ -domain was proposed in [64], but there are other possibilities. Consequently, it should be analyzed how each method affects the effectiveness of the delay compensation. This aspect has a significant relevance, since it will determine the stability at the resonant frequencies.

A single-phase APF laboratory prototype has been built to check the theoretical approaches, because it is an application very suitable for proving the controllers performance when tracking different frequencies, and results can be extrapolated to other single-phase and three-phase applications where a perfect tracking/rejection of references/disturbances is sought through resonant controllers.

The chapter is organized as follows. Section §2.2 presents alternative digital implementations of resonant controllers. The resonant peak displacement depending on the discretization method, as well as its influence on stability, is analyzed in section §2.3. Several discrete-time implementations including delay compensation, and a comparison among them, are exposed in section §2.4. Section §2.5 summarizes the performance of the digital implementations in each aspect and establishes the optimum alternatives depending on the existing requirements. Finally, experimental results of section §2.7 validate the theoretical analysis regarding the effects of discretization on the performance of resonant controllers.

TABLE 2.1  
RELATIONS FOR DISCRETIZING  $R_{1_h}(s)$  AND  $R_{2_h}(s)$  BY DIFFERENT METHODS

Discretization method	Equivalence	Notation ( $i \in \{1, 2\}$ )
Zero-order hold (step invariant)	$X(z) = (1 - z^{-1}) \mathcal{Z} \left\{ \mathcal{L}^{-1} \left[ \frac{X(s)}{s} \right] \Big _{t=kT_s} \right\}$	$R_{i_h}^{\text{zoh}}(z)$
First-order hold (triangle hold)	$X(z) = \frac{(1-z^{-1})^2}{z^{-1}T_s} \mathcal{Z} \left\{ \mathcal{L}^{-1} \left[ \frac{X(s)}{s^2} \right] \Big _{t=kT_s} \right\}$	$R_{i_h}^{\text{t}}(z)$
Forward Euler	$s = \frac{1-z^{-1}}{z^{-1}T_s}$	$R_{i_h}^{\text{f}}(z)$
Backward Euler	$s = \frac{1-z^{-1}}{T_s}$	$R_{i_h}^{\text{b}}(z)$
Tustin (trapezoid)	$s = \frac{2}{T_s} \frac{1-z^{-1}}{1+z^{-1}}$	$R_{i_h}^{\text{t}}(z)$
Tustin with prewarping	$s = \frac{h\omega_1}{\tan\left(\frac{h\omega_1 T_s}{2}\right)} \frac{1-z^{-1}}{1+z^{-1}}$	$R_{i_h}^{\text{tp}}(z)$
Zero-pole matching	$z = e^{sT_s}$	$R_{i_h}^{\text{zpm}}(z)$
Impulse invariant	$X(z) = T_s \mathcal{Z} \left\{ \mathcal{L}^{-1} [X(s)] \Big _{t=kT_s} \right\}$	$R_{i_h}^{\text{imp}}(z)$

## 2.2 Digital Implementations of Resonant Controllers without Delay Compensation

### 2.2.1 Implementations Based on the Continuous Transfer Function Discretization

Table 2.1 shows the most common discretization methods. The Simpson's Rule approximation has not been included because it transforms a second-order function to a fourth-order one, which is undesirable from an implementation viewpoint [306].

The techniques reflected in Table 2.1 have been applied to  $R_{1_h}(s)$  and  $R_{2_h}(s)$  [see (1.30) and (1.34)], leading to the discrete mathematical expressions shown in Table 2.2. The detailed mathematical operations can be found in Appendix A.1. From Table 2.2, it can be seen that the effect of each discretization method on the resonant poles displacement will be equal in both  $R_{1_h}(s)$  and  $R_{2_h}(s)$ , since each method leads to the same denominator in both resonant terms.

It should be noted that zero-pole matching (ZPM) permits a degree of freedom  $K_d$  to maintain the gain for a specific frequency [306].

### 2.2.2 Implementations Based on Two Discrete Integrators

From section §1.2.7.1,  $G_{\text{PR}_h}(s)$  can be implemented by decomposing  $R_{1_h}(s)$  into two simple integrators, as shown in Fig. 1.22a [63]. This structure is considered advantageous when frequency adaptation is required, since no explicit trigonometric functions are needed. An analogous reasoning can be applied to  $G_{\text{VPI}_h}(s)$ , leading to the block diagram proposed in Fig. 2.1. Instead of developing an equivalent scheme to the total transfer function  $G_{\text{VPI}_h}(s)$ , an individual scheme could be obtained for implementing each resonant term  $R_{1_h}(s)$  and  $R_{2_h}(s)$ , but in this case the former is preferable because of the saving of resources.



TABLE 2.3  
DISCRETE TRANSFER FUNCTIONS  $G_{PR_h}(s)$  AND  $G_{VPI_h}(s)$  OBTAINED BY TWO DISCRETIZED INTEGRATORS

Discretization	Discretized $G_{PR_h}(s)$	Discretized $G_{VPI_h}(s)$
Forward & backward	$G_{PR_h}^{f\&b}(z) = K_{P_h} + \frac{K_{I_h} T_s (z^{-1} - z^{-2})}{1 + z^{-1} (h^2 \omega_1^2 T_s^2 - 2) + z^{-2}}$	$G_{VPI_h}^{f\&b}(z) = \frac{K_{P_h} + z^{-1} (K_{I_h} T_s - 2K_{P_h}) - z^{-2} (K_{I_h} T_s - K_{P_h})}{1 + z^{-1} (h^2 \omega_1^2 T_s^2 - 2) + z^{-2}}$
Backward & backward + delay	$G_{PR_h}^{b\&b}(z) = K_{P_h} + \frac{K_{I_h} T_s (1 - z^{-1})}{1 + z^{-1} (h^2 \omega_1^2 T_s^2 - 2) + z^{-2}}$	$G_{VPI_h}^{b\&b}(z) = \frac{(K_{I_h} T_s + K_{P_h}) - z^{-1} (K_{I_h} T_s + 2K_{P_h}) + z^{-2} K_{P_h}}{1 + z^{-1} (h^2 \omega_1^2 T_s^2 - 2) + z^{-2}}$
Tustin & Tustin	$G_{PR_h}^{t\&t}(z) = G_{PR_h}^t(z) = K_{P_h} + \frac{2K_{I_h} T_s (1 - z^{-2})}{(h^2 \omega_1^2 T_s^2 + 4) + z^{-1} (2h^2 \omega_1^2 T_s^2 - 8) + z^{-2} (h^2 \omega_1^2 T_s^2 + 4)}$	$G_{VPI_h}^{t\&t}(z) = G_{VPI_h}^t(z) = \frac{4K_{P_h} + 2K_{I_h} - 8z^{-1} K_{P_h} + z^{-2} (4K_{P_h} - 2K_{I_h})}{(h^2 \omega_1^2 T_s^2 + 4) + z^{-1} (2h^2 \omega_1^2 T_s^2 - 8) + z^{-2} (h^2 \omega_1^2 T_s^2 + 4)}$

It has been suggested in [220] to discretize the direct integrator of Fig. 1.22a scheme using forward Euler method, and the feedback one using the backward Euler method. This is the most common approach [218–222]. Additional alternatives of discretization for both integrators have been analyzed in [221], and it was also proposed to use Tustin for both integrators, or to discretize both with backward Euler, adding a one step delay in the feedback line. In this chapter, these proposals have been also applied to the block diagram shown in Fig. 2.1. Table 2.3 shows these three discrete-time implementations of the schemes depicted in Fig. 1.22. The mathematical operations are developed in Appendix A.1.

It should be noted that  $G_{j_h}^{t\&t}(z)$  and  $G_{j_h}^t(z)$  are equivalent for both  $j = PR$  and  $j = VPI$ , since the Tustin transformation is based on a variable substitution. The same is true for the rest of methods that consist in substituting  $s$  as a function of  $z$ . However, zero-order hold (ZOH), first-order hold (FOH), ZPM and impulse invariant methods applied separately to each integrator do not lead to  $G_{j_h}^{zoh}$ ,  $G_{j_h}^{foh}$ ,  $G_{j_h}^{zpm}$  and  $G_{j_h}^{imp}$ , respectively. Indeed, to discretize an integrator with ZOH, FOH or ZPM yields the same way as a forward Euler substitution, while to discretize an integrator with the impulse invariant is equivalent to employ backward Euler.

## 2.3 Influence of Discretization on Roots Distribution

### 2.3.1 Resonant Poles Displacement

The  $z$ -domain transfer functions obtained in section §2.2 can be grouped in the sets of Table 2.4, since some of them present an identical denominator, and therefore, coinciding poles.

Fig. 2.2 represents the pole locus of the transfer functions in Table 2.4. Damped resonant controllers do not assure perfect tracking [65]; poles must be placed in the unit circumference, which corresponds to a zero damping factor (infinite gain). All discretization techniques apart from A and B lead to undamped poles; the former maps the poles outside of the unit circle, whereas the latter moves them toward the origin, causing a damping factor different from zero, so both methods should be avoided. This behavior finds its explanation in the fact that these two techniques do not map the left half-plane in the  $s$ -domain to the exact area of the unit circle [306].

TABLE 2.4  
GROUPS OF EXPRESSIONS WITH IDENTICAL POLES IN THE  $z$ -DOMAIN

Group	Expressions ( $i \in \{1, 2\}; j \in \{\text{PR}, \text{VPI}\}$ )	Denominator
A	$R_{i_h}^f(z)$	$1 - 2z^{-1} + z^{-2}(h^2\omega_1^2T_s^2 + 1)$
B	$R_{i_h}^b(z)$	$(h^2\omega_1^2T_s^2 + 1) - 2z^{-1} + z^{-2}$
C	$R_{i_h}^t(z), G_{j_h}^{t\&t}(z)$	$(h^2\omega_1^2T_s^2 + 4) + z^{-1}(2h^2\omega_1^2T_s^2 - 8) + z^{-2}(h^2\omega_1^2T_s^2 + 4)$
D	$G_{j_h}^{f\&b}(z), G_{j_h}^{b\&b}(z)$	$1 + z^{-1}(h^2\omega_1^2T_s^2 - 2) + z^{-2}$
E	$R_{i_h}^{\text{zoh}}(z), R_{i_h}^{\text{foh}}(z), R_{i_h}^{\text{tp}}(z), R_{i_h}^{\text{zpm}}(z), R_{i_h}^{\text{imp}}(z)$	$1 - 2z^{-1}\cos(h\omega_1T_s) + z^{-2}$

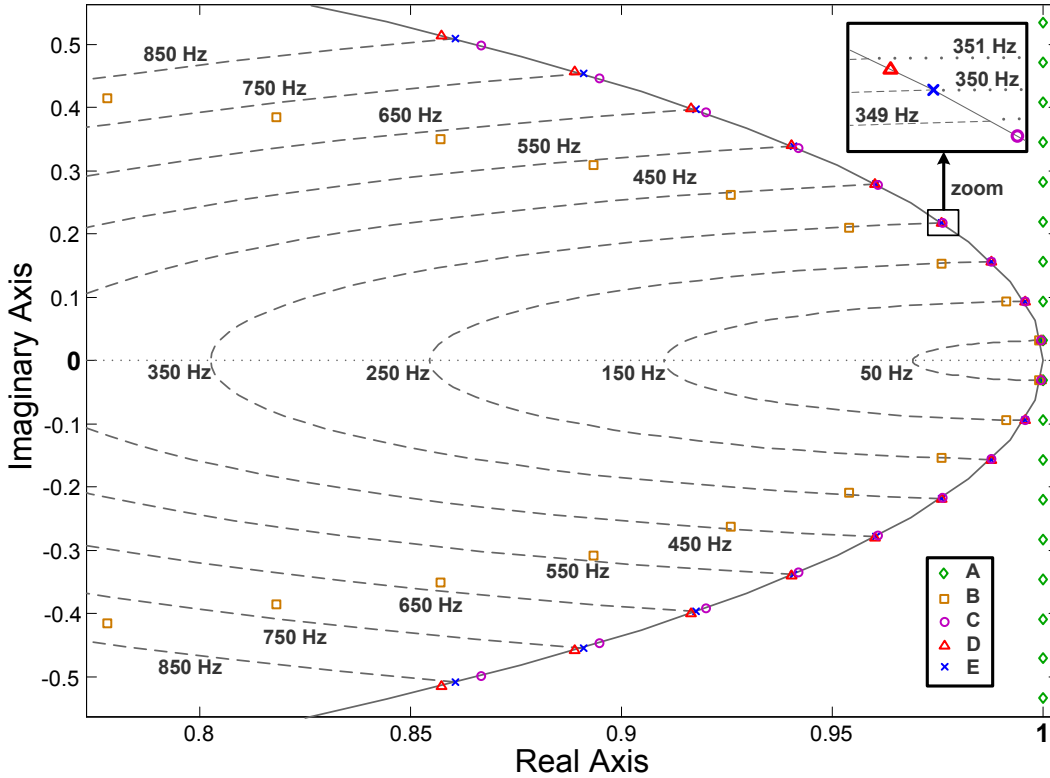
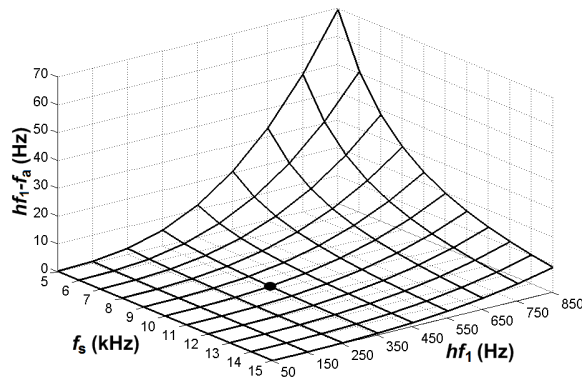


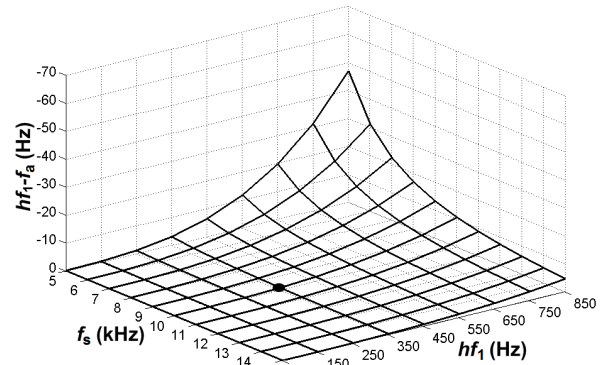
Figure 2.2: Pole locus of the discretized resonant controllers, at  $f_s = 10$  kHz (fundamental to 17th odd harmonics).

However, there is an additional issue that should be taken into account. Although groups C, D and E achieve infinite gain, it can be appreciated that, for an identical value of  $hf_1$ , their poles are located in different positions of the unit circumference. This fact reveals that there exists a difference between  $hf_1$  and the actual resonant frequency  $f_a$ , depending on the employed implementation, as also observed in Fig. 2.3d. Consequently, the infinite gain may not match the frequency of the controller references, causing steady-state error.

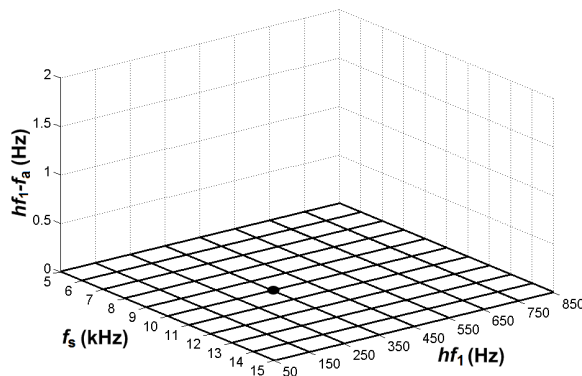
Figs. 2.3a to 2.3c depict the error  $hf_1 - f_a$  in hertz, as a function of  $hf_1$  and  $f_s$  for each group. The poles displacement increases with  $T_s$  and  $hf_1$ , with the exception of group E. The slope of the error is also greater as these parameters become higher. Actually, the denominator of group D is a second-order Taylor series approximation of group E. This fact explains the increasing difference between them as the product  $h\omega_1T_s$  becomes larger.



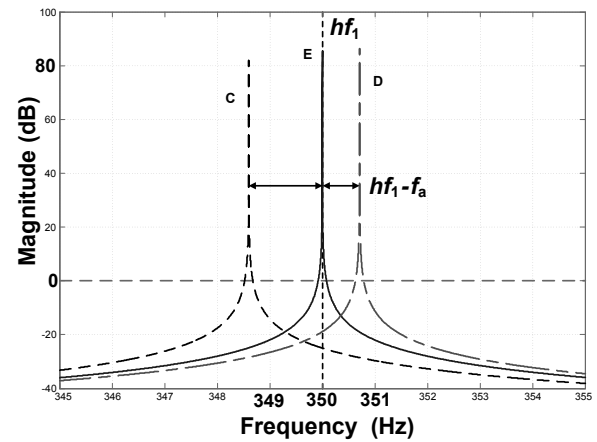
(a) Group C transfer functions.



(b) Group D transfer functions.



(c) Group E transfer functions.



(d) Open-loop frequency response of discrete-time resonant controllers tuned at  $hf_1 = 350\text{Hz}$ , with  $f_s = 10\text{kHz}$ .

Figure 2.3: Deviation of the actual resonant frequency  $f_a$  of the discretized controller from the resonant frequency  $hf_1$  of the continuous controller.

Some important outcomes from this study should be highlighted.

- The Tustin transformation, which is a typical choice in digital control due to its accuracy in most applications, features the most significant deviation in the resonant frequency.
- The error exhibited by the methods based on two discretized integrators becomes significant even for high sampling frequencies and low order harmonics. For instance, at  $f_s = 10$  kHz, group D exhibits an error of +0.7 Hz for the seventh harmonic, which causes a considerable gain loss (see Fig. 2.3d). When dealing with higher harmonic orders, such as 13 and 17, it raises to 4.6 Hz and 10.4 Hz, respectively, which is unacceptable.
- Group E leads to poles that match the original continuous ones, so the resonant peak always fits the design frequency  $hf_1$ .

## 2.3.2 Effects on Zeros Distribution

Once assured infinite gain due to a correct position of the poles, another factor to take into account is the displacement of zeros caused by the discretization. Resonant controllers that belong to group E have been proved to be more suitable for an optimum implementation in terms of resonant peak displacement. However, the numerators of these discrete transfer functions are not the same, and they depend on the discretization method. This aspect has a direct relation with stability, so it should not be ignored.

On the other hand, although group D methods produce a resonant frequency error, they avoid the calculation of explicit cosine functions when frequency adaptation is needed. This fact may imply an important saving of resources. Therefore, it is also of interest to establish which is the best option of that set.

The analysis will be carried out by means of the frequency response. The infinite gain at  $h\omega_1$  is given by the poles position, whereas zeros only have a visible impact on the gain at other frequencies. Concerning phase, the mapping of zeros provided by the discretization may affect all the spectrum, including the phase response near the resonant frequency. Due to the high gain around  $h\omega_1$ , the phase introduced by the resonant terms at  $\omega \approx h\omega_1$  will have much more impact on the phase response of the whole system than at the rest of the spectrum [64]. Therefore, the influence of discretization on the stability should be studied mainly by analyzing the phase lag caused at  $\omega \approx h\omega_1$ .

### 2.3.2.1 Displacement of $R_{1_h}(s)$ Zeros by Group E Discretizations

Fig. 2.4 compares the frequency response of a resonant controller  $R_{1_h}(s)$ , tuned at  $hf_1 = 350$  Hz, when discretization methods of group E are employed at  $f_s = 10$  kHz. An almost equivalent magnitude behavior is observed, even though  $R_{1_h}^{\text{imp}}(z)$  has a lower attenuation in the extremes, and both  $R_{1_h}^{\text{tp}}(z)$  and  $R_{1_h}^{\text{foh}}(z)$  tend to reduce the gain at high frequencies. However, the phase versus frequency plot differs more significantly.

From Fig. 2.4, it can be appreciated that  $R_{1_h}^{\text{tp}}(z)$  and  $R_{1_h}^{\text{foh}}(z)$  are the most accurate when comparing with  $R_{1_h}(s)$ . On the contrary, the phase lag introduced by  $R_{1_h}^{\text{zoh}}(z)$  and  $R_{1_h}^{\text{zpm}}(z)$  is higher than for the continuous model. This fact is particularly critical at  $\omega \approx h\omega_1$ , even though they also cause delay for higher frequencies. As shown in Fig. 2.4, they introduce a phase lag at  $hf_1 = 350$  Hz of  $6.3^\circ$ . For higher values of  $h\omega_1 T_s$ , it becomes greater. For instance, if

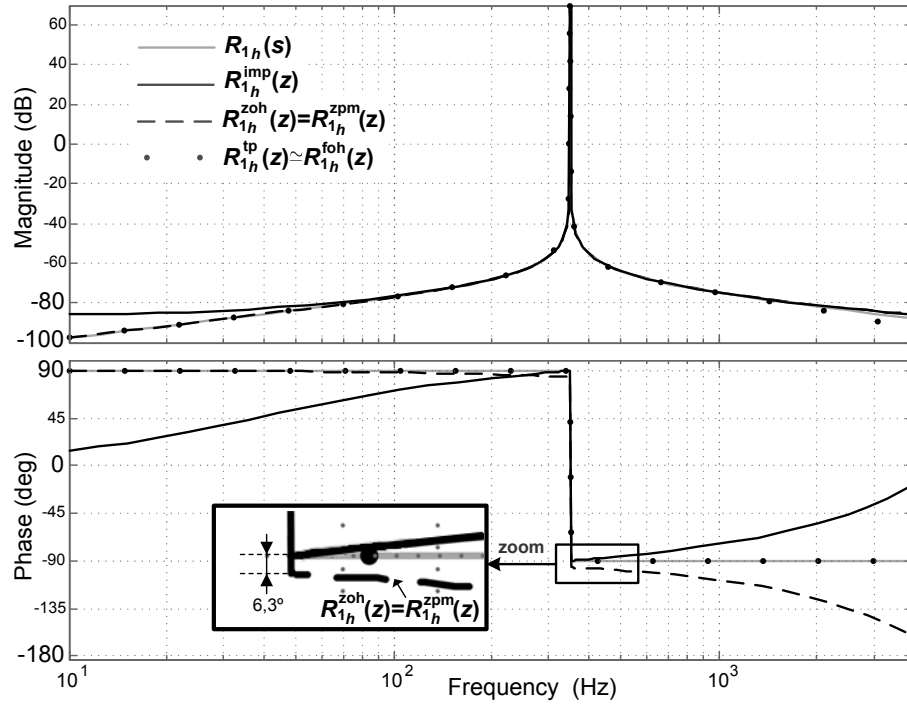


Figure 2.4: Bode plot of  $R_{1_h}(s)$  discretized with group E methods, tuned at  $hf_1 = 350$  Hz and with  $f_s = 10$  kHz.

tuned at a resonant frequency of  $hf_1 = 1750$  Hz with  $f_s = 10$  kHz, the delay is  $32^\circ$ . Therefore, the implementation of  $R_{1_h}^{zoh}(z)$  and  $R_{1_h}^{zpm}(z)$  may lead to instability. On the other hand,  $R_{1_h}^{tp}(z)$ ,  $R_{1_h}^{foh}(z)$  and  $R_{1_h}^{imp}(z)$  accurately reproduce the frequency response at the resonant frequency, maintaining the stability of the continuous controller at  $h\omega_1$ . Fig. 2.4 also shows that  $R_{1_h}^{imp}(z)$  introduces less phase lag in open-loop for the rest of the spectrum, thereby allowing for a larger phase margin.

In any case, the influence of the discretization at  $\omega \neq h\omega_1$  is not as important as its effect on the stability at  $\omega \approx h\omega_1$ , since the gain of  $R_{1_h}(z)$  is much lower at these frequencies. Consequently, the phase lead of  $R_{1_h}^{imp}(z)$  at high frequencies can be neglected unless great values of  $K_{I_h}/K_{P_T}$  are employed. In these cases, it can be taken into account in order to avoid unexpected reductions in the phase margin that could affect the stability, or even to increase its value over the phase margin of the continuous system by means of  $R_{1_h}^{imp}(z)$ .

### 2.3.2.2 Displacement of $R_{2_h}(s)$ Zeros by Group E Discretizations

The frequency response of  $R_{2_h}(s)$  discretizations is shown in Fig. 2.5a. It can be seen that ZOH produces a phase lag near the resonant frequency that could affect stability.

Among the rest of possibilities of group E, the impulse invariant method is also quite unfavorable: it provides much less gain after the resonant peak than the rest of the discretizations. This fact causes that the zero phase provided by  $R_{2_h}(z)$  for  $\omega > h\omega_1$  has much less impact on the global transfer function  $G_{VPI_h}(z)$ , in comparison to the phase delay introduced by  $R_{1_h}(z)$ . In this manner, the phase response of  $G_{VPI_h}(z)$  shows a larger phase lag if  $R_{2_h}(s)$  is discretized with impulse invariant instead of other methods, worsening the stability at  $\omega > h\omega_1$ .

Actually, as shown in Fig. 2.5b, if  $R_{2_h}^{\text{imp}}(z)$  is used, the delay of  $G_{\text{VPI}_h}(z)$  may become close to  $-45^\circ$  for certain frequencies, which is certainly not negligible. This is illustrated, as an example, in Fig. 2.5b, in which the Bode plot of  $G_{\text{VPI}_h}(z)$ , when it is implemented as  $R_{1_h}^{\text{imp}}(z)$  and  $R_{2_h}(s)$  is discretized with the different methods, is shown. Fixed values of  $K_{I_h}$  and  $K_{P_h}$  have been employed to make the comparison possible.  $K_{I_h} = K_{P_h} R_F/L_F$  has been chosen, so the cross-coupling due to the plant is canceled [56, 57], and an arbitrary value of 1 has been assigned to  $K_{P_h}$  as an example. According to the real parameters of the laboratory prototype,  $L_F = 5$  mH and  $R_F = 0.5 \Omega$ . If the ratio  $K_{I_h}/K_{P_h}$  is changed, the differences will become more or less noticeable, but essentially each method will still affect in the same manner. It should be remarked that the phase response of  $G_{\text{VPI}_h}(z)$  at  $\omega \approx h\omega_1$  is not modified by  $R_{1_h}^{\text{imp}}(z)$ , but only by the discretization of  $R_{2_h}(s)$ . Fig. 2.5b also shows that some implementations introduce less phase at low frequencies than  $G_{\text{VPI}_h}(z)$ , but the influence of this aspect on the performance can be neglected.

In conclusion, any of the discretization methods of group E, with the exception of impulse invariant and ZOH, are adequate for the implementation of  $R_{2_h}(z)$ . Actually, the influence of these two methods is so negative that they could easily lead to instability of continuous resonant controllers with considerable stability margins.

### 2.3.2.3 Displacement of Zeros by Group D Discretizations

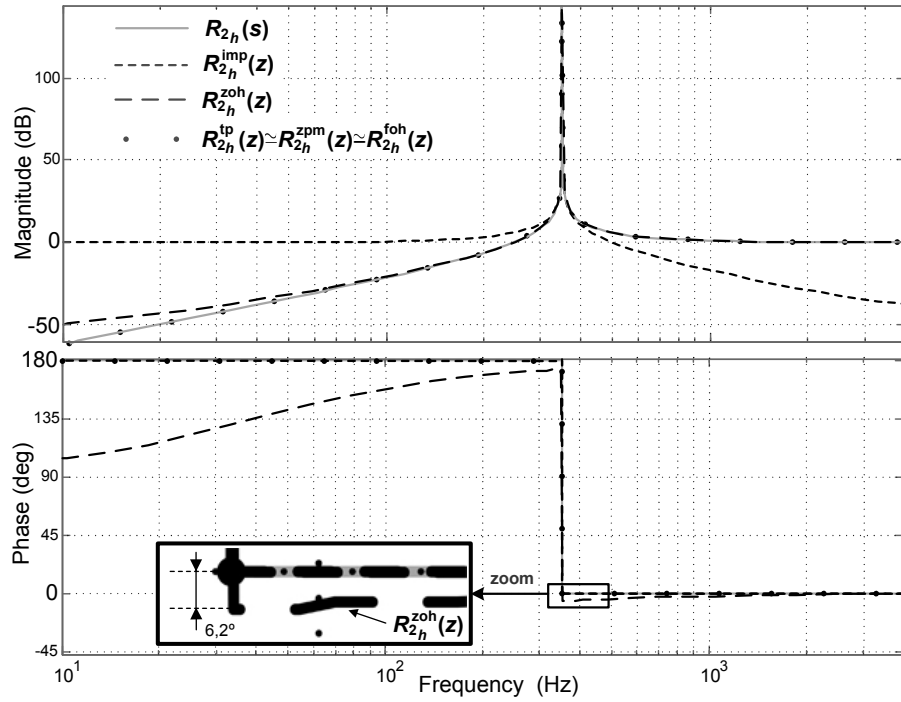
Fig. 2.6a shows the Bode plot of  $R_{1_h}(s)$  implemented with set D schemes.  $R_{1_h}^{\text{f&b}}(z)$  produces a phase lead in comparison to  $R_{1_h}(s)$ , whereas  $R_{1_h}^{\text{b&b}}(z)$  causes a phase lag. This is also true at  $\omega \approx h\omega_1$ , which are the most critical frequencies. Therefore,  $R_{1_h}^{\text{f&b}}(z)$  is preferable to  $R_{1_h}^{\text{b&b}}(z)$ . On the other hand, as can be appreciated in Fig. 2.6b, the Bode plots of  $G_{\text{VPI}_h}^{\text{f&b}}(z)$  and  $G_{\text{VPI}_h}^{\text{b&b}}(z)$  scarcely differ. They both achieve an accurate reproduction of  $G_{\text{VPI}_h}(s)$  frequency response. Actually, at  $\omega \approx h\omega_1$  they provide exactly the same phase. Consequently, they can be indistinctly employed with satisfactory results.

## 2.4 Influence of Discretization on Delay Compensation

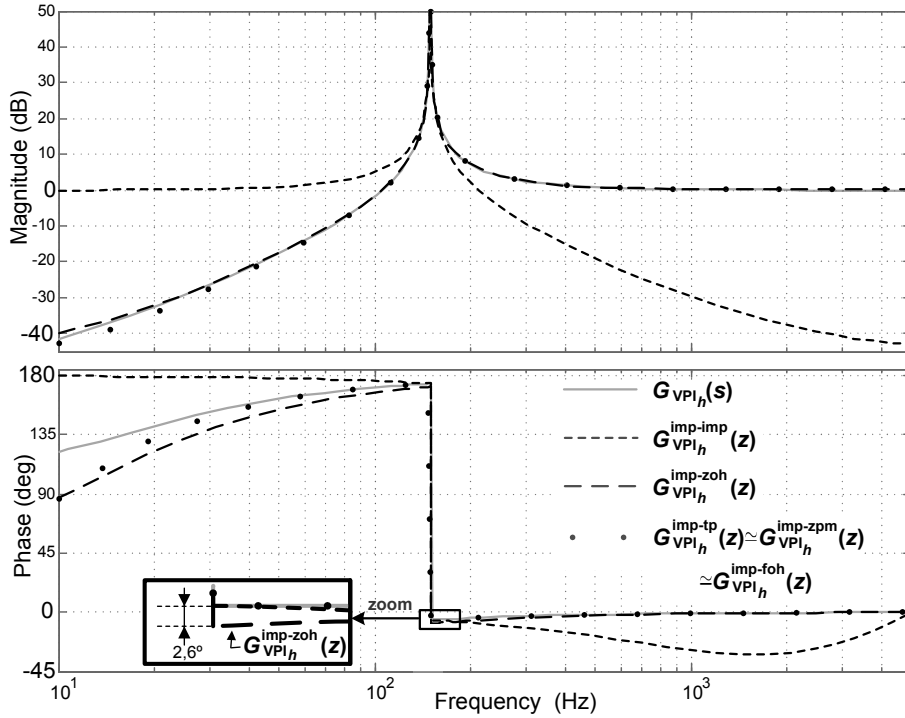
### 2.4.1 Delay Compensation in the Continuous Domain

A proportional-resonant (PR) controller with delay compensation can be implemented in the  $s$ -domain as (1.31). It is also possible to add a delay compensation technique to vector proportional-integral (VPI) controllers. This was actually done in several works [51, 57, 58]. Because of  $G_{\text{VPI}_h}(s)$  superior stability, it only requires delay compensation for much greater resonant frequencies than  $G_{\text{PR}_h}(s)$  [51, 56–58]. However, specific details about how to implement VPI controllers with delay compensation have not been presented.

Delay compensation for VPI controllers could be obtained by selecting  $K_{P_h} = \cos(\phi'_h)$  and  $K_{I_h} = -h\omega_1 \sin(\phi'_h)$ . Nevertheless, this approach would not permit to choose the parameters so as to satisfy  $K_{I_h}/K_{P_h} = R_F/L_F$ ; thus, it would not cancel the cross-coupling terms as proposed in [56, 57]. Instead, an alternative approach is proposed here.  $R_{1_h}(s)$  and  $R_{2_h}(s)$  may be individually implemented with a phase lead  $\phi'_h$  each, so  $K_{P_h}$  and  $K_{I_h}$  can be still adjusted in order to

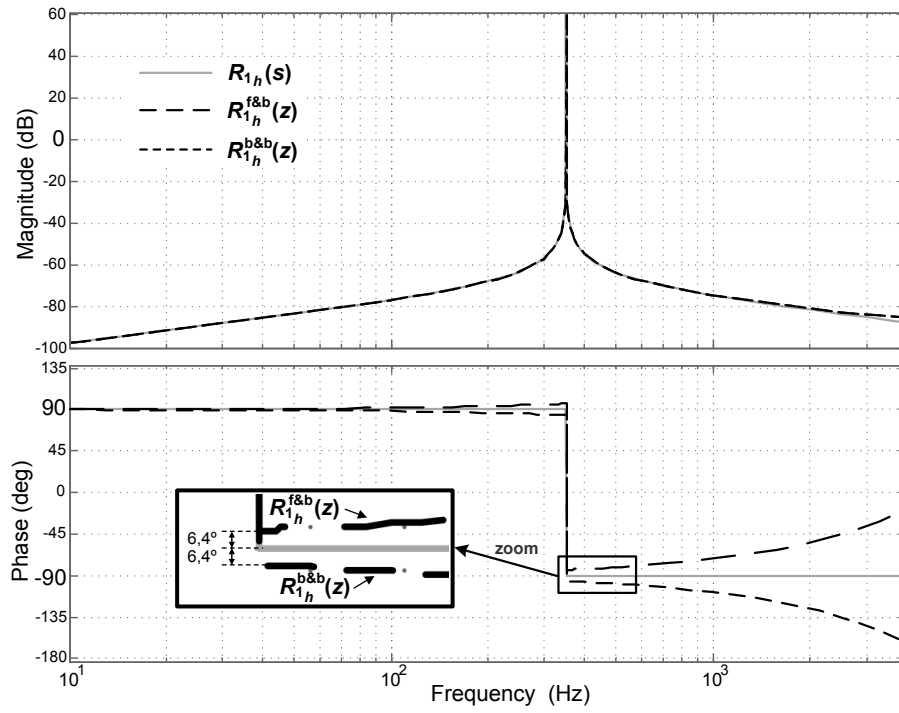


(a) Frequency response of  $R_{2h}(s)$  discretized with group E methods, tuned at  $hf_1 = 350\text{Hz}$  and with  $f_s = 10\text{kHz}$ .

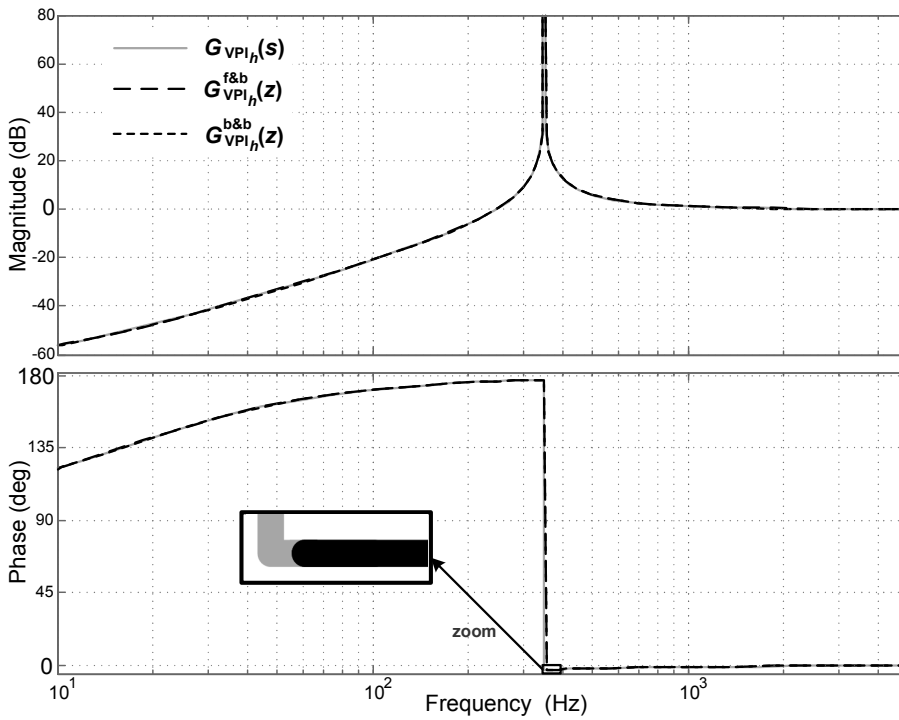


(b) Frequency response of  $G_{VPI_h}(z)$  for a third harmonic resonant controller at  $f_s = 10\text{kHz}$ , with  $R_{1h}^{imp}(z)$ , when  $R_{2h}(s)$  is discretized by each method of group E.  $K_{P_h} = 1$  and  $K_{I_h} = K_{P_h} R_F / L_F$ , with  $R_F = 0.5\ \Omega$  and  $L_F = 5\ \text{mH}$ .

Figure 2.5: Study of group E discretizations effect on  $R_{2h}(s)$  zeros.



(a)  $R_{1h}(s)$ .



(b)  $G_{vPI_h}(s)$ .  $K_{P_h} = 1$  and  $K_{I_h} = K_{P_h} R_F / L_F$ , with  $R_F = 0.5 \Omega$  and  $L_F = 5$  mH.

Figure 2.6: Frequency response of  $R_{1h}(s)$  and  $G_{vPI_h}(s)$  implemented with group D methods, tuned at  $hf_1 = 350$  Hz and with  $f_s = 10$  kHz.

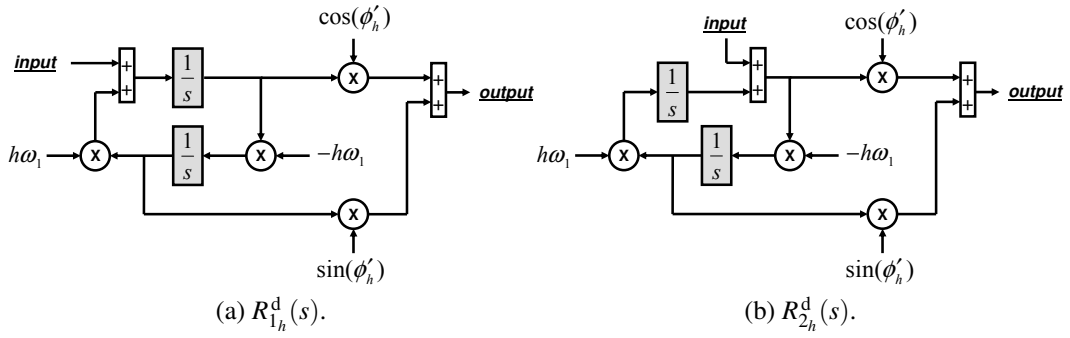


Figure 2.7: Implementations of  $R_{1h}^d(s)$  and  $R_{2h}^d(s)$  based on two integrators.

cancel the plant pole:

$$\begin{aligned} G_{\text{VPI}_h}^d(s) &= K_{P_h} \frac{s^2 \cos(\phi'_h) - s h \omega_1 \sin(\phi'_h)}{s^2 + h^2 \omega_1^2} + K_{I_h} \frac{s \cos(\phi'_h) - h \omega_1 \sin(\phi'_h)}{s^2 + h^2 \omega_1^2} \\ &= K_{P_h} R_{2h}^d + K_{I_h} R_{1h}^d. \end{aligned} \quad (2.1)$$

It should be noted that  $R_{1h}^d$  coincides with the resonant term in (1.31). Equation (2.1) can be rearranged as

$$G_{\text{VPI}_h}^d(s) = K_h \frac{(s L_F + R_F) [s \cos(\phi'_h) - h \omega_1 \sin(\phi'_h)]}{s^2 + h^2 \omega_1^2} \quad (2.2)$$

which, at the same time, is equal to  $G_{\text{cPI}_h}^+(s) e^{j\phi'_h} + G_{\text{cPI}_h}^-(s) e^{-j\phi'_h}$ . Nevertheless, (2.1) is the expression considered in this chapter, because the decomposition of  $G_{\text{VPI}_h}^d(s)$  into two separated transfer functions  $R_{1h}^d$  and  $R_{2h}^d$  permits to study a lot of different possibilities for discretization of  $G_{\text{VPI}_h}^d(s)$ . The optimum discretization approach for  $G_{\text{VPI}_h}^d(s)$  will be the combination of the optimum discrete-time implementations for each resonant term.

If the resonant terms are decomposed by the use of two integrators, it is possible to perform the delay compensation by means of the block diagrams depicted in Figs. 2.7a and 2.7b, for  $R_{1h}^d(s)$  and  $R_{2h}^d(s)$ , respectively. It should be remarked that, unlike  $G_{\text{VPI}_h}(s)$  (see Fig. 2.1), it is not possible to implement  $G_{\text{VPI}_h}^d(s)$  with a single scheme based on two integrators.

Fig. 2.8 illustrates the effect of the computational delay compensation for both  $R_{1h}^d(s)$  and  $R_{2h}^d(s)$ , setting  $h f_1 = 350 \text{ Hz}$  and  $f_s = 10 \text{ kHz}$  as an example. As the number of samples  $n_s$  to compensate increases ( $\phi'_h = h \omega_1 n_s T_s$  is considered), the  $180^\circ$  phase shift at  $h f_1$  rises, compensating the phase lag that would be caused by the system delay.

## 2.4.2 Discrete-Time Implementations of Delay Compensation Schemes

As stated in section §1.2.7, the delay compensation may be implemented for each resonant term separately. For this reason, it is convenient to study how each discretization method affects the effectiveness of the delay compensation for  $R_{1h}^d(z)$  and  $R_{2h}^d(z)$  individually. Effects on groups E and D implementations, due to their superior performance, are analyzed. Table 2.5 and Table 2.6 reflect the discrete transfer functions obtained by the application of these methods

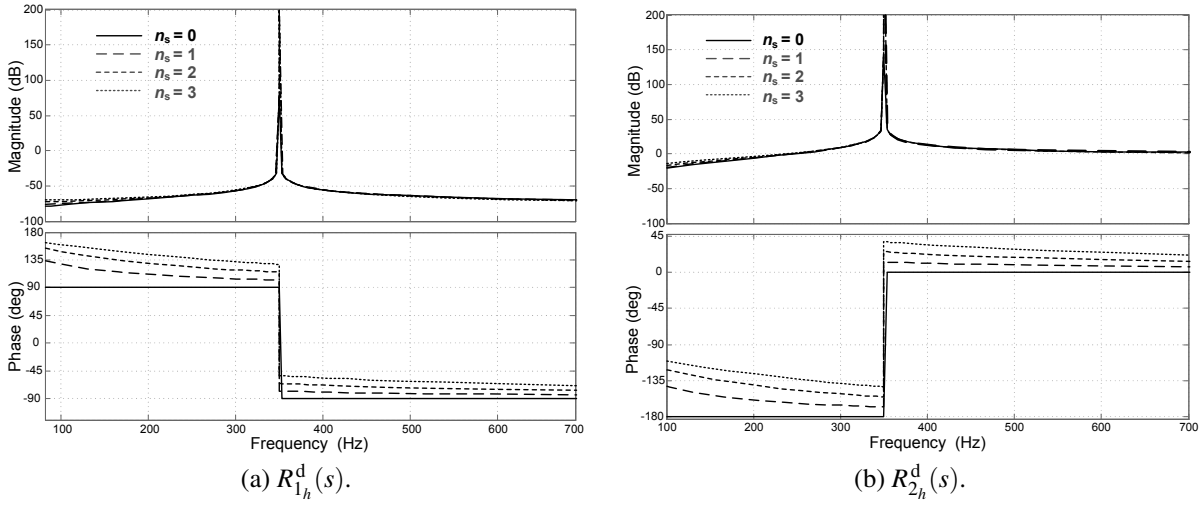


Figure 2.8: Frequency response of  $R_{1h}^d(s)$  and  $R_{2h}^d(s)$ , for different values of  $n_s$ . Parameters:  $hf_1 = 350\text{Hz}$  and  $f_s = 10\text{kHz}$ .

to  $R_{1h}^d(s)$  and  $R_{2h}^d(s)$ , respectively.  $R_{1h}^{d\text{f\&b}}(z)$  and  $R_{1h}^{d\text{b\&b}}(z)$  result of applying the corresponding discretization transforms to the scheme shown in Fig. 2.7a. On the other hand,  $R_{2h}^{d\text{f\&b}}(z)$  and  $R_{2h}^{d\text{b\&b}}(z)$  are obtained by discretizing the integrators shown in Fig. 2.7b. The mathematical operations are developed in Appendix A.2.

Substitution of  $n_s = 0$  in Table 2.5 and Table 2.6 leads to the expressions of Table 2.2 and Table 2.3, respectively. It can be also noted that  $R_{1h}^{d\text{imp}}(z)$  is approximately equivalent to the proposals of Yuan et al. [64] for digital implementation of the computational delay (further exposed in section §3.4.2).

### 2.4.3 Study of Discretization Effects on Delay Compensation

In order to quantify the influence of each discretization technique on the desired delay compensation, an error function  $\varepsilon_{\phi_h}$  is defined as follows:

$$\varepsilon_{\phi_h} = \lim_{\omega \rightarrow h\omega_1} \left[ \angle R_{i_h}^d(s) - \angle R_{i_h}^{dX}(z) \right] \quad (2.3)$$

for each discretization method  $X$ , with  $i \in \{1, 2\}$ . This parameter reflects the difference in degrees between the expected and the actual phase lead introduced. It can be evaluated as a function of  $f_s$ ,  $n_s$  and  $h\omega_1$ . Figs. 2.9 and 2.10 show the resulting values of applying the error function to discretization methods E and D, respectively.

Since the variables  $T_s$  and  $h\omega_1$  always appear together in the expressions as a product, both parameters have an analogous impact on the delay compensation. In this manner, the error increases with  $T_s$  with the same rate of change as with  $h\omega_1$ .

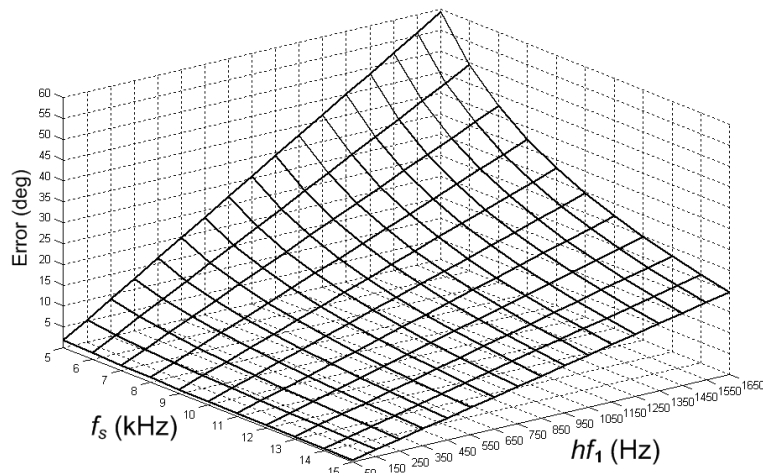
Fig. 2.9a represents  $\varepsilon_{\phi_h}$  evaluated in the cases of  $R_{1h}^{d\text{zoh}}(z)$  and  $R_{2h}^{d\text{zoh}}(z)$ . It assumes large values for most combinations of  $T_s$  and  $h\omega_1$ , so these discretizations are not appropriate. It should be also noted that, for  $R_{1h}^{d\text{zoh}}(z)$  and  $R_{2h}^{d\text{zoh}}(z)$ , the error is independent of  $n_s$ .

TABLE 2.5  
 $R_{1_h}^d(s)$  DISCRETIZED BY GROUPS E AND D

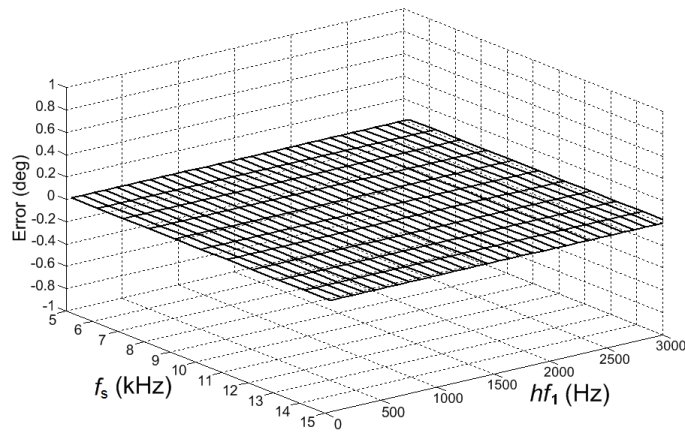
Zero-order hold	$R_{1_h}^{dzoh}(z) = \frac{z^{-1}[\sin(\phi'_h + h\omega_1 T_s) - \sin(\phi'_h)] + z^{-2}[\sin(\phi'_h - h\omega_1 T_s) - \sin(\phi'_h)]}{h\omega_1 [1 - 2z^{-1} \cos(h\omega_1 T_s) + z^{-2}]}$
First-order hold	$R_{1_h}^{dfoh}(z) = \cos(\phi'_h) \frac{(1-z^{-2})[1 - \cos(h\omega_1 T_s)]}{h^2 \omega_1^2 T_s [1 - 2z^{-1} \cos(h\omega_1 T_s) + z^{-2}]} + \sin(\phi'_h) \frac{(1+z^{-2})[\sin(h\omega_1 T_s - h\omega_1)] + 2z^{-1} [h\omega_1 \cos(h\omega_1 T_s) - \sin(h\omega_1 T_s)]}{h^2 \omega_1^2 T_s [1 - 2z^{-1} \cos(h\omega_1 T_s) + z^{-2}]}$
Tustin with prewarping	$R_{1_h}^{dtp}(z) = \frac{\frac{1}{2}(1-z^{-2}) \cos(\phi'_h) \sin(h\omega_1 T_s) - (1+2z^{-1} + z^{-2}) \sin(\phi'_h) \sin^2\left(\frac{h\omega_1 T_s}{2}\right)}{h\omega_1 [1 - 2z^{-1} \cos(h\omega_1 T_s) + z^{-2}]}$
Zero-pole matching	$R_{1_h}^{dzpm}(z) = K_d \frac{z^{-1} - z^{-2} e^{\tan(\phi'_h) h\omega_1 T_s}}{1 - 2z^{-1} \cos(h\omega_1 T_s) + z^{-2}}$
Impulse invariant	$R_{1_h}^{dimp}(z) = T_s \frac{\cos(\phi'_h) - z^{-1} \cos(\phi'_h - h\omega_1 T_s)}{1 - 2z^{-1} \cos(h\omega_1 T_s) + z^{-2}}$
Forward & backward	$R_{1_h}^{df&b}(z) = T_s \frac{z^{-1} [\cos(\phi'_h) - h\omega_1 T_s \sin(\phi'_h)] - z^{-2} \cos(\phi'_h)}{1 + z^{-1} (h^2 \omega_1^2 T_s^2 - 2) + z^{-2}}$
Backward & backward	$R_{1_h}^{db&b}(z) = T_s \frac{\cos(\phi'_h) - z^{-1} [\cos(\phi'_h) + h\omega_1 T_s \sin(\phi'_h)]}{1 + z^{-1} (h^2 \omega_1^2 T_s^2 - 2) + z^{-2}}$

TABLE 2.6  
 $R_{2_h}^d(s)$  DISCRETIZED BY GROUPS E AND D

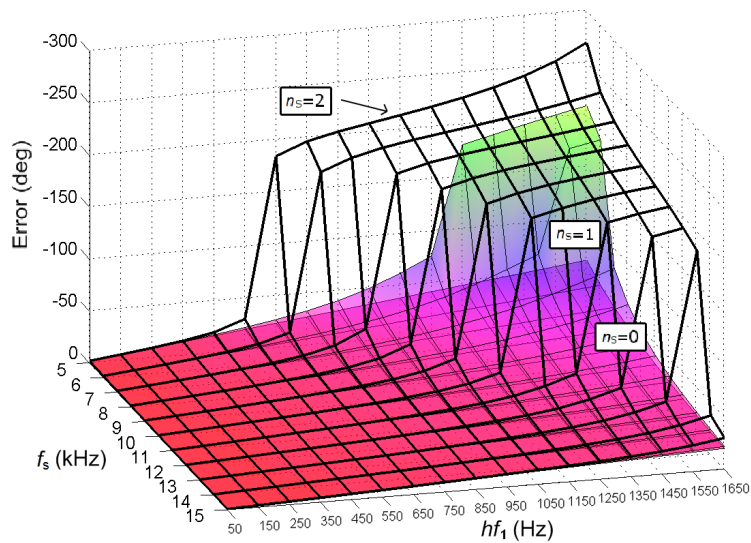
Zero-order hold	$R_{2_h}^{dzoh}(z) = \frac{(1-z^{-1}) \cos(\phi'_h) - (z^{-1} - z^{-2}) \cos(\phi'_h - h\omega_1 T_s)}{1 - 2z^{-1} \cos(h\omega_1 T_s) + z^{-2}}$
First-order hold	$R_{2_h}^{dfoh}(z) = \frac{[\sin(\phi'_h + h\omega_1 T_s) - \sin(\phi'_h)] - 2z^{-1} \sin(h\omega_1 T_s) \cos(\phi'_h) + z^{-2} [\sin(h\omega_1 T_s - \phi'_h) + \sin(\phi'_h)]}{h\omega_1 T_s [1 - 2z^{-1} \cos(h\omega_1 T_s) + z^{-2}]}$
Tustin with prewarping	$R_{2_h}^{dtp}(z) = \frac{\frac{1}{2}(-1+z^{-2}) \sin(\phi'_h) \sin(h\omega_1 T_s) + (1-2z^{-1} + z^{-2}) \cos(\phi'_h) \cos^2\left(\frac{h\omega_1 T_s}{2}\right)}{1 - 2z^{-1} \cos(h\omega_1 T_s) + z^{-2}}$
Zero-pole matching	$R_{2_h}^{dzpm}(z) = K_d \frac{1-z^{-1} [1 + e^{\tan(\phi'_h) h\omega_1 T_s}] + z^{-2} e^{\tan(\phi'_h) h\omega_1 T_s}}{1 - 2z^{-1} \cos(h\omega_1 T_s) + z^{-2}}$
Impulse invariant	$R_{2_h}^{dimp}(z) = h\omega_1 T_s \frac{-\sin(\phi'_h) + z^{-1} \sin(\phi'_h - h\omega_1 T_s)}{1 - 2z^{-1} \cos(h\omega_1 T_s) + z^{-2}}$
Forward & backward	$R_{2_h}^{df&b}(z) = \frac{(1-2z^{-1} + z^{-2}) \cos(\phi'_h) - (z^{-1} - z^{-2}) h\omega_1 T_s \sin(\phi'_h)}{1 + z^{-1} (h^2 \omega_1^2 T_s^2 - 2) + z^{-2}}$
Backward & backward	$R_{2_h}^{db&b}(z) = \frac{(1-2z^{-1} + z^{-2}) \cos(\phi'_h) - (1-z^{-1}) h\omega_1 T_s \sin(\phi'_h)}{1 + z^{-1} (h^2 \omega_1^2 T_s^2 - 2) + z^{-2}}$



(a)  $R_{1_h}^{d\text{zoh}}(z), R_{2_h}^{d\text{zoh}}(z)$ . The same error is obtained for  $n_s = 0, 1, 2$ .



(b)  $R_{1_h}^{d\text{foh}}(z), R_{1_h}^{d\text{lp}}(z), R_{1_h}^{d\text{imp}}(z), R_{2_h}^{d\text{foh}}(z), R_{2_h}^{d\text{lp}}(z), R_{2_h}^{d\text{imp}}(z)$ . The same error is obtained for  $n_s = 0, 1, 2$ .



(c)  $R_{1_h}^{d\text{zpm}}(z)$ .

Figure 2.9: Continued on next page.

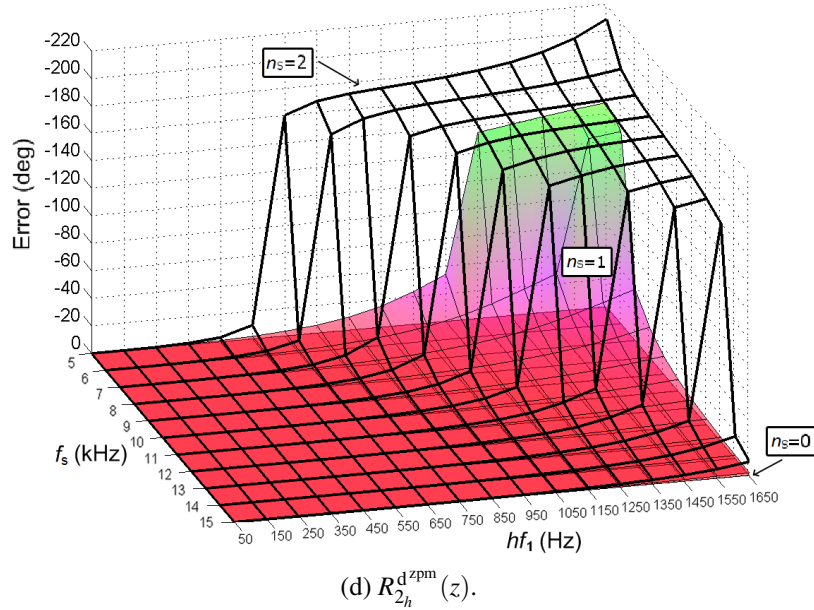


Figure 2.9: Study of the error in degrees  $\varepsilon_{\phi_h}$  between the expected and the actual phase within a vicinity of the resonant frequency, for  $R_{1_h}^{\text{d}}(s)$  and  $R_{2_h}^{\text{d}}(s)$  discretized with group E methods. This figure is continued from previous page.

On the other hand, as illustrated in Fig. 2.9b, three of the considered discretization methods provide an accurate delay compensation for both resonant terms: impulse invariant, Tustin with prewarping and FOH.

From Figs. 2.9c and 2.9d, it can be appreciated that the ZPM method is not recommendable for discretizing neither  $R_{1_h}^{\text{d}}(s)$  nor  $R_{2_h}^{\text{d}}(s)$ . Indeed, it provides the largest phase error. It is interesting to note that, on the contrary, ZPM is adequate for  $R_{2_h}(s)$  when delay compensation is not included (proved in section §2.3). This result is also confirmed by the surface  $n_s = 0$  shown in Fig. 2.9d.

Fig. 2.9 illustrates that, for E methods, the discrepancy is more significant as higher is  $h\omega_1$ . This is really important, since the effect of delay compensation should be taken into account for high resonant frequencies. Concerning group D implementations, they do not always lead to a positive slope  $\partial\varepsilon_{\phi_h}/\partial(h\omega_1)$ ; for certain intervals, as shown in Fig. 2.10, the opposite is true. In any case, the error is of great magnitude in both groups for most values of  $T_s$  and  $h\omega_1$ .

It can be observed in Figs. 2.10a and 2.10c that  $R_{1_h}^{\text{d b\&b}}$  and  $R_{2_h}^{\text{d b\&b}}$  introduce a phase lead greater than the continuous controller. This fact is preferable to the cases of  $R_{1_h}^{\text{d f\&b}}$  and  $R_{2_h}^{\text{d f\&b}}$ , in which stability is reduced by a phase lag, as depicted, respectively, in Figs. 2.10a and 2.10a. Nevertheless, the positive phase difference is actually so large that it could also lead to an unstable system. For these reasons, group D methods should be avoided if delay compensation is needed.

In summary, the only methods that provide an accurate discretization of delay compensation schemes are, for either resonant term, the impulse invariant, Tustin with prewarping or FOH transforms.

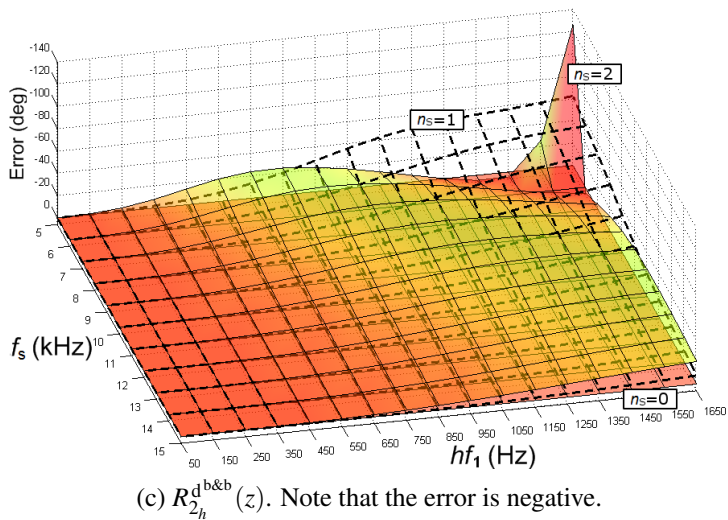
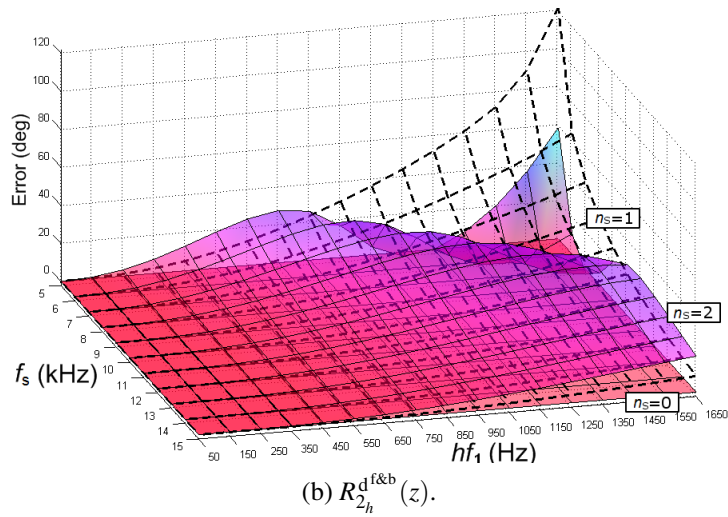
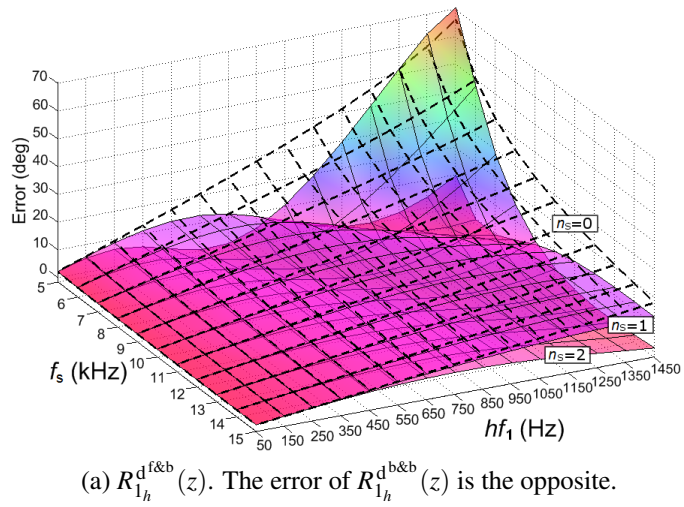


Figure 2.10: Study of the error in degrees  $\varepsilon_{\phi_h}$  between the expected and the actual phase within a vicinity of the resonant frequency, for  $R_{1h}^d(s)$  and  $R_{2h}^d(s)$  discretized with group D methods.

TABLE 2.7  
PERFORMANCE SUMMARY OF THE DISCRETE-TIME IMPLEMENTATIONS

Implementations	Infinite gain	Resonance deviation	Effect on zeros	Delay comp.	Trig. terms	References
$R_{1_h}^f(z), R_{1_h}^b(z)$ $R_{2_h}^f(z), R_{2_h}^b(z)$	No	-	-	-	No	[153, 276]
$R_{1_h}^t(z), G_{PR_h}^{t\&t}(z)$ $R_{2_h}^t(z), G_{VPI_h}^{t\&t}(z)$	Yes	Very Large	-	-	No	[210, 230, 246] [221–225]
$G_{PR_h}^{b\&b}(z)$	Yes	Large	Phase lag at $h\omega_1$	Inaccurate	No	[221]
$G_{PR_h}^{f\&b}(z)$	Yes	Large	Phase lead at $h\omega_1$	Inaccurate	No	[218–222, 298]
$G_{VPI_h}^{f\&b}(z), G_{VPI_h}^{b\&b}(z)$	Yes	Large	Accurate	Inaccurate	No	-
$R_{1_h}^{zoh}(z), R_{1_h}^{zpm}(z)$ $R_{2_h}^{zoh}(z)$	Yes	No	Phase lag at $h\omega_1$	Inaccurate	Yes	[277]
$R_{2_h}^{zpm}(z)$	Yes	No	Accurate	Inaccurate	Yes	-
$R_{1_h}^{imp}(z)$	Yes	No	Accurate at $h\omega_1$ and phase lead at $\uparrow \omega$	Accurate	Yes	[64, 205]
$R_{2_h}^{imp}(z)$	Yes	No	Accurate at $h\omega_1$ and phase lag at $\uparrow \omega$	Accurate	Yes	-
$R_{1_h}^{foh}(z), R_{1_h}^{tp}(z)$ $R_{2_h}^{foh}(z), R_{2_h}^{tp}(z)$	Yes	No	Accurate	Accurate	Yes	[46, 70, 91] [157, 226–228]

## 2.5 Summary of Optimum Discrete-Time Implementations

Table 2.7 summarizes the performance of the implementations in each of the aspects that have been carried out in the previous sections. The second and third columns correspond to section §2.3.1, the fourth column corresponds to section §2.3.2, and the fifth one corresponds to section §2.4. Table 2.7 also indicates which alternatives include explicit trigonometric functions in their difference equations, which lead to a higher computational burden if they are calculated on-line (frequency adaptation). Finally, the last column points out several previous works that employ certain implementations.

Different situations and requirements may arise when dealing with real applications. Table 2.8 shows the best tradeoff alternatives for discrete-time implementation depending on which are the specific requirements of a particular application.

It is known that one of the most important drawbacks of resonant regulators is their sensitivity to frequency variations of the signal to be controlled [24, 307]. Many of the existing proposals for frequency adaptation of resonant controllers are based on discretizing two separated integrators (defined as group D in section §2.2.2) [219–222]. Their main advantage is the fact that they do not require the on-line computation of explicit cosine functions. However, these schemes cause an error in the frequency at which the resonance occurs, as proved in section §2.3.1. Moreover, as concluded in section §2.4, group D implementations are not adequate

TABLE 2.8  
OPTIMUM DISCRETE-TIME IMPLEMENTATIONS

<b>No frequency adaptation</b>	
<b>No delay</b>	$G_{PR_h}^{imp,foh,tp}(z)$
<b>comp.</b>	$G_{VPI_h}(z) = K_{P_h} R_{2_h}^{foh,tp,zpm}(z) + K_{I_h} R_{1_h}^{imp,foh,tp}(z)$
<b>Delay</b>	$G_{PR_h}^{d,imp,foh,tp}(z)$
<b>comp.</b>	$G_{VPI_h}^d(z) = K_{P_h} R_{2_h}^{d,foh,tp}(z) + K_{I_h} R_{1_h}^{d,imp,foh,tp}(z)$
<b>Frequency adaptation</b>	
<b>No delay</b>	$G_{PR_h}^{f\&b}(z)$ $*G_{PR_h}^{imp,foh,tp}(z)$
<b>comp.</b>	$G_{VPI_h}^{f\&b}(z), G_{VPI_h}^{b\&b}(z)$ $*G_{VPI_h}(z) = K_{P_h} R_{2_h}^{foh,tp,zpm}(z) + K_{I_h} R_{1_h}^{imp,foh,tp}(z)$
<b>Delay</b>	$*G_{PR_h}^{d,imp,foh,tp}(z)$
<b>comp.</b>	$*G_{VPI_h}(z) = K_{P_h} R_{2_h}^{d,foh,tp}(z) + K_{I_h} R_{1_h}^{d,imp,foh,tp}(z)$

\* Requires the on-line computation of  $\cos(h\omega_1 T_s)$  terms as  $h\omega_1$  varies.

for delay compensation schemes. Therefore, they should only be employed when delay compensation is not required and frequency adaptation is needed in combination with a low value of the product  $h\omega_1 T_s$ . In these cases, their advantage in computational simplicity makes them an interesting solution, specially when low-cost digital devices are employed. From the whole study, the best alternatives among group D methods are  $G_{PR_h}^{f\&b}(z)$ ,  $G_{VPI_h}^{f\&b}(z)$  and  $G_{VPI_h}^{b\&b}(z)$ .

On the other hand, referring back to section §2.3.1, group E methods achieve an accurate resonant poles mapping. Furthermore, it is possible to provide frequency adaptation to group E expressions by calculating the coefficients as  $h\omega_1$  varies, as done in [308]. In that manner, the performance would be superior in terms of resonant poles displacement and stability, even when tracking high frequencies and employing low values of  $f_s$ . Nevertheless, it would require the on-line computation of a cosine function for each resonance in every sample, so the computational burden may increase significantly.

Among group E discretizations, the most appropriate from the point of view of stability have been demonstrated in section §2.3.2 to be FOH, Tustin with prewarping and ZPM in the case of  $R_{2_h}(s)$ ; on the other hand, the impulse invariant method, Tustin with prewarping and FOH are the most suitable ones for  $R_{1_h}(s)$ . However, ZPM is not adequate for implementing delay compensation for  $R_{2_h}(s)$ , as proved in section §2.4.

## 2.6 Experimental Setup Description

The experimental setup consists of a single-phase APF prototype; the choice of implementing the resonant controllers for an APF is mainly based on the fact that it is an application very suitable for testing their performance when tracking different frequencies. These results can be extended to other single-phase and three-phase applications where a perfect tracking/rejection of references/disturbances is sought through resonant controllers. The goal of the laboratory experimental setup is to assess the following main theoretical approaches.

TABLE 2.9  
POWER CIRCUIT VALUES

Parameter	Value
$v_{dc}^*$	220 V
$v_{S_{rms}}$	110 V
$C$	3.3 mF
$L_F$	5 mH
$R_F$	0.5 $\Omega$
$L_S$	50 $\mu$ H
$f_{sw} = f_s$	10 kHz

- 1) A comparison among discretization methods, testing the ability of different strategies to provide a good tracking/rejection of harmonic references/disturbances by means of an accurate mapping of the resonant poles (section §2.7.1).
- 2) Effectiveness of the discrete-time delay compensation provided by FOH, Tustin with pre-warping and impulse invariant discretizations. It is proved by checking the performance of resonant controllers tuned at high values of  $h\omega_1$  (section §2.7.2).
- 3) Regarding on-line frequency adaptation, assessment of the difference in terms of computational burden between the most accurate implementations and those that do not require on-line calculation of explicit trigonometric functions (section §2.7.3).

The tests carried out in order to prove 1) and 2) are performed without on-line frequency adaptation, since the aspect under study is the accuracy of the implementations when the input frequency is fixed and well-known, so the resonant controllers are implemented with constant coefficients (calculated off-line). Actually,  $h\omega_1$  should have a fixed value during these tests, so the different implementations are compared under the same conditions. Frequency adaptive resonant controllers are implemented for the last experiment, which provides a comparison in terms of computational effort.

It is not intended to provide a comparison between  $G_{PR_h}(s)$  and  $G_{VPI_h}(s)$  controllers. That kind of study has already been presented in other works [51, 57, 58, 120].

Fig. 2.11 shows the tested single-phase APF prototype. The APF is an insulated-gate bipolar transistor (IGBT) based voltage source converter (VSC) connected to the point of common coupling (PCC) through the interfacing inductor  $L_F$ . The equivalent series resistance  $R_F$  of this inductor has been measured and taken into account in the modeling of the plant. A programmable load (Hoche1 & Hackl ZSAC426) is connected in parallel to the APF. This load allows to specify the demanded current harmonic content up to the 15th harmonic. A programmable ac source (Chroma 61501) has been employed to supply the  $v_{ac}$  voltage. Note that  $v_{PCC}$  corresponds to the perturbation  $v_{ac}$  in section §1.2.2; the APF current  $i_F$  and its reference  $i_F^*$  correspond to the  $i$  and  $i^*$  variables in that section. Table 2.9 shows the values of the power circuit components. The variable  $f_{sw}$  is the IGBTs switching frequency. The source output inductance  $L_S$  is negligible with respect to  $L_F$ , so that the source voltage  $v_S$  verifies  $v_S \approx v_{PCC} = v_{ac}$ .

The control has been implemented in a prototyping platform (dSpace DS1104), which includes a PowerPC (PPC) MPC8240 and a Texas Instruments TMS320F240 DSP. The PPC is

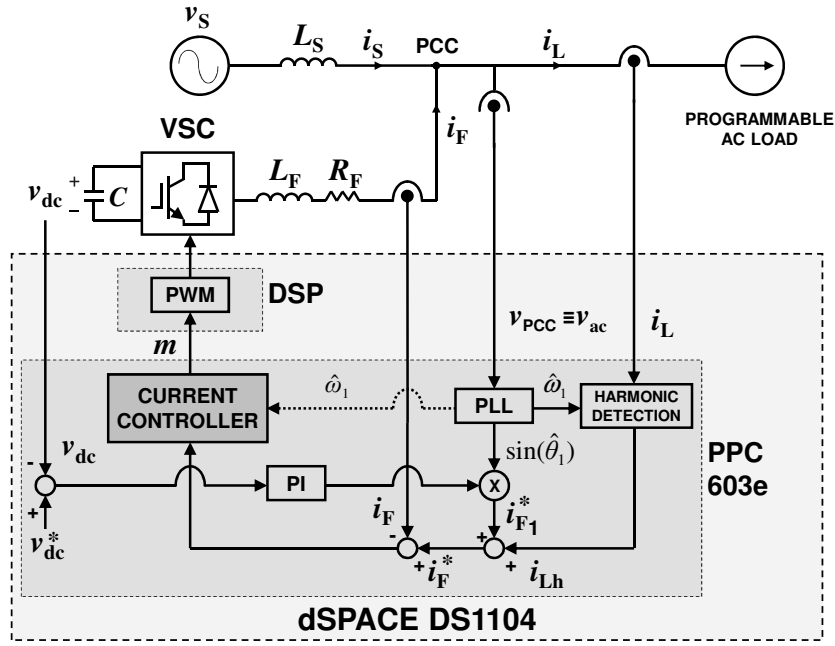


Figure 2.11: APF lab prototype circuit and controller.

a 64-bit floating-point processor with a CPU clock running at 250 MHz. The algorithms are designed using Matlab/Simulink and the real-time interface (RTI) toolbox. The PPC executes all tasks but the pulsewidth modulation (PWM) signals generation, which is done by the digital signal processor (DSP).

The discrete-time solver has been set at  $f_s = 10\text{kHz}$ . The goals of the digital controller are to compensate for the selected load harmonic currents  $i_{Lh}$  and to keep constant the dc-link voltage  $v_{dc}$ . The proposed controller works as follows:

- The harmonic currents to compensate  $i_{Lh}$  are extracted from the instantaneous load current  $i_L$  by means of digital signal processing. The method proposed in [309] to identify the fundamental current  $i_{L1}$  has been employed, so  $i_{Lh} = i_L - i_{L1}$ .
- The reference fundamental current  $i_{F1}^*$ , calculated to maintain  $v_{dc}$ , is obtained by means of a proportional-integral (PI) controller and the in-phase signal from the phase-locked loop (PLL) ( $\hat{\theta}_1$ ) [310]. Note that the subscript  $F$  makes reference to the current supplied by the APF.
- The total reference of current  $i_F^*$  for the APF is calculated as  $i_{Lh} + i_{F1}^*$ .
- The current regulator  $G_C(z)$  assures that  $\Delta i_F = i_F^* - i_F$  is zero in steady-state.
- The PLL estimates the fundamental frequency ( $\hat{\omega}_1$ ) in order to adapt the harmonic identification algorithm and, in the tests of computational burden, also the resonant controllers.

The resonant controllers are implemented in the stationary frame, which is a common choice due to the perfect tracking of both sequences and the lack of coordinates transformations [63–65, 119, 210, 280]. It is also an interesting alternative to implement them in synchronous reference frame (SRF), as exposed in section §1.2.7.4. However, the effects of discretization are analogous in both cases, so only one of these approaches is needed.

Further information about testing facilities can be found in chapter §D.

### 2.6.1 Tuning of $G_{PR_h}$ Controllers

From section §1.2.7.1, when the current controller  $G_C(s)$  is based on  $G_{PR_h}$ , it can be expressed as

$$G_C(s) = \sum_{h=1,3,\dots}^{n_h} G_{PR_h}(s) = K_{PT} + \sum_{h=1,3,\dots}^{n_h} K_{I_h} R_{I_h}(s) \quad (2.4)$$

with  $n_h$  being the highest harmonic order to be compensated. Two values of  $n_h$  will be employed in the experiments: 15 and 61. The computation and modulation delay is also taken into account in the plant model, that is,  $G_{PL}(z)$  takes the form of (1.12).

The parameters of  $G_{PR_h}$  are tuned by means of the open-loop frequency response, following the indications explained in section §1.2.7.6.

A value of  $K_{PT} = 32$  has been selected so that a bandwidth of about 1 kHz is achieved. Consequently, it is possible to employ resonant controllers without delay compensation for  $n_h = 15$ , which is necessary for some of the experiments. Fig. 2.12 depicts the open-loop frequency response obtained after the tuning process, for  $n_h = 15$ . The phase margin  $PM_P$  results in  $34^\circ$ , assuring stability.

The parameter  $K_{I_h}$  should be tuned to obtain an adequate compromise between selective filtering and dynamic response (see section §1.2.7.6). An identical integral gain has been selected for each harmonic  $h$  in order to achieve the same bandwidth for all of them. In this manner, a similar tradeoff between selectivity and transient response is assured for each resonant frequency. Actually, it is a common practice to tune PR controllers with identical gains  $K_{I_h}$  for all harmonics [64, 228, 229]. Furthermore, as the selectivity becomes independent of the harmonic order, it will be possible to assess in the experiments the dependence of the resonance deviation on  $h$ , which is one of the main objectives of the experiments. Taking into account all these aspects, a value of  $K_{I_h} = 2000$  has been selected. It can be mentioned that, from (1.28), this is equivalent to an integral gain of 1000 in a PI controller in SRF.

### 2.6.2 Tuning of $G_{VPI_h}$ Controllers

From section §1.2.7.2, the total current controller is

$$G_C(s) = \sum_{h=1,3,\dots}^{n_h} G_{VPI_h}(s). \quad (2.5)$$

The gains of  $G_{VPI_h}$  have been tuned according to the indications exposed in [56, 57], which were also reviewed in section §1.2.7.6.

- In order to cancel the cross-coupling caused by the L filter,  $K_{I_h}$  is selected as  $K_{P_h} R_F / L_F$ .
- There is a direct relation between  $K_{P_h}$  and the width of the peaks, determining the selectivity and the transient time. This parameter should be set in order to provide a given bandwidth centered at the resonant frequencies.  $K_{P_h} = 0.5$  and  $K_{I_h} = 50$  have been chosen to achieve a closed-loop bandwidth of 16 Hz at each resonant frequency  $h\omega_1$ , so an adequate tradeoff between selectivity and transient response is achieved.

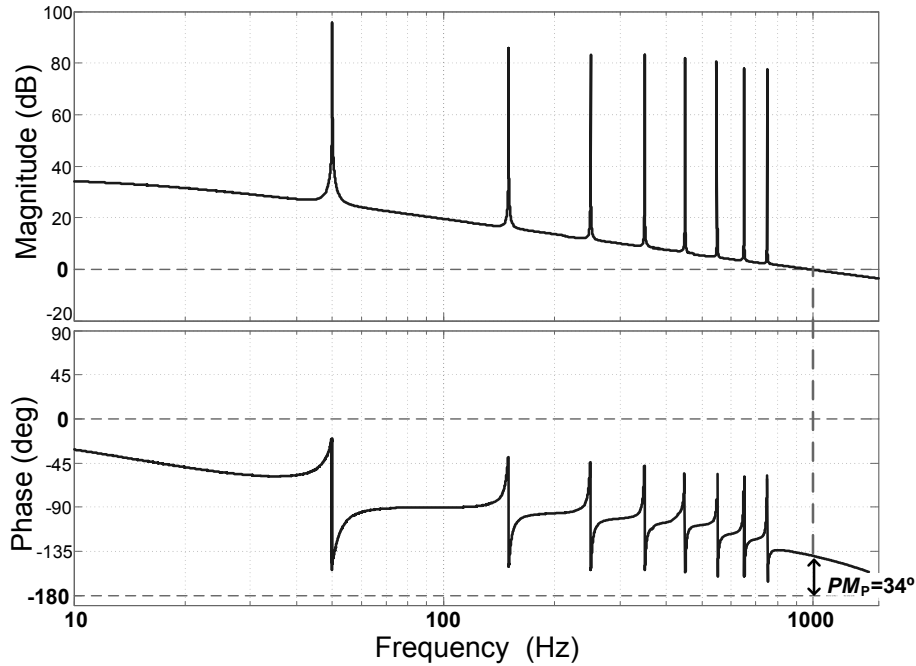


Figure 2.12: Open-loop Bode diagram of  $G_C(z) G_{PL}(z)$ , for PR controllers with  $n_h = 15$ .  $PM_P$  denotes the phase margin, which is set by  $K_{P_T}$ .

- So as to obtain the same bandwidth for all controllers, identical gains  $K_{P_h}$  and  $K_{I_h}$  are selected for each harmonic  $h$ , as proposed in [56, 57]. Moreover, it is necessary to employ the same gains for each resonant frequency in order to appreciate how the resonant poles deviation increases with the harmonic order.

## 2.7 Experimental Results

### 2.7.1 Comparison of Steady-State Error Provided by Discrete-Time Implementations

The load current  $i_L$  has been programmed with uniform harmonic spectrum for odd values between the 3rd and 15th order, as depicted in Fig. 2.13. It should be noted that total harmonic distortion (THD)-F, which means referred to fundamental, corresponds with the standard definition of THD. In this manner, the uniform spectrum of  $i_L$  leads to a THD of 31.9%. In most real applications, low harmonics exhibit higher amplitude, but  $i_L$  has been chosen in that manner to make possible the comparison of the performance as the harmonic order rises. The number of harmonics could be increased by performing compensation of the computational delay, but it is not done in this test due to the following reasons:

- Results obtained with  $n_h = 15$  are enough to prove the effect of discretization on the resonant frequency. The error expected for low order harmonics is already considerable (exposed in section §2.3.1), so testing resonant controllers tuned for higher harmonics would not contribute any additional information.
- If higher harmonics were to be compensated, delay compensation should be implemented

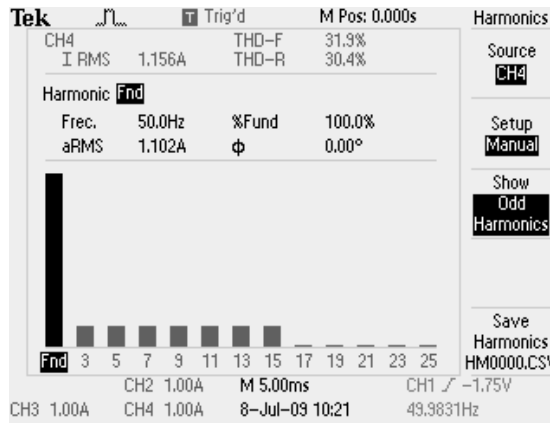


Figure 2.13: Spectrum of programmed load current  $i_L$  to test the effect of resonant poles displacement [both for  $G_{PR_h}(z)$  and  $G_{VPI_h}(z)$ ]. THD= 31.9%.

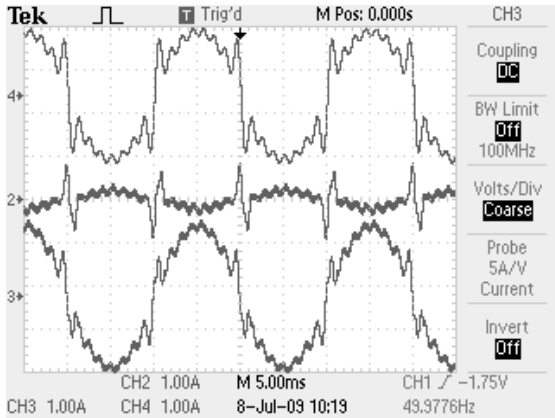
in order to assure stability of the resonant terms. However, as exposed in section §2.4, that would change the form of the original continuous transfer function to (1.31); thus, additional effects of the discretization would also affect the performance apart from the resonant poles displacement.

### 2.7.1.1 Steady-State Error of $G_{PR_h}(s)$ Discretizations

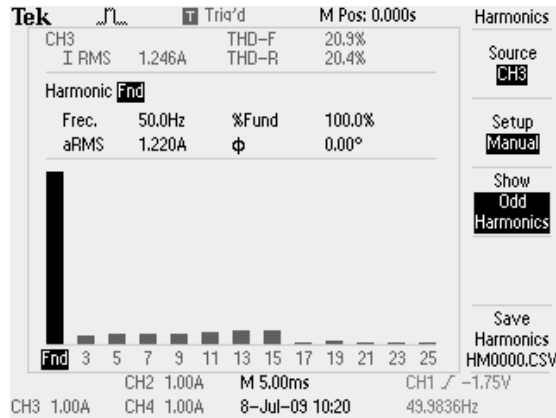
Fig. 2.14 illustrates steady-state currents and corresponding spectra of  $i_S$  for different discrete-time implementations of the PR current controller  $G_{PR_h}(s)$ . As expected from the theoretical analysis provided in section §2.3.1, the steady-state error caused by the pole displacement of the implementations of groups C and D is considerable and increases with the harmonic order, as shown in Fig. 2.14d and Fig. 2.14f. Actually, for high-order harmonics, the  $i_S$  spectrum achieved by  $R_{1_h}^{f\&b}(z)$  and  $R_{1_h}^t(z)$  schemes is more similar to the one provided by a simple proportional controller (see Fig. 2.14b), than to the harmonic content achieved by  $R_{1_h}^{imp}(z)$  (see Fig. 2.14h). This fact reveals that the high-order resonant peaks of the former are so displaced that they almost have no influence on the performance. On the other hand,  $R_{1_h}^{imp}(z)$  provides almost complete rejection of load current harmonics, which proves the accuracy of its resonant peaks locations. The THD values also reflect the large performance difference: its value for  $R_{1_h}^{f\&b}(z)$  (THD= 11.1%) and  $R_{1_h}^t(z)$  (THD= 18.5%) doubles and triples, respectively, that of  $R_{1_h}^{imp}(z)$  (THD= 5.66%). Therefore, the superiority of group E methods for  $R_{1_h}(z)$  implementation in terms of accuracy is proved.

### 2.7.1.2 Steady-State Error of $G_{VPI_h}(s)$ Discretizations

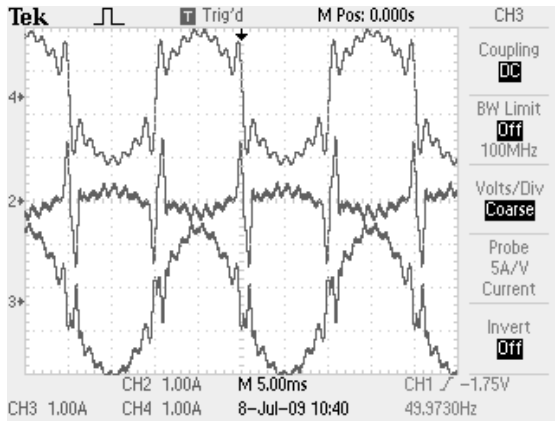
Fig. 2.15 compares the steady-state currents and  $i_S$  spectrum obtained by the different stable groups of discretization methods when applied to  $G_{VPI_h}(s)$ : C, D and E. As shown in Fig. 2.15e, group E achieves a high rejection of all programmed harmonics between  $h = 3$  and  $h = 15$ , due to an accurate mapping of the resonant poles. On the contrary, the other groups fail to track with unity gain the harmonic references. They produce a difference in the resonant frequency that increases with the harmonic order, which causes steady-state error. This fact can be also



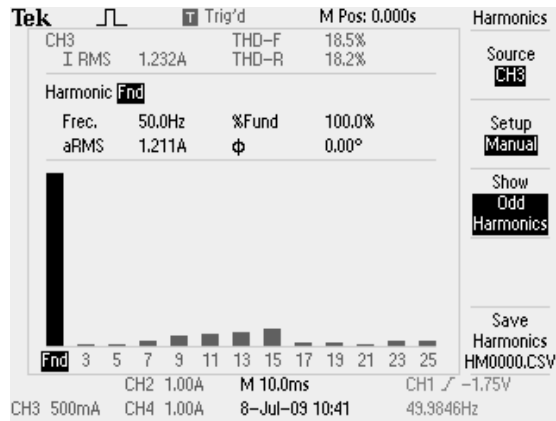
(a) Steady-state currents for only proportional current controller.



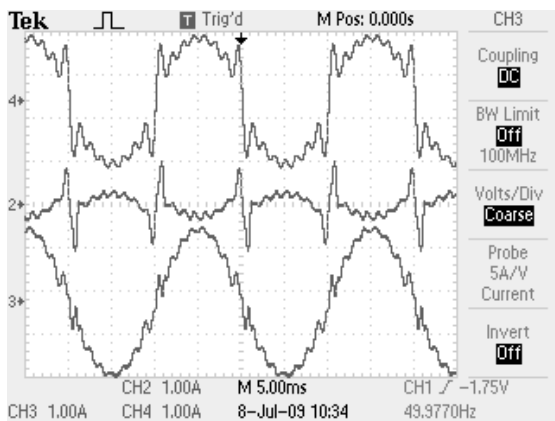
(b) Spectrum of  $i_S$  shown in Fig. 2.14a. THD= 20.9%.



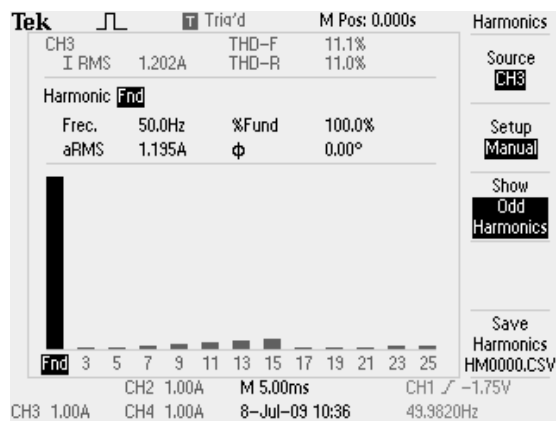
(c) Steady-state currents for  $G_{PR_h}^t(z)$  implementation.



(d) Spectrum of  $i_S$  shown in Fig. 2.14c. THD= 18.5%.

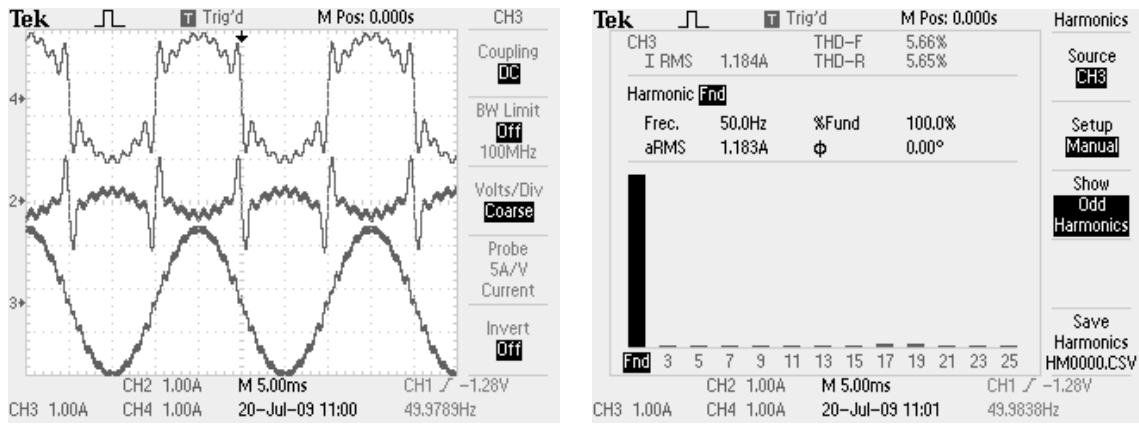


(e) Steady-state currents for  $G_{PR_h}^{f\&b}(z)$  implementation.



(f) Spectrum of  $i_S$  shown in Fig. 2.14e. THD= 11.1%.

Figure 2.14: Continued on next page.



(g) Steady-state currents for  $G_{PR_h}^{\text{imp}}(z)$  implementation.

(h) Spectrum of  $i_s$  shown in Fig. 2.14g. THD= 5.66%.

Figure 2.14: Steady-state currents and spectra of  $i_s$  for different discrete implementations of  $G_{PR_h}(s)$ , with  $n_h = 15$  and  $f_1 = 50\text{Hz}$ . Ch2 is  $i_F$ , Ch3 is  $i_s$  and Ch4 is  $i_L$ . This figure is continued from previous page.

appreciated in the THD values: it rises from 4.89% to 12.7% and 18.2% (groups E, D and C, respectively). In summary, E techniques have been proved to provide a superior performance for  $G_{VPI_h}(s)$  controllers in terms of resonant poles accuracy.

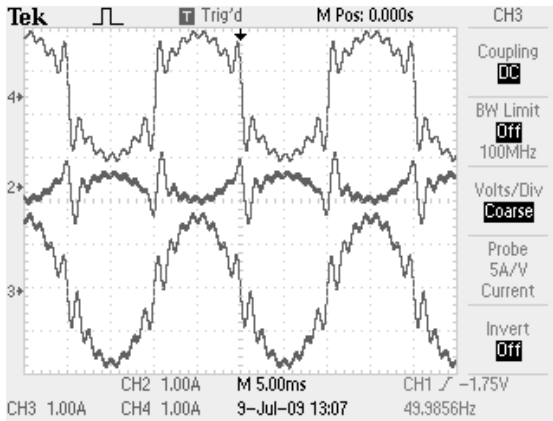
## 2.7.2 Test of Discrete-Time Delay Compensation

The effectiveness of the digital implementations of the delay compensation will be tested by checking their stability when compensating high order harmonics. For this reason,  $i_L$  has been programmed as a square wave with rise time and fall time of  $39\ \mu\text{s}$ . It contains a very demanding spectrum of odd harmonics up to high frequencies. Its harmonic content can be observed in Fig. 2.16. In these experiments, the fast Fourier transform (FFT) tool of the oscilloscope math mode has been employed instead of the application used in the previous tests. This is because of the fact that the latter is only able to show harmonics up to  $h = 49$ , whereas the former is only limited by the bandwidth of the oscilloscope.

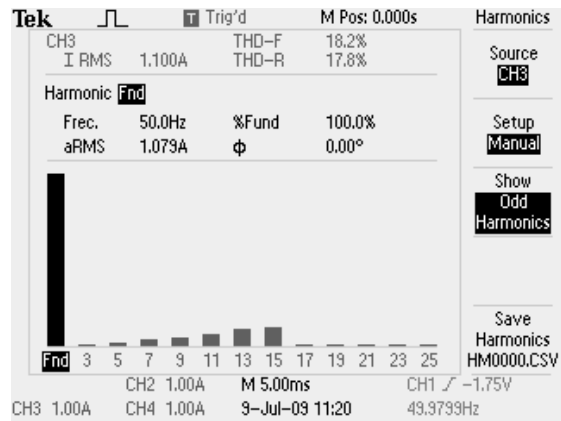
The number of samples compensated has been set at  $n_s = 2$ , since it is considered to be the optimum value [58, 64, 120, 260].

Resonant controllers are tuned at each odd harmonic between  $h = 1$  and  $h = n_h = 61$ . Higher frequencies could be tracked, but the precision would become really low, as the number of samples in a period gets too small. In any case,  $n_h = 61$  is considered to be enough for proving robustness of current controllers [57].

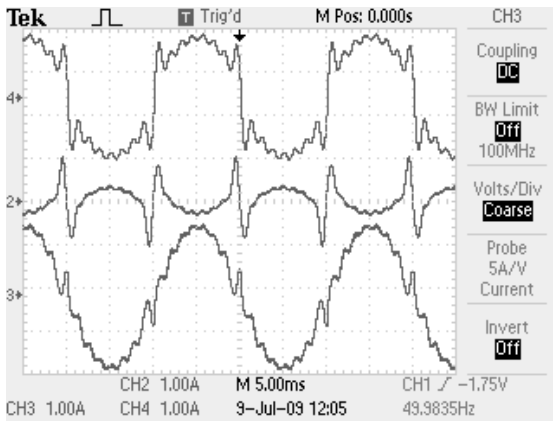
It should be noted that the aim of the experiment is not a proposal for an industrial prototype, but to provide a study about the accuracy of the resonant poles locations and the delay compensation achieved by several discretization methods. The main reason to implement resonant controllers tuned at such high frequencies is to serve as a useful test for applications in which tracking of high frequencies with respect to sampling frequency may be required, such as in aeronautic APFs [70], high-speed ac drives [311, 312] or high-power converters (low  $f_{sw}$



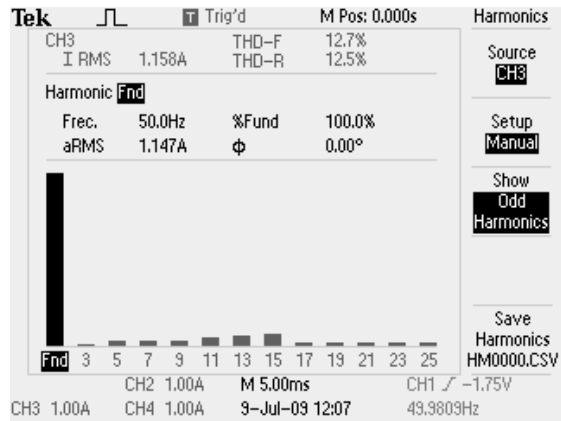
(a) Steady-state currents for  $G_{VPI_h}^{t-t}(z)$ .



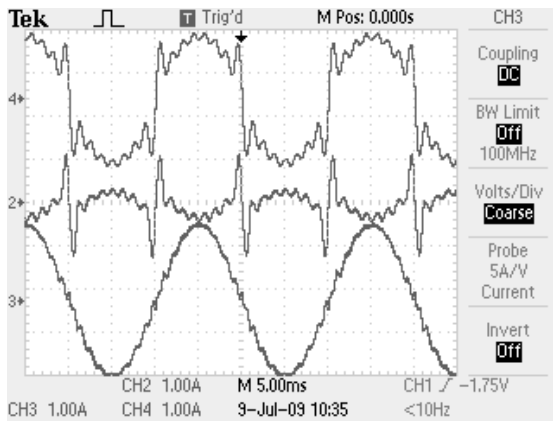
(b) Spectrum of  $i_S$  shown in Fig. 2.15a. THD= 18.2%.



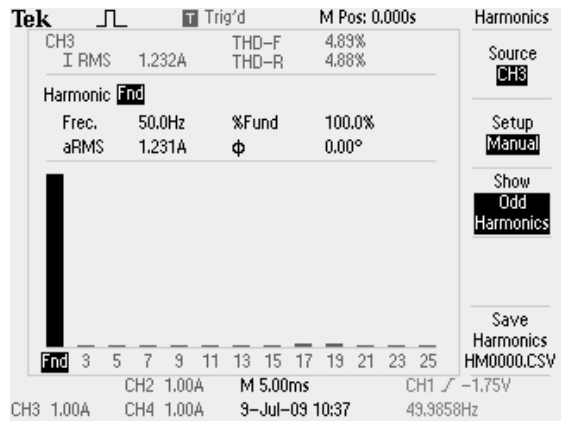
(c) Steady-state currents for  $G_{VPI_h}^{f\&b}(z)$  implementation.



(d) Spectrum of  $i_S$  shown in Fig. 2.14c. THD= 12.7%.



(e) Steady-state currents for  $G_{VPI_h}^{imp-tp}(z)$  implementation.



(f) Spectrum of  $i_S$  shown in Fig. 2.14e. THD= 4.89%.

Figure 2.15: Steady-state currents and spectra of  $i_S$  for different discrete implementations of  $G_{VPI_h}(s)$ , with  $n_h = 15$  and  $f_1 = 50$  Hz. Ch2 is  $i_F$ , Ch3 is  $i_S$  and Ch4 is  $i_L$ .

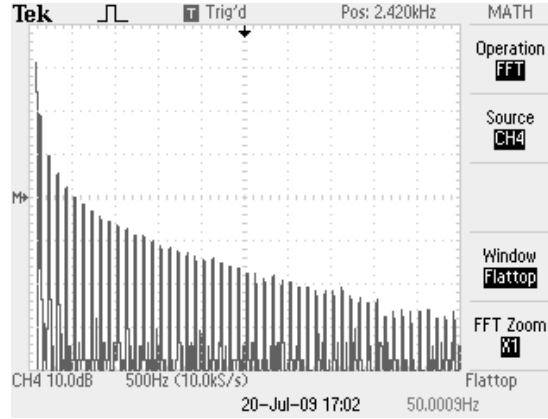


Figure 2.16: Spectrum of programmed load current  $i_L$  for the tests of discrete-time delay compensation.

in order to reduce losses) [313–317]. Obviously, so many resonant controllers are not required in these cases, but the results provided confirm that there would be no problems of accuracy when few resonant controllers with relatively high ratio  $hf_1/f_s$  are implemented.

### 2.7.2.1 Delay Compensation in PR controllers

If a delay compensation method is not included,  $G_{PR_h}(s)$  controllers are inherently unstable starting from the 19th harmonic (at  $f_s = 10\text{kHz}$ ) [57, 120]. Fig. 2.17a shows the steady-state currents obtained by  $R_{1_h}^{\text{dimp}}(z)$  implementation, proving its stability. Therefore, it can be stated that the discrete-time delay compensation fulfills its mission of providing stability to the resonant controllers. The same results have been obtained by  $R_{1_h}^{\text{dfoh}}(z)$  and  $R_{1_h}^{\text{dtp}}(z)$ .

Moreover, from the spectrum of  $i_S$  shown in Fig. 2.17b, it can be also concluded that the mapping of the resonant poles of group E is still accurate for such high values of  $h\omega_1$ . Indeed, a similar amplitude is achieved for high and low values of  $k$ . It should be remarked that the harmonic components are not entirely eliminated mainly due to the error of the current sensors.

It should be also noted that the discretization of the controllers including the computational delay does not affect the denominator of each group, so the resonant poles will be the same for each group indistinctly if the delay compensation is included or not. Because of this reason, these experimental results can be also considered as an extension of the results of section §2.7.1, in the sense of proving the correct mapping of the poles for harmonics higher than  $h = 15$ .

The average execution time of this experiment has been  $24.6\ \mu\text{s}$  (whole control). The PR current control, which includes 31 resonant controllers with fixed coefficients, employs  $15.2\ \mu\text{s}$ .

### 2.7.2.2 Delay Compensation in VPI controllers

The VPI controller is not able to compensate harmonics higher than approximately  $h = 37$  (with  $f_s = 10\text{kHz}$ ) unless delay compensation is implemented [57]. As can be observed in Fig. 2.17c, the proposed implementation of digital delay compensation for  $G_{VPI_h}(z)$  is capable of providing stability even to really high harmonic orders. Therefore, its suitability has been satisfactorily proved. The results shown in these figures have been obtained with  $R_{1_h}^{\text{dimp}}(z)$  and  $R_{2_h}^{\text{dtp}}(z)$ , but identical results have been also achieved with  $R_{1_h}^{\text{dfoh}}(z)$ ,  $R_{1_h}^{\text{dtp}}(z)$ ,  $R_{2_h}^{\text{dfoh}}(z)$  and  $R_{2_h}^{\text{dtp}}(z)$ .

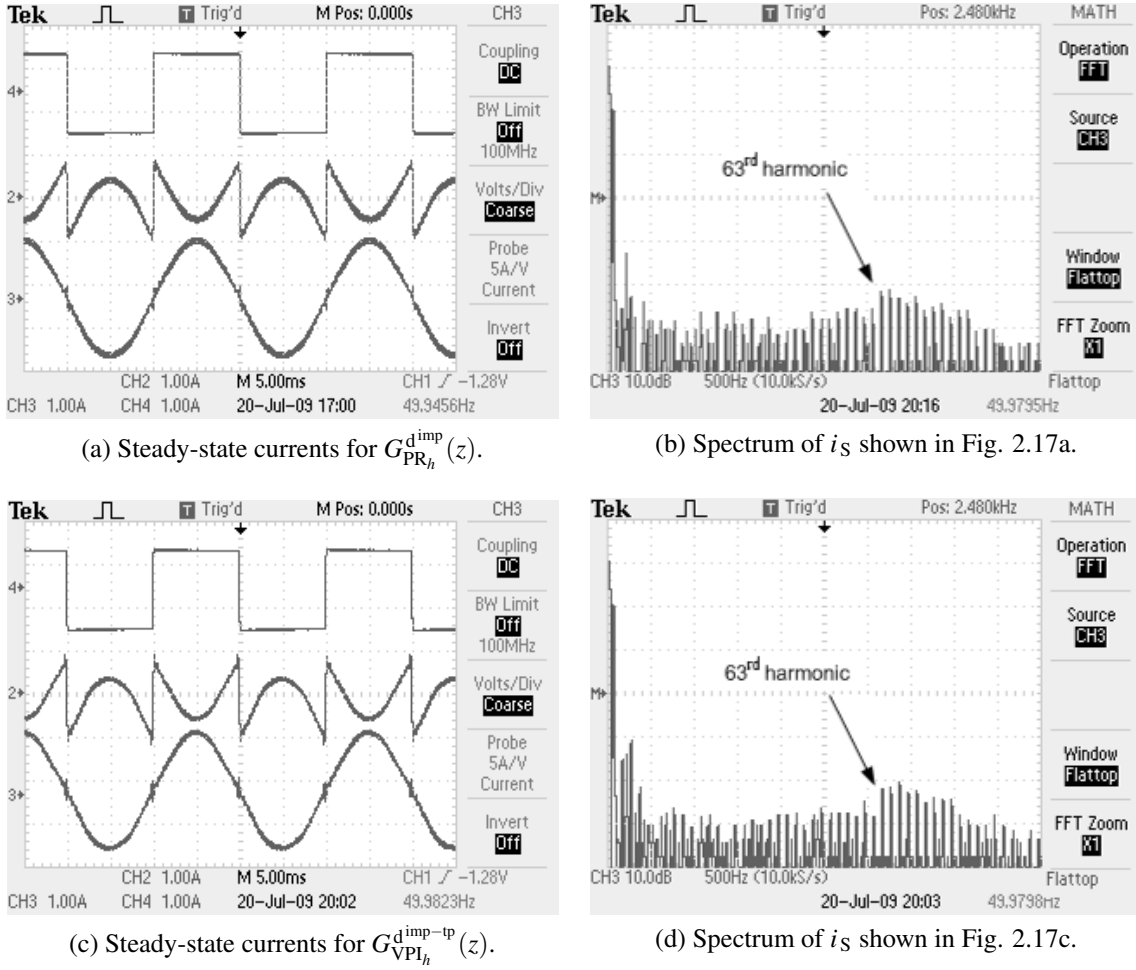


Figure 2.17: Steady-state currents and spectra of  $i_s$  when implementing digital compensation of the computational delay, with  $n_s = 2$ ,  $n_h = 61$  and  $f_1 = 50$  Hz. Ch2 is  $i_F$ , Ch3 is  $i_s$  and Ch4 is  $i_L$ .

Fig. 2.17d also demonstrates the accuracy of the resonant poles locations provided by group E, in the case of  $G_{VPI_h}^{dimp-ip}(z)$ .

The average execution time of this experiment has been  $25.9 \mu\text{s}$  (whole control). The PR current control employs  $16.5 \mu\text{s}$ . It should be noted that these execution times are quite reduced due to the powerful microprocessor employed (250 MHz clock rate) and the fact that constant coefficients (calculated off-line) were employed in the resonant controllers. The effect of on-line calculation of coefficients involving trigonometric functions is assessed in the next section.

### 2.7.3 Comparison of Computational Burden

In the previous experiments, the discretization methods that provide the best accuracy have been established. However, these implementations require on-line computation of trigonometric functions, as opposed to the schemes based on two integrators. In this manner, it can be said that there exists a tradeoff between accuracy and resource consumption, when frequency adaptation

TABLE 2.10  
IMPLEMENTATION CODE FOR THE TESTS OF COMPUTATIONAL BURDEN

PR controllers		
$R_{1_h}^{f\&b}$	$y[0]=x[1]*Ts+y[0];$	58
	$x[0]=w[0]*w[0]*y[0]*Ts+x[0];$	59
	$x[1]=u[0]-x[0];$	60
$R_{1_h}^{imp}$	<b><math>b1=\cos(w[0]*Ts);</math></b>	<b>68</b>
	$y[0]=Ts*u[0]-b1*x[0]+2*b1*x[2]-x[1];$	69
	$x[0]=Ts*u[0];$	70
	$x[1]=x[2];$	71
	$x[2]=y[0];$	72
VPI controllers		
$G_{VPI_h}^{f\&b}$	$x[0]=x[2]*Ts+x[0];$	61
	$x[1]=w[0]*w[0]*x[0]*Ts+x[1];$	62
	$x[2]=u[0]-x[1];$	63
	$y[0]=Kp*x[2]+Ki*x[0];$	64
$G_{VPI_h}^{imp-tp}$	<b><math>b1=\cos(w[0]*Ts);</math></b>	<b>72</b>
	$b2=0.5*Kp*(b1+1);$	73
	$y[0]=u[0]*(Ki*Ts+b2)-x[1]*(Ki*Ts*b1+2*b2)+x[0]*b2+2*x[3]*b1-x[2];$	74
	$x[0]=x[1];$	75
	$x[1]=u[0];$	76
	$x[2]=x[3];$	77
	$x[3]=y[0];$	78

is required. Therefore, it is interesting to assess the difference in execution time between groups D and E implementations.

One implementation of group D and one of group E have been chosen, both for the PR and the VPI controllers, to perform the comparison of execution time:  $G_{PR_h}^{f\&b}$ ,  $G_{PR_h}^{imp}$ ,  $G_{VPI_h}^{f\&b}$  and  $G_{VPI_h}^{imp-tp}$ . Results with other implementations of the same groups would be very similar, due to the fact that the most critical operation is the cosine calculation, which is necessary in all methods of group E and none of group D. The most important instructions of the code of the tested controllers (implemented with S-Functions in C language) are shown in Table 2.10.

Seven resonant controllers of each type are implemented ( $n_h = 15$ ), and the load current is programmed with a uniform spectrum up to the 15th harmonic, as done in the experiments of section §2.7.1. Fig. 2.18 depicts the currents obtained by the frequency adaptive implementations of Table 2.10, with  $f_1 = 52$  Hz. Fig. 2.18 proves the effectiveness of Table 2.10 code to implement the original transfer functions even in presence of frequency deviations.

Table 2.11 shows the average execution times of Table 2.10 controllers running in steady-state. These results corroborate the observations posed in section §2.5 concerning the simplicity of the implementations based on two integrators. From Table 2.11, the schemes of group D permit to reduce the execution time by a factor of approximately four. This result is explained by the fact that the RTI implements, by default, sine/cosine terms by means of high order

TABLE 2.11  
EXECUTION TIME OF THE CONTROLLERS IN THE TESTS OF STEADY-STATE ERROR

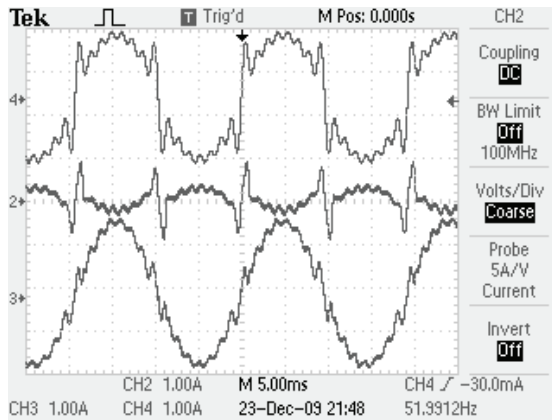
Controller ( $n_h = 15$ )	Current control execution time	Whole control execution time
$G_{PR_h}^{f\&b}$	$2.5 \mu s$	$11.9 \mu s$
$G_{PR_h}^{imp}$	$8.3 \mu s$	$17.7 \mu s$
$G_{VPI_h}^{f\&b}$	$2.7 \mu s$	$12.1 \mu s$
$G_{VPI_h}^{imp-tp}$	$8.6 \mu s$	$18.0 \mu s$

(15th) Taylor series, which demand a lot of PPC clock cycles (low-level instructions); whereas, methods based on two discrete integrators approximate the cosine function as a Taylor series of second-order (as shown in Table 2.3) with much fewer low level instructions. Consequently, the best tradeoff depends on available resources and required accuracy.

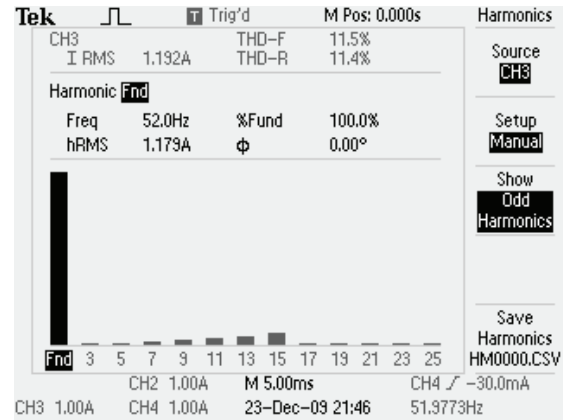
## 2.8 Conclusions

An exhaustive analysis of the importance of the discrete-time implementations of resonant controllers is contributed in this chapter. Some important outcomes should be taken into account when implementing digital resonant controllers.

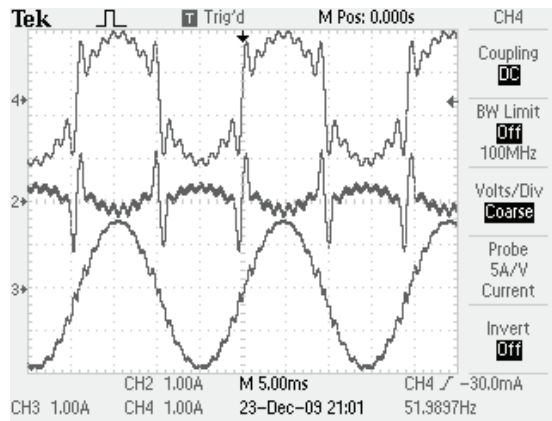
- Forward Euler [276] and backward Euler methods are not suitable for discretizing resonant controllers, since they map the poles out of the unit circumference. On the other hand, the rest of the implementations are able to achieve infinite gain in open-loop.
- The discrete-time implementations based on the Tustin transformation [210, 221, 223, 230] and the ones based on two integrators [58, 63, 120, 203, 219–222, 228, 282, 298] produce a significant steady-state error due to resonant poles displacement. This error increases with the sampling period and the harmonic order. Therefore, they are not recommended for applications in which high frequencies should be tracked. However, this deviation can be negligible when low frequencies (low  $h\omega_1 T_s$ ), such as fundamental components and low order harmonics, are tracked. Furthermore, the schemes based on two integrators, which approximate a cosine function by a second-order Taylor series, permit to reduce the computational burden with respect to more accurate implementations. Consequently, their simplicity may be advantageous in cases in which their steady-state error is acceptable and frequency adaptation is required.
- Implementations obtained by ZOH [277], FOH [70, 157], impulse invariant [64, 205], Tustin with prewarping [46, 91, 226, 228] and ZPM provide an accurate location of the resonant peaks even for high frequencies and reduced sampling rates. Consequently, they are more suitable to achieve zero steady-state error. When frequency adaptation is implemented, the on-line calculation of trigonometric functions is required, which may be very resource consuming.



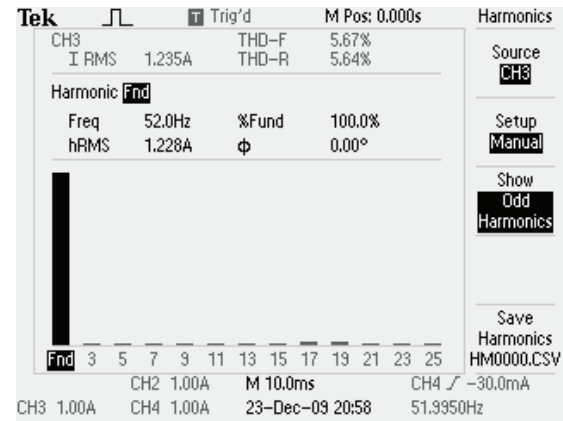
(a) Steady-state currents for  $G_{PR_h}^{f\&b}(z)$  implementation.



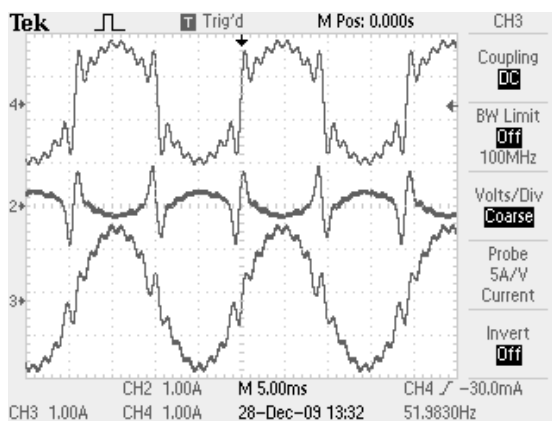
(b) Spectrum of  $i_s$  shown in Fig. 2.18a. THD= 11.5%.



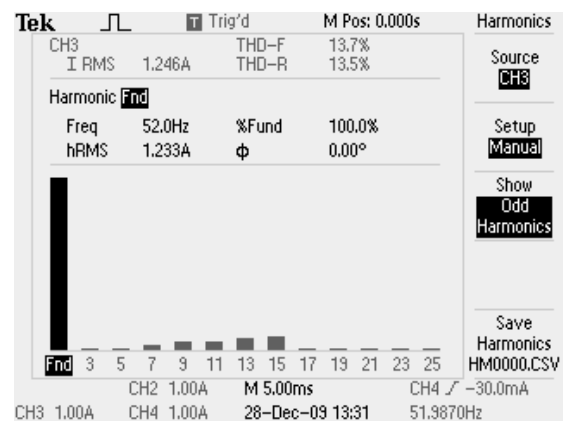
(c) Steady-state currents for  $G_{PR_h}^{imp}(z)$  implementation.



(d) Spectrum of  $i_s$  shown in Fig. 2.18c. THD= 5.67%.

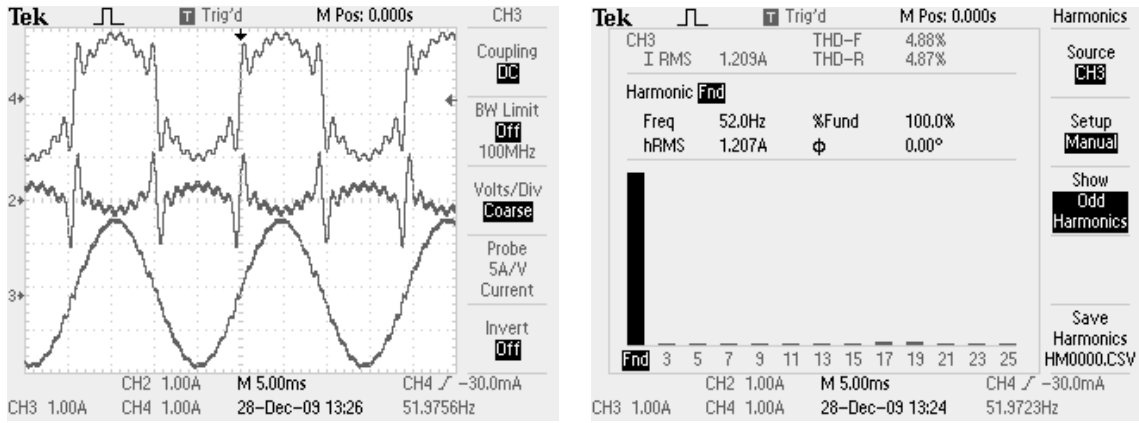


(e) Steady-state currents for  $G_{VPI_h}^{f\&b}(z)$  implementation.



(f) Spectrum of  $i_s$  shown in Fig. 2.18e. THD= 13.7%.

Figure 2.18: Continued on next page.



(g) Steady-state currents for  $G_{VPI_h}^{imp-tp}(z)$  implementation.

(h) Spectrum of  $i_S$  shown in Fig. 2.18g. THD= 4.88%.

Figure 2.18: Steady-state currents and spectra of  $i_S$  for frequency adaptive implementations of Table 2.10, with  $n_h = 15$  and  $f_1 = 52$  Hz. Ch2 is  $i_F$ , Ch3 is  $i_S$  and Ch4 is  $i_L$ . This figure is continued from previous page.

- Concerning PR controllers, the discrete transfer function obtained by FOH and Tustin with prewarping provide the most accurate phase response with respect to the continuous expression. Nevertheless, the impulse invariant method can be considered advantageous when using large gains for the resonant term, since the zeros distribution provided by this technique causes less phase lag at high frequencies, thereby improving stability. On the other hand, ZOH is unfavorable, because it introduces a delay near the resonant frequency.
- Concerning VPI controllers, they can be separated into two resonant terms, one of which is identical to the resonant term included in PR controllers. Therefore, the statements from the previous point can be also applied to this equivalent resonant term. In relation with the other resonant term included in the VPI controller, either FOH, Tustin with prewarping or ZPM are adequate options. On the contrary, ZOH and impulse invariant may cause instability.
- The methods that provide an effective discrete-time implementation of the delay compensation are FOH, Tustin with prewarping and impulse invariant, for either resonant term. Other techniques can easily lead to instability, due to the large difference they produce in the phase response near the resonant frequency.

Experimental results obtained with a shunt APF laboratory prototype validate the most important outcomes of the theoretical analysis. In summary, it has been proved that the choice of the discretization method is a crucial aspect for resonant controllers, and the most suitable alternatives have been established. The effectiveness of the proposed optimum implementations of the digital delay compensation have been tested by compensating odd harmonics up to the 61th order.

Contributions of this chapter have been published in the journal IEEE Transactions on Power Electronics [3] and presented at an international conference [14].

## Chapter 3

# High Performance Digital Resonant Current Controllers Implemented with Two Integrators

*Abstract* — The implementations based on two integrators are widely employed to achieve frequency adaptation without substantial computational burden. However, the discretization of these schemes causes a significant error both in the resonant frequency and in the phase lead provided by the delay compensation. Therefore, perfect tracking is not assured and stability may be compromised. This chapter proposes solutions for both problems without adding a significant resource consumption by correction of the roots placement. A simple expression to calculate the target leading angle, in delay compensation schemes, is also proposed to improve stability margins by means of a better accuracy than previous approaches. Experimental results obtained with a laboratory prototype corroborate the theoretical analysis and the improvement achieved by the proposed discrete-time implementations.

### 3.1 Introduction

The implementations of resonant controllers based on two interconnected integrators are a widely employed option, mainly due to their simplicity regarding frequency adaptation [58, 63, 120, 203, 219–222, 228, 282, 298]. Actually, in chapter §2, it is proved that the ones based on two integrators require lower resource consumption, but at the expense of significant inaccuracies that are exposed in the following.

- The discretization of these schemes based on two integrators leads to a displacement of the resonant poles. This fact results in a deviation of the frequency at which the infinite gain is located with respect to the expected resonant frequency, so a large error may appear in steady-state [58, 63, 65, 120, 203, 211].
- In any implementation of resonant controllers, it should be taken into account that, as the resonant frequency and sampling period increase, the system delay affects the performance and may cause instability. Therefore, a delay compensation scheme, which introduces a phase lead to cancel this delay (phase lag), should be implemented [57, 58, 64, 70, 120, 203, 318]. As proved in the chapter §2, the existing proposals to add delay compensation to the schemes based on two integrators do not provide the expected phase

lead (its target value) when they are implemented in digital devices. This error should be avoided, because if the system delay is not well compensated, stability margins are reduced and anomalous peaks appear in the closed-loop frequency response [58].

Additionally, if the target value for the leading angle does not correspond with the actual phase lag of the system, its delay is not effectively compensated either, even if the resonant controller implementation is accurate enough to make the actual leading angle coincide with its target value. The optimum target leading angle is often assumed to be a phase lead of two samples [58, 64, 120, 260, 276]. In fact, this has been proved to solve the problem of instability of proportional-resonant (PR) controllers that appears at high resonant frequencies [120]. However, as proved in this chapter, a significant portion of the plant delay is not effectively compensated by this approach, so the phase margins are reduced and anomalous peaks appear in the closed-loop frequency response. In the case of implementations with two integrators, this error is added to their inaccuracy between the actual and the expected phase lead, causing an even greater degradation of stability.

Alternative implementations based on two integrators are proposed in this chapter, which achieve higher performance by means of more accurate resonant peak locations and delay compensation, while maintaining the advantage on low computational burden and good frequency adaptation of the original schemes. This is achieved by means of a correction of the resonant poles (associated with the resonant frequency), a correction of zeros (related to delay compensation), and a simple linear expression for the target leading angle that achieves a greater accuracy with respect to the phase lag caused by the plant.

A single-phase shunt active power filter (APF) laboratory prototype has been built to check the theoretical approaches. This is an application very suitable for proving the controllers performance when tracking different and variable frequencies, and results can be extrapolated to other single-phase and three-phase applications where a perfect tracking/rejection of references/disturbances of variable frequency is sought.

The chapter is organized as follows. Section §3.2 exposes the fundamentals of resonant controllers and the implementations based on two interconnected integrators. The proposed correction to improve the resonant frequency accuracy of these schemes is addressed in section §3.3. In section §3.4, the proposed expression for the target leading angle is exposed and compared with previous approaches, and superior delay compensation techniques based on two integrators are provided. Finally, section §3.5 presents experimental results that validate the theoretical analysis and the effectiveness of the proposed digital implementations.

## 3.2 Review of Resonant Controllers Implemented with Two Integrators

### 3.2.1 Resonant Controllers in the Continuous Domain

The schemes based on two integrators for implementation of  $G_{PR_h}(s)$ ,  $G_{VPI_h}(s)$  and  $G_{PR_h}^d(s)$  have been exposed in sections §1.2.7.1 and §2.2.2. To facilitate further developments that will start from these block diagrams, they are shown again together in Fig. 3.1. It should be noted that it is not possible to implement  $G_{VPI_h}^d(s)$  with two interconnected integrators, because (2.2) presents two zeros.

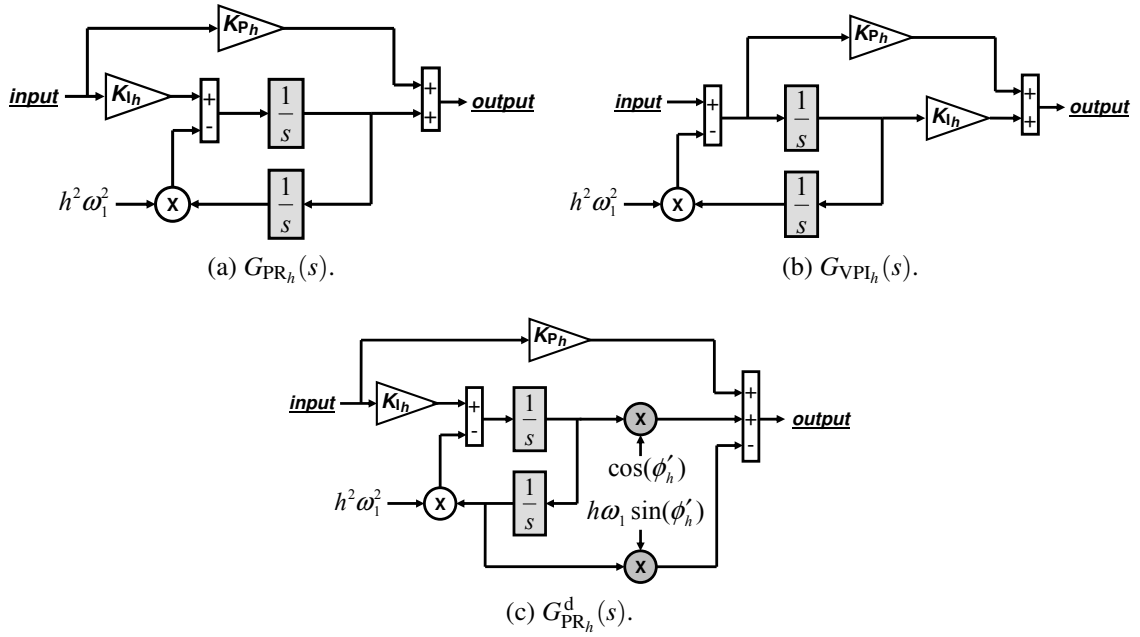


Figure 3.1: Block diagrams of continuous resonant controllers based on two integrators.

In these schemes, the parameter  $h\omega_1$  can be easily modified in real-time according to the actual value of the frequency to be controlled;  $\omega_1$  can be estimated with, e.g., a phase-locked loop (PLL). This advantage is maintained if the two integrators are discretized separately, whereas others discrete-time implementations require the on-line computation of cosine terms (as exposed in the chapter §2). In this manner, the structure based on two integrators is a widely employed choice, mainly due to the simplicity it permits when implementing frequency adaptation [58, 63, 120, 203, 219–222, 228, 282, 298].

As exposed in section §1.2, the scheme shown in Fig. 3.1c introduces a phase lead  $\phi'_h$  in the vicinity of the resonant frequency  $h\omega_1$  of a resonant controller in order to compensate the system delay (mainly due to computation and modulation). It is useful to define an additional parameter  $\phi_h$  as the difference between the actual phase provided by a given resonant controller at frequencies infinitely close to  $h\omega_1$  and that provided by  $G_{PR_h}(s)$ . The meaning of this variable is illustrated in the open-loop Bode diagrams shown in Fig. 3.2. For different values of  $\phi_h$ , the variation of the phase lead with respect to  $G_{PR_h}(s)$  can be appreciated. Note that  $G_{PR_h}(s)$  satisfies  $\phi_h = 0$ , and  $G_{PR_h}^d(s)$  provides  $\phi_h = \phi'_h$ . On the other hand,  $G_{VPI_h}(s)$  introduces a phase lead  $\phi_h = \arctan(h\omega_1 L_F/R_F) \neq 0$  even though  $\phi'_h$  is not included in (1.34).

For PR controllers with delay compensation,  $\phi'_h$  is the expected (design) value for its actual phase lead  $\phi_h$ . For this reason,  $\phi'_h$  can be defined as the target leading angle. In the continuous domain they always coincide, but this does not necessarily happen when implemented in digital devices.

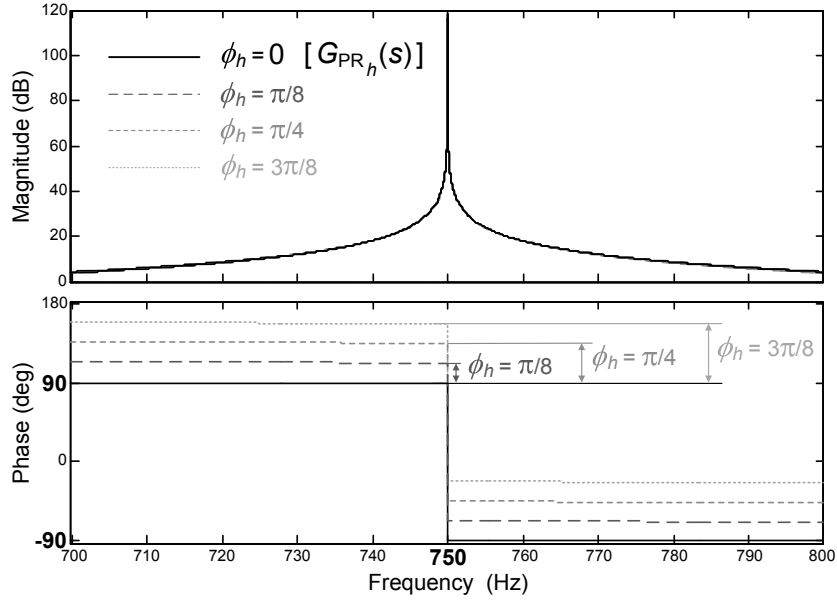


Figure 3.2: Open-loop Bode diagrams provided by PR controllers (the plant is not included) with different  $\phi_h$  values. Parameters:  $f_s = 10$  kHz,  $hf_1 = 750$  Hz,  $K_{P_h} = K_{P_T} = 20$  and  $K_{I_h} = 2000$ .

### 3.2.2 Discretization of Schemes Based on Two Integrators and Its Inaccuracies

It should be remarked that Fig. 3.1 schemes cannot be implemented in digital devices, since they are expressed in the continuous domain. As exposed in the following, the discretization process worsens some of their most important features.

In order to implement the scheme shown in Fig. 3.1a in digital devices, the direct integrator is usually discretized with the forward Euler method, and the feedback one using the backward Euler method [218–222]. From chapter §2 (it is briefly repeated here for clarity), this approach leads to the following transfer function in the  $z$ -domain:

$$G_{PR_h}(z) = K_{P_h} + K_{I_h} T_s \frac{z^{-1} - z^{-2}}{1 - 2z^{-1}(1 - h^2 \omega_1^2 T_s^2 / 2) + z^{-2}} \quad (3.1)$$

The same approach can be applied to Figs. 3.1b and 3.1c, which, respectively, results in

$$G_{VPI_h}(z) = \frac{K_{P_h} + z^{-1}(K_{I_h} T_s - 2K_{P_h}) - z^{-2}(K_{I_h} T_s - K_{P_h})}{1 - 2z^{-1}(1 - h^2 \omega_1^2 T_s^2 / 2) + z^{-2}} \quad (3.2)$$

and

$$G_{PR_h}^d(z) = K_{P_h} + K_{I_h} T_s \frac{z^{-1} [\cos(\phi'_h) - h\omega_1 T_s \sin(\phi'_h)] - z^{-2} \cos(\phi'_h)}{1 - 2z^{-1}(1 - h^2 \omega_1^2 T_s^2 / 2) + z^{-2}}. \quad (3.3)$$

Note that the superscripts that refer to discretization methods are omitted in this chapter for simplicity.

As proved in chapter §2, the discretization process causes the following inaccuracies.

- The transfer functions (3.1), (3.2) and (3.3) do not provide infinite gain at the desired frequency  $h\omega_1$ , so a significant error may appear in steady-state when ac references are tracked in closed-loop.
- Expression (3.3) provides a phase lead different from the expected ( $\phi_h \neq \phi'_h$ ), so stability margins and performance are worsened. In fact, this discrepancy is quite dependent on the combination of  $h\omega_1$  and  $T_s$ , leading to a large and random uncertainty.

These two problems should be overcome in order to achieve high performance digital implementations of resonant controllers. The issue of resonant poles accuracy is approached in section §3.3, and the improvement in delay compensation accuracy is addressed in section §3.4.

It should be also remarked that the other existing possibilities for discretizing both separated integrators do not lead to better results, as exposed in the chapter §2. Consequently, the method that combines forward Euler and backward Euler can be considered to be the optimum as a starting point for subsequent improvements.

### 3.3 Correction of Poles: Improvement in Resonant Frequency Accuracy

An accurate resonant poles placement is required in order to achieve perfect tracking [58, 63, 65, 120, 203]. From chapter §2, it can be obtained by placing the poles at  $e^{-jh\omega_1 T_s}$  and  $e^{jh\omega_1 T_s}$ . The product of both terms leads to a denominator of the form:

$$1 - 2z^{-1} \cos(h\omega_1 T_s) + z^{-2}. \quad (3.4)$$

The denominators of (3.1), (3.2) and (3.3) differ from (3.4) in the fact that the  $\cos(h\omega_1 T_s)$  term appears in them as a second-order Taylor series approximation. This discrepancy explains the resonant frequency deviation of those schemes as the product  $h\omega_1 T_s$  increases.

To implement the resonant poles as (3.4) provides the most accurate resonant peak location. However, the on-line calculation of explicit trigonometric functions implies a greater consumption of resources. Therefore, it is interesting to improve the accuracy of the implementations based on two integrators by increasing the order of the approximation, as proposed in the following.

The second-order Taylor series that appear in (3.1), (3.2) and (3.3) may be improved to a higher order  $n_T$  if the input signal  $h^2\omega_1^2$  (from the PLL) that appears in the schemes of Fig. 3.1 is modified as

$$h^2\omega_1^2 \rightarrow C_h = 2 \sum_{n=1}^{n_T/2} \frac{(-1)^{n+1} h^{2n} \omega_1^{2n} T_s^{2n-2}}{(2n)!} \quad (3.5)$$

which, for low values of  $n_T$ , becomes

$$h^2\omega_1^2 \rightarrow C_h = \underbrace{h^2\omega_1^2 - h^4 \frac{\omega_1^4 T_s^2}{12} + h^6 \frac{\omega_1^6 T_s^4}{360} + \dots}_{n_T=6} \quad (3.6)$$

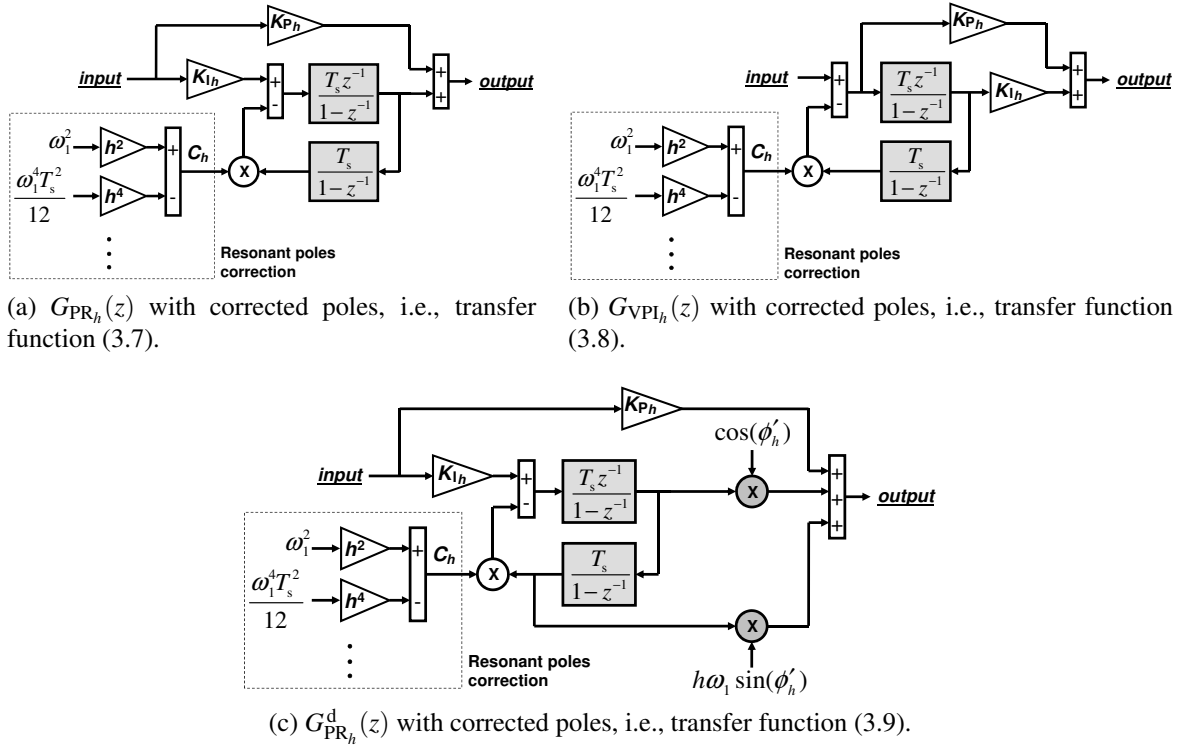


Figure 3.3: Block diagrams of digital resonant controllers based on two integrators, including proposed correction (3.5) for the resonant poles.

It should be noted that only even values of  $n_T$  are possible. If the correction (3.5) is applied to the schemes shown in Figs. 3.1a, 3.1b and 3.1c, and they are discretized with forward Euler and backward Euler, the block diagrams shown in Figs. 3.3a, 3.3b and 3.3c are obtained, respectively. In the same manner, the application of correction (3.5) to the transfer functions (3.1), (3.2) and (3.3) leads respectively to

$$G_{PR_h}(z) = K_{P_h} + K_{I_h} T_s \frac{z^{-1} - z^{-2}}{1 - 2z^{-1}(1 - C_h T_s^2/2) + z^{-2}} \quad (3.7)$$

$$G_{VPI_h}(z) = \frac{K_{P_h} + z^{-1}(K_{I_h} T_s - 2K_{P_h}) - z^{-2}(K_{I_h} T_s - K_{P_h})}{1 - 2z^{-1}(1 - C_h T_s^2/2) + z^{-2}} \quad (3.8)$$

and

$$G_{PR_h}^d(z) = K_{P_h} + K_{I_h} T_s \frac{z^{-1} [\cos(\phi'_h) - h\omega_1 T_s \sin(\phi'_h)] - z^{-2} \cos(\phi'_h)}{1 - 2z^{-1}(1 - C_h T_s^2/2) + z^{-2}}. \quad (3.9)$$

Fig. 3.4 depicts the resonant peak location error of Fig. 3.3 schemes, which implement (3.7), (3.8) and (3.9). It can be appreciated that the deviation increases with  $T_s$  and  $hf_1$ , and it is kept constant when the product of both terms is the same (i.e., when the ratio  $hf_1/f_s$  is constant). Each surface represents a different order  $n_T$  for the Taylor series approximation in (3.5). It should be noted that a value of  $n_T = 2$  means that no correction is applied. A great improvement can be appreciated with respect to the original second-order expression, when higher values of  $n_T$  are employed.

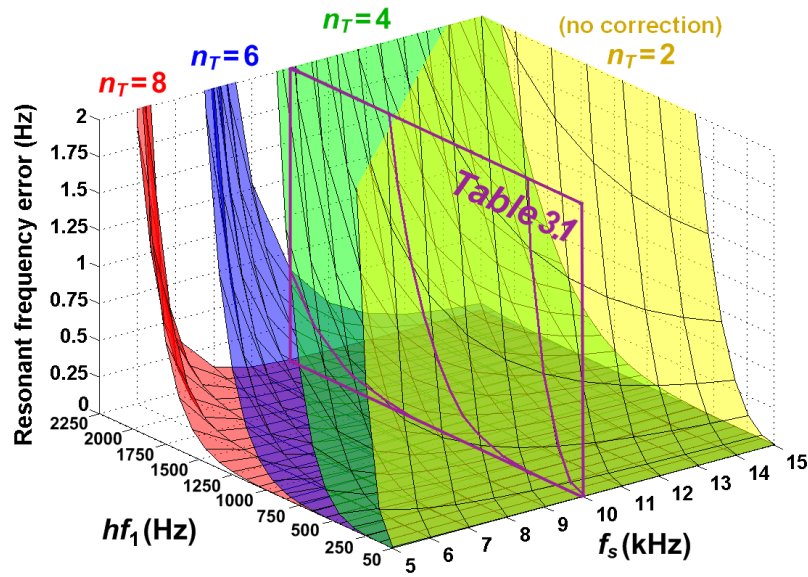


Figure 3.4: Resonant frequency error with the proposed correction (3.5) for the implementations based on two discrete integrators (Fig. 3.3 schemes), as a function of  $hf_1$  and  $f_s$ .

TABLE 3.1  
RESONANT FREQUENCY ERROR (Hz) WITH  $f_s = 10$  kHz

$hf_1$ (Hz)	$hf_1 / f_s$	$n_T = 2$	$n_T = 4$	$n_T = 6$	$n_T = 8$
50	0.005	$2.06 \cdot 10^{-3}$	$67.65 \cdot 10^{-9}$	$\approx 0$	$\approx 0$
150	0.015	$55.57 \cdot 10^{-3}$	$16.46 \cdot 10^{-6}$	$2.61 \cdot 10^{-9}$	$\approx 0$
250	0.025	0.26	$0.21 \cdot 10^{-3}$	$93.5 \cdot 10^{-9}$	$\approx 0$
350	0.035	0.71	$1.14 \cdot 10^{-3}$	$0.99 \cdot 10^{-6}$	$0.53 \cdot 10^{-9}$
450	0.045	1.51	$4.04 \cdot 10^{-3}$	$5.77 \cdot 10^{-6}$	$5.13 \cdot 10^{-9}$
550	0.055	2.77	$11.09 \cdot 10^{-3}$	$23.67 \cdot 10^{-6}$	$31.42 \cdot 10^{-9}$
650	0.065	4.6	$25.75 \cdot 10^{-3}$	$76.78 \cdot 10^{-6}$	$0.14 \cdot 10^{-6}$
750	0.075	7.12	$53.11 \cdot 10^{-3}$	$0.21 \cdot 10^{-3}$	$0.52 \cdot 10^{-6}$
850	0.085	10.44	0.1	$0.51 \cdot 10^{-3}$	$1.62 \cdot 10^{-6}$
950	0.095	14.7	0.18	$1.13 \cdot 10^{-3}$	$4.47 \cdot 10^{-6}$
1050	0.105	20	0.29	$2.3 \cdot 10^{-3}$	$11.14 \cdot 10^{-6}$
1150	0.115	26.6	0.47	$4.41 \cdot 10^{-3}$	$25.63 \cdot 10^{-6}$
1250	0.125	34.6	0.73	$8.03 \cdot 10^{-3}$	$55.13 \cdot 10^{-6}$
1350	0.135	44.15	1.08	$14 \cdot 10^{-3}$	$0.11 \cdot 10^{-3}$
1450	0.145	55.5	1.57	$23.5 \cdot 10^{-3}$	$0.22 \cdot 10^{-3}$
1550	0.155	68.9	2.24	$38.22 \cdot 10^{-3}$	$0.4 \cdot 10^{-3}$
1650	0.165	84.6	3.13	$60.47 \cdot 10^{-3}$	$0.72 \cdot 10^{-3}$
1750	0.175	102.8	4.29	$93.4 \cdot 10^{-3}$	$1.26 \cdot 10^{-3}$
1850	0.185	124.1	5.8	0.14	$2.13 \cdot 10^{-3}$
1950	0.195	148.8	7.74	0.21	$3.51 \cdot 10^{-3}$
2050	0.205	177.3	10.21	0.31	$5.67 \cdot 10^{-3}$
2150	0.215	210.5	13.34	0.44	$8.97 \cdot 10^{-3}$
2250	0.225	248.9	17.26	0.62	$13.95 \cdot 10^{-3}$

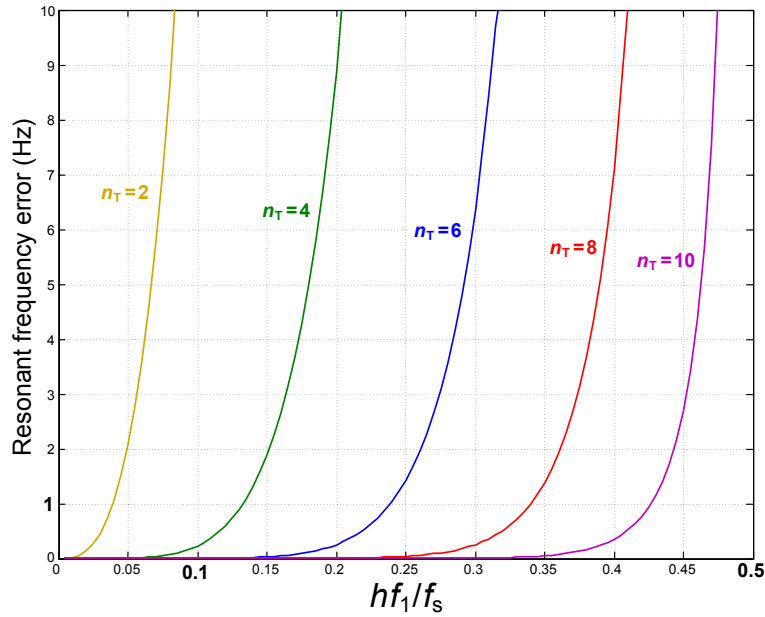


Figure 3.5: Resonant frequency error with the proposed correction (3.5) for the implementations based on two discrete integrators (Fig. 3.3 schemes), as a function of the ratio  $hf_1/f_s$ .

Table 3.1 shows the error values of Fig. 3.4 with a sampling frequency of  $f_s = 10$  kHz, which is a reasonable and typical choice in systems that do not involve high power. From Table 3.1, an approximation of fourth-order seems enough to provide a good accuracy for a wide range of the spectrum. For instance, the error achieved with  $n_T = 4$  and  $hf_1 = 1250$  Hz is similar to that of  $n_T = 2$  and  $hf_1 = 350$  Hz.

Fig. 3.5 takes advantage of the constant behavior of the phase lead error when  $hf_1/f_s$  is maintained, to represent in a single two-dimensional graphic its variation with this parameter. Concerning applications with not very high ratio  $hf_1/f_s$  (lower than approximately 0.1), it can be concluded that a correction of fourth-order is the most adequate solution. For instance, with sampling frequencies close to 10 kHz,  $n_T = 4$  would be suitable for most grid-connected APFs, which are mainly aimed at low frequencies. However, if very high frequencies should be tracked (such as in aeronautic APFs [70] or high-speed ac drives [311, 312]) with a similar  $f_s$ , it may be convenient to employ a sixth- or eighth-order correction for the highest frequencies ( $n_T = 10$  would be only needed in very extreme cases, close to the Nyquist frequency). That would be also the case if low resonant frequencies were required in combination with lower  $f_s$  (for example, in order to reduce losses in high-power converters [313–317]).

It should be remarked that these results can be also applied to other implementations, apart from those based on two integrators, in which (3.4) is approximated by Taylor series.

### 3.4 Correction of Zeros: Improvement in Delay Compensation Accuracy

An accurate compensation of the system phase lag is required in order to achieve wider stability margins and to avoid closed-loop anomalous peaks around resonant frequencies [58]. The digital implementations based on two integrators do not effectively cancel this delay, due

to two different reasons.

- The target leading angle  $\phi'_h$  employed in previous works is quite different from the actual delay in the system (proved in section §3.4.1). Note that this problem does not only apply to implementations with two integrators.
- As exposed in section §3.2.2, these schemes provide a phase lead  $\phi_h$  different from the expected  $\phi'_h$ . Thus, even if  $\phi'_h$  is well calculated, the obtained phase lead is not the adequate value (due to discretization).

These two problems accumulate error in the actual phase lead  $\phi_h$  with respect to the phase lag to compensate. The first issue is approached in section §3.4.1; an accurate expression for  $\phi'_h$  is calculated based on plant parameters. In section §3.4.2, a novel method is provided to correct inaccuracies in the actual phase lead  $\phi_h$  due to discretization influence on zeros.

### 3.4.1 Improvement in Target Leading Angle Expression

The plant should be modelled in order to define an appropriate target leading angle  $\phi'_h$  to compensate the phase lag that it introduces in the system. The plant model  $G_{\text{PL}}(z)$  for current-controlled voltage source converters (VSCs) taking into account the computational delay, the pulsewidth modulation (PWM) and the L filter is given by (1.12).

The leading angle  $\phi_h$  should compensate the delay introduced by the plant, in order to improve the stability margins and to avoid anomalous peaks in the closed-loop frequency response [58]. Consequently,  $\phi_h = -\angle G_{\text{PL}}(z)$  should be always sought. Fig. 3.6 shows the variation of  $|\angle G_{\text{PL}}(z)|$  with frequency.

From Fig. 3.6, the vector proportional-integral (VPI) controller provides a phase lead  $\phi_h$  very similar to  $|\angle G_{\text{PL}}(z)|$  at low frequencies. However, due to the fact that  $G_{\text{VPI}_h}(z)$  does not take into account the delay caused by the computation and the modulation, the difference  $\phi_h - |\angle G_{\text{PL}}(z)|$  becomes quite significant as the frequency increases. This difference explains why  $G_{\text{VPI}_h}(z)$  becomes unstable at high frequencies, as reported in [56, 57], if delay compensation is not included. Indeed, the phase  $\phi_h - |\angle G_{\text{PL}}(z)|$  in combination with the additional  $90^\circ$  phase lag (shown in Fig. 3.2) after each resonance leads to a  $180^\circ$  delay (stability limit) for frequencies higher than approximately 1250 Hz. If VPI controllers are implemented with delay compensation of  $3/2$  samples, it is possible to achieve a very accurate compensation of  $\angle G_{\text{PL}}(z)$  for all frequencies, as depicted in Fig. 3.6. However, this approach is not developed in this study due to the fact that it would add a significant complexity to the original schemes based on two integrators. Instead, an optimum leading angle is sought for PR implementations with two integrators [ $G_{\text{PR}_h}^{\text{d}}(z)$ ], so a similarly good  $\angle G_{\text{PL}}(z)$  compensation is obtained with a simpler scheme, as approached in the following.

The most convenient  $\phi'_h$  value is often assumed to be of two samples [58, 64, 120, 260, 276]. In fact, this value has been proved to be enough for solving the problem of instability of PR controllers that appears at  $hf_1/f_s > 0.1$  [120]. However, as illustrated in Fig. 3.6, a significant portion of the plant delay is not effectively compensated by this approach either. Therefore, an alternative expression should be sought to provide a more accurate compensation of the plant delay for PR controllers. It can be observed in Fig. 3.6 that, except for the lowest frequencies,  $\angle G_{\text{PL}}(z)$  is linear. Thus, the following simple linear equation for the target leading angle is proposed:

$$\phi'_h = \lambda h \omega_1 + \phi'_o \quad (3.10)$$

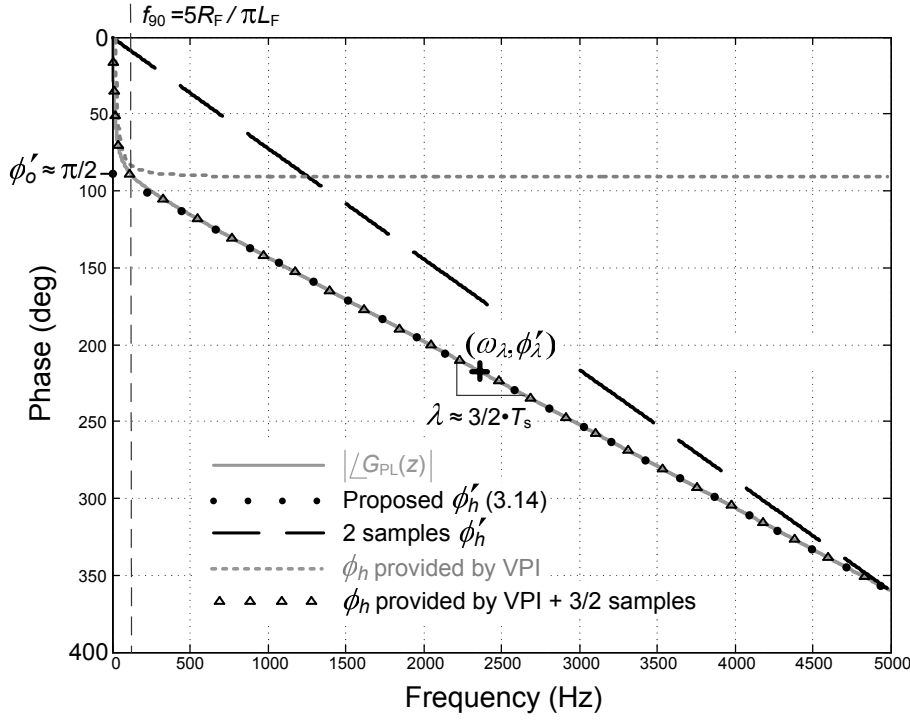


Figure 3.6: Comparison of  $|\angle G_{PL}(z)|$  and leading angle provided by different expressions. Parameters:  $L_F = 5 \text{ mH}$ ,  $R_F = 0.5 \Omega$  and  $f_s = 10 \text{ kHz}$ .

where  $\lambda$  is the slope of  $-\angle G_{PL}(z)$  at a selected frequency  $\omega_\lambda$ ,

$$\lambda = -\frac{\partial \angle G_{PL}(z)}{\partial \omega}(\omega_\lambda) = T_s \frac{2 + \rho^{-2} - 3\rho^{-1} \cos(\omega_\lambda T_s)}{1 + \rho^{-2} - 2\rho^{-1} \cos(\omega_\lambda T_s)} \quad (3.11)$$

$\phi'_0$  is the ordinate at the origin,

$$\phi'_0 = \phi'_\lambda - \lambda \omega_\lambda \quad (3.12)$$

and  $\phi'_\lambda$  being the phase of  $-G_{PL}(z)$  at  $\omega_\lambda$ ,

$$\phi'_\lambda = -\angle G_{PL}(e^{j\omega_\lambda T_s}) = -\arctan\left(\frac{\rho^{-1} \sin(\omega_\lambda T_s) - \sin(2\omega_\lambda T_s)}{\cos(2\omega_\lambda T_s) - \rho^{-1} \cos(\omega_\lambda T_s)}\right). \quad (3.13)$$

Equations (3.13) and (3.11) are obtained in Appendix B.1 and B.2, respectively. The value of  $\omega_\lambda$  has to be chosen so that its corresponding slope  $\lambda$  can be assumed to be adequate for most frequencies to be tracked. Once  $\omega_\lambda$  is fixed, both  $\lambda$  and  $\phi'_0$  are constants, which are calculated off-line.

Nevertheless, (3.11) and (3.13) may be simplified in most situations. This is due to the fact that the phase lag caused by the inductive filter almost reaches a constant value of  $90^\circ$  a decade above the L filter pole ( $f_{90} = 5R_F/\pi L_F$ ), so for higher frequencies  $\angle G_{PL}(z)$  can be considered linear with negligible error. Consequently, it can be assumed  $\phi'_\lambda = \pi/2$  and  $\lambda = 3/2 T_s$ , which leads to the following linear expression:

$$\phi'_h = \frac{\pi}{2} + \frac{3}{2} h \omega_1 T_s. \quad (3.14)$$

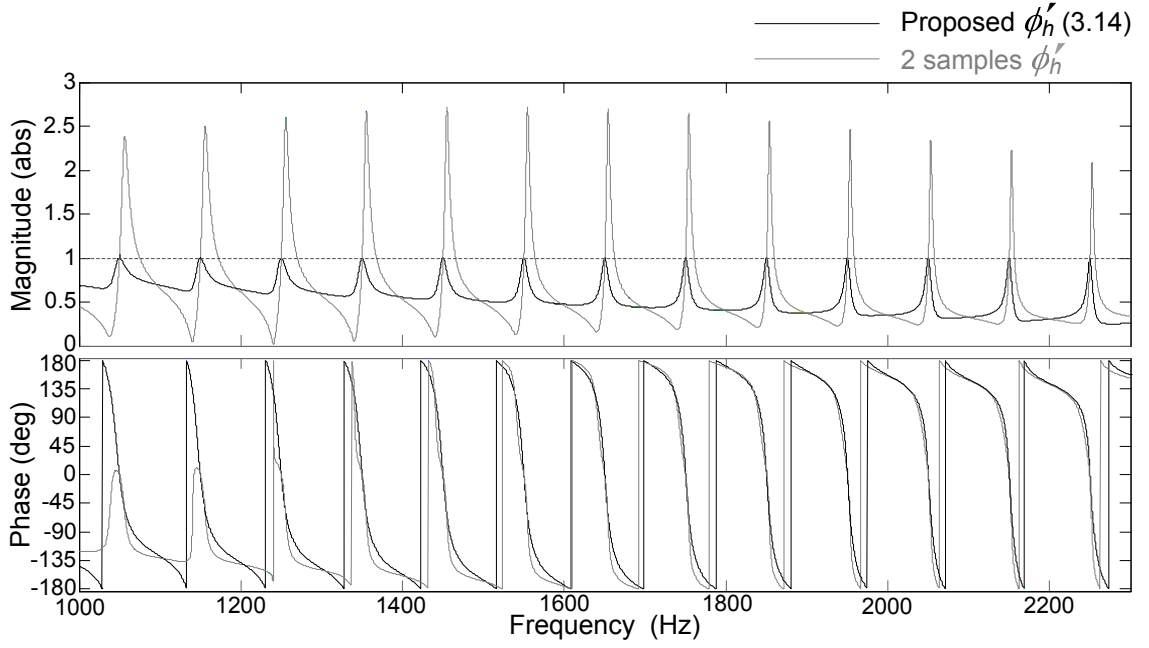


Figure 3.7: Closed-loop Bode diagrams using PR controllers with phase lead of two samples and according to (3.14), for  $hf_1 \in \{1050, 1150, \dots, 2250\}$  Hz. In both cases,  $\phi_h = \phi_h'$  has been assured. The diagrams of negative frequencies are symmetrical of these. Parameters:  $L_F = 5$  mH,  $R_F = 0.5 \Omega$ ,  $f_s = 10$  kHz,  $K_{p_T} = 15$  and  $K_{I_h} = 2000 \forall h$ .

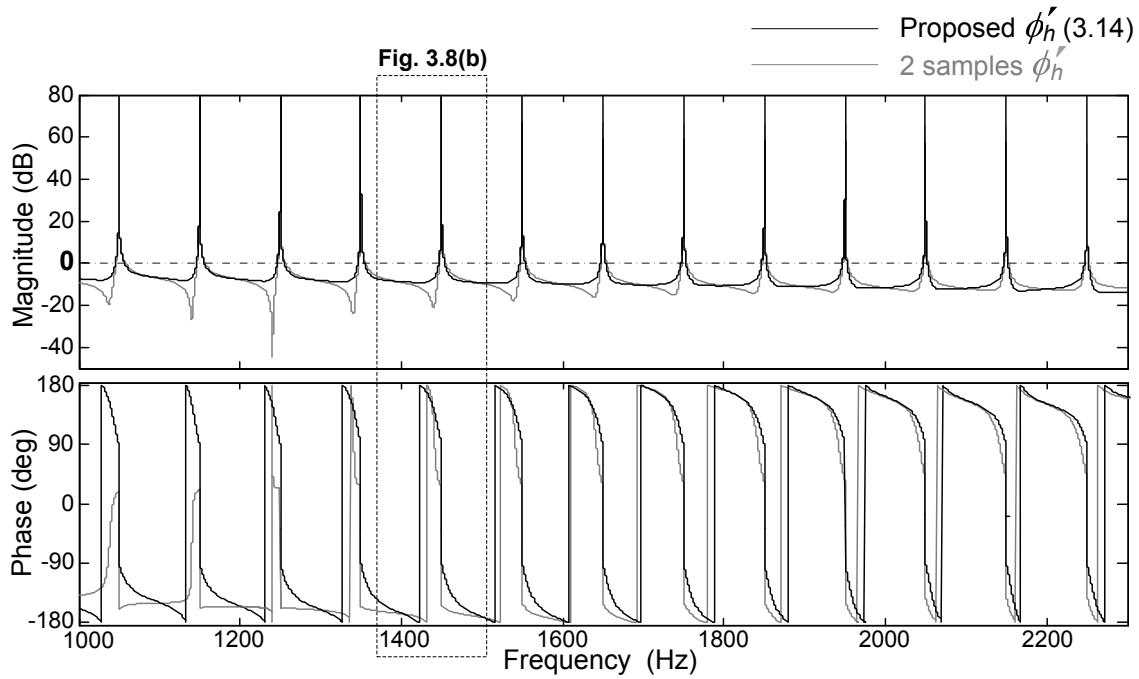
As depicted in Fig. 3.6, (3.14) provides a very accurate approximation of  $|\angle G_{PL}(z)|$  for frequencies higher than approximately  $f_{90}$  (this generally includes all harmonics). It should be noted that  $f_{90} \ll f_s$  is usually satisfied, since the L filter should be designed to cancel the commutation harmonics.

For very low resonant frequencies it may be preferable to employ  $G_{VPI_h}(z)$  instead of  $G_{PR_h}^d(z)$  with (3.14), since the former provides a very accurate approximation of  $\angle G_{PL}(z)$  for approximately  $hf_1 < f_{90}$ . In any case, it should be remarked that delay compensation is more critical for high frequencies [56–58, 70, 120, 203].

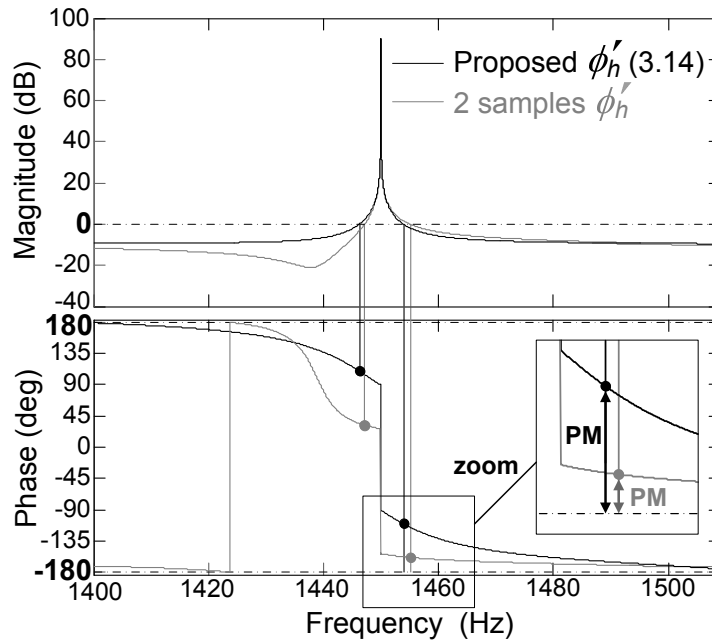
Fig. 3.7 compares the closed-loop Bode diagrams using  $G_{PR_h}^d(z)$  with  $\phi_h$  according to (3.14) and with a two samples phase lead, for odd harmonic orders between 21 and 45 (these are very unfavorable cases). The closed-loop Bode diagram depicted in Fig. 3.7 shows the lack of anomalous peaks provided by the proposal, whereas significant undesired peaks appear in the case of two samples phase lead. Furthermore, it can be also appreciated that the gain/frequency slope at the resonant frequencies is much lower in the case of (3.14), which means that small frequency deviations cause smaller steady-state error.

Fig. 3.8a shows the open-loop Bode Diagrams  $[G_C(z) G_{PL}(z)]$  for high frequencies. The same parameters of Fig. 3.7 are employed. It can be observed in Fig. 3.8a that, around each resonant frequency, there are two 0 dB crossings [63]. This implies that individual phase margins can be defined for each resonant controller. Fig. 3.8b illustrates that these margins represent the phase delay that may be introduced until  $180^\circ$  is reached (stability limit), at the frequency at which the gain crosses 0 dB just after  $h\omega_1$ .

Table 3.2 compares the phase margins that correspond to each individual resonant controller, with both leading angle expressions. With a two samples  $\phi_h'$ , a drastic reduction in the stability



(a) Resonant controllers tuned at  $hf_1 \in \{1050, 1150, \dots, 2250\}$  Hz. Note the multiple 0 dB crossings (multiple phase margins).



(b) Example of phase margin (PM) measurement for an individual resonant controller ( $hf_1 = 1450$  Hz). The second 0 dB crossing is the one considered because it is more critical.

Figure 3.8: Open-loop Bode diagrams  $G_C(z) G_{PL}(z)$  using PR controllers with phase lead of two samples and according to (3.14). In both cases,  $\phi_h = \phi'_h$  has been assured. The diagrams of negative frequencies are symmetrical of these. Parameters:  $L_F = 5$  mH,  $R_F = 0.5 \Omega$ ,  $f_s = 10$  kHz,  $K_{PT} = 15$  and  $K_{I_h} = 2000 \forall h$ .

TABLE 3.2  
PHASE MARGIN (deg) OF INDIVIDUAL RESONANT CONTROLLERS

$hf_1$ (Hz)	1050	1150	1250	1350	1450	1550	1650
2 samples $\phi'_h$	25.7	24	22.8	22	21.6	21.4	21.6
Proposed $\phi'_h$ (3.14)	67.2	67.8	68.5	69.3	70.1	71	71.9
$hf_1$ (Hz)	1750	1850	1950	2050	2150	2250	
2 samples $\phi'_h$	22	22.7	23.7	24.9	26.3	27.9	
Proposed $\phi'_h$ (3.14)	72.9	73.9	74.9	76	77.1	78.2	

margins occurs. On the other hand, (3.14) leads to larger phase margins; in fact, they are greater than the phase margin that corresponds to  $K_{PT} G_{PL}(z)$  ( $65.6^\circ$ ). In this manner, it can be stated that when  $\phi_h$  satisfies the proposed expression (3.14), unexpected results are less probable to occur if the phase margin of  $K_{PT} G_{PL}(z)$  is employed for the tuning.

It is also interesting to note that, from (3.14) and section §1.2.6, implementation of the proposed target leading angle does not seem possible in repetitive controllers (instead of resonant ones), since their phase lead should be proportional to the resonant frequency.

### 3.4.2 Enhanced Discrete-Time Delay Compensation Schemes Based on Two Integrators

As exposed in section §3.2.2, the original delay compensation scheme  $G_{PR_h}^d(z)$  derived from [203] fails to provide the expected phase lead in the  $z$ -domain ( $\phi_h \neq \phi'_h$ ). Therefore, in order to avoid uncertainties that could lead to an unstable system or a poor performance, it is preferable to seek for an alternative method to perform the discrete-time delay compensation.

#### 3.4.2.1 Correction of Delay Compensation Technique

From chapter §2, an accurate phase lead ( $\phi_h = \phi'_h$ ) for PR controllers in the  $z$ -domain can be achieved by discretizing  $G_{PR_h}^d(s)$  with the impulse invariant method:

$$G_{PR_h}^{d\text{imp}}(z) = K_{P_h} + K_{I_h} T_s \frac{\cos(\phi'_h) - z^{-1} \cos(\phi'_h - h\omega_1 T_s)}{1 - 2z^{-1} \cos(h\omega_1 T_s) + z^{-2}}. \quad (3.15)$$

The goal is to modify the original Fig. 3.3c scheme, which implements (3.9), so that the numerator (zeros) of (3.9) becomes equivalent to that of (3.15). Equation (3.15) can be slightly modified to obtain an expression more similar to (3.9), without worsening the accuracy of (3.15) in the vicinity of the resonant frequency, that is, assuring that  $\phi_h = \phi'_h$  is still verified: the second addend of (3.15) is multiplied by an additional  $z^{-1}$  term, and the phase that corresponds to one sample delay at the resonant frequency ( $h\omega_1 T_s$ ) is added to  $\phi'_h$ . In this manner, the delay introduced by the  $z^{-1}$  term is compensated by the increase in the leading angle, so the resulting

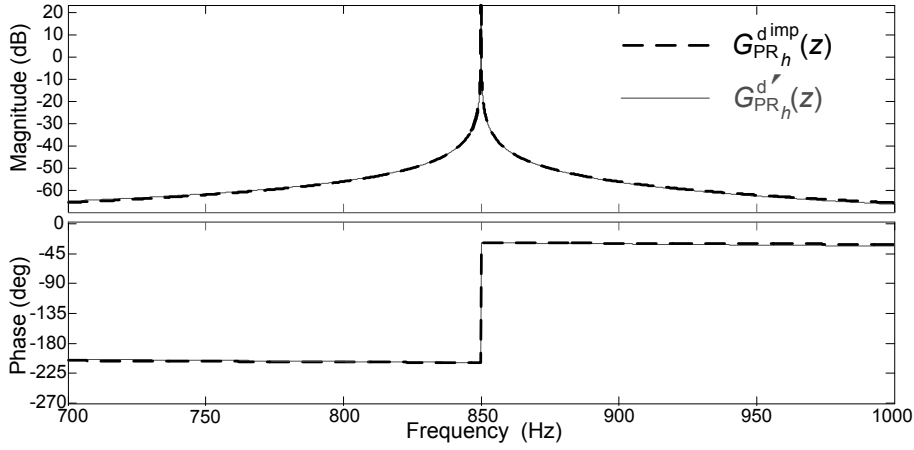


Figure 3.9: Open-loop Bode diagrams provided by  $G_{PR_h}^{d'imp}(z)$  and  $G_{PR_h}^{d'}(z)$ . Parameters:  $f_s = 10\text{ kHz}$ ,  $hf_1 = 850\text{ Hz}$ ,  $K_{P_h} = K_{P_T} = 0$ ,  $K_{I_h} = 2000$  and  $\phi'_h = 30.6^\circ$ .

$\phi_h$  is equal to that of (3.15). This leads to

$$G_{PR_h}^{d'}(z) = K_{P_h} + K_{I_h} T_s \frac{z^{-1} \cos(h\omega_1 T_s + \phi'_h) - z^{-2} \cos(\phi'_h)}{1 - 2z^{-1} \cos(h\omega_1 T_s) + z^{-2}}. \quad (3.16)$$

Fig. 3.9 shows the equivalence between the Bode diagrams of  $G_{PR_h}^{d'imp}(z)$  and  $G_{PR_h}^{d'}(z)$ . In fact, it can be noted that the proposals of Yuan et al. in [64] for delay compensation are particular cases of (3.16). The effect of the additional  $z^{-1}$  delay for frequencies very far from  $h\omega_1$  has no relevance because of the low gain provided by  $G_{PR_h}^{d'}(z)$  at them. This is reinforced by the fact that  $K_{I_h}$  is not needed to assume high values in order to provide robustness to frequency deviations, since the implementations based on two integrators are easily adapted to  $h\omega_1$  variations.

It can be also appreciated that the coefficient of the  $z^{-1}$  term of the numerator in (3.9) is actually a first-order Taylor series approximation of that in (3.16), with  $\phi'_h$  as center point:

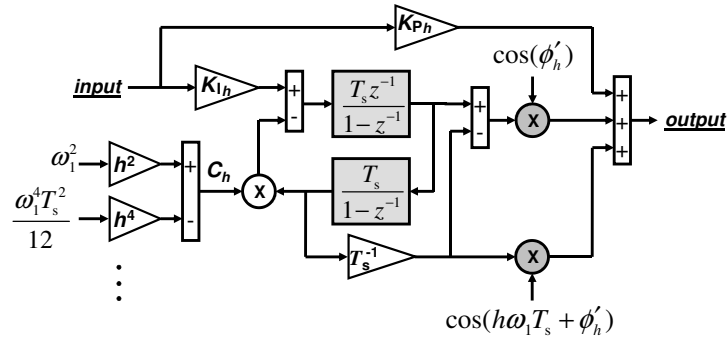
$$\underbrace{\cos(\phi'_h) - h\omega_1 T_s \sin(\phi'_h)}_{\text{Original (3.9)}} \longleftrightarrow \underbrace{\cos(h\omega_1 T_s + \phi'_h)}_{\text{Accurate (3.16)}} \quad (3.17)$$

This is not a good approximation, because  $h\omega_1 T_s + \phi'_h$  may be much greater than  $\phi'_h$ . This fact explains the leading angle inaccuracy of (3.9) as  $h\omega_1 T_s$  increases.

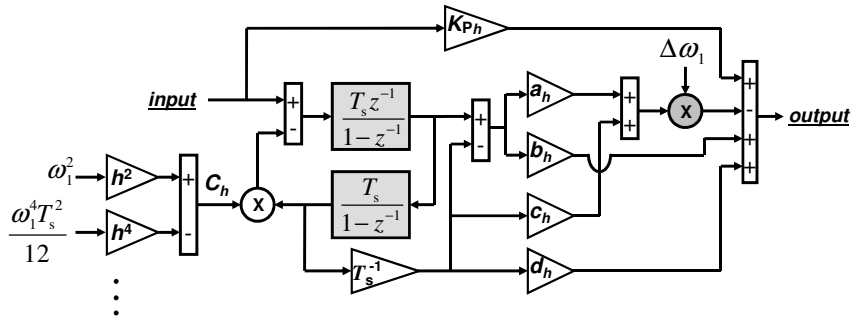
The numerator in (3.9) can be transformed into that of (3.16) if the input  $h\omega_1 \sin(\phi'_h)$  of Fig. 3.3c is modified as:

$$h\omega_1 \sin(\phi'_h) \rightarrow \frac{1}{T_s} \cos(\phi'_h) - \frac{1}{T_s} \cos(h\omega_1 T_s + \phi'_h). \quad (3.18)$$

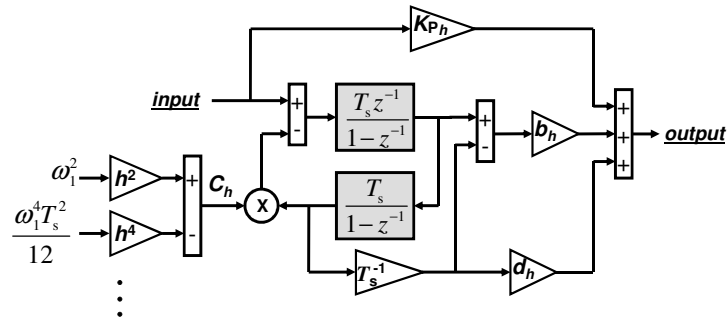
The resulting discrete-time implementation of a PR controller with accurate delay compensation takes the form of the block diagram depicted in Fig. 3.10a. This scheme provides a satisfying behavior for any possible combination of  $h\omega_1$  and  $T_s$ , whereas  $G_{PR_h}^d(z)$  is subject to the uncertainty given by the fact that the error it introduces in  $\phi_h$  varies a lot depending on the value of  $h\omega_1 T_s$  (proved in chapter §2). Furthermore, it can be observed that both Fig. 3.3c and Fig. 3.10a schemes are quite similar in terms of complexity; in fact, both require explicit on-line calculation of two trigonometric functions.



(a) Delay compensation with accurate frequency adaptation.



(b) Delay compensation with approximated frequency adaptation.



(c) Fixed delay compensation.

Figure 3.10: High performance proposed implementations of PR controllers based on two integrators, including resonant poles correction (3.5) and with different delay compensation techniques.

In any case, in the same manner as the trigonometric terms related to resonant poles were simplified in section §3.3, it is also interesting to optimize the calculation of those in Fig. 3.10a. Nevertheless, the variation of the reference signal frequency is less critical for the delay compensation techniques than for the resonant peak locations. A small deviation in the resonant frequency leads to an important steady-state error, but slight errors in the actual phase margin with respect to its expected value are not so relevant. Large frequency deviations should occur in order to cause a substantial phase margin degradation. Therefore, the trigonometric expressions of Fig. 3.10a can be approximated by lower order Taylor series than (3.4).

It is possible to obtain a much more accurate simplification than (3.17) by using  $h\omega_{1n}T_s + \phi'_{hn}$  as center point instead of  $\phi'_h$ , where  $\phi'_{hn} = \phi'_o + \lambda h\omega_{1n}$  is the phase lead for the harmonic  $h$  of the nominal fundamental frequency  $\omega_{1n}$ . In this manner, if  $\omega_1$  deviates from  $\omega_{1n}$  a value  $\Delta\omega_1 = \omega_1 - \omega_{1n}$ , it can be assumed:

$$\cos(h\omega_1 T_s) \approx \cos(h\omega_{1n} T_s + \phi'_{hn}) - \Delta\omega_1 h(T_s + \lambda) \sin(h\omega_{1n} T_s + \phi'_{hn}). \quad (3.19)$$

Applying the same reasoning to the coefficient of the  $z^{-2}$  term in (3.16):

$$\cos(\phi'_h) \approx \cos(\phi'_{hn}) - \lambda h \Delta\omega_1 \sin(\phi'_{hn}). \quad (3.20)$$

By means of (3.19) and (3.20), Fig. 3.10a leads to the scheme shown in Fig. 3.10b, where

$$a_h = K_{I_h} \lambda h \sin(\phi'_{hn}) \quad (3.21)$$

$$b_h = K_{I_h} \cos(\phi'_{hn}) \quad (3.22)$$

$$c_h = K_{I_h} h(T_s + \lambda) \sin(h\omega_{1n} T_s + \phi'_{hn}) \quad (3.23)$$

$$d_h = K_{I_h} \cos(h\omega_{1n} T_s + \phi'_{hn}). \quad (3.24)$$

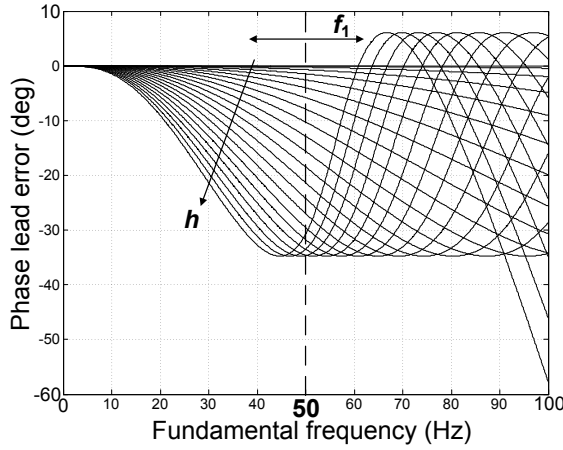
Each of these parameters does not depend on  $\Delta\omega_1$ , so they are constants that can be calculated off-line and implemented as simple gains.

Finally, if very low frequency deviations are expected, it may be convenient to implement Fig. 3.10c scheme, which does not adapt the delay compensation to  $\Delta\omega_1$ . In this manner, zeros are calculated off-line and implemented as fixed coefficients. It can be noted that Fig. 3.10c block diagram is equivalent to Fig. 3.10b with  $\Delta\omega_1 = 0$

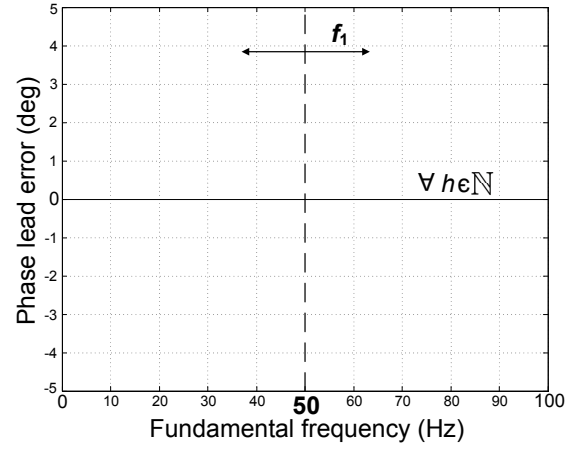
Figs. 3.11a, 3.11b, 3.11c and 3.11d represent the phase error  $\phi_h - \phi'_h$  provided by the schemes of respectively Figs. 3.3c, 3.10a, 3.10b and 3.10c. The different curves correspond to odd harmonic orders up to  $h = 45$ . It should be remarked that the open-loop phase just after the resonant frequency is approximately  $\phi_h - \phi'_h - \pi/2$  for most  $hf_1$  values ( $hf_1 > f_{90}$ ), so these figures are also representative of the phase margins that would be obtained by means of these implementations.

It can be appreciated in Fig. 3.11d that if only small variations from  $\omega_{1n}$  are expected (such as in most grid-connected converters), no adaptation of the delay compensation is necessary. This permits to avoid the complexity and computational resources that would be needed in order to adapt the controllers to  $\omega_1$  variations. However, for greater fluctuations of the reference frequency (such as in aeronautic APFs [70] and ac drives [65–67, 210, 214, 215]), it is recommended to recalculate  $\phi'_h$  accordingly, so stability and good tracking can be assured.

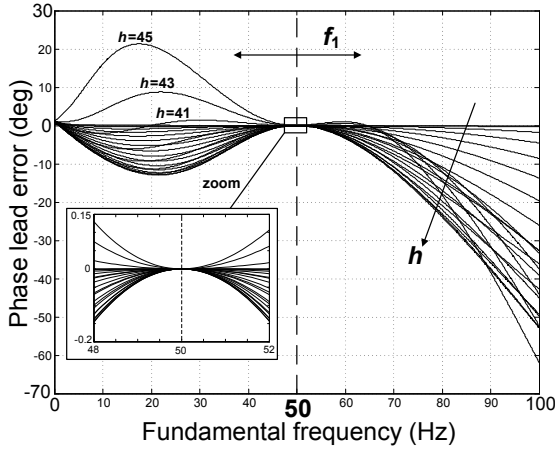
By comparison of Figs. 3.11c and 3.11d, it can be appreciated that the scheme proposed in Fig. 3.10b permits a great improvement of the delay compensation effectiveness with respect to non-adaptive implementations, so anomalous peaks are reduced and stability can be maintained for much greater frequency variations. Actually, from Fig. 3.11c, a resonant controller



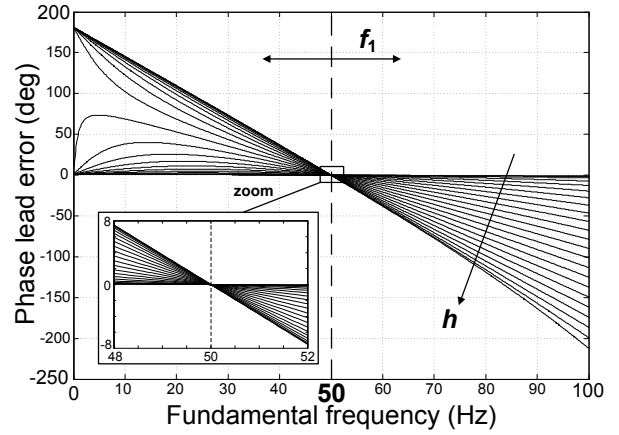
(a) Original Fig. 3.3c delay compensation technique.



(b) Block diagram proposed in Fig. 3.10a.



(c) Block diagram proposed in Fig. 3.10b.



(d) Block diagram proposed in Fig. 3.10c.

Figure 3.11: Leading angle error  $\phi_h - \phi'_h$  provided by different implementations in presence of  $f_1$  deviations, with  $\phi'_h$  according to (3.14), and for  $h \in \{1, 3, 5, \dots, 45\}$ . Parameters:  $L_F = 5$  mH,  $R_F = 0.5 \Omega$ ,  $f_{1n} = 50$  Hz and  $f_s = 10$  kHz.

implemented as in Fig. 3.10b and tuned at a nominal resonant frequency of 2250 Hz ( $h = 45$ ) is stable for a frequency range of about 4500 Hz.

### 3.4.2.2 Comparison of Leading Angle Accuracy of the Different Delay Compensation Techniques

Nevertheless, it may be preferable to implement Fig. 3.10a scheme instead of Fig. 3.10b one, if the anomalous peaks caused by the latter in such extreme frequency deviations (due to the large  $\phi_h - \phi'_h$  error) pose significant performance degradation in particular situations. That is the case, for instance, when the  $\omega_1$  estimation error may be large enough to cause substantial steady-state error.

It should be also remarked that, due to the explicit trigonometric terms, the error curves shown in Figs. 3.11c and 3.11a can be obtained with lower resources than those of Figs. 3.11b

and 3.11a. On the other hand, if Figs. 3.3c and 3.10a are compared, it can be stated that, even though Figs. 3.11b and 3.11a show very different results, their corresponding schemes are similar in terms of complexity and resource-consumption. Furthermore, it can be appreciated in Fig. 3.11a that the original Fig. 3.3c scheme is the only one in which zero phase lead error is not obtained even in nominal conditions ( $f_1 = f_{1n} = 50$  Hz), due to the fact that it uses a very low value as center point for the Taylor approximation.

Different values of  $f_s$ ,  $f_{1n}$ ,  $L_F$  and  $R_F$  ( $K_{P_T}$  and  $K_{I_h}$  do not affect) with respect to those employed in Fig. 3.11 lead to overall variations in the  $\phi_h - \phi'_h$  extreme values, but the shape of the curves is essentially the same. Therefore, these advantages of Figs. 3.10a and 3.10b proposed schemes can be applied to general conditions.

## 3.5 Experimental Results

### 3.5.1 Experimental Setup

A single-phase APF application has been chosen because it is very suitable for proving the controllers performance when tracking different and variable frequencies, and results can be extrapolated to other single-phase and three-phase applications. The experimental setup is the same as the one employed in chapter §2 (see Fig. 2.11 and Table 2.9). Only the tuning values of the resonant controllers are different.

The PR controllers have been tuned with  $K_{P_T} = 15$ , so that a phase margin of  $65.6^\circ$  is achieved for  $K_{P_T} G_{PL}(z)$ . An integral gain  $K_{I_h} = 2000$  has been selected to provide an adequate compromise between selective filtering and dynamic response [70, 71]. Identical gains have been chosen for each harmonic order to achieve similar bandwidth for all values of  $h$ . In this manner, as the selectivity becomes independent of the harmonic order, it will be possible to assess in the experiments the dependence of the resonance deviation on  $h$ , which is one of the main objectives of the experiments.

### 3.5.2 Improvement in Resonant Frequency Accuracy

The aim is to prove the improvement in resonant frequency accuracy provided by the proposed correction of poles, that is, the transformation posed in (3.5).

For this experiment, the load current is programmed as a square wave (high harmonic content) with rise and fall times of  $39 \mu s$ , which leads to the spectrum shown in Fig. 3.12.

Fig. 3.13 shows the results obtained when the proposed correction (3.5) is employed with different orders  $n_T$  for resonant controllers tuned at odd harmonics up to  $h = 45$ . The delay compensation technique proposed in Fig. 3.10a (which provides the greatest  $\phi_h$  accuracy) and  $\phi'_h$  according to proposed relation (3.14) are employed.

Table 3.3 shows the main lines of the code employed for each of the resonant controllers, which are implemented as S-functions written in C. Note that  $u$ ,  $y$ ,  $x$ ,  $w1$  and  $T$  represent the input of the controller, the output, the internal variables, the fundamental frequency and the inputs for the  $C_h$  (variable  $c$  in the code) correction as shown in Fig. 3.10a, respectively. The multiplications by the sampling period have been relocated to different points with respect to those shown in Fig. 3.10a, in order to optimize the number of operations. This example represents the  $n_T = 8$  case; for lower  $n_T$  values, line 66 should be modified accordingly.

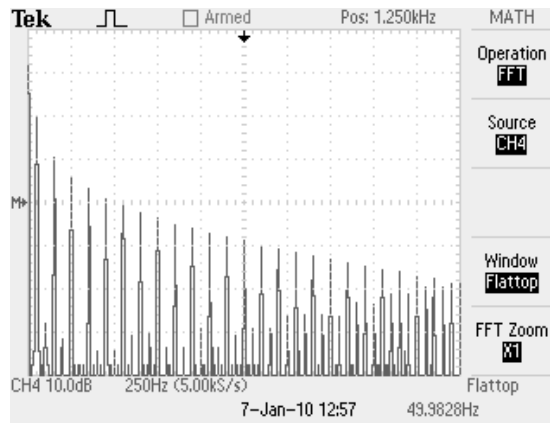
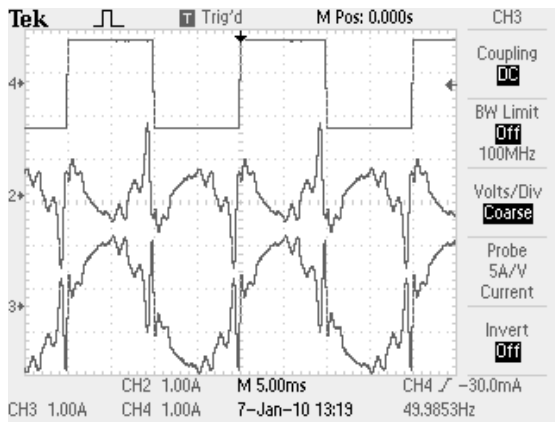


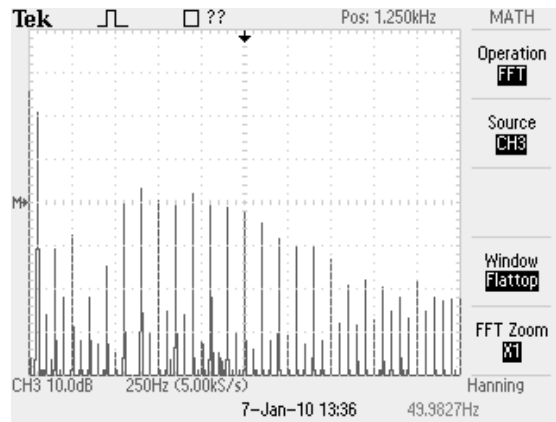
Figure 3.12: Spectrum of programmed load current  $i_L$ . THD= 42.3%.

TABLE 3.3  
IMPLEMENTATION CODE FOR THE TESTS OF SECTION §3.5.2

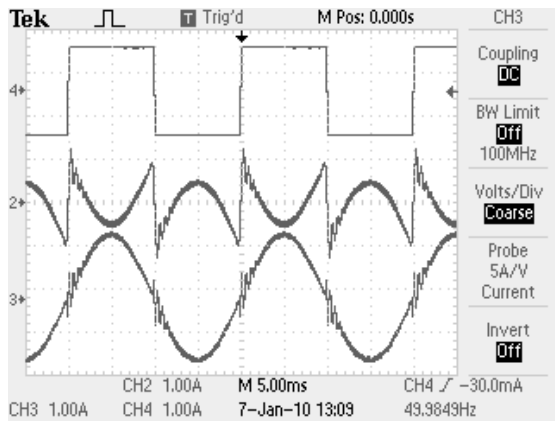
$\text{phi}=1.55082+0.00015073*\text{h}*\text{w1}[0];$	65
$\text{c}=\text{h}2*\text{T}[0]+\text{h}4*\text{T}[1]+\text{h}6*\text{T}[2]+\text{h}8*\text{T}[3];$	66
$\text{x}[2]=\text{x}[0]+\text{x}[3];$	67
$\text{x}[4]=\text{x}[2]+\text{x}[5];$	68
$\text{y}[0]=(\text{x}[2]-\text{x}[4])*T_s*\cos(\text{phi})+\text{x}[4]*T_s*\cos(\text{h}*\text{w1}[0]*T_s+\text{phi});$	69
$\text{x}[5]=\text{x}[4];$	70
$\text{x}[3]=\text{x}[2];$	71
$\text{x}[0]=\text{u}[0]-\text{c}*\text{x}[4];$	72



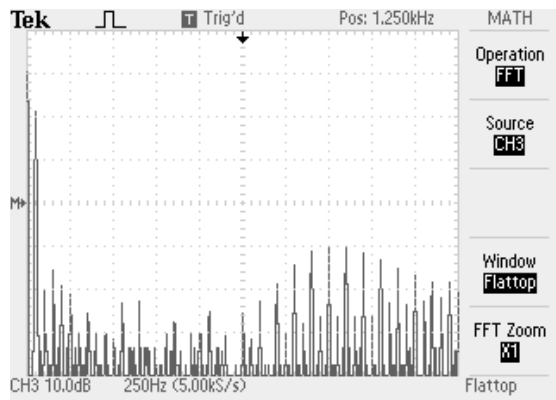
(a) Steady-state currents with  $n_T = 2$ , i.e., proposed correction (3.5) not applied.



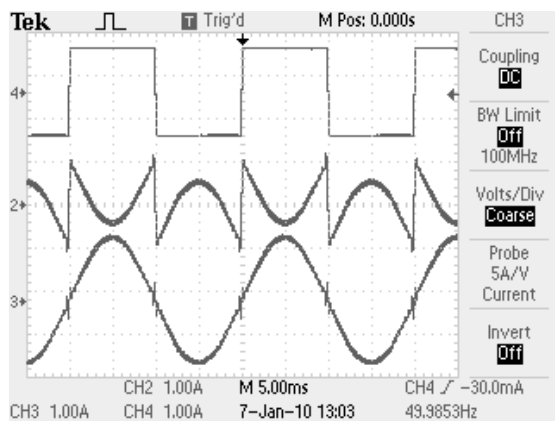
(b) Spectrum of  $i_S$  in Fig. 3.13a. THD= 26.16%.



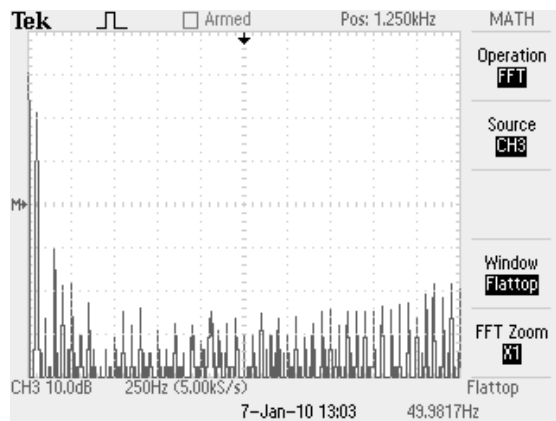
(c) Steady-state currents with  $n_T = 4$ .



(d) Spectrum of  $i_S$  in Fig. 3.13c. THD= 9.04%.

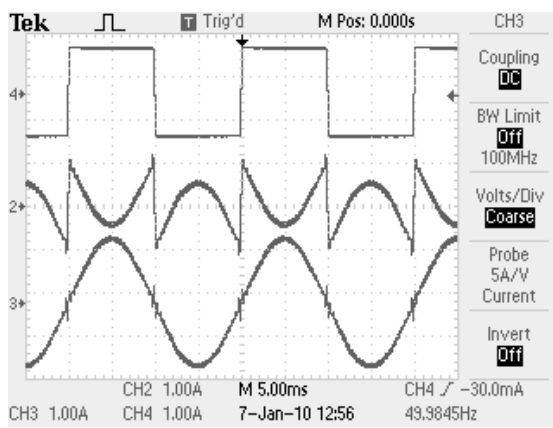


(e) Steady-state currents with  $n_T = 6$ .

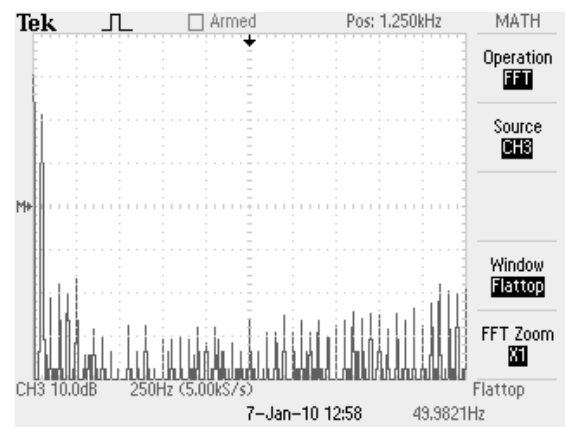


(f) Spectrum of  $i_S$  in Fig. 3.13e. THD= 5.67%.

Figure 3.13: Continued on next page.



(g) Steady-state currents with  $n_T = 8$ .



(h) Spectrum of  $i_S$  in Fig. 3.13g. THD= 5.56%.

Figure 3.13: Steady-state currents and spectra of source current  $i_S$  for different values of  $n_T$ , with  $f_1 = f_{1n} = 50$  Hz. Ch2 is  $i_F$ , Ch3 is  $i_S$  and Ch4 is  $i_L$ . This figure is continued from previous page.

TABLE 3.4  
CURRENT CONTROL EXECUTION TIMES

$n_T$	Time ( $\mu\text{s}$ )
2	25.8
4	29.8
6	32.1
8	34.7

Figs. 3.13a and 3.13b show tests of the original implementation without correction of resonant frequency ( $n_T = 2$ ). From Fig. 3.13, a great improvement is achieved by the proposed correction (3.5) in terms of resonant frequency accuracy, providing much better harmonic cancellation than that achieved by the original scheme. To increase  $n_T$  just from 2 to 4 permits to reduce the THD of  $i_S$  from 26.26% to 9.04%.

From Figs. 3.13c and 3.13d, a correction of fourth-order is accurate enough for frequencies up to approximately 1200 Hz; whereas  $n_T = 6$  is more suitable for higher frequencies, as shown in Figs. 3.13e and 3.13f. On the other hand,  $n_T = 8$  does not achieve a noticeable improvement over  $n_T = 6$ , as can be appreciated in Figs. 3.13g and 3.13h.

The accuracy provided by  $n_T$  greater than 6 may become more significant for higher resonant frequencies (or lower  $f_{sw}$ ). However, it should be taken into account that compensating beyond such high frequency values (or such frequencies with lower  $f_{sw}$ ) may be problematic due to appearance of side-band harmonics [70].

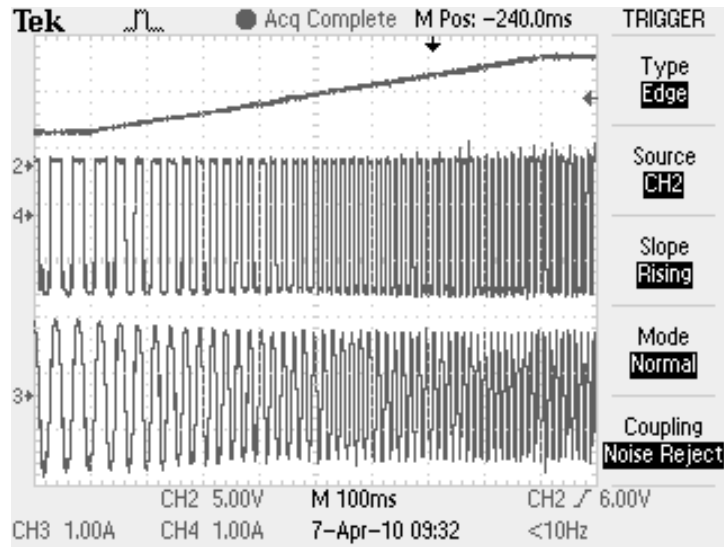
The average execution times of the current controller  $G_C(z)$ , with different values of  $n_T$ , are shown in Table 3.4. The computation of the  $\omega_1$  powers is also taken into account. Bearing in mind that there are 23 resonant controllers involved, it can be appreciated that the calculation time increase with small variations of  $n_T$  is not significant (specially if it is compared with the great improvement achieved regarding steady-state error). In any case, it seems recommendable to employ  $n_T = 4$  except for very high  $hf_1/f_s$  values, so almost perfect tracking is achieved and the computational burden that would be required by higher (and not necessary) values of  $n_T$  is avoided.

### 3.5.3 Improvement in Delay Compensation Accuracy

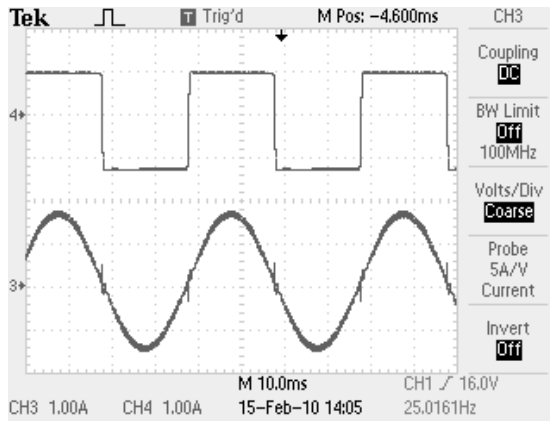
The improvement in leading angle accuracy achieved by the approaches proposed in section §3.4 should be established. This includes the proposed target leading angle expression (3.14) and the delay compensation techniques proposed in Figs. 3.10a, 3.10b and 3.10c.

#### 3.5.3.1 Nominal Conditions

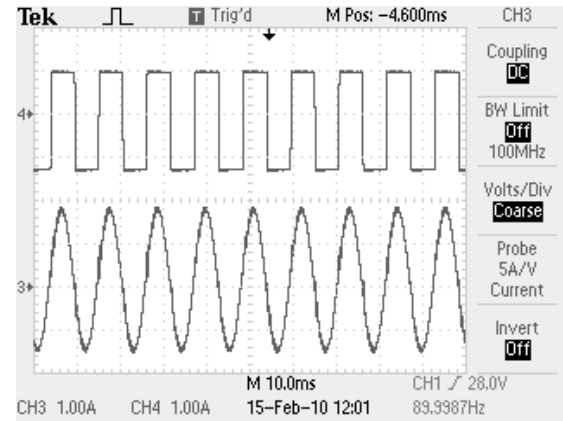
In section §3.5.2, Fig. 3.10a implementation and  $\phi'_h$  according to (3.14) have been employed. Consequently, the results shown in Fig. 3.13 do not only illustrate the influence of  $n_T$  on the resonant frequency accuracy, but also the capability of this delay compensation technique to achieve stability even while compensating very high frequencies. The same experiment has been performed with Figs. 3.10b and 3.10c schemes, and identical results have been obtained (the three implementations in Fig. 3.10 are equivalent in nominal conditions, i.e., when  $f_1 = f_{1n}$ ).



(a) Response to  $f_1$  ramp from 25 Hz to 90 Hz in 800 ms, with  $f_{1n} = 50$  Hz. The frequency scale of  $f_1$  (Ch2) is 10 Hz/V.



(b) Steady-state currents with  $f_1 = 25$  Hz and  $f_{1n} = 50$  Hz.



(c) Steady-state currents with  $f_1 = 90$  Hz and  $f_{1n} = 50$  Hz.

Figure 3.14: Test of frequency adaptation provided by Fig. 3.10b proposed scheme. Ch2 is  $f_1$ , Ch3 is  $i_s$  and Ch4 is  $i_L$ .

On the other hand, the original delay compensation technique based on two integrators (shown in Fig. 3.3c) with a two samples  $\phi'_h$  has been also tested for comparison in terms of stability. This controller led to instability when employed for harmonic orders up to  $h = 45$ . This fact proves that the stability margins provided by the proposed approaches are indeed larger, allowing for stable operation in more demanding conditions.

### 3.5.3.2 Frequency Deviations from Nominal

The stability provided by Figs. 3.10a, 3.10b and 3.10c schemes has been proved in nominal conditions. However, Fig. 3.10b approximates as a linear relation the  $\phi'_h$  variation with  $f_1$ . Thus, the effectiveness of Fig. 3.10b implementation in providing stable operation in presence of large frequency deviations from  $f_{1n}$  should be also tested.

In this experiment, the load current is programmed with the same waveform as in the previous test, and resonant controllers are also tuned at odd harmonic orders up to  $h = 45$ . In order to provide a good tracking of all frequencies,  $n_T = 8$  is chosen. The ac voltage source performs a  $f_1$  transient from 25 Hz to 90 Hz in 800 ms. Note that this means a 3375 Hz variation for the resonant controller tuned at  $h = 45$ , with a 4.22 kHz/s slope.

Obviously, so great deviations from nominal frequency are not usual in grid-connected converters, and so many resonant controllers are usually not required either. The main reason to test resonant controllers tuned at such high frequencies and so large frequency variations is to serve as an useful test for applications in which both requirements are common, such as aeronautic APFs, ac drives or torque ripple minimization in high speed permanent magnet drives. The objective is to confirm that, in those cases, the proposed Fig. 3.10b scheme avoids stability problems with resonant controllers tuned at high frequencies and large frequency variations.

Fig. 3.14a shows the response of the controller to the frequency transient. It can be observed that Fig. 3.10b proposed scheme provides stable operation within a very wide range of frequencies. Figs. 3.14b and 3.14c show the steady-state currents obtained with  $f_1 = 25$  Hz and  $f_1 = 90$  Hz ( $f_{1n} = 50$  Hz in both cases), respectively. It can be appreciated that at these frequencies the resonant controllers are also able to achieve a very high rejection of the harmonic components.

Figs. 3.10a and 3.10c implementations have been also tested in presence of the same frequency ramp. The former provided a similar behavior to 3.10b scheme, whereas the latter was unstable.

### 3.5.3.3 Summary

- The original delay compensation technique based on two discrete integrators is unstable when compensating harmonic orders up to  $h = 45$ .
- Fig. 3.10c scheme is only suitable when small deviations from nominal frequency occur.
- Both schemes in Figs. 3.10a and 3.10b do not present stability problems, even in presence of very demanding frequency fluctuations, in spite of the fact that the latter is much simpler than the former.

## 3.6 Conclusions

Enhanced digital implementations of resonant controllers implemented with two integrators are contributed in this chapter. These proposals provide a significant improvement over the previously existing schemes based on two discrete integrators, in terms of lower steady-state error and larger stability margins, while their low computational burden and good frequency adaptation are maintained.

The resonant frequency error is reduced by means of a correction of the input frequency. In this manner, the order of the Taylor series approximation is increased. It is proved that a fourth-order expansion is a very adequate solution for tracking frequencies such that the relation between resonant frequency and sampling frequency is not really large (until the former becomes ten times smaller than the latter, approximately).

On the other hand, the delay compensation inaccuracy is overcome by means of a correction of the zeros placement, and also by a linear expression to accurately calculate the target leading angle. These improvements lead to wider stability margins and less sensitivity to frequency deviations around the resonant frequencies.

Finally, experimental results obtained with a laboratory prototype have validated the main outcomes of the theoretical approach and the improvement provided by the proposed digital implementations of resonant controllers.

Contributions of this chapter have been published in the journal *IEEE Transactions on Power Electronics* [5] and presented at an international conference [16].



## Chapter 4

# Analysis and Design of Resonant Current Controllers for Voltage Source Converters by Means of Nyquist Diagrams and Sensitivity Function

*Abstract* — Mainly two types of resonant controllers are employed to obtain high performance in voltage source converters: PR and VPI. The analysis and design of PR controllers is usually performed by Bode diagrams and phase margin criterion. However, this approach presents some limitations when resonant frequencies are higher than the crossover frequency defined by the proportional gain. This occurs in selective harmonic control and applications with high reference frequency with respect to switching frequency, such as high-power converters with low switching frequency. In such cases, additional 0dB crossings (phase margins) appear, so the usual methods for simple systems are no longer valid. Additionally, VPI controllers always present multiple 0dB crossings in their frequency response. In this chapter, the proximity to instability of PR and VPI controllers is evaluated and optimized by means of Nyquist diagrams. A systematic method is proposed to obtain the highest stability and avoidance of closed-loop anomalous peaks, as well as an improved transient response: it is achieved by minimization of the inverse of the Nyquist trajectory distance to the critical point, that is, the sensitivity function. Finally, several experimental tests, including an active power filter operating at low switching frequency and compensating harmonics up to the Nyquist frequency, validate the theoretical approach.

### 4.1 Introduction

In proportional-resonant (PR) controllers, an usual approach is to employ Bode diagrams, and to study the stability by means of the phase margin at the crossover frequency  $f_c$  defined by the proportional gain [51, 65, 68, 219, 225, 230, 246, 276, 297, 298]. In many practical situations, this is enough to achieve satisfying results. However, this method has some limitations in more demanding scenarios. When resonant controllers are needed to track frequencies higher than  $f_c$ , two additional 0dB crossings (phase margins) appear around each of these frequencies. These extra stability margins may be much lower than the phase margin at  $f_c$ , and hence lead to instability of the system. Consequently, the value of this phase margin is no longer representative of the whole system stability.

This limitation gains particular relevance in applications in which the frequency of the reference signal (which should coincide with a resonant frequency of the control) is relatively high with respect to the switching frequency. This happens in high-power converters tracking harmonics while operating at low switching frequency, which is actually often required in order to reduce switching losses of semiconductor devices in high-power applications [313–317]. It is also the case of medium/low-power grid-connected active power filters (APFs) compensating high frequency components (up to 3000 Hz) [51, 56, 57, 120], as well as aeronautic APFs (fundamental frequency between 400 Hz and 800 Hz) [70, 277, 319] and medium voltage drives operating at very low switching frequency [314, 320]. Furthermore, even in cases in which resonant frequencies are not that high with respect to the switching frequency, it may be also desirable to set a low  $f_c$  in order to have very selective control; in that manner, the inverter rating can be reduced while tracking the most relevant harmonics, and greater robustness to parameter uncertainties is achieved [56, 57, 64, 230]. Therefore, it is of paramount interest to establish an effective and simple method to perform the analysis and design of PR controllers in these situations.

Concerning vector proportional-integral (VPI) controllers, indications to tune them in order to obtain certain closed-loop bandwidth around each resonant peak have been exposed in [56, 57]. However, a method to measure and optimize the proximity to instability of VPI controllers has not been proposed. Whereas PR controllers only present more than one 0 dB crossing when higher resonant frequencies than  $f_c$  are employed, the VPI controllers always exhibit this kind of complex frequency response. Thus, the tuning of VPI resonant controllers also requires to seek for a more adequate method than the usual approaches involving Bode plots and the phase margin criterion.

As an alternative to Bode diagrams, Nyquist plots are more suitable to analyze complex systems in which the magnitude and phase curves may cross respectively 0 dB or 180° several times [321]. Furthermore, the Nyquist diagrams permit the inspection of the sensitivity function, defined as the inverse of the distance between the Nyquist trajectory and the critical point  $(-1, 0j)$ . The maximum of the sensitivity function is known as sensitivity peak, which is a more compact and reliable indicator of stability than gain and phase margins [322]. In fact, it is proved in this chapter that the minimization of the sensitivity peak permits to achieve better results in resonant controllers rather than by maximizing the gain or phase margins, the latter of which is the most common approach [45, 51, 65, 68, 70, 225, 230, 246, 260, 276, 297, 298].

Nyquist diagrams have been employed for resonant current controllers with delay compensation in [51, 260]. In those works, the Nyquist plots are used to check the stability (the critical point is not encircled) when delay compensation is performed. However, as shown in this chapter, the Nyquist diagrams are also a powerful tool to measure and optimize the actual proximity to instability (not only to check if the system is stable or not). Consequently, it is also interesting to analyze the influence of each freedom degree on the plots, studying how they affect the sensitivity function, and to establish the optimum combinations.

A problem of resonant controllers regarding their closed-loop frequency response has been reported in [57]: due to non-compensated terms of the plant, undesired gain peaks may appear at frequencies close to the resonant frequencies. This fact may cause magnification of interharmonics found in the vicinity of integer harmonics (e.g., in variable speed drive applications). Moreover, it would also cause a significant amplification of integer harmonics, instead of unity gain (perfect tracking), when small frequency deviations occur. It is proved in this work that the presence of these closed-loop undesired resonances is inversely related to the distance of the

Nyquist trajectory to the critical point (sensitivity function). In this manner, by minimization of the sensitivity function, not only stability is improved, but these anomalous peaks are also avoided.

In this chapter, both PR and VPI controllers, aimed at current control in VSCs with plants that can be modeled as L filters, are analyzed by means of Nyquist diagrams. The effect of each freedom degree on the trajectories is studied, and their relation with the distance to the critical point (inverse of the sensitivity function) is established. It is proved that minimization of the sensitivity peak permits to achieve a greater performance and stability than maximizing the gain or phase margins. A systematic method is proposed to obtain the highest stability and avoidance of closed-loop anomalous peaks by means of minimization of the sensitivity function and its peak value. The proposed method is valid even when there are multiple 0 dB crossings. Finally, several experimental tests, including an APF operating at 2 kHz and compensating harmonics up to the Nyquist frequency, have been performed to validate the theoretical approach.

## 4.2 Analysis of Stability Margins by Means of Nyquist Diagrams

In section §3.2.1, the variable  $\phi_h$  is defined as the difference between the actual phase provided by a given resonant controller at frequencies infinitely close to  $h\omega_1$  and that provided by  $G_{PR_h}(s)$ . From that section,  $G_{PR_h}(s)$  satisfies  $\phi_h = 0$ ,  $G_{PR_h}^d(s)$  provides  $\phi_h = \phi_h'$  and  $G_{VPI_h}(s)$  introduces a phase lead  $\phi_h = \arctan(h\omega_1 L_F/R_F)$ . It can be also obtained from (2.2) that  $G_{VPI_h}^d(s)$  provides a phase lead

$$\phi_h = \phi_h' + \arctan(h\omega_1 L_F/R_F). \quad (4.1)$$

Each of these controllers should be discretized in order to be implemented in digital devices. Tustin with prewarping discretization is chosen, due to the fact that it provides very similar characteristics to the continuous resonant controllers (see chapter §2). In this manner, the analysis carried out in this chapter acquires a generic value.

The plant model  $G_{PL}(z)$  for current-controlled voltage source converters (VSCs) taking into account the computational delay, the pulsewidth modulation (PWM) and the L filter is given by (1.12).

The error rejection can be quantified by means of the sensitivity function as

$$S(z) = \frac{E(z)}{I^*(z)} = \frac{1}{1 + G_C(z) G_{PL}(z)} \quad (4.2)$$

where  $E(z)$  is the tracking error  $I^*(z) - I(z)$  [321, 323]. Actually,  $E(z)$  is the Z transform of the signal  $e$  shown in Fig. 1.5. The maximum value of  $|S(z)|$  is denoted as sensitivity peak  $1/\eta$ , which can be employed as a compact indicator of relative stability [322]. The function

$$D(z) = 1 + G_C(z) G_{PL}(z) \quad (4.3)$$

represents the distance of the open-loop transfer function  $G_C(z) G_{PL}(z)$  to the critical point  $(-1, 0j)$  at each frequency  $\omega$  ( $z = e^{j\omega T_s}$ ) in the Nyquist diagram. It can be concluded from (4.2) and (4.3) that the steady-state error when tracking  $I^*(z)$  is proportional to the inverse of  $D(z)$ . This corresponds with the well-known fact that an infinite value of  $D(z)$  (infinite gain)

assures  $E(z) = 0$ . It should be also remarked that  $D(z)$  is bounded below by  $\eta$  in magnitude, that is,  $|D(z)| \geq \eta$ .

In simple systems where the open-loop frequency response is monotonically decreasing and it does not present abrupt changes, either gain or phase margins provide enough information about the stability. However, in complex systems with more complicated trajectories these indicators do not give a reliable stability measurement. Instead, the minimum distance  $\eta$  to the critical point can be employed to quantify the actual proximity to instability, regardless of the frequency response complexity and abrupt changes (such as those of resonant controllers) [322].

Resonant controllers define the behavior of the system within a very narrow band of frequencies [51, 58, 65, 203, 260, 276]. Consequently, the stability of the whole system can be studied by separated analysis of the Nyquist diagrams that correspond to each individual resonant controller included in  $G_C(z)$ .

### 4.2.1 Nyquist Diagrams of PR Controllers

Fig. 4.1 represents the Nyquist diagram of a generic  $G_{PR_h}^d(z)$  controller in combination with the plant and the total proportional gain (instead of just  $K_{P_h}$ ), that is, the Nyquist plot of  $[K_{P_T} + K_{I_h} R_{I_h}^d(z)] G_{PL}(z)$ . It should be noted that this also includes the particular case of  $R_{I_h}(z)$ , since  $R_{I_h}(z) = R_{I_h}^d(z)$  when  $\phi_h' = 0$ . The trajectory of the Nyquist plots is expressed as a function of  $G_{PL}(z)$  and the freedom degrees of the controller:  $K_{P_T}$ ,  $K_{I_h}$ ,  $\phi_h$  and  $h\omega_1$ .

The Nyquist plot of  $K_{P_T} G_{PL}(z)$  is also represented in Fig. 4.1, so the effect of  $R_{I_h}^d(z)$  addition can be easily assessed. The  $K_{P_T} G_{PL}(z)$  plot starts from the real axis at  $\omega = 0$  rad/s, and it turns  $360^\circ$  clockwise until  $\omega = \pi f_s$ . The gain rapidly decreases with  $\omega$ , according to the low-pass filter nature of  $G_{PL}(z)$ .

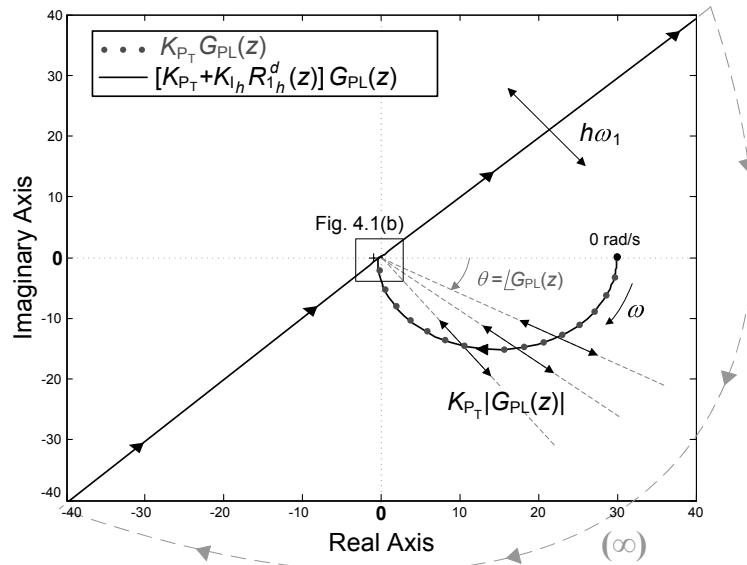
From Fig. 4.1, a phase value  $\theta = \angle G_{PL}(z)$  corresponds to each frequency  $\omega$ , and the distance to the origin (the gain at  $\omega$ ) is proportional to  $K_{P_T}$ . It can be appreciated that, as expected, the addition of  $R_{I_h}^d(z)$  only affects the plot within a very small range of frequencies around  $h\omega_1$ . The well-known fact that  $K_{I_h}$  is directly related to this bandwidth around the resonance [64, 225] is also corroborated.

At the resonant frequency  $h\omega_1$ , the gain abruptly rises to infinite and the phase shifts  $180^\circ$  clockwise, as depicted in Fig. 4.1. The angle between the asymptote at  $h\omega_1$  (limit from the left) and the real axis is given by

$$\gamma_h = \pi/2 + \phi_h + \angle G_{PL}(e^{jh\omega_1 T_s}). \quad (4.4)$$

According to Nyquist theory, the system is stable if and only if its trajectory does not encircle the critical point  $(-1, 0j)$  [51, 260, 280, 321, 322]. Various indicators of relative stability are employed for each  $R_{I_h}^d(z)$ : phase margin  $PM_h$ , gain margin  $GM_h$  and sensitivity peak  $1/\eta_h$  [322]. In this manner, the following conclusions concerning stability of PR controllers can be extracted from inspection of the Nyquist diagrams.

- $K_{P_T}$  establishes the crossover frequency  $\omega_c$ , the phase margin  $PM_P$ , the gain margin  $GM_P$  and the sensitivity peak  $1/\eta_P$  of  $K_{P_T} G_{PL}(z)$ . Note that, for each indicator of stability, the subindex P refers to  $K_{P_T} G_{PL}(z)$  and the subindex  $h$  refers to the trajectory including  $R_{I_h}^d$ .



(a) Global view of the Nyquist diagram.

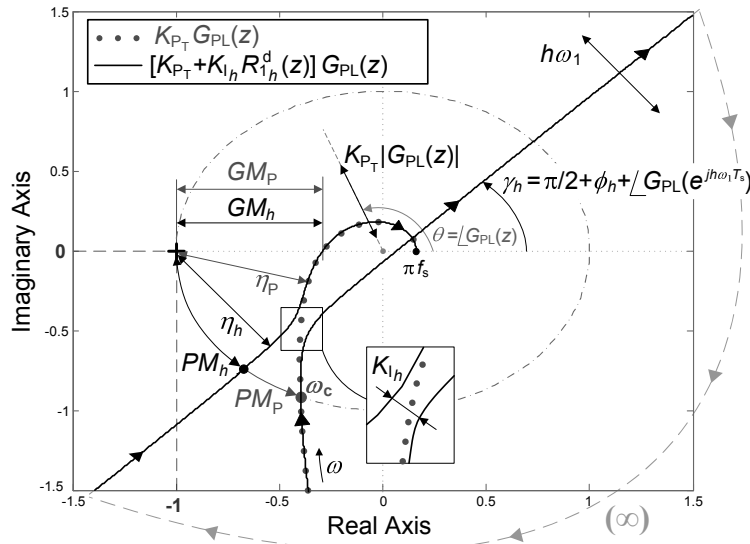

 (b) Zoom around the critical point of Fig. 4.1a. Note the influence of  $\phi_h$  on the stability margins.

Figure 4.1: Nyquist diagram of generic  $[K_{P_T} + K_{I_h} R_{1_h}^d(z)] G_{PL}(z)$ , for positive frequencies (the plots of negative frequencies are symmetrical of these). Note that  $R_{1_h}(z) = R_{1_h}^d(z)$  when  $\phi_h' = 0$ . The Nyquist plot of  $K_{P_T} G_{PL}(z)$  is also included for comparison. Parameters:  $L_F = 5$  mH,  $R_F = 0.5 \Omega$ ,  $f_s = 10$  kHz,  $hf_1 = 750$  Hz,  $\gamma_h \approx \pi/4$ ,  $K_{P_T} = 15$  and  $K_{I_h} = 2000$ .

- $PM_P > 0$  and a  $\gamma_h$  value such that the system becomes unstable are compatible conditions with each other. An example of this fact can be observed in the trajectory with  $K_{P_T} = 15$  in Fig. 4.2. Therefore,  $PM_P$  does not provide enough information to assess stability of PR controllers. This is an important fact, since  $PM_P$  is often considered to be the most important indicator of stability, even in PR implementations [65, 68, 219, 225, 230, 246, 276, 297].

- In general,  $PM_h \leq PM_P$ ,  $GM_h \leq GM_P$  and  $\eta_h \leq \eta_P$ . Consequently, the stability margins of  $K_{P_T} G_{PL}(z)$  should not be considered to be representative of  $G_C(z) G_{PL}(z)$ . The actual stability margins of  $G_C(z) G_{PL}(z)$  are bounded above by those of  $K_{P_T} G_{PL}(z)$ .
- An increase in  $K_{P_T}$  allows for faster transient response by means of a greater bandwidth [64], and high values of  $K_{P_T}$  imply less selective filtering (which is actually an interesting feature in many cases [51, 56–58, 64, 120, 203, 228, 230, 280]). Thus,  $K_{P_T}$  should be tuned to achieve a tradeoff between fast transient response, selective filtering and large upper bounds of stability margins. It should be also assured that  $\omega_c$  is not higher than approximately one decade below the switching frequency [71], so the commutation harmonics are effectively filtered.
- Unless very large values of  $K_{I_h}$  are employed, its effect on stability can be neglected. It should be tuned to provide an adequate compromise between selective filtering and dynamic response to transients in signals oscillating at  $h\omega_1$  [71, 280].
- It is often assumed that  $G_{PR_h}(z)$  ( $\phi'_h = 0$ ) is unstable if not included within the bandwidth set by  $K_{P_T}$  [47, 64, 70, 205, 246, 296]. Nevertheless, it can be inferred from Fig. 4.1 that for certain combinations of  $h\omega_1$  and  $K_{P_T}$ ,  $G_{PR_h}(z)$  may be stable even if  $h\omega_1 > \omega_c$ . For instance, in Fig. 4.2, it is possible to appreciate that  $G_{PR_h}(z)$  with  $hf_1 = 850$  Hz is stable from  $K_{P_T}$  values from approximately 20 on, in spite of the fact that  $h\omega_1 > \omega_c$  up to  $K_{P_T} = 25$ .
- $GM_h > 0$  is neither sufficient nor necessary condition for stability. Fig. 4.2 illustrates a situation ( $K_{P_T} = 15$ ) in which the system is unstable (the critical point is encircled) in spite of satisfying  $GM_h > 0$ . On the other hand, the trajectories in Fig. 4.2 that correspond to  $K_{P_T} > 25$  are stable, even though  $GM_h < 0$ . Additionally, for each resonant controller, there is always a positive and a negative phase margin. These facts corroborate that the general rules for stability analysis in simple systems, such as those usually employed for proportional-integral (PI) and PID controllers (in which  $GM_h > 0$  and  $PM_h > 0$  are both sufficient and necessary conditions for stability), should no longer be assumed to be suitable when dealing with resonant controllers.
- Analysis and design of resonant controllers by inspection of phase margins is a very common approach [45, 51, 65, 68, 70, 225, 230, 246, 260, 276, 298]. Nevertheless,  $\eta_h$  is a more compact and reliable indicator of the actual proximity to instability than  $PM_h$ , because it indicates the minimum distance to the critical point evaluated among all possible frequencies instead of only at the crossover frequency [322]. In this manner,  $\eta_h$  permits to quantify by means of just one parameter the robustness to both gain and phase uncertainties. For instance, Fig. 4.3 compares two cases in which  $PM_h$  is the same, but  $\eta_h$  permits to appreciate that one is actually much closer to instability ( $\eta_{17} = 0.24$ ) than the other one ( $\eta_{21} = 0.40$ ). Therefore,  $\eta_h$  should be the main parameter to study when analyzing stability of PR controllers.
- It can be concluded from the Nyquist plots that the  $\gamma_h$  angle (and thus the  $\phi'_h$  tuning) has a crucial influence on stability. It is often assumed that the  $\phi'_h$  value should be set to compensate the phase lag caused by the plant at  $h\omega_1$ , so that a good  $PM_h$  is achieved [70,

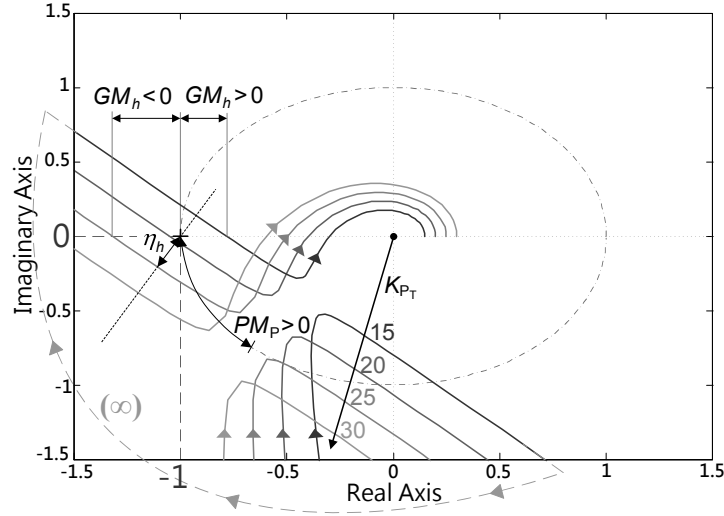


Figure 4.2: Nyquist diagrams of  $[K_{P_T} + G_{PR_h}(z)] G_{PL}(z)$  ( $\phi'_h = 0$ ) for different values of  $K_{P_T}$ . Note that  $GM_h > 0$  is neither necessary nor sufficient condition for stability,  $PM_P > 0$  is not a sufficient condition for stability and  $G_{PR_h}(z)$  ( $\phi'_h = 0$ ) may be stable even if  $h\omega_1 > \omega_c$ . Parameters:  $L_F = 5$  mH,  $R_F = 0.5$   $\Omega$ ,  $f_s = 10$  kHz,  $hf_1 = 850$  Hz and  $K_{I_h} = 2000$ .

260].<sup>1</sup> In that manner, it is usually intended to achieve  $\phi'_h = \angle G_{PL}(e^{jh\omega_1 T_s})$ , which implies  $\gamma_h = \pi/2$  (the asymptote at  $h\omega_1$  becomes vertical). However, this approach achieves a high  $PM_h$  at the expense of a non-optimized  $\eta_h$ . This can be appreciated, for instance, in the situation depicted in Fig. 4.4: the trajectory becomes closer to instability at certain frequencies (lower  $\eta_h$  than with other  $\phi'_h$  values). Therefore, it is preferable to seek for an alternative method to adjust  $\phi'_h$ , with  $\eta_h$  maximization being its main objective (this is further approached in section §4.4.1).

- In general, the transient response becomes more oscillatory (i.e., lower damping) if the trajectory is closer to the critical point [324]. Thus, to seek for large  $\eta_h$  values also serves to avoid very low damping associated to the resonant poles of those frequencies  $hf_1$  that in the  $K_{P_T} G_{PL}(z)$  plot are closer to  $(-1, 0j)$ .

In this manner, the optimum values for the freedom degrees of the whole  $G_C(z)$  controller will result from the combination of the best parameters for the Nyquist plot of each resonant controller  $G_{PR_h}^d(z)$ . It can be stated:  $G_C(z) G_{PL}(z)$  is stable if and only if  $[K_{P_T} + K_{I_h} R_{I_h}^d(z)] G_{PL}(z)$  is stable for all  $h$ .

The  $K_{P_T}$  value can be calculated so that a certain sensitivity peak  $1/\eta_P$  is obtained, by means of

$$K_{P_T} = F_1(\eta_P, T_s, R_F, L_F) \quad (4.5)$$

<sup>1</sup>It is often assumed that the leading angle should be equal to the system delay at the resonant frequency, so that the phase margin is maximized. Nevertheless, it has been proved in chapter §3 that the previous attempts (mainly based on compensating two samples [58, 64, 120, 260, 276]) were quite inaccurate with respect to the actual phase lag. An accurate expression is proposed in chapter §3 to assure  $\phi'_h = \angle G_{PL}(e^{jh\omega_1 T_s})$ . This permits to achieve a significant improvement over the two samples phase lead. However, as proved in this chapter, there are other possibilities that allow for even better performance and stability than trying to compensate the delay of the plant, specially when  $K_{P_T}$  is large.

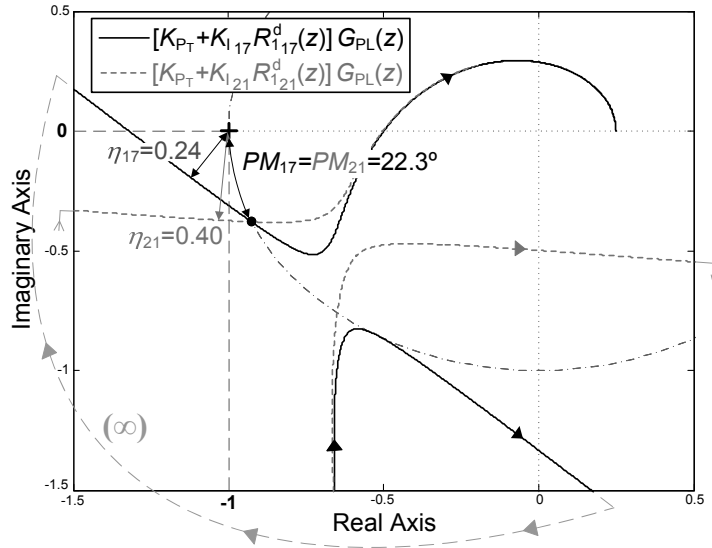


Figure 4.3: Examples of  $[K_{P_T} + K_{I_h} R_{1_h}^d(z)] G_{PL}(z)$  with two different  $R_{1_h}^d$ , which show that  $\eta_h$  provides more information about the actual proximity to instability than  $PM_h$ . Parameters:  $L_F = 5$  mH,  $R_F = 0.5$   $\Omega$ ,  $f_s = 10$  kHz,  $f_1 = 50$  Hz,  $\phi'_{17} = 0$  rad,  $\phi'_{21} = 0.8727$  rad,  $K_{P_T} = 25$  and  $K_{I_{17}} = K_{I_{21}} = 2000$ .

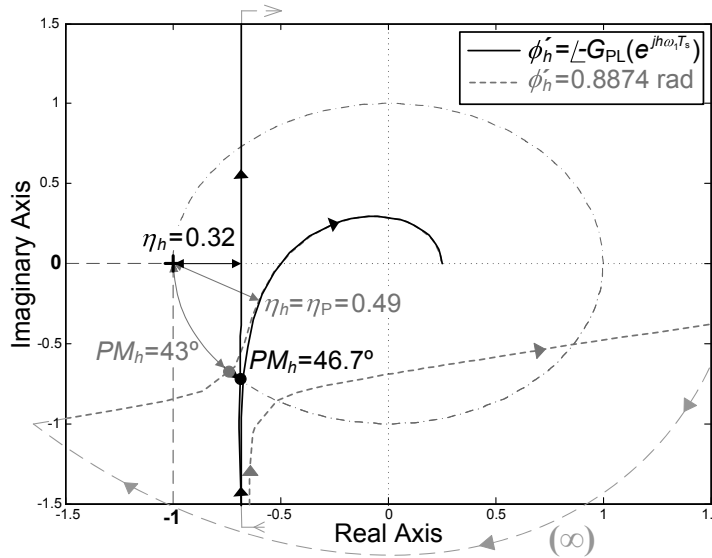


Figure 4.4: Examples of  $[K_{P_T} + K_{I_h} R_{1_h}^d(z)] G_{PL}(z)$  with two different  $\phi'_h$ , which show that  $\phi'_h = \angle G_{PL}(e^{jh\omega_1 T_s})$  increases  $PM_h$  at the expense of reducing  $\eta_h$  with respect to other  $\phi'_h$  values. However, it is preferable to have a larger  $\eta_h$  (the actual proximity to instability is reduced). Parameters:  $L_F = 5$  mH,  $R_F = 0.5$   $\Omega$ ,  $f_s = 10$  kHz,  $hf_1 = 750$  Hz,  $K_{P_T} = 25$  and  $K_{I_h} = 2000$ .

where  $F_1$  is a function developed in Appendix §C.1, and it corresponds to (C.9). Fig. 4.5 represents (4.5) as a function of  $\eta_P$  for several  $L_F$  and  $R_F$  combinations. This equation is quite relevant from a practical point of view. It gives a closed-form analytical expression to calculate the  $K_{P_T}$  value as a function of the minimum distance  $\eta_P$  to the critical point, which defines at the same time the system stability margin and the maximum steady-state error  $|E(z)| = |I^*(z)|/\eta_P$ .

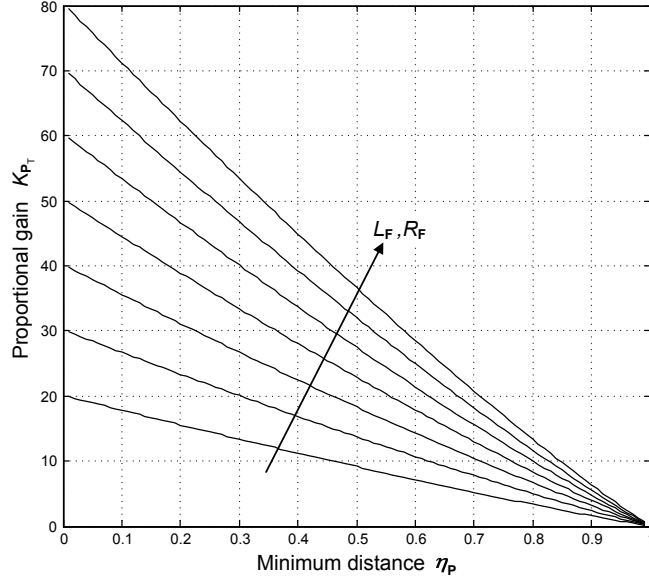


Figure 4.5:  $K_{P_T}$  tuning to obtain a certain  $\eta_p$ , according to (4.5). Parameters:  $f_s = 10$  kHz,  $R_F/L_F = 100 \Omega/\text{H}$ ,  $L_F \in \{2, 3, 4, \dots, 8\}$  mH and  $R_F \in \{0.2, 0.3, 0.4, \dots, 0.8\} \Omega$ .

In this manner, the laborious trial and error process is avoided.

Nevertheless, a certain target for  $\eta_p$  may lead to  $K_{P_T}$  values so high that the commutation harmonics would interfere with the current control. This can be avoided by assuring that the crossover frequency is lower than a decade below the switching frequency (i.e.,  $\omega_c < \pi f_s/5$ ), so the attenuation at  $f_s$  is at least 20 dB. Thus, the maximum acceptable  $K_{P_T}$  value is such that satisfies  $\omega_c = \pi f_s/5$ . This condition can be written as

$$\left| K_{P_T} G_{PL}(e^{j\pi/5}) \right| = 1. \quad (4.6)$$

Equation (B.2) in Appendix §C.1, which describes  $G_{PL}(z)$  as a function of a certain frequency  $\omega$ , can be substituted in (4.6), which results in

$$K_{P_T} = \frac{R_F}{(1 - \rho^{-1})\sqrt{2}} \sqrt{2 + 2\rho^{-2} - (1 + \sqrt{5})\rho^{-1}}. \quad (4.7)$$

Note that  $f_s$  has been assumed to be equal to the switching frequency. If this is not true, the  $T_s$  variable in (4.7) should be modified accordingly. It should be also noted that the maximum  $K_{P_T}$  should satisfy the initial hypothesis that the plant can be modeled as an L filter in the range of frequencies to be controlled.

In this manner, (4.5) gives the highest  $K_{P_T}$  to fulfill certain stability and steady-state error limits, and (4.7) gives the highest  $K_{P_T}$  (approximately) to effectively filter the commutation harmonics. The most restrictive of the two values should be the one implemented in the final control.

Once  $\eta_p$  is set by an adequate  $K_{P_T}$  value according to (4.5) and (4.7),  $\eta_h = \eta_p \forall h$  should be sought to assure the best stability margins. A method to achieve this by means of appropriate  $\phi'_h$  choices is approached in section §4.4.1.

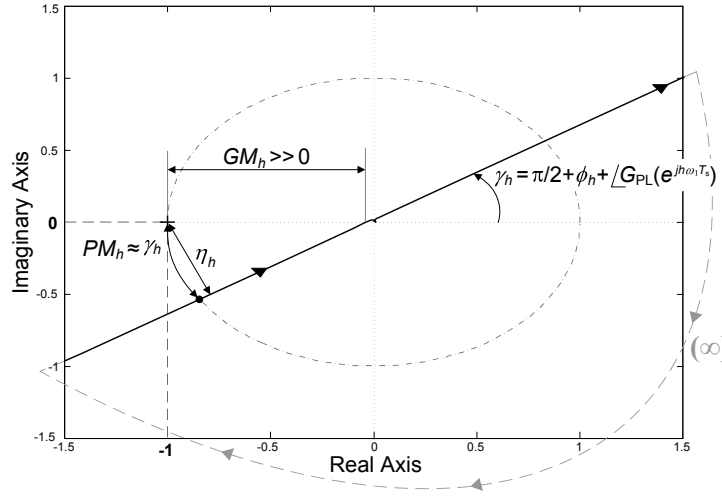


Figure 4.6: Nyquist diagram of generic  $G_{VPI_h}^d(z) G_{PL}(z)$ . Note that  $G_{VPI_h}(z) = G_{VPI_h}^d(z)$  when  $\phi'_h = 0$ . Parameters:  $L_F = 5$  mH,  $R_F = 0.5$   $\Omega$ ,  $f_s = 10$  kHz,  $hf_1 = 1050$  Hz and  $K_h = 50$ .

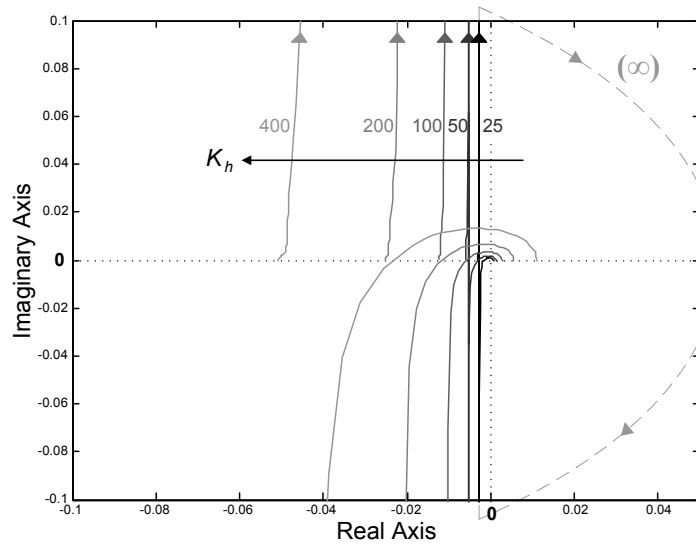
## 4.2.2 Nyquist Diagrams of VPI Controllers

Fig. 4.6 represents the Nyquist plot of a generic  $G_{VPI_h}^d(z)$  controller in combination with the plant, that is,  $G_{VPI_h}^d(z) G_{PL}(z)$ . This also includes the particular case of  $G_{VPI_h}(z)$ , in which  $\phi'_h = 0$  and  $\phi_h = \arctan(h\omega_1 L_F/R_F)$ .

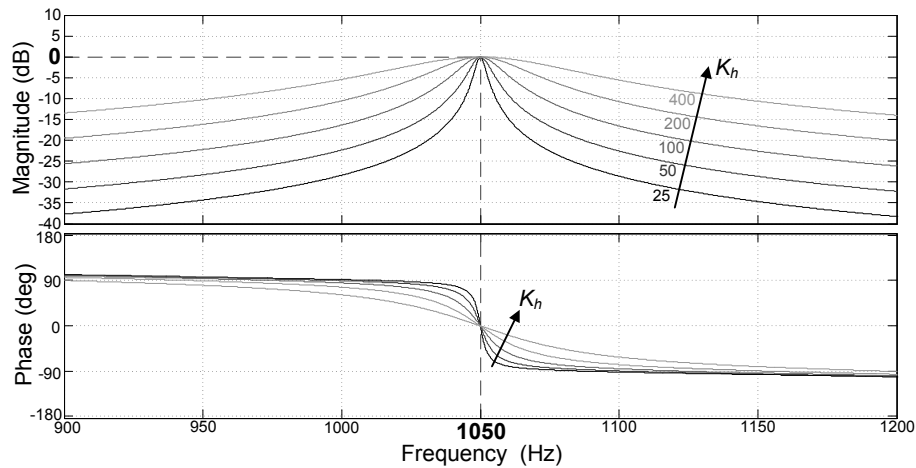
In the case of PR controllers, the trajectory of  $G_C(z) G_{PL}(z)$  is strongly influenced by  $G_{PL}(z)$  at all frequencies, both in magnitude and phase (previously shown in Fig. 4.1). On the contrary, it can be seen in Fig. 4.6 that in the case of VPI controllers the Nyquist trajectory presents only non-negligible magnitude around  $h\omega_1$ . Several direct consequences of this fact can be pointed out:  $GM_h \gg 0$ ,  $PM_h \approx \gamma_h$ , and  $\eta_h$  is much more related to  $PM_h$  than in PR controllers (to make one of them larger also implies to increase the other one). These aspects permit to improve the stability margins with respect to those of PR controllers, and they also facilitate  $G_C(z)$  design. In fact, it can be stated with much certainty that the control is stable if and only if  $\gamma_h > 0$  for all VPI controllers included in  $G_C(z)$ .

In a similar manner to the case of PR controllers, Fig. 4.6 illustrates that the angle  $\angle G_{PL}(z)$  is also reflected as a  $\gamma_h$  rotation of the asymptotes at resonant frequencies, depending on the  $\phi_h$  value. However, whereas  $G_{PR_h}(z)$  verifies  $\phi_h = \phi'_h = 0$ , according to (4.1) the phase lead provided by  $G_{VPI_h}(z)$  is higher:  $\phi_h = \arctan(h\omega_1 L_F/R_F) > \phi'_h = 0$ . This means that, when delay compensation is not included, the VPI controllers permit wider stability margins than PR ones, since  $G_{VPI_h}(z)$  manages to cancel the part of  $G_{PL}(z)$  delay that corresponds to the L filter. In any case, the phase lag in  $G_{PL}(z)$  caused by computation and modulation is not compensated by  $G_{VPI_h}(z)$ . Thus, instability occurs when computation and modulation cause a delay greater than  $\pi/2$  ( $\gamma_h < \pi$ ). This explains why  $G_{VPI_h}(z)$  becomes unstable at high frequencies, as reported in [56, 57], if delay compensation is not included.

Fig. 4.7a illustrates the effect of an increase in the  $K_h$  value when the rest of  $G_{VPI_h}^d(z)$  freedom degrees ( $\phi_h$  and  $h\omega_1$ ) are kept constant. For clarity,  $\gamma_h \approx \pi/2$  has been chosen. As the gain becomes greater, two effects appear simultaneously: the range of frequencies affected by the resonance widens (as stated in [56, 57]) and the asymptotes move slightly away from the origin. In any case, it can be appreciated in Fig. 4.7a that these variations scarcely affect the



(a) Zoom on the origin of the Nyquist diagrams. Note that the effect of  $K_h$  on the stability margins is negligible.



(b) Closed-loop Bode diagrams around  $hf_1$ . These  $K_h$  values are high enough to obtain large bandwidths.

Figure 4.7: Effect of  $K_h$  variation in  $G_{VPI_h}^d(z)$  controller. Parameters:  $L_F = 5 \text{ mH}$ ,  $R_F = 0.5 \Omega$ ,  $f_s = 10 \text{ kHz}$ ,  $hf_1 = 1050 \text{ Hz}$  and  $\gamma_h \approx \pi/2$ .

stability margins.

The closed-loop Bode plots around  $h\omega_1$  that correspond to each  $K_h$  in Fig. 4.7a are shown in Fig. 4.7b. It can be seen that these  $K_h$  values lead to unnecessary large bandwidths, which are not required in most applications. Therefore, it is corroborated that in normal conditions the asymptotes pass very close to the origin. Consequently, the assumptions  $GM_h \gg 0$ ,  $PM_h \approx \gamma_h$  and that  $\eta_h$  is very related to  $PM_h$ , are still valid for reasonable (not extremely high) values of  $K_h$ .

Concerning transient response, its time is defined by each  $K_h$ . The response speed to changes at  $h\omega_1$  components increases with the bandwidth of the resonant peak centered at that frequency, that is, as the  $K_h$  value becomes greater [56, 57]. This fact is in contradiction with the general assumption in simpler controllers (those with monotonically decreasing frequency response,

such as PI ones) which states that the phase margin should be tuned to achieve a trade-off between stability and transient response speed. In VPI controllers, once  $K_h$  is defined to achieve an adequate compromise between selective filtering and transient response [56, 57],  $\phi'_h$  should be adjusted so that  $PM_h \approx \pi/2$  (this is approached in section §4.4.2), and this does not imply a larger transient response than if  $\phi'_h$  was set to make  $PM_h$  lower.

### 4.3 Relation Between Closed-Loop Anomalous Peaks and the Sensitivity Function

Due to non-compensated terms of the plant, undesired gain peaks may appear in the closed-loop frequency response at frequencies close to  $h\omega_1$  [57]. This can cause a significant magnification of inter-harmonics found in the vicinity of integer harmonics, or amplification of integer harmonics when small frequency deviations occur. Furthermore, these undesired closed-loop resonances are also related to low damping in the resonant poles at those frequencies; transient response becomes more oscillatory as the anomalous peaks become greater [322]. In the following, a direct method to quantify the presence of closed-loop anomalous peaks by means of the sensitivity function is exposed. Then, the design process to minimize it in both PR and VPI controllers is established in section §4.4.

#### 4.3.1 Relation Between the Closed-Loop Transfer Function and the Sensitivity Function

As exposed in section §4.2, the inspection of the sensitivity function  $S(z) = 1/D(z)$  is quite straightforward by means of the Nyquist plots. Thus, in order to establish a systematic approach to analyze the presence of anomalous gain peaks, the relation between the closed-loop response and  $S(z)$  should be studied.

The closed-loop transfer function between the actual current  $I(z)$  and its reference  $I^*(z)$  is

$$C_L(z) = \frac{I(z)}{I^*(z)} = \frac{G_C(z) G_{PL}(z)}{1 + G_C(z) G_{PL}(z)}. \quad (4.8)$$

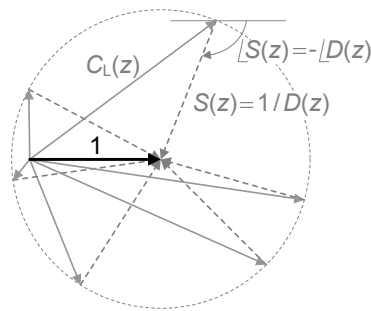
From (4.2),  $C_L(z)$  is related to  $S(z)$  according to

$$C_L(z) = 1 - S(z) = \frac{D(z) - 1}{D(z)}. \quad (4.9)$$

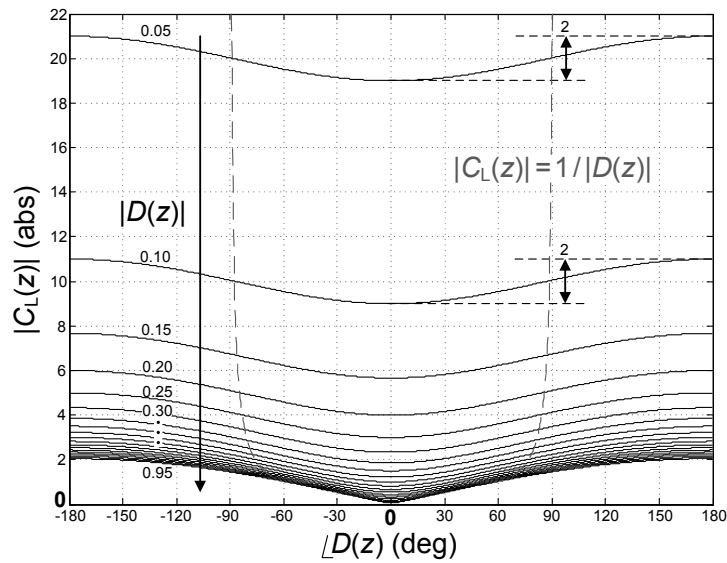
Fig. 4.8a represents the  $C_L(z)$  vectors that result from different  $S(z)$  if their magnitude  $|S(z)| = 1/|D(z)|$  is kept constant. It can be observed that, depending on  $\angle S(z)$ , both  $|C_L(z)|$  and  $\angle C_L(z)$  vary within a certain range. A high  $|S(z)|$  does not necessarily mean a large  $|C_L(z)|$ . Instead, it can be stated that a large  $|S(z)|$  implies a great steady-state error, and this error is distributed among  $|C_L(z)|$  and  $\angle C_L(z)$  depending on the phase of  $D(z)$ :

$$|C_L(z)| = \frac{1}{|D(z)|} \sqrt{|D(z)|^2 + 1 - 2|D(z)| \cos(\angle D(z))} \quad (4.10)$$

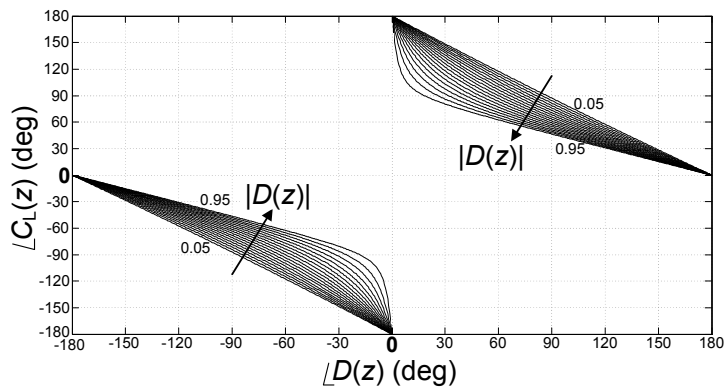
$$\angle C_L(z) = \arctan \left( \frac{\sin(\angle D(z))}{|D(z)| - \cos(\angle D(z))} \right). \quad (4.11)$$



(a) Representation of (4.9) by means of vectors. The modulus  $|S(z)| = 1/|D(z)|$  is kept constant.



(b) Variation of  $|C_L(z)|$  as a function of  $\angle D(z)$ , given by (4.10).  $|D(z)| \in \{0.05, 0.10, 0.15, \dots, 0.95\}$ . The extremes of each curve are  $1/|D(z)| \pm 1$ , and the average value is  $1/|D(z)|$ , which coincides with  $|C_L(z)|$  at the points marked with the dashed line.



(c) Variation of  $\angle C_L(z)$  as a function of  $\angle D(z)$ , given by (4.11).  $|D(z)| \in \{0.05, 0.10, 0.15, \dots, 0.95\}$ .

Figure 4.8: Relation between  $C_L(z)$  and  $S(z) = 1/D(z)$ , according to (4.9). Note that, for a given  $|S(z)|$ , the steady-state error is distributed among  $|C_L(z)|$  and  $\angle C_L(z)$  depending on the angle  $\angle S(z) = -\angle D(z)$ .

These equations have been obtained by substitution of

$$D(z) = |D(z)| \cos(\angle D(z)) + j|D(z)| \sin(\angle D(z)) \quad (4.12)$$

in (4.9).

Figs. 4.8b and 4.8c show  $|C_L(z)|$  and  $\angle C_L(z)$  as a function of  $\angle D(z)$ , according to (4.10) and (4.11), respectively. Cases with  $|D(z)| < 1$  are studied because it is a more critical situation.

From Fig. 4.8b, the lowest  $|C_L(z)|$  for a given  $|D(z)|$  results when  $\angle D(z) = 0$ , and its maximum occurs when  $\angle D(z) = \pm\pi$ . The difference between both extremes is always 2, independently of the  $D(z)$  magnitude:

$$|C_L(z)| = \underbrace{1/|D(z)|}_{\text{average value}} + \varepsilon_d(z), \quad \varepsilon_d(z) \in [-1, 1]. \quad (4.13)$$

In any case, when  $|D(z)|$  is small,  $|C_L(z)| \approx 1/|D(z)|$  can be assumed in order to have an intuitive estimation of the closed-loop gain.

It can be deduced from (4.10) that  $|C_L(z)|$  coincides with its average value  $1/|D(z)|$  when

$$\angle D(z) = \arccos\left(\frac{|D(z)|}{2}\right) \quad (4.14)$$

which is represented in Fig. 4.8b by a dashed line. For low values of  $|D(z)|$ , this occurs at approximately  $\angle D(z) = \pm\pi/2$ .

Concerning the extreme values of  $\angle C_L(z)$ , it can be observed in Fig. 4.8c that  $\angle C_L(z)$  is zero when  $\angle D(z) = \pm\pi$  and it is equal to  $\pm\pi$  when  $\angle D(z) = 0$ .

In general, for a given  $|D(z)|$ , a great  $\angle C_L(z)$  is preferable to a large  $|C_L(z)|$ , since the latter means an undesired amplification of the reference signal. Therefore, a  $\angle D(z)$  value close to zero, which permits to reduce the closed-loop magnitude, is usually more convenient.

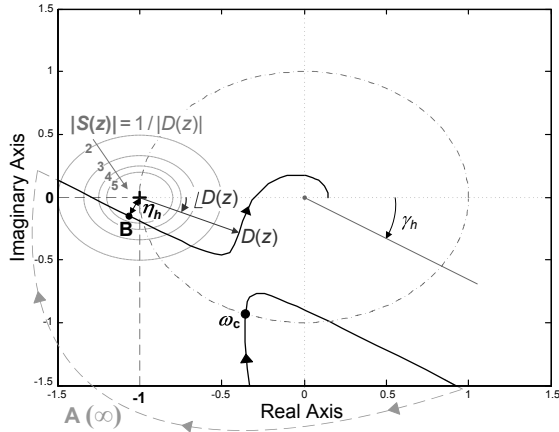
### 4.3.2 Anomalous Closed-Loop Peaks

Because of the abrupt change in magnitude that occurs around the resonant frequency, the Nyquist trajectory may pass very close to the critical point [low  $|D(z)|$ ]. This situation can be observed in the examples depicted in Figs. 4.9a and 4.9b, which correspond to  $G_{PR_h}(z)$  with  $hf_1 = 650$  Hz and  $G_{VPI_h}(z)$  with  $hf_1 = 1350$  Hz, respectively.

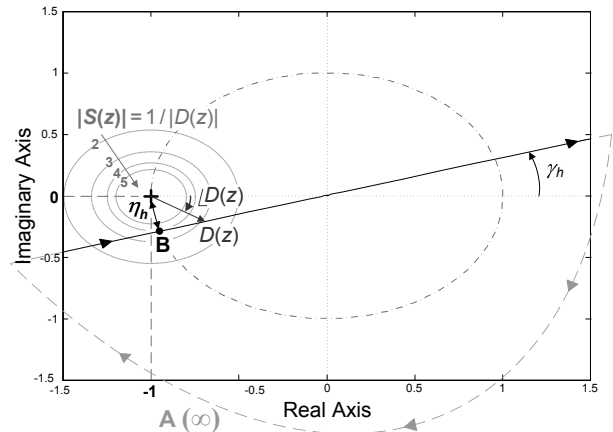
In Figs. 4.9a and 4.9b, point B indicates the minimum value of  $D(z)$ , and the corresponding frequency is defined as  $\omega_B$  [note that  $|D(e^{j\omega_B T_s})| = \eta_h$ ]. The resonant frequency  $h\omega_1$  is marked with point A [ideally at  $|D(z)| = \infty$ ]. In both figures, such low values of  $\eta_h$  are caused by the abrupt change in magnitude in the vicinity of the resonant frequency and the low  $\gamma_h$ .

Figs. 4.9c and 4.9d represent the  $S(z)$  Bode diagrams obtained with the same controllers as in Figs. 4.9a and 4.9b. It can be observed in Figs. 4.9c and 4.9d that, as expected from (4.2), the steady-state error increases as  $D(z)$  becomes lower. Actually, points A and B exhibit the smallest (ideally zero) and greatest [ $|S(e^{j\omega_B T_s})| = 1/\eta_h$ ] error in steady-state, respectively. This fact is quite compromising, because of the proximity between A and B. It should be also taken into account that a  $\Delta f_1$  frequency shift at fundamental frequency means a  $h\Delta f_1$  deviation at the harmonic  $h$ .

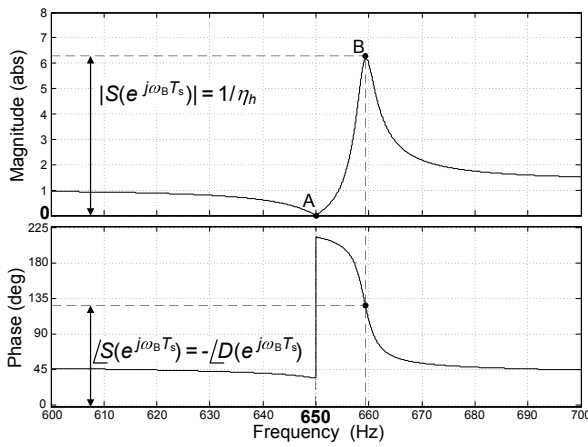
Finally, Figs. 4.9e and 4.9f represent the  $C_L(z)$  Bode diagrams obtained with the controllers of Figs. 4.9a and 4.9b. These diagrams are related to those of  $S(z)$  according to (4.10) and



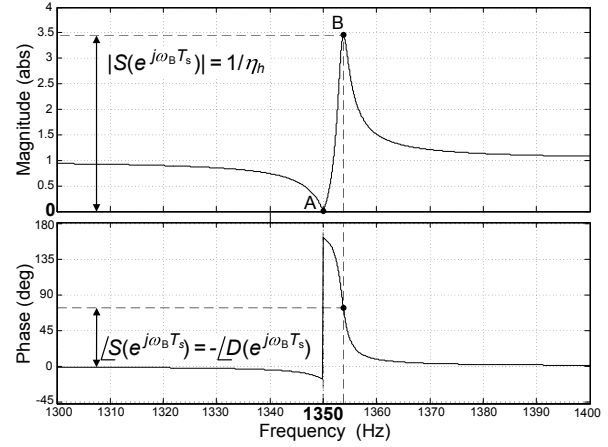
(a) Nyquist diagram of  $[K_{P_T} + K_{I_h} R_{I_h}^d(z)] G_{PL}(z)$ . Parameters:  $L_F = 5$  mH,  $R_F = 0.5 \Omega$ ,  $f_s = 10$  kHz,  $hf_1 = 650$  Hz,  $\phi'_h = 0$ ,  $K_{P_T} = 15$  and  $K_{I_h} = 2000$ .



(b) Nyquist diagram of  $G_{VPI_h}^d(z) G_{PL}(z)$ . Parameters:  $L_F = 5$  mH,  $R_F = 0.5 \Omega$ ,  $f_s = 10$  kHz,  $hf_1 = 1350$  Hz,  $\phi'_h = 0$  and  $K_h = 50$ .

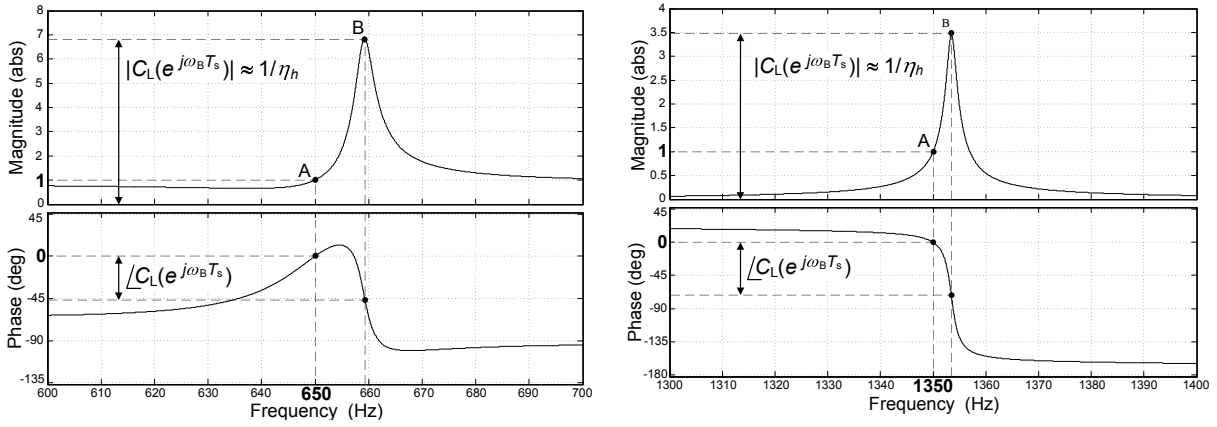


(c)  $S(z) = E(z)/I^*(z)$  Bode diagram using  $G_{PR_h}^d(z)$ . Note that  $|S(z)| = 1/|D(z)|$  and  $\angle S(z) = -\angle D(z)$ , being  $D(z)$  the distance to the critical point in Fig. 4.9a. Parameters:  $L_F = 5$  mH,  $R_F = 0.5 \Omega$ ,  $f_s = 10$  kHz,  $hf_1 = 650$  Hz,  $\phi'_h = 0$ ,  $K_{P_T} = 15$  and  $K_{I_h} = 2000$ .



(d)  $S(z) = E(z)/I^*(z)$  Bode diagram using  $G_{VPI_h}^d(z)$ . Note that  $|S(z)| = 1/|D(z)|$  and  $\angle S(z) = -\angle D(z)$ , being  $D(z)$  the distance to the critical point in Fig. 4.9b. Parameters:  $L_F = 5$  mH,  $R_F = 0.5 \Omega$ ,  $f_s = 10$  kHz,  $hf_1 = 1350$  Hz,  $\phi'_h = 0$  and  $K_h = 50$ .

Figure 4.9: Continued on next page.



(e)  $C_L(z) = I(z)/I^*(z)$  Bode diagram using  $G_{PR_h}^d(z)$ . Parameters:  $L_F = 5$  mH,  $R_F = 0.5 \Omega$ ,  $f_s = 10$  kHz,  $hf_1 = 650$  Hz,  $\phi'_h = 0$ ,  $K_{PT} = 15$  and  $K_{I_h} = 2000$ .

(f)  $C_L(z) = I(z)/I^*(z)$  Bode diagram using  $G_{VPI_h}^d(z)$ . Parameters:  $L_F = 5$  mH,  $R_F = 0.5 \Omega$ ,  $f_s = 10$  kHz,  $hf_1 = 1350$  Hz,  $\phi'_h = 0$  and  $K_h = 50$ .

Figure 4.9: Examples of closed-loop anomalous peaks. Point A corresponds with the resonant frequency  $hf_1$ , and B is the closest point to  $(-1, 0j)$ . Note the inverse relation between the distance  $D(z)$  to the critical point ( $\eta_h$  being its magnitude minimum value) and the steady-state error. This figure is continued from previous page.

(4.11). It can be appreciated that, due to the low values of  $\eta_h$ , the variation of  $|C_L(z)|$  around its average value can be neglected in (4.13), so  $|C_L(e^{j\omega_B T_s})| \approx 1/\eta_h$ .

From section §4.2.1, to select  $\phi_h = \angle G_{PL}(e^{j\omega_1 T_s})$  implies  $\gamma_h = \pi/2$ . Thus,  $\angle D(e^{j\omega_B T_s}) = 0$  would be satisfied. Consequently, from section §4.3.1, it can be stated that when the leading angle is chosen to exactly compensate the delay caused by the plant, the minimum closed-loop gain at  $\omega_B$  for a given  $\eta_h$  is achieved, that is,  $|C_L(e^{j\omega_B T_s})| = 1/\eta_h - 1$ . However, in PR controllers,  $|C_L(e^{j\omega_B T_s})|$  could be reduced even more if  $\eta_h$  was increased at the expense of making  $\angle D(e^{j\omega_B T_s})$  slightly higher. Furthermore, the proximity to instability would be also reduced (greater stability margin) and transient response would be improved (higher damping). This issue is approached in the method for sensitivity peak minimization proposed in section §4.4.

In summary:

- the magnitude  $|C_L(e^{j\omega_B T_s})|$  of each closed-loop anomalous gain peak varies within the extremes  $1/\eta_h \pm 1$ , rising from the minimum to the maximum as  $\angle D(e^{j\omega_B T_s})$  grows from zero.
- an appropriate value of  $\phi'_h$  should be sought in both PR and VPI controllers to maximize the value of  $D(z)$  [minimize  $S(z)$ ] around each resonant frequency  $h\omega_1$ . This is approached in the following section.

## 4.4 Minimization of Sensitivity Function

As proved in sections §4.2 and §4.3, both proximity to instability and closed-loop anomalous peaks can be reduced by minimization of the sensitivity function  $S(z)$  and its peak value  $1/\eta_h$ . In the following, a design method is proposed to obtain the optimum values of  $S(z)$  in PR and VPI controllers.

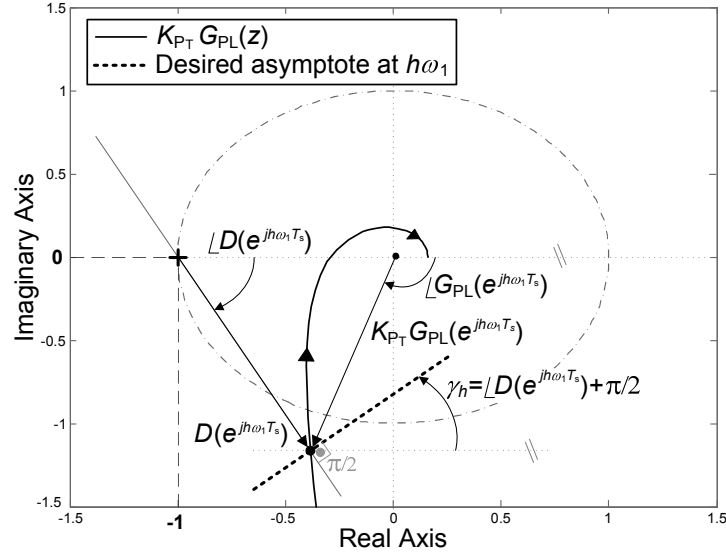


Figure 4.10: Optimum asymptote at  $h\omega_1$  in order to maximize  $D(z)$  (and consequently, minimize proximity to instability and steady-state error) at frequencies around  $h\omega_1$ , in  $G_{PR_h}^d(z)$  controllers. Parameters:  $L_F = 5$  mH,  $R_F = 0.5$   $\Omega$ ,  $f_s = 10$  kHz,  $hf_1 = 400$  Hz and  $K_{P_T} = 15$ .

#### 4.4.1 Sensitivity Minimization in PR Controllers

Once  $\eta_P$  is set by an adequate value of  $K_{P_T}$  according to (4.5) and (4.7), an optimum  $\phi'_h$  should be sought for each  $G_{PR_h}^d(z)$  controller so that  $S(z)$  is minimized at the vicinity of  $h\omega_1$ , and  $\eta_h = \eta_P \forall h$  is assured (from section §4.2.1,  $\eta_P$  is the maximum of each  $\eta_h$ ). This issue is approached in the following.

From (4.3),  $D(e^{jh\omega_1 T_s})$  is the vector that links the point of  $G_C(z) G_{PL}(z)$  at the resonant frequency  $h\omega_1$  with the critical point. As depicted in Fig. 4.10, in order to maximize  $D(z)$  at frequencies around  $h\omega_1$ , the asymptote at  $h\omega_1$  should be perpendicular to  $D(e^{jh\omega_1 T_s})$  [note that  $G_C(z) = K_{P_T}$  is assumed, because the  $G_{PR_h}^d(z)$  parameters still have to be defined]. This implies:

$$\gamma_h = \angle D(e^{jh\omega_1 T_s}) + \pi/2. \quad (4.15)$$

Finally, from (4.4) and (4.15), the leading angle should be

$$\phi'_h = -\angle G_{PL}(e^{jh\omega_1 T_s}) + \angle D(e^{jh\omega_1 T_s}). \quad (4.16)$$

The terms of (4.16) are expanded in Appendix C.2, so an equation of the form

$$\phi'_h = F_2(h\omega_1, T_s, R_F, L_F) \quad (4.17)$$

is finally obtained. By means of these values of  $\phi'_h$ , the best stability margins (the sensitivity peak  $1/\eta_h$  is minimized to its lower bound  $1/\eta_P$ ), avoidance of anomalous closed-loop peaks [lowest  $S(z)$  around each resonant frequency] and damping (related to the anomalous peaks reduction) can be achieved.

It can be also noted that the frequency  $\omega_\eta$  such that  $|D(e^{j\omega_\eta T_s})| = \eta_P$ , also verifies that  $\angle D(e^{j\omega_\eta T_s})$  is low, so, from section §4.3.1, this means that the closed-loop gain peak at  $\omega_\eta$  is close to its minimum among all its possible values for a given  $\eta_P$ :  $|C_L(e^{j\omega_\eta T_s})| \approx 1/\eta_P - 1$ .

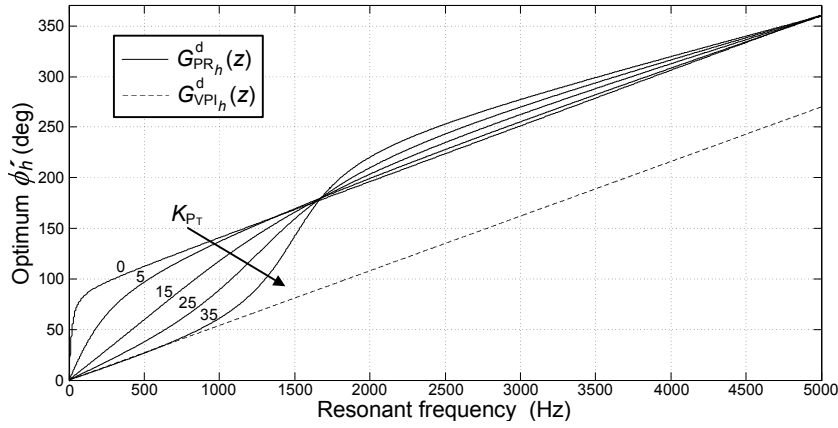


Figure 4.11: Optimum  $\phi'_h$  values in order to maximize  $D(z)$  around  $hf_1$ , as a function of  $hf_1$  and  $K_{P_T}$ . This implies that the best stability margins and avoidance of anomalous closed-loop peaks [lowest  $S(z)$  around  $hf_1$ ] are achieved. Parameters:  $L_F = 5$  mH,  $R_F = 0.5 \Omega$  and  $f_s = 10$  kHz.

Fig. 4.11 shows (4.16) as a function of  $hf_1$ . When  $K_{P_T}$  becomes larger,  $\angle D(z)$  gains more weight with respect to  $\angle G_{PL}(z)$ . This means that if a low value of  $K_{P_T}$  is selected, to calculate the leading angle simply as  $\phi_h = \angle G_{PL}(e^{jh\omega_1 T_s})$  (as done in chapter §3) is still an adequate choice for obtaining an optimum  $\eta_h$ . However, for greater bandwidths, the effect of  $|K_{P_T} G_{PL}(z)|$  should be also taken into account in order to obtain the largest distance to the critical point.

If only small frequency deviations  $\Delta hf_1$  of  $I^*(z)$  are expected, the complexity of (4.17) is not a problem, because  $\phi'_h$  can be calculated off-line for the nominal resonant frequency. On the contrary, if large fluctuations of  $hf_1$  may occur, other options such as low order approximations or look-up tables seem to be good alternatives.

#### 4.4.2 Sensitivity Minimization in VPI Controllers

Because of the  $|G_{PL}(z)|$  cancellation provided by the VPI controller, it can be observed in Fig. 4.9b that the sensitivity peak  $1/\eta_h$  is directly related to  $\gamma_h$ . In this manner, the closed-loop anomalous peaks are minimized when  $\gamma_h = \pi/2$  (this also implies  $\eta_h \approx 1$ ). According to (4.1), (4.4) and the fact that the delay due to computation and modulation can be approximated by  $3/2$  samples [260, 280], the following is obtained:

$$\gamma_h = \pi/2 \Rightarrow \phi_h = -\angle G_{PL}(e^{jh\omega_1 T_s}) \Rightarrow \phi'_h = \frac{3}{2}h\omega_1 T_s. \quad (4.18)$$

This result is actually intermediate between the leading angles employed for the VPI controller in previous works: one and two sample phase leads, in [57] and chapter §2 of this thesis, respectively. Fig. 4.11 shows (4.18) as a function of  $hf_1$ . Because of the linearity of (4.18), it can be employed to obtain frequency adaptive resonant controllers without a significant resource-consumption.

It should be noted that, as expected, if  $K_{P_T} = 0$  is considered in PR controllers, the difference between the optimum  $\phi'_h$  curves of  $G_{PR_h}^d(z)$  and  $G_{VPI_h}^d(z)$  in Fig. 4.11 is equal to  $\arctan(h\omega_1 L_F/R_F)$ .

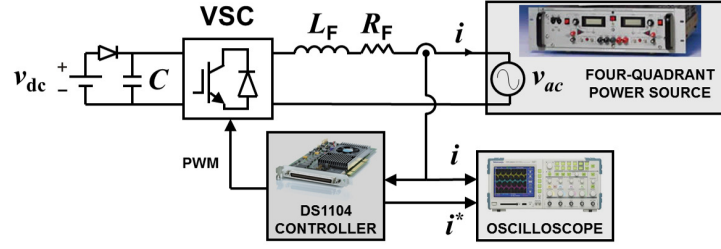


Figure 4.12: Experimental setup for the tests of section §4.5.1.

TABLE 4.1  
POWER CIRCUIT VALUES FOR TESTS OF SECTION §4.5.1

Parameter	Value
$v_{dc}^*$	150 V
$v_{ac}$ (RMS)	60 V
$C$	3.3 mF
$L_F$	4.3 mH
$R_F$	0.2 $\Omega$
$f_{sw} = f_s$	10 kHz

## 4.5 Experimental Results

### 4.5.1 Sensitivity Minimization by Means of Optimum Leading Angle

The aim of this experiment is to prove, through several tests, the advantage (in terms of stability and avoidance of anomalous gain peaks) provided by the approach proposed in section §4.4 to minimize the sensitivity function by means of  $\phi'_h$  according to (4.17) and (4.18).

Fig. 4.12 depicts the experimental lab prototype that has been employed for these tests. The VSC consists of four insulated-gate bipolar transistor (IGBT), and it is connected to the power source through the interfacing inductance  $L_F$ . Its equivalent series resistance is  $R_F$ . A four-quadrant power supply Kepco BOP 100-4D, which provides a voltage  $v_{ac}$ , is employed so that it is able to absorb power from the VSC. The dc-link voltage  $v_{dc}$  is kept constant by an HP 6035A power supply, so no fundamental current is required to maintain  $v_{dc}$ . Table 4.1 shows the values of the power circuit main parameters.

The control is implemented in a prototyping platform (dSpace DS1104), which includes a PowerPC (PPC) MPC8240 and a Texas Instruments TMS320F240 digital signal processor (DSP).

The current reference  $i^*$  is internally generated in the digital controller as a sinusoidal wave oscillating at a certain frequency with an arbitrary phase. This signal is converted to an analog voltage output and compared in an oscilloscope (appropriately scaled) with the actual current value  $i$ , which is sensed in the power circuit by means of a current sensor.

The digital control  $G_C(z)$  includes two resonant controllers: one tuned at the fundamental frequency  $f_1$  of the ac source voltage  $v_{ac}$ , and another one tuned at the resonant frequency  $hf_1$ . The former provides perfect cancellation of  $f_1$  components in  $i$  without the need of a  $v_{ac}$  feedforward signal, and the latter provides tracking of  $i^*$ . In each test, the frequency of  $i^*$  is modified around  $hf_1$  to check if there are frequencies close to  $hf_1$  such that the distance

to the critical point is low [that would be seen as a high gain in the closed-loop tracking, i.e.,  $|C_L(z)| \gg 1$ ].

#### 4.5.1.1 Sensitivity Minimization in PR Controllers

Fig. 4.13 shows the experimental tests obtained with  $G_{PR_h}^d(z)$  controllers tuned at  $hf_1 = 650$  Hz ( $h = 13$ ). The resonant controller used in Figs. 4.13a and 4.13b has been implemented with  $\phi'_h = 0$ . On the other hand,  $\phi'_h$  according to proposed expression (4.17) is employed in Figs. 4.13c and 4.13d (the remaining freedom degrees  $K_{PT} = 15$  and  $K_{I_h} = 2000$  are identical in both cases).

When the reference frequency coincides with the resonant frequency  $hf_1$ , it can be appreciated in Figs. 4.13a and 4.13c that perfect tracking is achieved in both cases [ $|D(e^{jh\omega_1 T_s})| \rightarrow \infty \Rightarrow |E(e^{jh\omega_1 T_s})| \approx 0$ ]. The zero order hold effect of the digital to analog converter in  $i^*$  can be also observed in the oscilloscope captures. Even though this effect may lead to think that there is a phase delay between  $i$  and  $i^*$ , it may be checked that  $i$  actually coincides with the  $i^*$  values at the sampling points. It can be also seen in Fig. 4.13 that two abrupt changes in  $i$  occur during each sampling period, due to the fact that unipolar PWM is employed to reduce the distortion. In any case, these aspects related to sampling will be appreciated more clearly in the oscilloscope captures of section §4.5.1.2, in which the time scale is larger.

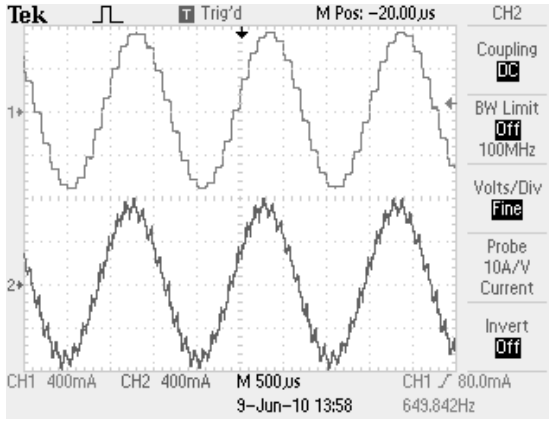
The reference frequency has been modified around the nominal value  $hf_1$  to seek for the presence of anomalous gain peaks. It has been found that when  $i^*$  oscillates at 656 Hz (which corresponds to a  $f_1$  deviation of just 0.46 Hz), the  $i$  amplitude is very much amplified with respect to that of  $i^*$ . This situation is shown in Fig. 4.13b (note the different scale in Ch2). This fact reveals that the system is close to instability (high sensitivity peak  $1/\eta_{13}$ ).

Analogously, different frequencies around  $hf_1$  were also tried for  $i^*$  in the case of the  $G_{PR_h}^d(z)$  controller with the proposed  $\phi'_h$ . Nevertheless, no appreciable increase over unity gain could be noticed in  $|C_L(z)|$ . Thus, the distance of the Nyquist trajectory to the critical point at frequencies close to  $hf_1$  is effectively maximized [low  $\eta_{13}$  and low  $S(z)$  around  $hf_1$ ] by (4.17).

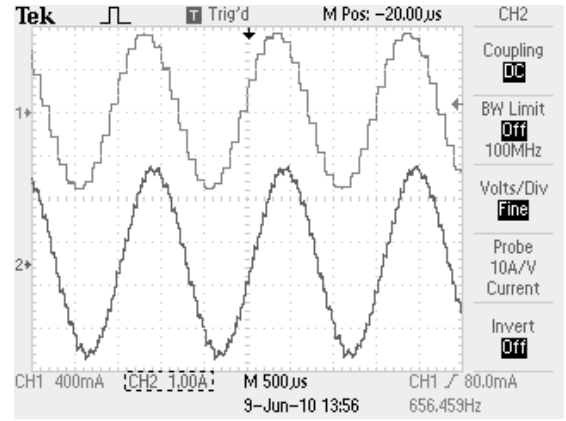
In the following experiment, shown in Fig. 4.14, a different case is considered: one  $G_{PR_h}^d(z)$  controller is implemented with  $\phi'_h = \angle G_{PL}(e^{jh\omega_1})$  (Figs. 4.14a and 4.14b) and another one with  $\phi'_h$  according to (4.17) (Figs. 4.14c and 4.14d). The remaining freedom degrees  $hf_1 = 750$  Hz,  $K_{PT} = 25$  and  $K_{I_h} = 2000$  are identical in both controllers, so the relevance of the  $\phi'_h$  tuning can be clearly assessed.

When the leading angle is adjusted to compensate the phase lag of  $G_{PL}(z)$  at  $hf_1 = 750$  Hz, the Nyquist trajectory becomes quite close to the critical point at approximately 744 Hz (low  $\eta_{15}$ ). This fact can be observed in the amplification of  $i^*$  shown in the  $i$  signal of Fig. 4.14b. It should be noted that, besides the undesired high gain at 744 Hz, this fact also reveals that the system may become easily unstable due to uncertainties or variations in  $G_{PL}(z)$  parameters.

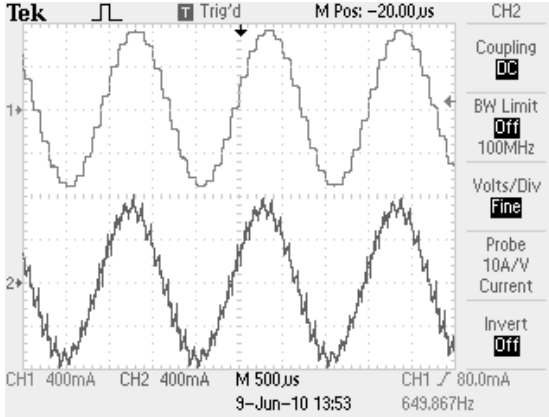
On the other hand, it has been checked that the proposed expression for the leading angle provides an effective avoidance of closed-loop anomalous gain peaks around the resonant frequency. This fact also assures a good stability margin  $1/\eta_{15}$ . Fig. 4.14d corroborates that (4.17) permits to assure  $|C_L(e^{j2\pi 744 T_s})| < 1$ . Therefore, it can be concluded that the proposal based on  $S(z)$  minimization provides a more satisfying performance and stability margins than the approaches aimed at maximizing the phase margin (i.e., compensating the phase lag of the plant), specially if high values of  $K_{PT}$  are employed. This conclusion is quite relevant, since tuning of resonant controllers by inspection of phase margins is a very widely employed approach



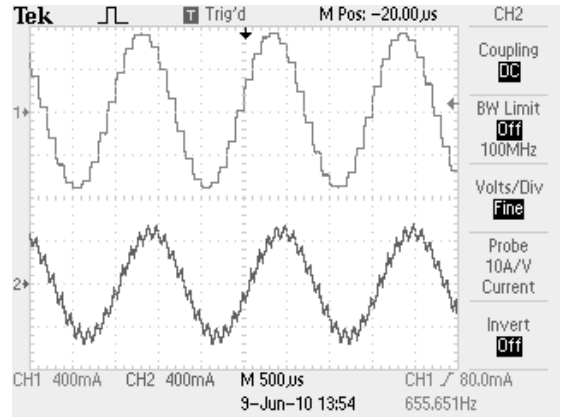
(a) Tracking provided by a  $G_{PR_h}^d(z)$  controller with  $\phi'_h = 0$  and tuned at  $hf_1 = 650$  Hz, when the reference frequency is 650 Hz.  $|C_L(z)| \approx 1$ .



(b) Tracking provided by a  $G_{PR_h}^d(z)$  controller with  $\phi'_h = 0$  and tuned at  $hf_1 = 650$  Hz, when the reference frequency is 656 Hz. Note the different scale in Ch2 with respect to the other figures, due to the anomalous gain peak:  $|C_L(z)| \gg 1$ .



(c) Tracking provided by a  $G_{PR_h}^d(z)$  controller with  $\phi'_h$  according to proposed expression (4.17) and tuned at  $hf_1 = 650$  Hz, when the reference frequency is 650 Hz.  $|C_L(z)| \approx 1$ .



(d) Tracking provided by a  $G_{PR_h}^d(z)$  controller with  $\phi'_h$  according to proposed expression (4.17) and tuned at  $hf_1 = 650$  Hz, when the reference frequency is 656 Hz.  $|C_L(z)| < 1$ .

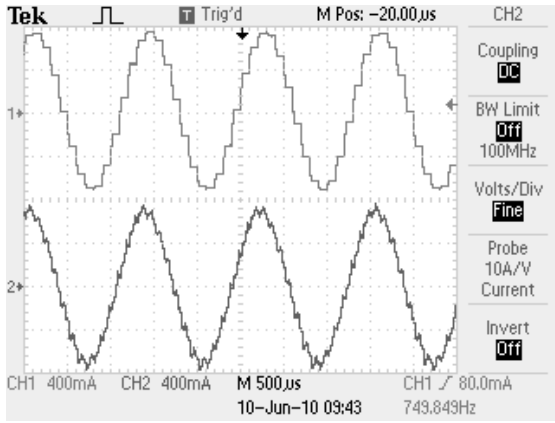
Figure 4.13: Experimental tests that compare the effect of a  $i^*$  deviation from  $f_1 = 50$  Hz to  $f_1 = 50.46$  Hz on a  $G_{PR_h}^d(z)$  controller tuned at  $h = 13$ , when  $\phi'_h = 0$  and  $\phi'_h$  according to proposed expression (4.17) are employed. Note that the latter avoids the anomalous gain peak. Ch1 is the reference  $i^*$  and Ch2 is the actual current  $i$ . In both cases,  $K_{PT} = 15$  and  $K_{I_h} = 2000$ .

[45, 51, 65, 68, 70, 225, 230, 246, 260, 276, 298].

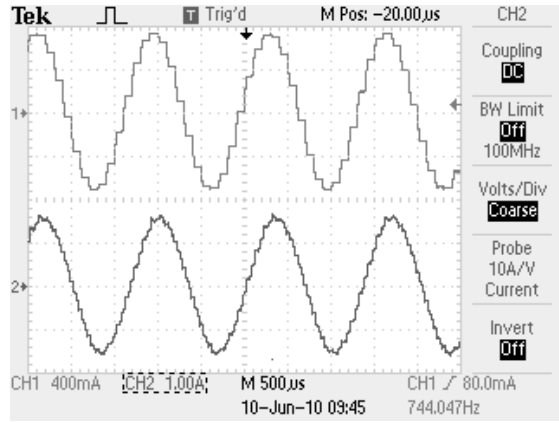
#### 4.5.1.2 Sensitivity Minimization in VPI controllers

Two  $G_{VPI_h}^d$  controllers are tested in Fig. 4.15 at  $hf_1 = 1300$  Hz: one with  $\phi'_h = 0$  and another one with  $\phi'_h$  according to proposed expression (4.18). In both cases,  $K_h = 50$ .

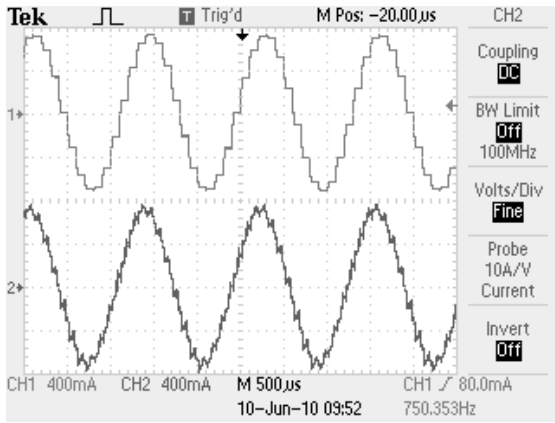
As expected, Figs. 4.15a and 4.15c corroborate that perfect tracking is achieved when the reference frequency coincides with  $hf_1$ . However, when small  $f_1$  deviations are tested, a significant difference can be appreciated between the results obtained with the different leading



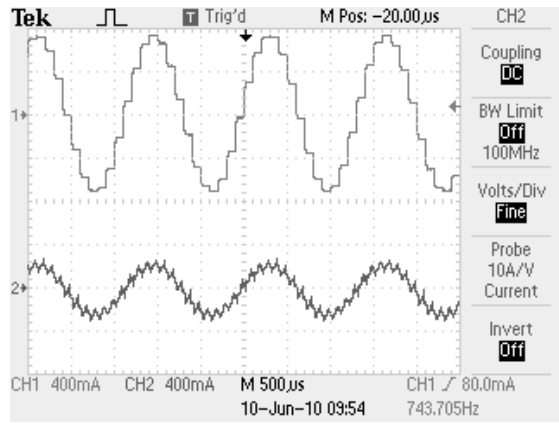
(a) Tracking provided by a  $G_{PR_h}^d(z)$  controller with  $\phi'_h = 2.2698 \text{ rad} \approx \angle G_{PL}(e^{jh\omega_1 T_s})$  and tuned at  $hf_1 = 750 \text{ Hz}$ , when the reference frequency is  $750 \text{ Hz}$ .  $|C_L(z)| \approx 1$ .



(b) Tracking provided by a  $G_{PR_h}^d(z)$  controller with  $\phi'_h = 2.2698 \text{ rad} \approx \angle G_{PL}(e^{jh\omega_1 T_s})$  and tuned at  $hf_1 = 750 \text{ Hz}$ , when the reference frequency is  $744 \text{ Hz}$ . Note the different scale in Ch2 with respect to the other figures, due to the anomalous gain peak:  $|C_L(z)| \gg 1$ .



(c) Tracking provided by a  $G_{PR_h}^d(z)$  controller with  $\phi'_h$  according to proposed expression (4.17) and tuned at  $hf_1 = 750 \text{ Hz}$ , when the reference frequency is  $750 \text{ Hz}$ .  $|C_L(z)| \approx 1$ .

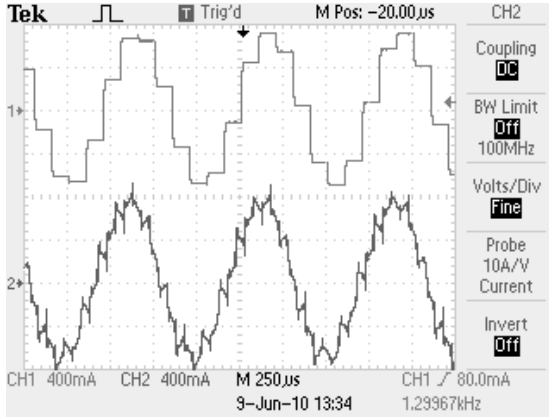


(d) Tracking provided by a  $G_{PR_h}^d(z)$  controller with  $\phi'_h$  according to proposed expression (4.17) and tuned at  $hf_1 = 750 \text{ Hz}$ , when the reference frequency is  $744 \text{ Hz}$ .  $|C_L(z)| < 1$ .

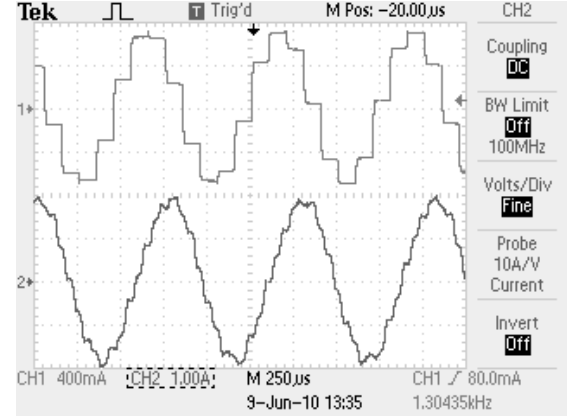
Figure 4.14: Experimental tests that compare the effect of a  $i^*$  deviation from  $f_1 = 50 \text{ Hz}$  to  $f_1 = 49.6 \text{ Hz}$  on a  $G_{PR_h}^d(z)$  controller tuned at  $h = 15$ , when  $\phi'_h = 2.2698 \text{ rad} \approx \angle G_{PL}(e^{jh\omega_1 T_s})$  and  $\phi'_h$  according to proposed expression (4.17) are employed. Note that the latter avoids the anomalous gain peak. Ch1 is the reference  $i^*$  and Ch2 is the actual current  $i$ . In both cases,  $K_{P_T} = 25$  and  $K_{I_h} = 2000$ .

angles. Fig. 4.15b shows a very high gain anomalous peak when the reference frequency is  $1303 \text{ Hz}$  and  $\phi'_h = 0$  (note the different scale in Ch2). On the contrary, it has been checked that the proposed  $\phi'_h$  assures that the closed-loop gain  $|C_L(z)|$  is not higher than unity at any frequency ( $\eta_{26} \approx 1$ ). Particularly, Fig. 4.15d proves that no amplification of  $i^*$  appears at  $1303 \text{ Hz}$  when  $\phi'_h$  is chosen to satisfy (4.18).

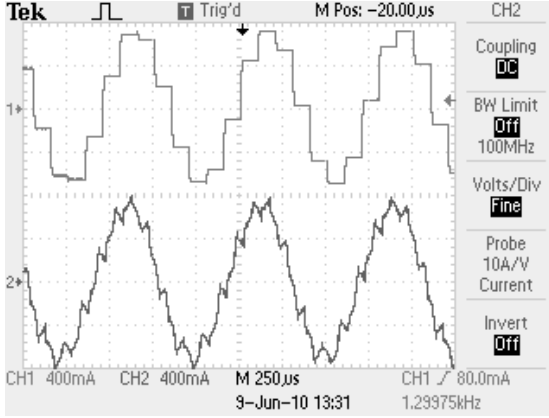
In this manner, the high stability margins and avoidance of closed-loop anomalous peaks provided by (4.18) have been proved.



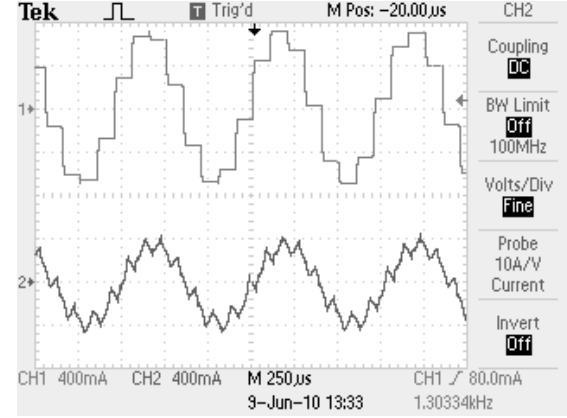
(a) Tracking provided by a  $G_{VPI_h}^d(z)$  controller with  $\phi'_h = 0$  and tuned at  $hf_1 = 1300\text{Hz}$ , when the reference frequency is  $1300\text{Hz}$ .  $|C_L(z)| \approx 1$ .



(b) Tracking provided by a  $G_{VPI_h}^d(z)$  controller with  $\phi'_h = 0$  and tuned at  $hf_1 = 1300\text{Hz}$ , when the reference frequency is  $1303\text{Hz}$ . Note the different scale in Ch2 with respect to the other figures, due to the anomalous gain peak:  $|C_L(z)| \gg 1$ .



(c) Tracking provided by a  $G_{VPI_h}^d(z)$  controller with  $\phi'_h$  according to proposed expression (4.18) and tuned at  $hf_1 = 1300\text{Hz}$ , when the reference frequency is  $1300\text{Hz}$ .  $|C_L(z)| \approx 1$ .



(d) Tracking provided by a  $G_{VPI_h}^d(z)$  controller with  $\phi'_h$  according to proposed expression (4.18) and tuned at  $hf_1 = 1300\text{Hz}$ , when the reference frequency is  $1303\text{Hz}$ .  $|C_L(z)| < 1$ .

Figure 4.15: Experimental tests that compare the effect of a  $i^*$  deviation from  $f_1 = 50\text{Hz}$  to  $f_1 = 50.12\text{Hz}$  on a  $G_{VPI_h}^d(z)$  controller tuned at  $h = 26$ , when  $\phi'_h = 0$  and  $\phi'_h$  according to proposed expression (4.17) are employed. Note that the latter avoids the anomalous gain peak. Ch1 is the reference  $i^*$  and Ch2 is the actual current  $i$ . In both cases,  $K_h = 50$ .

## 4.5.2 APF Operating at Low Switching Frequency

This experiment is carried out to prove the practical validity of the proposed systematic method to design resonant controllers. An APF application at low switching frequency is selected because it is a very demanding situation, in which most frequencies to be tracked are higher than the first crossover frequency  $f_c$  (set by  $K_{PT}$ ).

The constraint of setting a low switching frequency is actually a requirement in high-power converters, in which a small  $f_{sw}$  is needed in order to reduce switching losses of semiconductor devices [313–317].

TABLE 4.2  
POWER CIRCUIT VALUES FOR TESTS OF SECTION §4.5.2

Parameter	Value
$v_{dc}^*$	220 V
$v_S$ (RMS)	110 V
$C$	3.3 mF
$L_F$	26.6 mH
$R_F$	2.3 $\Omega$
$L_S$	50 $\mu$ H
$f_{sw} = f_s$	2 kHz

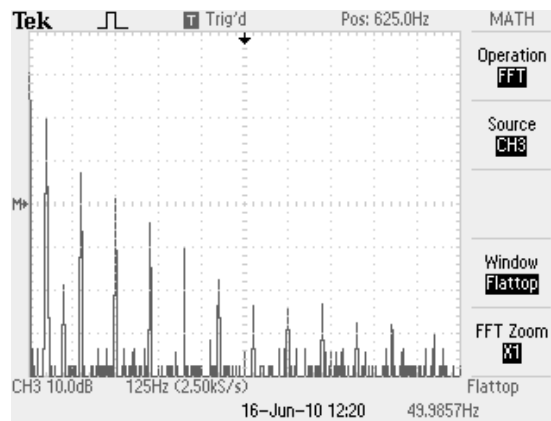


Figure 4.16: Spectrum of the current  $i_L$  demanded by the load, in the APF tests. THD= 28.4%.

The experimental lab prototype employed for these tests is the same as the one employed in chapter §2 (see Fig. 2.11). There are only some particular differences, which are exposed in the following. As shown in Table 4.2, some of the main parameters are different (in accordance with the lower switching frequency  $f_{sw}$ ). The tuning values of the resonant controllers are also different in this case: the proposed approach based on Nyquist diagrams and sensitivity function is employed.

The nonlinear load employed in this experiment (instead of the programmable load shown in Fig. 2.11) is an uncontrolled rectifier with very inductive load, which demands the highly distorted spectrum shown in Fig. 4.16. Its total harmonic distortion (THD) with respect to the fundamental component has been computed up to the harmonic 50, which resulted in 28.4%.

Odd harmonics up to 950 Hz, which almost reaches the Nyquist frequency  $f_s/2 = 1$  kHz, are compensated. That is, the current controller  $G_C(z)$  includes resonant controllers tuned at  $hf_1$ , with  $h \in \{1, 3, 5, 7, 9, \dots, 19\}$ .

The leading angles are adapted by means of a look-up table in the case of PR controllers and with a simple linear relation [according to (4.18)] in VPI controllers, as suggested in sections §4.4.1 and §4.4.2, respectively.

#### 4.5.2.1 APF with PR Controllers

The gain of each  $G_{PR_h}^d(z)$  controller has been set as  $K_{I_h} = 1000$  for all  $h$ , so a good trade-off between transient response and selective filtering is obtained.

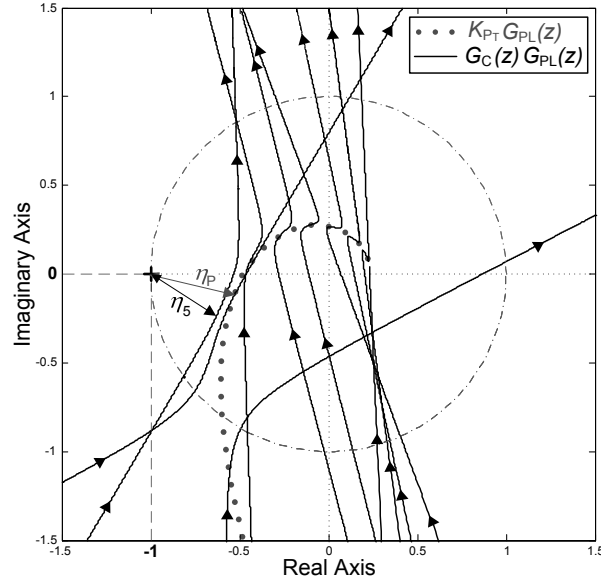


Figure 4.17: Nyquist diagram of APF current control  $G_C(z)G_{PL}(z)$  with PR controller. The Nyquist plot of  $K_{P_T}G_{PL}(z)$  is also included for comparison. Note that the proposed design method effectively maximizes  $|D(z)|$  around each resonant frequency.

A target value  $\eta_P = 0.5$  is selected in order to assure a wide stability margin and a maximum steady-state error  $|E(z)| = |I^*(z)|/\eta_P = 2|I^*(z)|$ . From section §4.4.1, due to the fact that in general the closest point of the Nyquist trajectory to  $(-1, 0j)$  satisfies that  $\angle D(z)$  is low, the highest closed-loop gain  $|C_L(z)|$  will be close to  $1/\eta_P - 1 = 1$ . A proportional gain  $K_{P_T} = 25$  is obtained in (4.5) to achieve  $\eta_P = 0.5$ .

With this  $K_{P_T}$  choice, the crossover frequency  $f_c$  of the  $K_{P_T}G_{PL}(z)$  system is placed at 150.4 Hz. In this manner,  $f_c$  is more than a decade below the switching frequency, so there is no need to further reduce the proportional gain in order to achieve a satisfying filtering of the commutation harmonics.

Fig. 4.17 represents the Nyquist diagram of  $G_C(z)G_{PL}(z)$ , with  $G_C(z)$  including all resonant controllers. It can be observed that the proposed design method effectively maximizes  $|D(z)|$  around each resonant frequency. The asymptote at each  $hf_1$  frequency becomes perpendicular to  $D(e^{jh\omega_1 T_s})$  applied to the  $K_{P_T}G_{PL}(z)$  system, as it was intended in section §4.4.1. Note that the discrepancy between  $\eta_P$  and the actual minimum distance to the critical point  $\eta_5$  can be neglected.

The steady-state currents obtained with the prototype are shown in Fig. 4.18. All odd harmonics up to  $h = 19$  are almost completely canceled by the PR current control, so the source current, instead of being equal to that of the load, is almost sinusoidal. This fact is corroborated by the  $i_S$  spectrum shown in Fig. 4.18b, which lacks the  $i_L$  harmonics displayed in Fig. 4.16.

The APF transient response when the harmonic compensation is enabled is shown in Fig. 4.19. Even though this test is quite demanding (very abrupt change in the current reference  $i_F^*$ ) with respect to the transients that usually take place in APFs, the control exhibits a good transient response. The most significant harmonic during this transient is the fifth order component. This finds its explanation in the fact that the Nyquist trajectory is very close to the critical point for frequencies around 250 Hz (see Fig. 4.17), because in general the damping decreases with  $D(z)$  [324]. This is an inherent limitation of the PR controller, which does not cancel the effect of

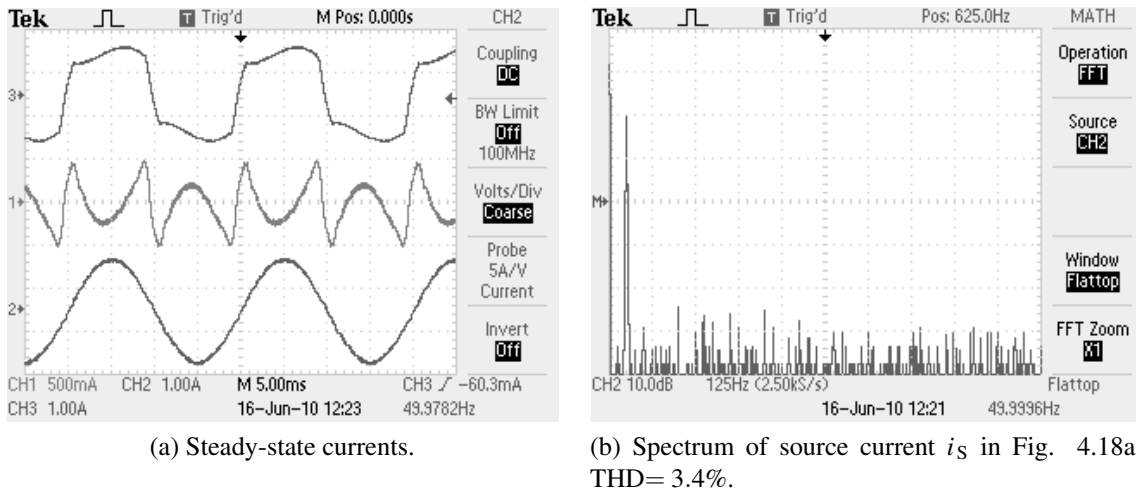


Figure 4.18: Experimental captures of APF operating at low switching frequency ( $f_{sw} = 2$  kHz) and with PR current controller. Ch1 is  $i_F$ , Ch2 is  $i_S$  and Ch3 is  $i_L$ .

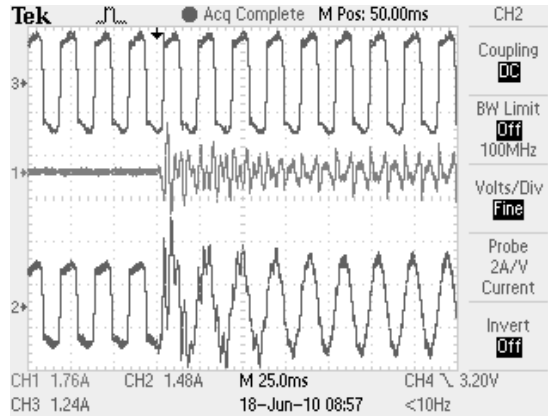


Figure 4.19: APF transient performance with PR controller when the harmonic compensation is enabled.

the plant trajectory. It should be also remarked that, for a fixed  $\eta_P$ , the selected  $\phi'_h$  according to (4.17) assures a large damping factor among its possible values. In any case, if desired, damping could be increased more by selecting a greater  $\eta_P$  than 0.5. This may be interesting, for instance, in case of fluctuating loads.

#### 4.5.2.2 APF with VPI controllers

The gains of each VPI controller have been set as  $K_h = 50$  in order to obtain an adequate compromise between selectiveness and transient response speed [56, 57].

Fig. 4.20 represents the Nyquist diagram of  $G_C(z)G_{PL}(z)$ . An effective maximization of  $|D(z)|$  is achieved at all frequencies by means of the proposed design method. The stability margins verify  $GM_h \gg 0$ ,  $PM_h \approx \pi/2$  and  $\eta_h \approx 1$  for all  $h$ . The worst case is that of the first resonant frequency ( $h = 1$ ):  $\eta_1 = 0.82$  (at 37.8 Hz), which is still quite close to unity.

Fig. 4.21a, which shows the steady-state performance of the APF, proves that the filtered  $i_S$  is almost sinusoidal. Its harmonic spectrum, shown in Fig. 4.21b, is as good as that achieved

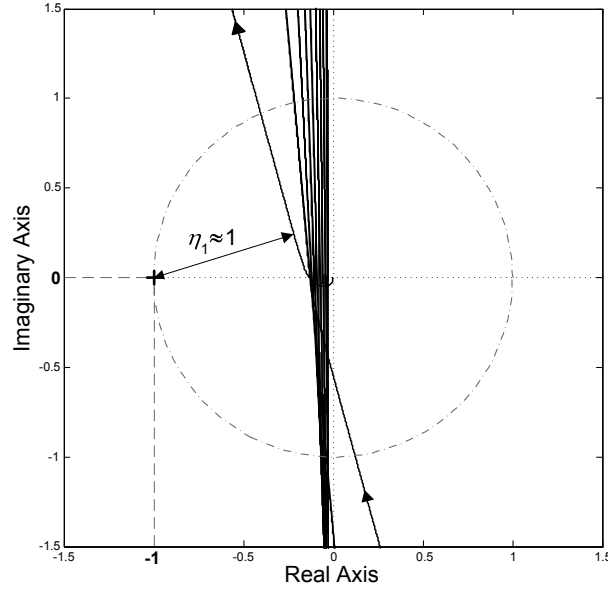
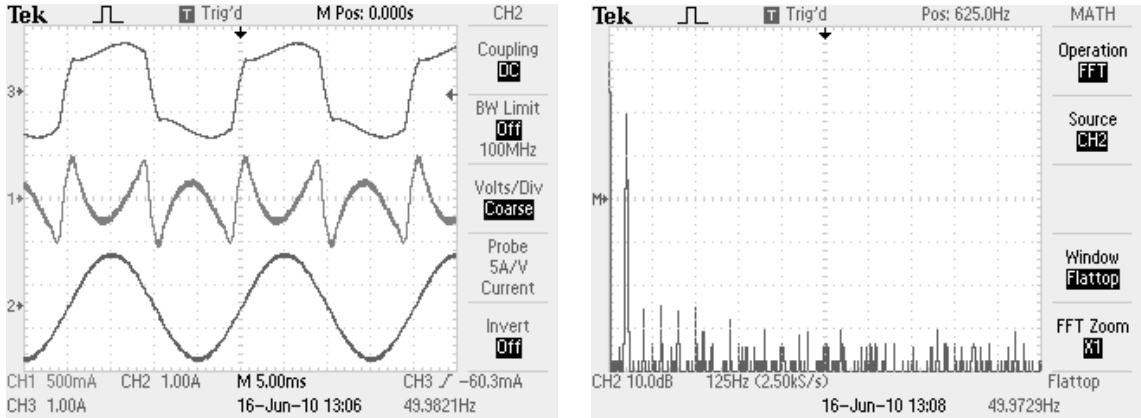


Figure 4.20: Nyquist diagram of APF current control  $G_C(z)G_{PL}(z)$  with VPI controllers. Note that the actual minimum distance to the critical point  $\eta_1 = 0.82$  is close to 1; the proposed design method effectively maximizes  $|D(z)|$  around each resonant frequency:  $GM_h \gg 0$ ,  $PM_h \approx \pi/2$  and  $\eta_h \approx 1 \forall h$ .



(a) Steady-state currents.

(b) Spectrum of source current  $i_s$  in Fig. 4.21a. THD= 3.5%.

Figure 4.21: Experimental captures of APF operating at low switching frequency ( $f_{sw} = 2$  kHz) and with VPI current controllers. Ch1 is  $i_F$ , Ch2 is  $i_S$  and Ch3 is  $i_L$ .

with the PR control: all the odd harmonics are almost completely canceled.

Fig. 4.22 proves that the VPI controllers provide a satisfying transient response. It is also interesting to note that, while in the PR controller some harmonics were more dominant during transients than others, in VPI controllers the amplitudes of each harmonic decay with a similar speed. This is due to the fact that, as shown in Fig. 4.20, the distance between the Nyquist plot and the critical point is very large for all frequencies. This difference between the transient response of PR controllers and VPI controllers is in agreement with the comparison presented in [25] between their equivalent controllers in synchronous reference frame: conventional PI

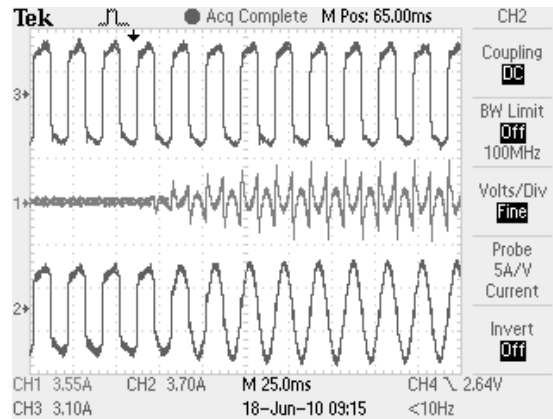


Figure 4.22: APF transient performance with VPI controllers when the harmonic compensation is enabled.

controllers without cross-coupling decoupling and complex vector PI controllers, respectively. In [25] it was concluded that in the former the transient response was very dependent on the value of the resonant frequency, but in the latter it was quite independent.

## 4.6 Conclusions

In this chapter, both PR and VPI resonant controllers including delay compensation, and aimed at current control in VSCs with plants that can be modeled as L filters, are analyzed by means of Nyquist diagrams. The effect of each freedom degree on the trajectories is studied, and their relation with the sensitivity function and its peak value is assessed. It is proved that the minimization of the sensitivity peak permits to achieve a better performance and stability in resonant controllers rather than by maximizing the gain or phase margins. A systematic method, supported by closed-form analytical expressions, is proposed to obtain the highest stability and avoidance of closed-loop anomalous peaks, as well as a significant improvement in transient response (greater damping): it is achieved by maximization of the Nyquist trajectory distance to the critical point (minimization of the sensitivity function). Finally, several experimental tests, including an active power filter operating at low switching frequency and compensating current harmonics up to the Nyquist frequency, validate the theoretical approach.

Contributions of this chapter have been published in the journal *IEEE Transactions on Industrial Electronics* [8].

# Chapter 5

## Conclusions and Future Research

### 5.1 Conclusions

This dissertation addresses digital resonant current controllers for voltage source converters. Its main contributions and conclusions are summarized below.

- An exhaustive comparison regarding the performance obtained by a wide variety of discretization techniques applied to resonant controllers has been presented. The optimum discrete-time implementation alternatives are assessed, in terms of their influence on the resonant peak location (capability of achieving zero steady-state error) and phase versus frequency response (stability). It is proved that some popular implementations, such as the ones based on two interconnected integrators, cause a large steady-state error unless the quotient between resonant frequency and sampling frequency is kept low enough. Discretization methods such as Tustin with prewarping and impulse invariant are demonstrated to be more advantageous due to their resonant frequency accuracy and positive influence on stability.
- Alternative implementations based on two interconnected integrators, that overcome the issues associated to the original ones, have been proposed. These enhanced schemes achieve higher performance by means of more accurate resonant peak locations and delay compensation, while maintaining the advantage on low computational burden and good frequency adaptation of the original ones.
- It is proved that to minimize the sensitivity peak permits to achieve a better performance and stability in resonant controllers than to maximize the gain or phase margins. The effect of each freedom degree on the Nyquist trajectories is studied, and their relation with the distance to the critical point (inverse of the sensitivity function) is established. A systematic method, supported by closed-form analytical expressions, is proposed to obtain the highest stability and avoidance of closed-loop anomalous peaks, as well as an improved transient response (greater damping): it is achieved by minimization of the sensitivity function and its peak value.

## 5.2 Publications

Research work included in the dissertation has been published in three JCR-indexed journal papers [3, 5, 8] and two conference papers [14, 16]. The contributions of each paper are summarized in the following.

- The analysis of the performance obtained by different discretization methods applied to resonant controllers (chapter §2) is included in the journal *IEEE Transactions on Power Electronics* [3]. Some conclusions regarding the particular case of proportional-resonant controllers without delay compensation have been presented at *IEEE Industrial Electronics Society Conference (IECON) 2009* [14].
- The proposals for enhancing the performance of the implementations based on two interconnected integrators (chapter §3) have been presented at *IEEE Energy Conversion Congress and Exposition (ECCE) 2010* [16] and published with more depth in the journal *IEEE Transactions on Power Electronics* [5].
- The analysis and design methodology based on Nyquist diagrams and sensitivity function (chapter §4) has been published in the journal *IEEE Transactions on Industrial Electronics* [8].

## 5.3 Future Research

It is expected to perform further research on the topics exposed in this thesis with regard to the application of resonant controllers to several promising applications.

- It is suggested to perform research on the optimization of transient response of resonant controllers in order to assure fast response for distributed power generation systems in case of faults (low voltage ride through).
- Torque ripple in electric machines can be minimized by selective closed-loop control of certain current harmonics. Particularizations of the contributions of this thesis to this application can be studied, with special emphasis on the issues associated to the implementation of resonant controllers in a fundamental positive-sequence synchronous reference frame.
- Certain current harmonics may be injected in multi-phase drives for several objectives, including fault-tolerance and increase of average torque. Due to the need for tracking several frequencies and sequences simultaneously, it seems to be a promising field for application of resonant controllers.
- It has been recently assessed that inverters' dead-times can be specially problematic in multi-phase applications, in which low frequency voltage components give rise to greater currents (and, hence, losses) than in three-phase systems. The selective nature of resonant controllers could provide satisfying results for active compensation of these undesired effects.

# References

- [1] A. G. Yepes, F. D. Freijedo, J. Doval-Gandoy, O. Lopez, P. Fernandez-Comesaña, and J. Malvar, “Harmonic identification algorithms based on DCT for power quality applications,” *ETRI Journal*, vol. 32, no. 1, pp. 33–43, Feb. 2010.
- [2] O. Lopez, F. D. Freijedo, A. G. Yepes, P. Fernandez-Comesaña, J. Malvar, R. Teodorescu, and J. Doval-Gandoy, “Eliminating ground current in a transformerless photovoltaic application,” *IEEE Transactions on Energy Conversion*, vol. 25, no. 1, pp. 140–147, Mar. 2010.
- [3] A. G. Yepes, F. D. Freijedo, J. Doval-Gandoy, O. Lopez, J. Malvar, and P. Fernandez-Comesaña, “Effects of discretization methods on the performance of resonant controllers,” *IEEE Transactions on Power Electronics*, vol. 25, no. 7, pp. 1692–1712, Jul. 2010.
- [4] F. D. Freijedo, A. G. Yepes, O. Lopez, A. Vidal, and J. Doval-Gandoy, “Three-phase PLLs with fast postfault retracking and steady-state rejection of voltage unbalance and harmonics by means of lead compensation,” *IEEE Transactions on Power Electronics*, vol. 26, no. 1, pp. 85–97, Jan. 2011.
- [5] A. G. Yepes, F. D. Freijedo, O. Lopez, and J. Doval-Gandoy, “High-performance digital resonant controllers implemented with two integrators,” *IEEE Transactions on Power Electronics*, vol. 26, no. 2, pp. 563–576, Feb. 2011.
- [6] F. D. Freijedo, A. G. Yepes, J. Malvar, O. Lopez, P. Fernandez-Comesaña, A. Vidal, and J. Doval-Gandoy, “Frequency tracking of digital resonant filters for control of power converters connected to public distribution systems,” *IET Power Electronics*, vol. 4, no. 4, pp. 454–462, Apr. 2011.
- [7] F. D. Freijedo, A. G. Yepes, O. Lopez, P. Fernandez-Comesana, and J. Doval-Gandoy, “An optimized implementation of phase locked loops for grid applications,” *IEEE Transactions on Instrumentation and Measurement*, vol. 60, no. 9, pp. 3110–3119, Sep. 2011.
- [8] A. G. Yepes, F. D. Freijedo, O. Lopez, and J. Doval-Gandoy, “Analysis and design of resonant current controllers for voltage-source converters by means of Nyquist diagrams and sensitivity function,” *IEEE Transactions on Industrial Electronics*, vol. 58, no. 11, pp. 5231–5250, Nov. 2011.
- [9] P. Fernandez-Comesana, F. D. Freijedo, J. Doval-Gandoy, O. Lopez, A. G. Yepes, and J. Malvar, “Mitigation of voltage sags, imbalances and harmonics in sensitive industrial

- loads by means of a series power line conditioner,” *Electric Power Systems Research*, vol. 84, no. 1, pp. 20–30, Mar. 2012.
- [10] F. D. Freijedo, J. Doval-Gandoy, O. Lopez, C. Martinez-Peñalver, A. G. Yepes, P. Fernandez-Comesaña, J. Malvar, A. Nogueiras, J. Marcos, and A. Lago, “Grid-synchronization methods for power converters,” in *Proceedings of IEEE Industrial Electronics Conference, IECON*, Nov. 2009, pp. 522–529.
- [11] O. Lopez, J. Alvarez, F. D. Freijedo, A. G. Yepes, P. Fernandez-Comesaña, J. Malvar, J. Doval-Gandoy, A. Nogueiras, A. Lago, and C. M. Peñalver, “Multilevel multiphase space vector PWM algorithm with switching state redundancy applied to three-phase converters,” in *Proceedings of IEEE Industrial Electronics Conference, IECON*, Nov. 2009, pp. 651–657.
- [12] P. Fernandez-Comesaña, J. Doval-Gandoy, F. D. Freijedo, O. Lopez, J. Malvar, A. G. Yepes, E. Diaz-Dorado, and D. Alvira-Baeza, “Evolutive algorithm for power flow optimization,” in *Proceedings of IEEE Industrial Electronics Conference, IECON*, Nov. 2009, pp. 3323–3328.
- [13] A. G. Yepes, F. D. Freijedo, J. Doval-Gandoy, O. Lopez, P. Fernandez-Comesaña, and J. Malvar, “Harmonic detection methods for active power filters based on discrete cosine transform and dithering,” in *Proceedings of IEEE Industrial Electronics Conference, IECON*, Nov. 2009, pp. 530–535.
- [14] A. G. Yepes, F. D. Freijedo, J. Doval-Gandoy, O. Lopez, J. Malvar, and P. Fernandez-Comesaña, “On the discrete-time implementation of resonant controllers for active power filters,” in *Proceedings of IEEE Industrial Electronics Conference, IECON*, 3-5 Nov. 2009, pp. 3686–3691.
- [15] F. D. Freijedo, A. Vidal, A. G. Yepes, P. Fernandez-Comesaña, J. Malvar, O. Lopez, A. Nogueiras, and J. Doval-Gandoy, “WLSE for fast, accurate and robust generation of references in power converter applications,” in *Proceedings of IEEE International Symposium on Industrial Electronics, ISIE*, Jul. 2010, pp. 2946–2951.
- [16] A. G. Yepes, F. D. Freijedo, P. Fernandez-Comesaña, J. Malvar, O. Lopez, and J. Doval-Gandoy, “Performance enhancement for digital implementation of resonant controllers,” in *Proceedings of IEEE Energy Conversion Congress and Exposition, ECCE*, Sep. 2010.
- [17] A. Vidal, F. D. Freijedo, A. G. Yepes, P. Fernandez-Comesaña, J. Malvar, O. Lopez, and J. Doval-Gandoy, “A fast, accurate and robust algorithm to detect fundamental and harmonic sequences,” in *Proceedings of IEEE Energy Conversion Congress and Exposition, ECCE*, Sep. 2010, pp. 1047–1052.
- [18] A. G. Yepes, F. D. Freijedo, P. Fernandez-Comesaña, J. Malvar, O. Lopez, and J. Doval-Gandoy, “Torque ripple minimization in surface-mounted PM drives by means of PI+multi-resonant controller in synchronous reference frame,” in *Proceedings of IEEE Industrial Electronics Conference, IECON*, Nov. 2010.

- [19] G. Escobar, J. Leyva-Ramos, P. Martinez, and A. Valdez, "A repetitive-based controller for the boost converter to compensate the harmonic distortion of the output voltage," *IEEE Transactions on Control Systems Technology*, vol. 13, no. 3, pp. 500–508, May 2005.
- [20] E. Clarke, *Circuit Analysis of AC Power Systems*. Wiley, 1950.
- [21] R. Park, "Two reaction theory of synchronous machines," *AIEE Transactions*, vol. 48, pp. 716–730, 1929.
- [22] S. Buso, S. Fasolo, L. Malesani, and P. Mattavelli, "A dead-beat adaptive hysteresis current control," *IEEE Transactions on Industry Applications*, vol. 36, no. 4, pp. 1174–1180, Jul. 2000.
- [23] Y.-R. Mohamed and E. El-Saadany, "An improved deadbeat current control scheme with a novel adaptive self-tuning load model for a three-phase PWM voltage-source inverter," *IEEE Transactions on Industrial Electronics*, vol. 54, no. 2, pp. 747–759, Apr. 2007.
- [24] Y. A. R. Mohamed and E. F. El-Saadany, "Adaptive discrete-time grid-voltage sensorless interfacing scheme for grid-connected DG-inverters based on neural-network identification and deadbeat current regulation," *IEEE Transactions on Power Electronics*, vol. 23, no. 1, pp. 308–321, Jan. 2008.
- [25] F. Briz, M. Degner, and R. Lorenz, "Analysis and design of current regulators using complex vectors," *IEEE Transactions on Industry Applications*, vol. 36, no. 3, pp. 817–825, May 2000.
- [26] P. Jansen and R. Lorenz, "A physically insightful approach to the design and accuracy assessment of flux observers for field oriented induction machine drives," *IEEE Transactions on Industry Applications*, vol. 30, no. 1, pp. 101–110, Jan. 1994.
- [27] Y. A.-R. I. Mohamed, "Mitigation of dynamic, unbalanced, and harmonic voltage disturbances using grid-connected inverters with LCL filter," *IEEE Transactions on Industrial Electronics*, vol. 58, no. 9, pp. 3914–3924, Sep. 2011.
- [28] P. Channegowda and V. John, "Filter optimization for grid interactive voltage source inverters," *IEEE Transactions on Industrial Electronics*, vol. 57, no. 12, pp. 4106–4114, Dec. 2010.
- [29] M. Liserre, F. Blaabjerg, and S. Hansen, "Design and control of an LCL-filter-based three-phase active rectifier," *IEEE Transactions on Industry Applications*, vol. 41, no. 5, pp. 1281–1291, Sep./Oct. 2005.
- [30] L. Serpa, S. Ponnaluri, P. Barbosa, and J. Kolar, "A modified direct power control strategy allowing the connection of three-phase inverters to the grid through LCL filters," *IEEE Transactions on Industry Applications*, vol. 43, no. 5, pp. 1388–1400, Sep./Oct. 2007.
- [31] S. Bhattacharyya, E. Deprettere, R. Leupers, and J. Takala, Eds., *Handbook of Signal Processing Systems*. Springer, October 2010.

- [32] I. Gabe, V. Montagner, and H. Pinheiro, "Design and implementation of a robust current controller for VSI connected to the grid through an LCL filter," *IEEE Transactions on Power Electronics*, vol. 24, no. 6, pp. 1444–1452, Jun. 2009.
- [33] G. Shen, D. Xu, L. Cao, and X. Zhu, "An improved control strategy for grid-connected voltage source inverters with an LCL filter," *IEEE Transactions on Power Electronics*, vol. 23, no. 4, pp. 1899–1906, Jul. 2008.
- [34] F. Liu, Y. Zhou, S. Duan, J. Yin, B. Liu, and F. Liu, "Parameter design of a two-current-loop controller used in a grid-connected inverter system with LCL filter," *IEEE Transactions on Industrial Electronics*, vol. 56, no. 11, pp. 4483–4491, Nov. 2009.
- [35] J. Dannehl, C. Wessels, and F. Fuchs, "Limitations of voltage-oriented PI current control of grid-connected PWM rectifiers with LCL filters," *IEEE Transactions on Industrial Electronics*, vol. 56, no. 2, pp. 380–388, Feb. 2009.
- [36] M. Malinowski and S. Bernet, "A simple voltage sensorless active damping scheme for three-phase PWM converters with an LCL filter," *IEEE Transactions on Industrial Electronics*, vol. 55, no. 4, pp. 1876–1880, Apr. 2008.
- [37] B. Bolsens, K. De Brabandere, J. Van den Keybus, J. Driesen, and R. Belmans, "Model-based generation of low distortion currents in grid-coupled PWM-inverters using an LCL output filter," *IEEE Transactions on Power Electronics*, vol. 21, no. 4, pp. 1032–1040, Jul. 2006.
- [38] K. Jalili and S. Bernet, "Design of LCL filters of active-front-end two-level voltage-source converters," *IEEE Transactions on Industrial Electronics*, vol. 56, no. 5, pp. 1674–1689, May 2009.
- [39] A. Rockhill, M. Liserre, R. Teodorescu, and P. Rodriguez, "Grid-filter design for a multimegawatt medium-voltage voltage-source inverter," *IEEE Transactions on Industrial Electronics*, vol. 58, no. 4, pp. 1205–1217, Apr. 2011.
- [40] X. Wang, X. Ruan, S. Liu, and C. Tse, "Full feedforward of grid voltage for grid-connected inverter with LCL filter to suppress current distortion due to grid voltage harmonics," *IEEE Transactions on Power Electronics*, vol. 25, no. 12, pp. 3119–3127, Dec. 2010.
- [41] H.-G. Jeong, K.-B. Lee, S. Choi, and W. Choi, "Performance improvement of LCL-filter-based grid-connected inverters using PQR power transformation," *IEEE Transactions on Power Electronics*, vol. 25, no. 5, pp. 1320–1330, May 2010.
- [42] V. Blasko and V. Kaura, "A novel control to actively damp resonance in input LC filter of a three-phase voltage source converter," *IEEE Transactions on Industry Applications*, vol. 33, no. 2, pp. 542–550, Mar./Apr. 1997.
- [43] J. Dannehl, F. Fuchs, and P. Thøandgersen, "PI state space current control of grid-connected PWM converters with LCL filters," *IEEE Transactions on Power Electronics*, vol. 25, no. 9, pp. 2320–2330, Sep. 2010.

- [44] E. Twining and D. Holmes, "Grid current regulation of a three-phase voltage source inverter with an LCL input filter," *IEEE Transactions on Power Electronics*, vol. 18, no. 3, pp. 888–895, May 2003.
- [45] G. Shen, X. Zhu, J. Zhang, and D. Xu, "A new feedback method for PR current control of LCL-filter-based grid-connected inverter," *IEEE Transactions on Industrial Electronics*, vol. 57, no. 6, pp. 2033–2041, Jun. 2010.
- [46] J. Dannehl, M. Liserre, and F. W. Fuchs, "Filter-based active damping of voltage source converters with LCL filter," *IEEE Transactions on Industrial Electronics*, vol. 58, no. 8, pp. 3623–3633, Aug. 2011.
- [47] M. Liserre, R. Teodorescu, and F. Blaabjerg, "Stability of photovoltaic and wind turbine grid-connected inverters for a large set of grid impedance values," *IEEE Transactions on Power Electronics*, vol. 21, no. 1, pp. 263–272, Jan. 2006.
- [48] M. Bierhoff and F. Fuchs, "Active damping for three-phase PWM rectifiers with high-order line-side filters," *IEEE Transactions on Industrial Electronics*, vol. 56, no. 2, pp. 371–379, Feb. 2009.
- [49] L. Harnefors, L. Zhang, and M. Bongiorno, "Frequency-domain passivity-based current controller design," *IET Power Electronics*, vol. 1, no. 4, pp. 455–465, Dec. 2008.
- [50] S. Yang, Q. Lei, F. Z. Peng, and Z. Qian, "A robust control scheme for grid-connected voltage-source inverters," *IEEE Transactions on Industrial Electronics*, vol. 58, no. 1, pp. 202–212, Jan. 2011.
- [51] R. Bojoi, L. Limongi, D. Ruiu, and A. Tenconi, "Frequency-domain analysis of resonant current controllers for active power conditioners," in *Proceedings of IEEE Industrial Electronics Conference, IECON*, Nov. 2008, pp. 3141–3148.
- [52] J. Espi, J. Castello, R. García-Gil, G. Garcera, and E. Figueres, "An adaptive robust predictive current control for three-phase grid-connected inverters," *IEEE Transactions on Industrial Electronics*, vol. 58, no. 8, pp. 3537–3546, Aug. 2011.
- [53] R. I. Bojoi, L. R. Limongi, D. Ruiu, and A. Tenconi, "Enhanced power quality control strategy for single-phase inverters in distributed generation systems," *IEEE Transactions on Power Electronics*, vol. 26, no. 3, pp. 798–806, Mar. 2011.
- [54] S. Y. Park, C. L. Chen, and J. S. Lai, "A wide-range active and reactive power flow controller for a solid oxide fuel cell power conditioning system," *IEEE Transactions on Power Electronics*, vol. 23, no. 6, pp. 2703–2709, Nov. 2008.
- [55] S. Y. Park, C. L. Chen, J. S. Lai, and S. R. Moon, "Admittance compensation in current loop control for a grid-tie LCL fuel cell inverter," *IEEE Transactions on Power Electronics*, vol. 23, no. 4, pp. 1716–1723, Jul. 2008.
- [56] C. Lascu, L. Asiminoaei, I. Boldea, and F. Blaabjerg, "High performance current controller for selective harmonic compensation in active power filters," *IEEE Transactions on Power Electronics*, vol. 22, no. 5, pp. 1826–1835, Sep. 2007.

- [57] ———, “Frequency response analysis of current controllers for selective harmonic compensation in active power filters,” *IEEE Transactions on Industrial Electronics*, vol. 56, no. 2, pp. 337–347, Feb. 2009.
- [58] R. Bojoi, L. Limongi, F. Profumo, D. Ruiu, and A. Tenconi, “Analysis of current controllers for active power filters using selective harmonic compensation schemes,” *IEEE Transactions on Electrical and Electronic Engineering*, vol. 4, no. 2, pp. 139–157, 2009.
- [59] K. Macken, K. Vanthournout, J. Van den Keybus, G. Deconinck, and R. Belmans, “Distributed control of renewable generation units with integrated active filter,” *IEEE Transactions on Power Electronics*, vol. 19, no. 5, pp. 1353–1360, Sep. 2004.
- [60] P. Mattavelli, F. Polo, F. Dal Lago, and S. Saggini, “Analysis of control-delay reduction for the improvement of UPS voltage-loop bandwidth,” *IEEE Transactions on Industrial Electronics*, vol. 55, no. 8, pp. 2903–2911, Aug. 2008.
- [61] H. Akagi, E. H. Watanabe, and M. Aredes, *Instantaneous Power Theory and Applications to Power Conditioning*, M. E. El-Hawari, Ed. Wiley-IEEE Press, 2007.
- [62] Y. Sato, T. Ishizuka, K. Nezu, and T. Kataoka, “A new control strategy for voltage-type PWM rectifiers to realize zero steady-state control error in input current,” *IEEE Transactions on Industry Applications*, vol. 34, no. 3, pp. 480–486, May/Jun. 1998.
- [63] S. Fukuda and T. Yoda, “A novel current-tracking method for active filters based on a sinusoidal internal model,” *IEEE Transactions on Industry Applications*, vol. 37, no. 3, pp. 888–895, May/Jun. 2001.
- [64] X. Yuan, W. Merk, H. Stemmler, and J. Allmeling, “Stationary-frame generalized integrators for current control of active power filters with zero steady-state error for current harmonics of concern under unbalanced and distorted operating conditions,” *IEEE Transactions on Industry Applications*, vol. 38, no. 2, pp. 523–532, Mar./Apr. 2002.
- [65] D. N. Zmood and D. G. Holmes, “Stationary frame current regulation of PWM inverters with zero steady-state error,” *IEEE Transactions on Power Electronics*, vol. 18, no. 3, pp. 814–822, May 2003.
- [66] R. Bojoi, E. Levi, F. Farina, A. Tenconi, and F. Profumo, “Dual three-phase induction motor drive with digital current control in the stationary reference frame,” in *IEE Proceedings - Electric Power Applications*, vol. 153, no. 1, Jan. 2006, pp. 129–139.
- [67] M.-C. Chou and C.-M. Liaw, “Development of robust current 2-DOF controllers for a permanent magnet synchronous motor drive with reaction wheel load,” *IEEE Transactions on Power Electronics*, vol. 24, no. 5, pp. 1304–1320, May 2009.
- [68] J. Hu, Y. He, L. Xu, and B. Williams, “Improved control of DFIG systems during network unbalance using PI-R current regulators,” *IEEE Transactions on Industrial Electronics*, vol. 56, no. 2, pp. 439–451, Feb. 2009.
- [69] P. Lezana, C. A. Silva, J. Rodriguez, and M. A. Perez, “Zero-steady-state-error input-current controller for regenerative multilevel converters based on single-phase cells,” *IEEE Transactions on Industrial Electronics*, vol. 54, no. 2, pp. 733–740, Apr. 2007.

- [70] R. P. Venturini, P. Mattavelli, P. Zanchetta, and M. Sumner, "Variable frequency adaptive selective compensation for active power filters," in *Proceedings of IET Conference on Power Electronics, Machines and Drives, PEMD*, Apr. 2008, pp. 16–21.
- [71] S. Buso and P. Mattavelli, *Digital Control in Power Electronics*, J. Hudgins, Ed. Morgan and Claypool Publishers, 2006.
- [72] M. Sedighy, S. Dewan, and F. Dawson, "A robust digital current control method for active power filters," *IEEE Transactions on Industry Applications*, vol. 36, no. 4, pp. 1158–1164, Jul./Aug. 2000.
- [73] S. Buso, L. Malesani, and P. Mattavelli, "Comparison of current control techniques for active filter applications," *IEEE Transactions on Industrial Electronics*, vol. 45, no. 5, pp. 722–729, Oct. 1998.
- [74] I. Nagy, "Novel adaptive tolerance band based PWM for field-oriented control of induction machines," *IEEE Transactions on Industrial Electronics*, vol. 41, no. 4, pp. 406–417, Aug. 1994.
- [75] M. Kazmierkowski and L. Malesani, "Current control techniques for three-phase voltage-source PWM converters: a survey," *IEEE Transactions on Industrial Electronics*, vol. 45, no. 5, pp. 691–703, Oct. 1998.
- [76] A. Shukla, A. Ghosh, and A. Joshi, "Improved multilevel hysteresis current regulation and capacitor voltage balancing schemes for flying capacitor multilevel inverter," *IEEE Transactions on Power Electronics*, vol. 23, no. 2, pp. 518–529, Mar. 2008.
- [77] B. Bose, "An adaptive hysteresis-band current control technique of a voltage-fed PWM inverter for machine drive system," *IEEE Transactions on Industrial Electronics*, vol. 37, no. 5, pp. 402–408, Oct. 1990.
- [78] A. Tripathi and P. Sen, "Comparative analysis of fixed and sinusoidal band hysteresis current controllers for voltage source inverters," *IEEE Transactions on Industrial Electronics*, vol. 39, no. 1, pp. 63–73, Feb. 1992.
- [79] L. Malesani and P. Tenti, "A novel hysteresis control method for current-controlled voltage-source PWM inverters with constant modulation frequency," *IEEE Transactions on Industry Applications*, vol. 26, no. 1, pp. 88–92, Jan./Feb. 1990.
- [80] L. Malesani, P. Tenti, E. Gaio, and R. Piovani, "Improved current control technique of VSI PWM inverters with constant modulation frequency and extended voltage range," *IEEE Transactions on Industry Applications*, vol. 27, no. 2, pp. 365–369, Mar./Apr. 1991.
- [81] L. Malesani, L. Rossetto, and A. Zuccato, "Digital adaptive hysteresis current control with clocked commutations and wide operating range," *IEEE Transactions on Industry Applications*, vol. 32, no. 2, pp. 316–325, Mar./Apr. 1996.
- [82] L. Malesani, P. Mattavelli, and P. Tomasin, "High-performance hysteresis modulation technique for active filters," *IEEE Transactions on Power Electronics*, vol. 12, no. 5, pp. 876–884, Sep. 1997.

- [83] ———, “Improved constant-frequency hysteresis current control of VSI inverters with simple feedforward bandwidth prediction,” *IEEE Transactions on Industry Applications*, vol. 33, no. 5, pp. 1194–1202, Sep./Oct. 1997.
- [84] W. Stefanutti and P. Mattavelli, “Fully digital hysteresis modulation with switching-time prediction,” *IEEE Transactions on Industry Applications*, vol. 42, no. 3, pp. 763–769, May 2006.
- [85] M. Mohseni and S. Islam, “A new vector-based hysteresis current control scheme for three-phase PWM voltage-source inverters,” *IEEE Transactions on Power Electronics*, vol. 25, no. 9, pp. 2299–2309, Sep. 2010.
- [86] B.-H. Kwon, T.-W. Kim, and J.-H. Youm, “A novel SVM-based hysteresis current controller,” *IEEE Transactions on Power Electronics*, vol. 13, no. 2, pp. 297–307, Mar. 1998.
- [87] G. Wang and Y. W. Li, “Parabolic PWM for current control of voltage-source converters (VSCs),” *IEEE Transactions on Industrial Electronics*, vol. 57, no. 10, pp. 3491–3496, Oct. 2010.
- [88] E. Aldabas, L. Romeral, A. Arias, and M. Jayne, “Software-based digital hysteresis-band current controller,” *IEE Proceedings - Electric Power Applications*, vol. 153, no. 2, pp. 184–190, Mar. 2006.
- [89] M. Rahman, T. Radwan, A. Osheiba, and A. Lashine, “Analysis of current controllers for voltage-source inverter,” *IEEE Transactions on Industrial Electronics*, vol. 44, no. 4, pp. 477–485, Aug. 1997.
- [90] C. Rossi and A. Tonielli, “Robust current controller for three-phase inverter using finite-state automaton,” *IEEE Transactions on Industrial Electronics*, vol. 42, no. 2, pp. 169–178, Apr. 1995.
- [91] P. C. Tan, P. C. Loh, and D. G. Holmes, “High-performance harmonic extraction algorithm for a 25 kV traction power quality conditioner,” in *IEE Proceedings - Electric Power Applications*, vol. 151, no. 5, Sep. 2004, pp. 505–512.
- [92] N. Rashidi, “Improved and less load dependent three-phase current-controlled inverter with hysteretic current controllers,” *IEEE Transactions on Industrial Electronics*, vol. 42, no. 3, pp. 325–330, Jun. 1995.
- [93] A. Shukla, A. Ghosh, and A. Joshi, “Hysteresis current control operation of flying capacitor multilevel inverter and its application in shunt compensation of distribution systems,” *IEEE Transactions on Power Delivery*, vol. 22, no. 1, pp. 396–405, Jan. 2007.
- [94] D. M. Brod and D. W. Novotny, “Current control of VSI-PWM inverters,” *IEEE Transactions on Industry Applications*, vol. IA-21, no. 3, pp. 562–570, May 1985.
- [95] L. Borle and C. Nayar, “Zero average current error controlled power flow for AC-DC power converters,” *IEEE Transactions on Power Electronics*, vol. 10, no. 6, pp. 725–732, Nov. 1995.

- [96] M. N. Kumar and K. Vasudevan, "Bi-directional real and reactive power control using constant frequency hysteresis control with reduced losses," *Electric Power Systems Research*, vol. 76, no. 1-3, pp. 127–135, Sep. 2005.
- [97] P.-C. Tan, R. Morrison, and D. Holmes, "Voltage form factor control and reactive power compensation in a 25-kV electrified railway system using a shunt active filter based on voltage detection," *IEEE Transactions on Industry Applications*, vol. 39, no. 2, pp. 575–581, Mar./Apr. 2003.
- [98] V. George and M. Mishra, "Design and analysis of user-defined constant switching frequency current-control-based four-leg DSTATCOM," *IEEE Transactions on Power Electronics*, vol. 24, no. 9, pp. 2148–2158, Sep. 2009.
- [99] P. C. Loh, D. Holmes, Y. Fukuta, and T. Lipo, "A reduced common mode hysteresis current regulation strategy for multilevel inverters," *IEEE Transactions on Power Electronics*, vol. 19, no. 1, pp. 192–200, Jan. 2004.
- [100] F. Zare and G. Ledwich, "A hysteresis current control for single-phase multilevel voltage source inverters: PLD implementation," *IEEE Transactions on Power Electronics*, vol. 17, no. 5, pp. 731–738, Sep. 2002.
- [101] O. Vodyakho, D. Hackstein, A. Steimel, and T. Kim, "Novel direct current-space-vector control for shunt active power filters based on the three-level inverter," *IEEE Transactions on Power Electronics*, vol. 23, no. 4, pp. 1668–1678, Jul. 2008.
- [102] R. Gupta, A. Ghosh, and A. Joshi, "Multiband hysteresis modulation and switching characterization for sliding-mode-controlled cascaded multilevel inverter," *IEEE Transactions on Industrial Electronics*, vol. 57, no. 7, pp. 2344–2353, Jul. 2010.
- [103] F. Liu and A. Maswood, "A novel variable hysteresis band current control of three-phase three-level unity PF rectifier with constant switching frequency," *IEEE Transactions on Power Electronics*, vol. 21, no. 6, pp. 1727–1734, Nov. 2006.
- [104] C.-M. Ho, V. Cheung, and H.-H. Chung, "Constant-frequency hysteresis current control of grid-connected VSI without bandwidth control," *IEEE Transactions on Power Electronics*, vol. 24, no. 11, pp. 2484–2495, Nov. 2009.
- [105] A. Kawamura and R. Hoft, "Instantaneous feedback controlled PWM inverter with adaptive hysteresis," *IEEE Transactions on Industry Applications*, vol. IA-20, no. 4, pp. 769–775, Jul. 1984.
- [106] C.-T. Pan, Y.-S. Huang, and C.-Y. Li, "An error bounded current controller with constant sampling frequency," *IEEE Transactions on Power Electronics*, vol. 19, no. 3, pp. 739–747, May 2004.
- [107] P. Tekwani, R. Kanchan, and K. Gopakumar, "Novel current error space phasor based hysteresis controller using parabolic bands for control of switching frequency variations," *IEEE Transactions on Industrial Electronics*, vol. 54, no. 5, pp. 2648–2656, Oct. 2007.

- [108] P. Lohia, M. Mishra, K. Karthikeyan, and K. Vasudevan, "A minimally switched control algorithm for three-phase four-leg VSI topology to compensate unbalanced and nonlinear load," *IEEE Transactions on Power Electronics*, vol. 23, no. 4, pp. 1935–1944, Jul. 2008.
- [109] N. Prabhakar and M. K. Mishra, "Dynamic hysteresis current control to minimize switching for three-phase four-leg VSI topology to compensate nonlinear load," *IEEE Transactions on Power Electronics*, vol. 25, no. 8, pp. 1935–1942, Aug. 2010.
- [110] M. Kazmierkowski and W. Sulkowski, "A novel vector control scheme for transistor PWM inverter-fed induction motor drive," *IEEE Transactions on Industrial Electronics*, vol. 38, no. 1, pp. 41–47, Feb. 1991.
- [111] K. Rahman, M. Khan, M. Choudhury, and M. Rahman, "Variable-band hysteresis current controllers for PWM voltage-source inverters," *IEEE Transactions on Power Electronics*, vol. 12, no. 6, pp. 964–970, Nov. 1997.
- [112] M. Mohseni, S. Islam, and M. Masoum, "Enhanced hysteresis-based current regulators in vector control of DFIG wind turbines," *IEEE Transactions on Power Electronics*, vol. 26, no. 1, pp. 223–234, Jan. 2011.
- [113] M. Kazmierkowski, M. Dzieniakowski, and W. Sulkowski, "Novel space vector based current controllers for PWM-inverters," *IEEE Transactions on Power Electronics*, vol. 6, no. 1, pp. 158–166, Jan. 1991.
- [114] C.-T. Pan and T.-Y. Chang, "An improved hysteresis current controller for reducing switching frequency," *IEEE Transactions on Power Electronics*, vol. 9, no. 1, pp. 97–104, Jan. 1994.
- [115] C.-T. Pan, Y.-S. Huang, and T.-L. Jong, "A constantly sampled current controller with switch status dependent inner bound," *IEEE Transactions on Industrial Electronics*, vol. 50, no. 3, pp. 528–535, Jun. 2003.
- [116] B.-H. Kwon, B.-D. Min, and J.-H. Youm, "An improved space-vector-based hysteresis current controller," *IEEE Transactions on Industrial Electronics*, vol. 45, no. 5, pp. 752–760, Oct. 1998.
- [117] D. Neacsu, "Current control with fast transient for three-phase ac/dc boost converters," *IEEE Transactions on Industrial Electronics*, vol. 51, no. 5, pp. 1117–1121, Oct. 2004.
- [118] J. Martins, A. Pires, and J. Silva, "A novel and simple current controller for three-phase PWM power inverters," *IEEE Transactions on Industrial Electronics*, vol. 45, no. 5, pp. 802–804, Oct. 1998.
- [119] A. Timbus, M. Liserre, R. Teodorescu, P. Rodriguez, and F. Blaabjerg, "Evaluation of current controllers for distributed power generation systems," *IEEE Transactions on Power Electronics*, vol. 24, no. 3, pp. 654–664, Mar. 2009.
- [120] L. Limongi, R. Bojoi, G. Griva, and A. Tenconi, "Digital current-control schemes," *IEEE Industrial Electronics Magazine*, vol. 3, no. 1, pp. 20–31, Mar. 2009.

- [121] P. Mattavelli, "An improved deadbeat control for UPS using disturbance observers," *IEEE Transactions on Industrial Electronics*, vol. 52, no. 1, pp. 206–212, Feb. 2005.
- [122] P. Mattavelli, G. Spiazzi, and P. Tenti, "Predictive digital control of power factor preregulators with input voltage estimation using disturbance observers," *IEEE Transactions on Power Electronics*, vol. 20, no. 1, pp. 140–147, Jan. 2005.
- [123] H. Fujita, "A single-phase active filter using an h-bridge PWM converter with a sampling frequency quadruple of the switching frequency," *IEEE Transactions on Power Electronics*, vol. 24, no. 4, pp. 934–941, Apr. 2009.
- [124] L. Malesani, P. Mattavelli, and S. Buso, "Robust dead-beat current control for PWM rectifiers and active filters," *IEEE Transactions on Industry Applications*, vol. 35, no. 3, pp. 613–620, May 1999.
- [125] T. Ahmed, K. Nishida, and M. Nakaoka, "Advanced control of PWM converter with variable-speed induction generator," *IEEE Transactions on Industry Applications*, vol. 42, no. 4, pp. 934–945, Jul./Aug. 2006.
- [126] T. Ahmed, K. Nishida, and M. Nakaoka., "A novel stand-alone induction generator system for AC and DC power applications," *IEEE Transactions on Industry Applications*, vol. 43, no. 6, pp. 1465–1474, Nov./Dec. 2007.
- [127] G. Bode, P. C. Loh, M. Newman, and D. Holmes, "An improved robust predictive current regulation algorithm," *IEEE Transactions on Industry Applications*, vol. 41, no. 6, pp. 1720–1733, Nov./Dec. 2005.
- [128] S.-H. Choi, J.-S. Ko, I.-D. Kim, J.-S. Park, and S.-C. Hong, "Precise position control using a PMSM with a disturbance observer containing a system parameter compensator," *IEE Proceedings - Electric Power Applications*, vol. 152, no. 6, pp. 1573–1577, Nov. 2005.
- [129] J. Espi Huerta, J. Castello-Moreno, J. Fischer, and R. Garcia-Gil, "A synchronous reference frame robust predictive current control for three-phase grid-connected inverters," *IEEE Transactions on Industrial Electronics*, vol. 57, no. 3, pp. 954–962, Mar. 2010.
- [130] L. Hang, S. Liu, G. Yan, B. Qu, and Z.-Y. Lu, "An improved deadbeat scheme with fuzzy controller for the grid-side three-phase PWM boost rectifier," *IEEE Transactions on Power Electronics*, vol. 26, no. 4, pp. 1184–1191, Apr. 2011.
- [131] Y. A. R. I. Mohamed and E. F. El-Saadany, "Robust high bandwidth discrete-time predictive current control with predictive internal model- a unified approach for voltage-source PWM converters," *IEEE Transactions on Power Electronics*, vol. 23, no. 1, pp. 126–136, Jan. 2008.
- [132] Y.-R. Mohamed and E. El-Saadany, "A control scheme for PWM voltage-source distributed-generation inverters for fast load-voltage regulation and effective mitigation of unbalanced voltage disturbances," *IEEE Transactions on Industrial Electronics*, vol. 55, no. 5, pp. 2072–2084, May 2008.

- [133] J. Moreno, J. Huerta, R. Gil, and S. Gonzalez, "A robust predictive current control for three-phase grid-connected inverters," *IEEE Transactions on Industrial Electronics*, vol. 56, no. 6, pp. 1993–2004, Jun. 2009.
- [134] K. Nishida, M. Rukonuzzman, and M. Nakaoka, "Advanced current control implementation with robust deadbeat algorithm for shunt single-phase voltage-source type active power filter," *IEE Proceedings - Electric Power Applications*, vol. 151, no. 3, pp. 283–288, May 2004.
- [135] K. Nishida, T. Ahmed, and M. Nakaoka, "Induction generator hybrid applications with active power filter," *IEE Proceedings - Electric Power Applications*, vol. 153, no. 2, pp. 197–205, Mar. 2006.
- [136] T. Kawabata, T. Miyashita, and Y. Yamamoto, "Dead beat control of three phase pwm inverter," *IEEE Transactions on Power Electronics*, vol. 5, no. 1, pp. 21–28, Jan. 1990.
- [137] J. Kolar, H. Ertl, and F. Zach, "Analysis of on- and off-line optimized predictive current controllers for PWM converter systems," *IEEE Transactions on Power Electronics*, vol. 6, no. 3, pp. 451–462, Jul. 1991.
- [138] Y. Ito and S. Kawauchi, "Microprocessor based robust digital control for UPS with three-phase PWM inverter," *IEEE Transactions on Power Electronics*, vol. 10, no. 2, pp. 196–204, Mar. 1995.
- [139] S.-G. Jeong and M.-H. Woo, "DSP-based active power filter with predictive current control," *IEEE Transactions on Industrial Electronics*, vol. 44, no. 3, pp. 329–336, Jun. 1997.
- [140] S.-M. Yang and C.-H. Lee, "A deadbeat current controller for field oriented induction motor drives," *IEEE Transactions on Power Electronics*, vol. 17, no. 5, pp. 772–778, Sep. 2002.
- [141] Y.-R. Mohamed and E. El-Saadany, "A control method of grid-connected PWM voltage source inverters to mitigate fast voltage disturbances," *IEEE Transactions on Power Systems*, vol. 24, no. 1, pp. 489–491, Feb. 2009.
- [142] A. Bouafia, J.-P. Gaubert, and F. Krim, "Predictive direct power control of three-phase pulsewidth modulation (PWM) rectifier using space-vector modulation (SVM)," *IEEE Transactions on Power Electronics*, vol. 25, no. 1, pp. 228–236, Jan. 2010.
- [143] A. Nasiri, "Full digital current control of permanent magnet synchronous motors for vehicular applications," *IEEE Transactions on Vehicular Technology*, vol. 56, no. 4, pp. 1531–1537, Jul. 2007.
- [144] ———, "Digital control of three-phase series-parallel uninterruptible power supply systems," *IEEE Transactions on Power Electronics*, vol. 22, no. 4, pp. 1116–1127, Jul. 2007.
- [145] Q. Zeng and L. Chang, "An advanced SVPWM-based predictive current controller for three-phase inverters in distributed generation systems," *IEEE Transactions on Industrial Electronics*, vol. 55, no. 3, pp. 1235–1246, Mar. 2008.

- [146] S. Buso, S. Fasolo, and P. Mattavelli, "Uninterruptible power supply multiloop control employing digital predictive voltage and current regulators," *IEEE Transactions on Industry Applications*, vol. 37, no. 6, pp. 1846–1854, Nov./Dec. 2001.
- [147] M. B. Delghavi and A. Yazdani, "Islanded-mode control of electronically coupled distributed-resource units under unbalanced and nonlinear load conditions," *IEEE Transactions on Power Delivery*, vol. 26, no. 2, pp. 661–673, Apr. 2011.
- [148] A. Ghosh, A. Jindal, and A. Joshi, "Design of a capacitor-supported dynamic voltage restorer (DVR) for unbalanced and distorted loads," *IEEE Transactions on Power Delivery*, vol. 19, no. 1, pp. 405–413, Jan. 2004.
- [149] Y. Han, L. Xu, M. M. Khan, C. Chen, G. Yao, and L.-D. Zhou, "Robust deadbeat control scheme for a hybrid APF with resetting filter and ADALINE-based harmonic estimation algorithm," *IEEE Transactions on Industrial Electronics*, vol. 58, no. 9, pp. 3893–3904, Sep. 2011.
- [150] M. Kojima, K. Hirabayashi, Y. Kawabata, E. Ejiogu, and T. Kawabata, "Novel vector control system using deadbeat-controlled PWM inverter with output LC filter," *IEEE Transactions on Industry Applications*, vol. 40, no. 1, pp. 162–169, Jan./Feb. 2004.
- [151] J. Mossoba and P. Lehn, "A controller architecture for high bandwidth active power filters," *IEEE Transactions on Power Electronics*, vol. 18, no. 1, pp. 317–325, Jan. 2003.
- [152] E. Wu and P. Lehn, "Digital current control of a voltage source converter with active damping of LCL resonance," *IEEE Transactions on Power Electronics*, vol. 21, no. 5, pp. 1364–1373, Sep. 2006.
- [153] J. Allmeling, "A control structure for fast harmonics compensation in active filters," *IEEE Transactions on Power Electronics*, vol. 19, no. 2, pp. 508–514, Mar. 2004.
- [154] C. D. Schauder and R. Caddy, "Current control of voltage-source inverters for fast four-quadrant drive performance," *IEEE Transactions on Industry Applications*, vol. IA-18, no. 2, pp. 163–171, Mar. 1982.
- [155] C. D. Schauder and S. A. Moran, "Multiple reference frame controller for active filters and power line conditioners," U.S. Patent 5 309 353, May, 1994.
- [156] F. D. Freijedo, "Contributions to grid-synchronization techniques for power electronic converters," Ph.D. dissertation, Department of Electronics Technology, University of Vigo, 2009.
- [157] P. Mattavelli, "A closed-loop selective harmonic compensation for active filters," *IEEE Transactions on Industry Applications*, vol. 37, no. 1, pp. 81–89, Jan./Feb. 2001.
- [158] ———, "Synchronous-frame harmonic control for high-performance AC power supplies," *IEEE Transactions on Industry Applications*, vol. 37, no. 3, pp. 864–872, May 2001.
- [159] L. Harnefors and H. P. Nee, "Model-based current control of AC machines using the internal model control method," *IEEE Transactions on Industry Applications*, vol. 34, no. 1, pp. 133–141, Jan./Feb. 1998.

- [160] F. Briz, M. Degner, and R. Lorenz, "Dynamic analysis of current regulators for AC motors using complex vectors," *IEEE Transactions on Industry Applications*, vol. 35, no. 6, pp. 1424–1432, /Dec. 1999.
- [161] P. Chapman and S. Sudhoff, "A multiple reference frame synchronous estimator/regulator," *IEEE Transactions on Energy Conversion*, vol. 15, no. 2, pp. 197–202, Jun. 2000.
- [162] S. Senini and P. Wolfs, "Analysis and design of a multiple-loop control system for a hybrid active filter," *IEEE Transactions on Industrial Electronics*, vol. 49, no. 6, pp. 1283–1292, Dec. 2002.
- [163] P. Xiao, K. A. Corzine, and G. K. Venayagamoorthy, "Multiple reference frame-based control of three-phase PWM boost rectifiers under unbalanced and distorted input conditions," *IEEE Transactions on Power Electronics*, vol. 23, no. 4, pp. 2006–2017, Jul. 2008.
- [164] C. Kempf, W. Messner, M. Tomizuka, and R. Horowitz, "Comparison of four discrete-time repetitive control algorithms," *IEEE Control Systems Magazine*, vol. 13, no. 6, pp. 48–54, Dec. 1993.
- [165] Y.-Y. Tzou, R.-S. Ou, S.-L. Jung, and M.-Y. Chang, "High-performance programmable AC power source with low harmonic distortion using DSP-based repetitive control technique," *IEEE Transactions on Power Electronics*, vol. 12, no. 4, pp. 715–725, Jul. 1997.
- [166] R. Costa-Castello, R. Grino, and E. Fossas, "Odd-harmonic digital repetitive control of a single-phase current active filter," *IEEE Transactions on Power Electronics*, vol. 19, no. 4, pp. 1060–1068, Jul. 2004.
- [167] R. Costa-Castello, J. Nebot, and R. Grino, "Demonstration of the internal model principle by digital repetitive control of an educational laboratory plant," *IEEE Transactions on Education*, vol. 48, no. 1, pp. 73–80, Feb. 2005.
- [168] R. Costa-Castello, R. Grino, R. Cardoner Parpal, and E. Fossas, "High-performance control of a single-phase shunt active filter," *IEEE Transactions on Control Systems Technology*, vol. 17, no. 6, pp. 1318–1329, Nov. 2009.
- [169] B. A. Francis and W. M. Wonham, "The internal model principle for linear multivariable regulators," *Applied Mathematics Optimization*, vol. 2, no. 2, pp. 170–194, 1975.
- [170] B. Francis and W. Wonham, "Internal model principle in control theory," *Automatica*, vol. 12, no. 5, pp. 457–465, 1976.
- [171] M.-C. Tsai and W.-S. Yao, "Design of a plug-in type repetitive controller for periodic inputs," *IEEE Transactions on Control Systems Technology*, vol. 10, no. 4, pp. 547–555, Jul. 2002.
- [172] R. Griñó and R. Costa-Castelló, "Digital repetitive plug-in controller for odd-harmonic periodic references and disturbances," *Automatica*, vol. 41, no. 1, pp. 153–157, 2005.

- [173] B.-S. Chen and Y.-Y. Hsu, "A minimal harmonic controller for a STATCOM," *IEEE Transactions on Industrial Electronics*, vol. 55, no. 2, pp. 655–664, Feb. 2008.
- [174] G. Pipeleers, B. Demeulenaere, J. De Schutter, and J. Swevers, "Generalised repetitive control: relaxing the period-delay-based structure," *IET Control Theory Applications*, vol. 3, no. 11, pp. 1528–1536, Nov. 2009.
- [175] P. Mattavelli, L. Tubiana, and M. Zigliotto, "Torque-ripple reduction in PM synchronous motor drives using repetitive current control," *IEEE Transactions on Power Electronics*, vol. 20, no. 6, pp. 1423–1431, Nov. 2005.
- [176] K. Zhang, Y. Kang, J. Xiong, and J. Chen, "Direct repetitive control of SPWM inverter for UPS purpose," *IEEE Transactions on Power Electronics*, vol. 18, no. 3, pp. 784–792, May 2003.
- [177] M. Yamada, Z. Riadh, and Y. Funahashi, "Design of discrete-time repetitive control system for pole placement and application," *IEEE/ASME Transactions on Mechatronics*, vol. 4, no. 2, pp. 110–118, Jun. 1999.
- [178] K. Zhou and D. Wang, "Digital repetitive learning controller for three-phase CVCF PWM inverter," *IEEE Transactions on Industrial Electronics*, vol. 48, no. 4, pp. 820–830, Aug. 2001.
- [179] —, "Unified robust zero-error tracking control of CVCF PWM converters," *IEEE Transactions on Circuits and Systems I: Fundamental Theory and Applications*, vol. 49, no. 4, pp. 492–501, Apr. 2002.
- [180] —, "Digital repetitive controlled three-phase PWM rectifier," *IEEE Transactions on Power Electronics*, vol. 18, no. 1, pp. 309–316, Jan. 2003.
- [181] X. Wu, S. Panda, and J. Xu, "Design of a plug-in repetitive control scheme for eliminating supply-side current harmonics of three-phase PWM boost rectifiers under generalized supply voltage conditions," *IEEE Transactions on Power Electronics*, vol. 25, no. 7, pp. 1800–1810, Jul. 2010.
- [182] T.-Y. Doh and M. Chung, "Repetitive control design for linear systems with time-varying uncertainties," *IEE Proceedings - Control Theory and Applications*, vol. 150, no. 4, pp. 427–432, Jul. 2003.
- [183] G. Weiss, Q.-C. Zhong, T. Green, and J. Liang, "H-infinity repetitive control of DC-AC converters in microgrids," *IEEE Transactions on Power Electronics*, vol. 19, no. 1, pp. 219–230, Jan. 2004.
- [184] J. Leyva-Ramos, G. Escobar, P. Martinez, and P. Mattavelli, "Analog circuits to implement repetitive controllers for tracking and disturbance rejection of periodic signals," *IEEE Transactions on Circuits and Systems II: Express Briefs*, vol. 52, no. 8, pp. 466–470, Aug. 2005.
- [185] G. Escobar, P. Martinez, J. Leyva-Ramos, and P. Mattavelli, "A negative feedback repetitive control scheme for harmonic compensation," *IEEE Transactions on Industrial Electronics*, vol. 53, no. 4, pp. 1383–1386, Jun. 2006.

- [186] S. Bolognani, L. Peretti, and M. Zigliotto, "Repetitive-control-based self-commissioning procedure for inverter nonidealities compensation," *IEEE Transactions on Industry Applications*, vol. 44, no. 5, pp. 1587–1596, Sep./Oct. 2008.
- [187] C. Roh and M. Chung, "Design of repetitive control system for an uncertain plant," *Electronics Letters*, vol. 31, no. 22, pp. 1959–1960, Oct. 1995.
- [188] Y.-Y. Tzou, S.-L. Jung, and H.-C. Yeh, "Adaptive repetitive control of PWM inverters for very low THD AC-voltage regulation with unknown loads," *IEEE Transactions on Power Electronics*, vol. 14, no. 5, pp. 973–981, Sep. 1999.
- [189] T. Su, S. Hattori, M. Ishida, and T. Hori, "Suppression control method for torque vibration of ac motor utilizing repetitive controller with fourier transform," *IEEE Transactions on Industry Applications*, vol. 38, no. 5, pp. 1316–1325, Sep./Oct. 2002.
- [190] Y. Ye, K. Zhou, B. Zhang, D. Wang, and J. Wang, "High-performance repetitive control of PWM DC-AC converters with real-time phase-lead FIR filter," *IEEE Transactions on Circuits and Systems II: Express Briefs*, vol. 53, no. 8, pp. 768–772, Aug. 2006.
- [191] K. Zhou, K.-S. Low, D. Wang, F.-L. Luo, B. Zhang, and Y. Wang, "Zero-phase odd-harmonic repetitive controller for a single-phase PWM inverter," *IEEE Transactions on Power Electronics*, vol. 21, no. 1, pp. 193–201, Jan. 2006.
- [192] A. Garcia-Cerrada, O. Pinzon-Ardila, V. Feliu-Battle, P. Roncero-Sanchez, and P. Garcia-Gonzalez, "Application of a repetitive controller for a three-phase active power filter," *IEEE Transactions on Power Electronics*, vol. 22, no. 1, pp. 237–246, Jan. 2007.
- [193] S. Chen, Y. Lai, S.-C. Tan, and C. Tse, "Analysis and design of repetitive controller for harmonic elimination in PWM voltage source inverter systems," *IET Power Electronics*, vol. 1, no. 4, pp. 497–506, Dec. 2008.
- [194] ———, "Fast response low harmonic distortion control scheme for voltage source inverters," *IET Power Electronics*, vol. 2, no. 5, pp. 574–584, Sep. 2009.
- [195] R. Cao and K.-S. Low, "A repetitive model predictive control approach for precision tracking of a linear motion system," *IEEE Transactions on Industrial Electronics*, vol. 56, no. 6, pp. 1955–1962, Jun. 2009.
- [196] B. Demirel and L. Gu andvenç and, "Parameter space design of repetitive controllers for satisfying a robust performance requirement," *IEEE Transactions on Automatic Control*, vol. 55, no. 8, pp. 1893–1899, Aug. 2010.
- [197] R. Grino, R. Cardoner, R. Costa-Castello, and E. Fossas, "Digital repetitive control of a three-phase four-wire shunt active filter," *IEEE Transactions on Industrial Electronics*, vol. 54, no. 3, pp. 1495–1503, Jun. 2007.
- [198] K. Zhou, D. Wang, B. Zhang, and Y. Wang, "Plug-in dual-mode-structure repetitive controller for CVCF PWM inverters," *IEEE Transactions on Industrial Electronics*, vol. 56, no. 3, pp. 784–791, Mar. 2009.

- [199] G. Escobar, A. Valdez, J. Leyva-Ramos, and P. Mattavelli, "Repetitive-based controller for a UPS inverter to compensate unbalance and harmonic distortion," *IEEE Transactions on Industrial Electronics*, vol. 54, no. 1, pp. 504–510, Feb. 2007.
- [200] G. Escobar, P. R. Martinez, and J. Leyva-Ramos, "Analog circuits to implement repetitive controllers with feedforward for harmonic compensation," *IEEE Transactions on Industrial Electronics*, vol. 54, no. 1, pp. 567–573, Feb. 2007.
- [201] G. Escobar, M. Hernandez-Gomez, P. R. Martinez, and M. F. Martinez-Montejano, "A repetitive-based controller for a power factor precompensator," *IEEE Transactions on Circuits and Systems I: Regular Papers*, vol. 54, no. 9, pp. 1968–1976, Sep. 2007.
- [202] G. Escobar, P. Hernandez-Briones, P. Martinez, M. Hernandez-Gomez, and R. Torres-Olguin, "A repetitive-based controller for the compensation of  $6\ell \pm 1$  harmonic components," *IEEE Transactions on Industrial Electronics*, vol. 55, no. 8, pp. 3150–3158, Aug. 2008.
- [203] R. I. Bojoi, G. Griva, V. Bostan, M. Guerriero, F. Farina, and F. Profumo, "Current control strategy for power conditioners using sinusoidal signal integrators in synchronous reference frame," *IEEE Transactions on Power Electronics*, vol. 20, no. 6, pp. 1402–1412, Nov. 2005.
- [204] M. Liserre, R. Teodorescu, and F. Blaabjerg, "Multiple harmonics control for three-phase grid converter systems with the use of PI-RES current controller in a rotating frame," *IEEE Transactions on Power Electronics*, vol. 21, no. 3, pp. 836–841, May 2006.
- [205] I. Etxeberria-Otadui, A. Lopez de Heredia, H. Gaztanaga, S. Bacha, and M. Reyero, "A single synchronous frame hybrid (SSFH) multifrequency controller for power active filters," *IEEE Transactions on Industrial Electronics*, vol. 53, no. 5, pp. 1640–1648, Oct. 2006.
- [206] P. Mattavelli and F. P. Marafao, "Repetitive-based control for selective harmonic compensation in active power filters," *IEEE Transactions on Industrial Electronics*, vol. 51, no. 5, pp. 1018–1024, Oct. 2004.
- [207] R. A. Mastromauro, M. Liserre, and A. Dell'Aquila, "Study of the effects of inductor nonlinear behavior on the performance of current controllers for single-phase PV grid converters," *IEEE Transactions on Industrial Electronics*, vol. 55, no. 5, pp. 2043–2052, May 2008.
- [208] R. A. Mastromauro, M. Liserre, T. Kerekes, and A. Dell'Aquila, "A single-phase voltage-controlled grid-connected photovoltaic system with power quality conditioner functionality," *IEEE Transactions on Industrial Electronics*, vol. 56, no. 11, pp. 4436–4444, Nov. 2009.
- [209] S. Dasgupta, S. K. Sahoo, S. K. Panda, and G. A. J. Amaratunga, "Single-phase inverter-control techniques for interfacing renewable energy sources with microgrid - part II: Series-connected inverter topology to mitigate voltage-related problems along with active power flow control," *IEEE Transactions on Power Electronics*, vol. 26, no. 3, pp. 732–746, Mar. 2011.

- [210] D. N. Zmood, D. G. Holmes, and G. H. Bode, "Frequency-domain analysis of three-phase linear current regulators," *IEEE Transactions on Industry Applications*, vol. 37, no. 2, pp. 601–610, Mar./Apr. 2001.
- [211] A. Dell'Aquila, M. Liserre, V. G. Monopoli, and P. Rotondo, "Overview of PI-based solutions for the control of DC buses of a single-phase H-bridge multilevel active rectifier," *IEEE Transactions on Industry Applications*, vol. 44, no. 3, pp. 857–866, May/Jun. 2008.
- [212] F. Wang, J. Duarte, and M. Hendrix, "Pliant active and reactive power control for grid-interactive converters under unbalanced voltage dips," *IEEE Transactions on Power Electronics*, vol. 26, no. 5, pp. 1511–1521, May 2011.
- [213] D. Ruiu, R. I. Bojoi, L. R. Limongi, and A. Tenconi, "New stationary frame control scheme for three-phase PWM rectifiers under unbalanced voltage dips conditions," *IEEE Transactions on Industry Applications*, vol. 46, no. 1, pp. 268–277, Jan./Feb. 2010.
- [214] Y.-S. Kwon, J.-H. Lee, S.-H. Moon, B.-K. Kwon, C.-H. Choi, and J.-K. Seok, "Standstill parameter identification of vector-controlled induction motors using the frequency characteristics of rotor bars," *IEEE Transactions on Industry Applications*, vol. 45, no. 5, pp. 1610–1618, Sep./Oct. 2009.
- [215] P. Zhou, Y. He, and D. Sun, "Improved direct power control of a DFIG-based wind turbine during network unbalance," *IEEE Transactions on Power Electronics*, vol. 24, no. 11, pp. 2465–2474, Nov. 2009.
- [216] R. Bojoi, G. Griva, F. Profumo, M. Cesano, and L. Natale, "Shunt active power filter implementation for induction heating applications," *COMPEL: The International Journal for Computation and Mathematics in Electrical and Electronic Engineering*, vol. 27, pp. 445–449, 2008.
- [217] F. Blaabjerg, R. Teodorescu, M. Liserre, and A. V. Timbus, "Overview of control and grid synchronization for distributed power generation systems," *IEEE Transactions on Industrial Electronics*, vol. 53, no. 5, pp. 1398–1409, Oct. 2006.
- [218] C. Wessels, F. Gebhardt, and F. W. Fuchs, "Fault ride-through of a DFIG wind turbine using a dynamic voltage restorer during symmetrical and asymmetrical grid faults," *IEEE Transactions on Power Electronics*, vol. 26, no. 3, pp. 807–815, Mar. 2011.
- [219] R. Teodorescu, M. Liserre, and P. Rodríguez, *Grid Converters for Photovoltaic and Wind Power Systems*, 1st ed. Wiley-IEEE Press, 2011.
- [220] R. Teodorescu, F. Blaabjerg, U. Borup, and M. Liserre, "A new control structure for grid-connected LCL PV inverters with zero steady-state error and selective harmonic compensation," in *Proceedings of IEEE Applied Power Electronics Conference, APEC*, vol. 1, 2004, pp. 580–586.
- [221] F. J. Rodriguez, E. Bueno, M. Aredes, L. G. B. Rolim, F. A. S. Neves, and M. C. Cavalcanti, "Discrete-time implementation of second order generalized integrators for grid converters," in *Proceedings of IEEE Industrial Electronics Conference, IECON*, Orlando, FL, Nov. 2008, pp. 176–181.

- [222] A. Kulka, T. Undeland, S. Vazquez, and L. Franquelo, "Stationary frame voltage harmonic controller for standalone power generation," in *Proceedings of European Conference on Power Electronics and Applications, EPE*, Sep. 2007, pp. 1–10.
- [223] M. Newman and D. Holmes, "Delta operator digital filters for high performance inverter applications," *IEEE Transactions on Power Electronics*, vol. 18, no. 1, pp. 447–454, Jan. 2003.
- [224] H. Tao, J. Duarte, and M. Hendrix, "Line-interactive UPS using a fuel cell as the primary source," *IEEE Transactions on Industrial Electronics*, vol. 55, no. 8, pp. 3012–3021, Aug. 2008.
- [225] M. Castilla, J. Miret, J. Matas, L. G. de Vicuna, and J. M. Guerrero, "Control design guidelines for single-phase grid-connected photovoltaic inverters with damped resonant harmonic compensators," *IEEE Transactions on Industrial Electronics*, vol. 56, no. 11, pp. 4492–4501, Nov. 2009.
- [226] L. Harnefors, "Implementation of resonant controllers and filters in fixed-point arithmetic," *IEEE Transactions on Industrial Electronics*, vol. 56, no. 4, pp. 1273–1281, Apr. 2009.
- [227] P. C. Loh, M. Newman, D. Zmood, and D. Holmes, "A comparative analysis of multiloop voltage regulation strategies for single and three-phase UPS systems," *IEEE Transactions on Power Electronics*, vol. 18, no. 5, pp. 1176–1185, Sep. 2003.
- [228] R. Teodorescu, F. Blaabjerg, M. Liserre, and P. C. Loh, "Proportional-resonant controllers and filters for grid-connected voltage-source converters," in *IEE Proceedings - Electric Power Applications*, vol. 153, no. 5, Sep. 2006, pp. 750–762.
- [229] S. Fukuda and R. Imamura, "Application of a sinusoidal internal model to current control of three-phase utility-interface converters," *IEEE Transactions on Industrial Electronics*, vol. 52, no. 2, pp. 420–426, Apr. 2005.
- [230] J. Miret, M. Castilla, J. Matas, J. Guerrero, and J. Vasquez, "Selective harmonic-compensation control for single-phase active power filter with high harmonic rejection," *IEEE Transactions on Industrial Electronics*, vol. 56, no. 8, pp. 3117–3127, Aug. 2009.
- [231] G. Escobar, A. Valdez, R. Torres-Olguin, and M. Martinez-Montejano, "A model-based controller for a three-phase four-wire shunt active filter with compensation of the neutral line current," *IEEE Transactions on Power Electronics*, vol. 22, no. 6, pp. 2261–2270, Nov. 2007.
- [232] A. Valdez, G. Escobar, and R. Ortega, "An adaptive controller for the shunt active filter considering a dynamic load and the line impedance," *IEEE Transactions on Control Systems Technology*, vol. 17, no. 2, pp. 458–464, Mar. 2009.
- [233] L. Asiminoaei, P. Rodriguez, F. Blaabjerg, and M. Malinowski, "Reduction of switching losses in active power filters with a new generalized discontinuous-PWM strategy," *IEEE Transactions on Industrial Electronics*, vol. 55, no. 1, pp. 467–471, Jan. 2008.

- [234] L. Asiminoaei, C. Lascu, F. Blaabjerg, and I. Boldea, "Performance improvement of shunt active power filter with dual parallel topology," *IEEE Transactions on Power Electronics*, vol. 22, no. 1, pp. 247–259, Jan. 2007.
- [235] L. Asiminoaei, E. Aeloiza, P. Enjeti, and F. Blaabjerg, "Shunt active-power-filter topology based on parallel interleaved inverters," *IEEE Transactions on Industrial Electronics*, vol. 55, no. 3, pp. 1175–1189, Mar. 2008.
- [236] Z. Shuai, A. Luo, J. Shen, and X. Wang, "Double closed-loop control method for injection-type hybrid active power filter," *IEEE Transactions on Power Electronics*, vol. 26, no. 9, pp. 2393–2403, Sep. 2011.
- [237] J. Hu and Y. He, "Reinforced control and operation of dfig-based wind-power-generation system under unbalanced grid voltage conditions," *IEEE Transactions on Energy Conversion*, vol. 24, no. 4, pp. 905–915, Dec. 2009.
- [238] J. Hu, H. Nian, H. Xu, and Y. He, "Dynamic modeling and improved control of DFIG under distorted grid voltage conditions," *IEEE Transactions on Energy Conversion*, vol. 26, no. 1, pp. 163–175, Mar. 2011.
- [239] L. Fan, R. Kavasseri, H. Yin, C. Zhu, and M. Hu, "Control of DFIG for rotor current harmonics elimination," in *Proceedings of IEEE Power Energy Society General Meeting, PES*, Jul. 2009, pp. 1–7.
- [240] G. K. Andersen, K. B. Larsen, and F. B. Bendixen, "Variable speed wind turbine, a resonant control system, a method of operating a variable speed wind turbine, use of a resonant control system and use of a method in a variable speed wind turbine," DK Patent 20 100 072 751, Mar., 2010.
- [241] V. Phan and H. Lee, "Enhanced proportional-resonant current controller for unbalanced stand-alone DFIG-based wind turbines," *Journal of Electrical Engineering & Technology*, vol. 5, no. 3, pp. 443–450, Sep. 2010.
- [242] V. Phan, H. Lee, and T. Chun, "An improved control strategy using a PI-resonant controller for an unbalanced stand-alone doubly-fed induction generator," *Journal of Power Electronics*, vol. 10, no. 2, pp. 194–202, Mar. 2010.
- [243] V.-T. Phan and H.-H. Lee, "Control strategy for harmonic elimination in stand-alone DFIG applications with nonlinear loads," *IEEE Transactions on Power Electronics*, vol. 26, no. 9, pp. 2662–2675, Sep. 2011.
- [244] M. A. Vallet, S. Bacha, I. Munteanu, A. I. Bratcu, and D. Roye, "Management and control of operating regimes of cross-flow water turbines," *IEEE Transactions on Industrial Electronics*, vol. 58, no. 5, pp. 1866–1876, May 2011.
- [245] R. Teodorescu, F. Blaabjerg, U. Borup, and M. Liserre, "A new control structure for grid-connected LCL PV inverters with zero steady-state error and selective harmonic compensation," in *Proceedings of IEEE Applied Power Electronics Conference, APEC*, vol. 1, 2004, pp. 580–586.

- [246] M. Castilla, J. Miret, J. Matas, L. G. de Vicuna, and J. M. Guerrero, "Linear current control scheme with series resonant harmonic compensator for single-phase grid-connected photovoltaic inverters," *IEEE Transactions on Industrial Electronics*, vol. 45, no. 7, pp. 2724–2733, Jul. 2008.
- [247] H. Cha, T.-K. Vu, and J.-E. Kim, "Design and control of proportional-resonant controller based photovoltaic power conditioning system," in *Proceedings of IEEE Energy Conversion Congress and Exposition, ECCE*, Sep. 2009, pp. 2198–2205.
- [248] A. Zue and A. Chandra, "Simulation and stability analysis of a 100 kW grid connected LCL photovoltaic inverter for industry," in *Proceedings of IEEE Power Engineering Society General Meeting*, Jun. 2006.
- [249] G. Valderrama, P. Mattavelli, and A. Stankovic, "Reactive power and imbalance compensation using STATCOM with dissipativity-based control," *IEEE Transactions on Control Systems Technology*, vol. 9, no. 5, pp. 718–727, Sep. 2001.
- [250] G. Escobar, A. Stankovic, and P. Mattavelli, "An adaptive controller in stationary reference frame for D-STATCOM in unbalanced operation," *IEEE Transactions on Industrial Electronics*, vol. 51, no. 2, pp. 401–409, Apr. 2004.
- [251] I. Etxeberria-Otadui, U. Viscarret, M. Caballero, A. Rufer, and S. Bacha, "New optimized PWM VSC control structures and strategies under unbalanced voltage transients," *IEEE Transactions on Industrial Electronics*, vol. 54, no. 5, pp. 2902–2914, Oct. 2007.
- [252] G. Escobar, P. Mattavelli, A. Stankovic, A. Valdez, and J. Leyva-Ramos, "An adaptive control for UPS to compensate unbalance and harmonic distortion using a combined capacitor/load current sensing," *IEEE Transactions on Industrial Electronics*, vol. 54, no. 2, pp. 839–847, Apr. 2007.
- [253] A. Hasanzadeh, O. Onar, H. Mokhtari, and A. Khaligh, "A proportional-resonant controller-based wireless control strategy with a reduced number of sensors for parallel-operated UPSs," *IEEE Transactions on Power Delivery*, vol. 25, no. 1, pp. 468–478, Jan. 2010.
- [254] M. Newman, D. Holmes, J. Nielsen, and F. Blaabjerg, "A dynamic voltage restorer (DVR) with selective harmonic compensation at medium voltage level," *IEEE Transactions on Industry Applications*, vol. 41, no. 6, pp. 1744–1753, Nov./Dec. 2005.
- [255] Y. W. Li, F. Blaabjerg, D. M. Vilathgamuwa, and P. C. Loh, "Design and comparison of high performance stationary-frame controllers for DVR implementation," *IEEE Transactions on Power Electronics*, vol. 22, no. 2, pp. 602–612, Mar. 2007.
- [256] Y. W. Li, "Control and resonance damping of voltage-source and current-source converters with LC filters," *IEEE Transactions on Industrial Electronics*, vol. 56, no. 5, pp. 1511–1521, May 2009.
- [257] J. D. Barros and J. F. Silva, "Multilevel optimal predictive dynamic voltage restorer," *IEEE Transactions on Industrial Electronics*, vol. 57, no. 8, pp. 2747–2760, Aug. 2010.

- [258] F. M. Mahdianpoor, R. A. Hooshmand, and M. Ataei, "A new approach to multifunctional dynamic voltage restorer implementation for emergency control in distribution systems," *IEEE Transactions on Power Delivery*, vol. 26, no. 2, pp. 882–890, Jan. 2011.
- [259] Y. Suh and T. Lipo, "Control scheme in hybrid synchronous stationary frame for PWM ac/dc converter under generalized unbalanced operating conditions," *IEEE Transactions on Industry Applications*, vol. 42, no. 3, pp. 825–835, May 2006.
- [260] D. Basic, V. S. Ramsden, and P. K. Muttik, "Harmonic filtering of high-power 12-pulse rectifier loads with aselective hybrid filter system," *IEEE Transactions on Industrial Electronics*, vol. 48, no. 6, pp. 1118–1127, Dec. 2001.
- [261] G. Escobar, A. Valdez, J. Leyva-Ramos, and P. Martinez, "A controller for a boost converter with harmonic reduction," *IEEE Transactions on Control Systems Technology*, vol. 12, no. 5, pp. 717–726, Sep. 2004.
- [262] R. Bojoi, A. Tenconi, G. Griva, and F. Profumo, "Vector control of dual-three-phase induction-motor drives using two current sensors," *IEEE Transactions on Industry Applications*, vol. 42, no. 5, pp. 1284–1292, Sep./Oct. 2006.
- [263] M.-C. Chou and C.-M. Liaw, "Dynamic control and diagnostic friction estimation for an SPMSM-driven satellite reaction wheel," *IEEE Transactions on Industrial Electronics*, vol. 58, no. 10, pp. 4693–4707, Oct. 2011.
- [264] P. Degobert, G. Remy, J. Zeng, P.-J. Barre, and J.-P. Hautier, "High performance control of the permanent magnet synchronous motor using self-tuning resonant controllers," in *Proceeding of the Southeastern Symposium on System Theory, SSST*, Mar. 2006, pp. 382–386.
- [265] J. Zeng, P. Degobert, and J.-P. Hautier, "Minimum torque ripple control of permanent magnet synchronous motor in the stationary reference frame," in *Proceedings of IET Conference on Power Electronics, Machines and Drives, PEMD*, 15-15 2005, pp. 667–673.
- [266] H. Yu, "A novel digital current control strategy for torque ripple reduction in permanent magnet synchronous motor drives," in *Proceedings of IEEE Applied Power Electronics Conference, APEC*, Feb. 2010, pp. 2025–2029.
- [267] Z. Wang, H. Nian, and J. Hu, "Enhanced control strategies of permanent magnet synchronous wind power generation system under unbalanced grid voltage conditions," in *Proceeding of Conference on Power and Energy Engineering Conference, APPEEC*, Mar. 2010, pp. 1–4.
- [268] H. Wang, W. Zhang, J. Hu, and Y. He, "Design and optimization of proportional resonant controller for rotor current of a wind turbine driven DFIG," in *Proceedings of International Conference on Electrical Machines and Systems, ICEMS*, Oct. 2008, pp. 2502–2506.

- [269] Z. Tan, X. Yuan, C. Wang, R. Qu, R. W. Delmerico, and P. L. Jansen, "System and method for controlling torque ripples in synchronous machines," U.S. Patent 20 110 018 281, Jan., 2011.
- [270] T. Hornik and Q.-C. Zhong, "A current-control strategy for voltage-source inverters in microgrids based on  $H^\infty$  and repetitive control," *IEEE Transactions on Power Electronics*, vol. 26, no. 3, pp. 943–952, Mar. 2011.
- [271] Y. W. Li, D. M. Vilathgamuwa, and P. C. Loh, "Robust control scheme for a microgrid with PFC capacitor connected," *IEEE Transactions on Industry Applications*, vol. 43, no. 5, pp. 1172–1182, Sep./Oct. 2007.
- [272] A. M. Roslan, K. H. Ahmed, S. J. Finney, and B. W. Williams, "Improved instantaneous average current-sharing control scheme for parallel-connected inverter considering line impedance impact in microgrid networks," *IEEE Transactions on Power Electronics*, vol. 26, no. 3, pp. 702–716, Mar. 2011.
- [273] J. Rocabert, G. M. S. Azevedo, A. Luna, J. M. Guerrero, J. I. Candela, and P. Rodríguez, "Intelligent connection agent for three-phase grid-connected microgrids," *IEEE Transactions on Power Electronics*, vol. 26, no. 10, pp. 2993–3005, Oct. 2011.
- [274] F. Wang, J. L. Duarte, and M. A. M. Hendrix, "Grid-interfacing converter systems with enhanced voltage quality for microgrid application - concept and implementation," *IEEE Transactions on Power Electronics*, vol. 26, no. 12, pp. 3501–3513, Dec. 2011.
- [275] J.-S. Lai, S. Y. Park, and C.-L. Chen, "Control system and method for a universal power conditioning system," U.S. Patent 20 080 205 096, Aug., 2008.
- [276] W. Lenwari, M. Sumner, and P. Zanchetta, "The use of genetic algorithms for the design of resonant compensators for active filters," *IEEE Transactions on Industrial Electronics*, vol. 56, no. 8, pp. 2852–2861, Aug. 2009.
- [277] Z. Li, Y. Li, P. Wang, H. Zhu, C. Liu, and F. Gao, "Single-loop digital control of high-power 400-Hz ground power unit for airplanes," *IEEE Transactions on Industrial Electronics*, vol. 57, no. 2, pp. 532–543, Feb. 2010.
- [278] P. C. Loh and D. Holmes, "Analysis of multiloop control strategies for LC/CL/LCL-filtered voltage-source and current-source inverters," *IEEE Transactions on Industry Applications*, vol. 41, no. 2, pp. 644–654, / 2005.
- [279] D. De and V. Ramanarayanan, "A proportional + multiresonant controller for three-phase four-wire high-frequency link inverter," *IEEE Transactions on Power Electronics*, vol. 25, no. 4, pp. 899–906, Apr. 2010.
- [280] A. Garcia-Cerrada, P. Roncero-Sanchez, P. Garcia-Gonzalez, and V. Feliu-Batlle, "Detailed analysis of closed-loop control of output-voltage harmonics in voltage-source inverters," in *IEE Proceedings - Electric Power Applications*, vol. 151, no. 6, Nov. 2004, pp. 734–743.

- [281] L. Della Flora and H. Grundling, "Time domain sinusoidal acceleration controller for an electrodynamic shaker," *IET Control Theory Applications*, vol. 2, no. 12, pp. 1044–1053, Dec. 2008.
- [282] S. Grogan, D. Holmes, and B. McGrath, "High-performance voltage regulation of current source inverters," *IEEE Transactions on Power Electronics*, vol. 26, no. 9, pp. 2439 – 2448, Sep. 2011.
- [283] D. Halim and S. Moheimani, "Spatial resonant control of flexible structures-application to a piezoelectric laminate beam," *IEEE Transactions on Control Systems Technology*, vol. 9, no. 1, pp. 37–53, Jan. 2001.
- [284] J. Hwang, P. Lehn, and M. Winkelkemper, "A generalized class of stationary frame-current controllers for grid-connected ac-dc converters," *IEEE Transactions on Power Delivery*, vol. 25, no. 4, pp. 2742–2751, Oct. 2010.
- [285] J. G. Hwang and P. W. Lehn, "A single-input space vector for control of ac-dc converters under generalized unbalanced operating conditions," *IEEE Transactions on Power Electronics*, vol. 25, no. 8, pp. 2068–2081, Aug. 2010.
- [286] I. Mahmood, S. Moheimani, and B. Bhikkaji, "Precise tip positioning of a flexible manipulator using resonant control," *IEEE/ASME Transactions on Mechatronics*, vol. 13, no. 2, pp. 180–186, Apr. 2008.
- [287] E. Pereira, S. Aphale, V. Feliu, and S. Moheimani, "Integral resonant control for vibration damping and precise tip-positioning of a single-link flexible manipulator," *IEEE/ASME Transactions on Mechatronics*, vol. 16, no. 2, pp. 232–240, Apr. 2011.
- [288] H. Qian, J. Zhang, J.-S. Lai, and W. Yu, "A high-efficiency grid-tie battery energy storage system," *IEEE Transactions on Power Electronics*, vol. 26, no. 3, pp. 886–896, Mar. 2011.
- [289] T. M. Rowan and R. J. Kerkman, "A new synchronous current regulator and an analysis of current-regulated PWM inverters," *IEEE Transactions on Industry Applications*, vol. IA-22, no. 4, pp. 678–690, Jul. 1986.
- [290] A. Leon, J. Mauricio, J. Solsona, and A. Gómez-Expósito, "Adaptive control strategy for VSC-based systems under unbalanced network conditions," *IEEE Transactions on Smart Grid*, vol. 1, no. 3, pp. 311–319, Dec. 2010.
- [291] M. Bodson, A. Sacks, and P. Khosla, "Harmonic generation in adaptive feedforward cancellation schemes," *IEEE Transactions on Automatic Control*, vol. 39, no. 9, pp. 1939–1944, Sep. 1994.
- [292] R. Cardenas-Dobson, C. Juri, R. Pena, P. Wheeler, and J. Clare, "The application of resonant controllers to 4-leg matrix converters feeding unbalanced or non-linear loads," *IEEE Transactions on Power Electronics*, accepted for publication.
- [293] W. Zhao, D. D.-C. Lu, and V. G. Agelidis, "Current control of grid-connected boost inverter with zero steady-state error," *IEEE Transactions on Power Electronics*, vol. 26, no. 10, pp. 2825 –2834, Oct. 2011.

- [294] J. He, Y. W. Li, and M. S. Munir, "A flexible harmonic control approach through voltage-controlled DG-grid interfacing converters," *IEEE Transactions on Industrial Electronics*, vol. 59, no. 1, pp. 444–455, Jan. 2012.
- [295] F. Cupertino, G. Pellegrino, P. Giangrande, and L. Salvatore, "Sensorless position control of permanent-magnet motors with pulsating current injection and compensation of motor end effects," *IEEE Transactions on Industry Applications*, vol. 47, no. 3, pp. 1371–1379, May/June. 2011.
- [296] Y.-R. Mohamed, "Mitigation of converter-grid resonance, grid-induced distortion, and parametric instabilities in converter-based distributed generation," *IEEE Transactions on Power Electronics*, vol. 26, no. 3, pp. 983–996, Mar. 2011.
- [297] D. Dong, T. Thacker, R. Burgos, F. Wang, and D. Boroyevich, "On zero steady-state error voltage control of single-phase PWM inverters with different load types," *IEEE Transactions on Power Electronics*, vol. 26, no. 11, pp. 3285–3297, Nov. 2011.
- [298] B. McGrath, D. Holmes, and S. Parker, "Current regulation strategies for vector controlled induction motor drives," *IEEE Transactions on Industrial Electronics*, in press.
- [299] B. Yin, R. Oruganti, S. Panda, and A. Bhat, "An output-power-control strategy for a three-phase PWM rectifier under unbalanced supply conditions," *IEEE Transactions on Industrial Electronics*, vol. 55, no. 5, pp. 2140–2151, May 2008.
- [300] Y. Suh, Y. Go, and D. Rho, "A comparative study on control algorithm for active front-end rectifier of large motor drives under unbalanced input," *IEEE Transactions on Industry Applications*, vol. 47, no. 3, pp. 1419–1431, May/June. 2011.
- [301] M. Rifai, T. Ortmeyer, and W. McQuillan, "Evaluation of current interharmonics from AC drives," *IEEE Transactions on Power Delivery*, vol. 15, no. 3, pp. 1094–1098, Jul. 2000.
- [302] G. Chang, S.-K. Chen, H.-J. Su, and P.-K. Wang, "Accurate assessment of harmonic and interharmonic currents generated by VSI-fed drives under unbalanced supply voltages," *IEEE Transactions on Power Delivery*, vol. 26, no. 2, pp. 1083–1091, Apr. 2011.
- [303] D. Basic, "Input current interharmonics of variable-speed drives due to motor current imbalance," *IEEE Transactions on Power Delivery*, vol. 25, no. 4, pp. 2797–2806, Oct. 2010.
- [304] G. Chang and S.-K. Chen, "An analytical approach for characterizing harmonic and interharmonic currents generated by VSI-fed adjustable speed drives," *IEEE Transactions on Power Delivery*, vol. 20, no. 4, pp. 2585–2593, Oct. 2005.
- [305] F. De Rosa, R. Langella, A. Sollazzo, and A. Testa, "On the interharmonic components generated by adjustable speed drives," *IEEE Transactions on Power Delivery*, vol. 20, no. 4, pp. 2535–2543, Oct. 2005.
- [306] H. T. N. Charles L. Phillips, *Digital Control System Analysis and Design. 3rd Edition*. Prentice Hall, 1995.

- [307] A. V. Timbus, M. Ciobotaru, R. Teodorescu, and F. Blaabjerg, "Adaptive resonant controller for grid-connected converters in distributed power generation systems," in *Proceedings of IEEE Applied Power Electronics Conference, APEC*, Mar. 2006.
- [308] X. Guillaud, P. Degobert, and R. Teodorescu, "Use of resonant controller for grid-connected converters in case of large frequency fluctuations," in *Proceedings of European Conference on Power Electronics and Applications, EPE*, Aalborg, Sep. 2007.
- [309] F. D. Freijedo, J. Doval-Gandoy, O. Lopez, P. Fernandez-Comesaña, and C. Martinez-Peñalver, "A signal-processing adaptive algorithm for selective current harmonic cancellation in active power filters," *IEEE Transactions on Industrial Electronics*, vol. 56, no. 8, pp. 2829–2840, Aug. 2009.
- [310] J. Doval-Gandoy, A. Nogueiras, C. M. Peñalver, and A. Lago., "Shunt active power filter with harmonic current control strategy," in *Proceedings of IEEE Power Electronics Specialists Conference, PESC*, 1998.
- [311] L. Zhao, C. Ham, Q. Han, T. Wu, L. Zheng, K. Sundaram, J. Kapat, and L. Chow, "Design of optimal digital controller for stable super-high-speed permanent-magnet synchronous motor," *IEE Proceedings Electric Power Applications*, vol. 153, no. 2, pp. 213–218, Mar. 2006.
- [312] R. Ancuti, I. Boldea, and G.-D. Andreescu, "Sensorless V/f control of high-speed surface permanent magnet synchronous motor drives with two novel stabilising loops for fast dynamics and robustness," *IET Electric Power Applications*, vol. 4, no. 3, pp. 149–157, Mar. 2010.
- [313] P. Zanchetta, D. Gerry, V. Monopoli, J. Clare, and P. Wheeler, "Predictive current control for multilevel active rectifiers with reduced switching frequency," *IEEE Transactions on Industrial Electronics*, vol. 55, no. 1, pp. 163–172, Jan. 2008.
- [314] J. Holtz and N. Oikonomou, "Fast dynamic control of medium voltage drives operating at very low switching frequency-an overview," *IEEE Transactions on Industrial Electronics*, vol. 55, no. 3, pp. 1005–1013, Mar. 2008.
- [315] H. Abu-Rub, J. Holtz, J. Rodriguez, and G. Baoming, "Medium-voltage multilevel converters;state of the art, challenges, and requirements in industrial applications," *IEEE Transactions on Industrial Electronics*, vol. 57, no. 8, pp. 2581–2596, Aug. 2010.
- [316] G. Abad, M. Rodriguez, and J. Poza, "Three-level NPC converter-based predictive direct power control of the doubly fed induction machine at low constant switching frequency," *IEEE Transactions on Industrial Electronics*, vol. 55, no. 12, pp. 4417–4429, Dec. 2008.
- [317] F. Vargas-Merino, M. Meco-Gutierrez, J. Heredia-Larrubia, and A. Ruiz-Gonzalez, "Low switching PWM strategy using a carrier wave regulated by the slope of a trapezoidal modulator wave," *IEEE Transactions on Industrial Electronics*, vol. 56, no. 6, pp. 2270–2274, Jun. 2009.

- [318] D. G. Holmes, T. A. Lipo, B. McGrath, and W. Kong, "Optimized design of stationary frame three phase AC current regulators," *IEEE Transactions on Power Electronics*, vol. 24, no. 11, pp. 2417–2426, Nov. 2009.
- [319] F. Cupertino, E. Lavopa, P. Zanchetta, M. Sumner, and L. Salvatore, "Running DFT-based PLL algorithm for frequency, phase, and amplitude tracking in aircraft electrical systems," *IEEE Transactions on Industrial Electronics*, vol. 58, no. 3, pp. 1027–1035, Mar. 2011.
- [320] A. Rathore, J. Holtz, and T. Boller, "Synchronous optimal pulsewidth modulation for low-switching-frequency control of medium-voltage multilevel inverters," *IEEE Transactions on Industrial Electronics*, vol. 57, no. 7, pp. 2374–2381, Jul. 2010.
- [321] G. F. Franklin, J. D. Powell, and A. Emami-Naeini, *Feedback Control of Dynamic Systems*. Pearson Education, 2002.
- [322] G. C. Goodwin, S. F. Graebe, and M. E. Salgado, *Control System Design*. Prentice Hall, 2000.
- [323] M. Takyar, A. Amini, and T. Georgiou, "Weight selection in feedback design with degree constraints," *IEEE Transactions on Automatic Control*, vol. 53, no. 8, pp. 1951–1955, Sep. 2008.
- [324] K. Ogata, *Modern Control Engineering*. Prentice Hall, 2009.



# Appendix A

## Mathematical Development of Expressions for Chapter 2

### A.1 Discretization of Resonant Controllers without Delay Compensation

#### A.1.1 Zero-Order Hold

Discretization of  $R_{1_h}(s)$  with the zero-order hold (ZOH) method yields

$$\begin{aligned} R_{1_h}^{\text{zoh}}(z) &= (1 - z^{-1}) \mathcal{Z} \left\{ \mathcal{L}^{-1} \left[ \frac{R_{1_h}(s)}{s} \right] \right\} = (1 - z^{-1}) \mathcal{Z} \left[ \mathcal{L}^{-1} \left( \frac{1}{s^2 + h^2 \omega_1^2} \right) \right] \\ &= (1 - z^{-1}) \mathcal{Z} \left[ \frac{1}{h\omega_1} \sin(h\omega_1 t) \right] = \frac{1 - z^{-1}}{h\omega_1} \frac{z^{-1} \sin(h\omega_1 T_s)}{1 - 2z^{-1} \cos(h\omega_1 T_s) + z^{-2}} \\ &= \frac{\sin(h\omega_1 T_s)}{h\omega_1} \frac{z^{-1} - z^{-2}}{1 - 2z^{-1} \cos(h\omega_1 T_s) + z^{-2}}. \end{aligned} \quad (\text{A.1})$$

Discretization of  $R_{2_h}(s)$  with the ZOH method yields

$$\begin{aligned} R_{2_h}^{\text{zoh}}(z) &= (1 - z^{-1}) \mathcal{Z} \left\{ \mathcal{L}^{-1} \left[ \frac{R_{2_h}(s)}{s} \right] \right\} = (1 - z^{-1}) \mathcal{Z} \left[ \mathcal{L}^{-1} \left( \frac{s}{s^2 + h^2 \omega_1^2} \right) \right] \\ &= (1 - z^{-1}) \mathcal{Z} [\cos(h\omega_1 t)] = (1 - z^{-1}) \frac{1 - z^{-1} \cos(h\omega_1 T_s)}{1 - 2z^{-1} \cos(h\omega_1 T_s) + z^{-2}} \\ &= \frac{1 - z^{-1} [\cos(h\omega_1 T_s) + 1] + z^{-2} \cos(h\omega_1 T_s)}{1 - 2z^{-1} \cos(h\omega_1 T_s) + z^{-2}}. \end{aligned} \quad (\text{A.2})$$

### A.1.2 First-Order Hold

Discretization of  $R_{1_h}(s)$  with the first-order hold (FOH) method yields

$$\begin{aligned}
R_{1_h}^{\text{foh}}(z) &= \frac{(1-z^{-1})^2}{z^{-1}T_s} \mathcal{Z} \left\{ \mathcal{L}^{-1} \left[ \frac{R_{1_h}(s)}{s^2} \right] \right\} = \frac{(1-z^{-1})^2}{z^{-1}T_s} \mathcal{Z} \left\{ \mathcal{L}^{-1} \left[ \frac{1}{s(s^2+h^2\omega_1^2)} \right] \right\} \\
&= \frac{(1-z^{-1})^2}{z^{-1}T_s} \mathcal{Z} \left[ \frac{1}{h^2\omega_1^2} - \frac{1}{h^2\omega_1^2} \cos(h\omega_1 t) \right] \\
&= \frac{(1-z^{-1})^2}{z^{-1}h^2\omega_1^2 T_s} \left[ \frac{1}{1-z^{-1}} - \frac{1-z^{-1}\cos(h\omega_1 T_s)}{1-2z^{-1}\cos(h\omega_1 T_s)+z^{-2}} \right] \\
&= \frac{1}{h^2\omega_1^2 T_s} \frac{(z-1) [1-2z^{-1}\cos(h\omega_1 T_s)+z^{-2}] - (z-2+z^{-1}) [1-z^{-1}\cos(h\omega_1 T_s)]}{1-2z^{-1}\cos(h\omega_1 T_s)+z^{-2}} \\
&= \frac{1-\cos(h\omega_1 T_s)}{h^2\omega_1^2 T_s} \frac{1-z^{-2}}{1-2z^{-1}\cos(h\omega_1 T_s)+z^{-2}}.
\end{aligned} \tag{A.3}$$

Discretization of  $R_{2_h}(s)$  with the FOH method yields

$$\begin{aligned}
R_{2_h}^{\text{foh}}(z) &= \frac{(1-z^{-1})^2}{z^{-1}T_s} \mathcal{Z} \left\{ \mathcal{L}^{-1} \left[ \frac{R_{2_h}(s)}{s^2} \right] \right\} = \frac{(1-z^{-1})^2}{z^{-1}T_s} \mathcal{Z} \left[ \mathcal{L}^{-1} \left( \frac{1}{s^2+h^2\omega_1^2} \right) \right] \\
&= \frac{(1-z^{-1})^2}{z^{-1}T_s} \mathcal{Z} \left[ \frac{1}{h\omega_1} \sin(h\omega_1 t) \right] = \frac{(1-z^{-1})^2}{z^{-1}h\omega_1 T_s} \frac{z^{-1}\sin(h\omega_1 T_s)}{1-2z^{-1}\cos(h\omega_1 T_s)+z^{-2}} \\
&= \frac{\sin(h\omega_1 T_s)}{h\omega_1 T_s} \frac{1-2z^{-1}+z^{-2}}{1-2z^{-1}\cos(h\omega_1 T_s)+z^{-2}}.
\end{aligned} \tag{A.4}$$

### A.1.3 Forward Euler

Discretization of  $R_{1_h}(s)$  with the forward Euler method yields

$$R_{1_h}^{\text{f}}(z) = \frac{\frac{1-z^{-1}}{z^{-1}T_s}}{\left(\frac{1-z^{-1}}{z^{-1}T_s}\right)^2 + h^2\omega_1^2} = \frac{z^{-1}(1-z^{-1})T_s}{(1-z^{-1})^2 + z^{-2}h^2\omega_1^2 T_s^2} = T_s \frac{z^{-1}-z^{-2}}{1-2z^{-1}+z^{-2}(h^2\omega_1^2 T_s^2+1)}. \tag{A.5}$$

Discretization of  $R_{2_h}(s)$  with the forward Euler method yields

$$R_{2_h}^{\text{f}}(z) = \frac{\left(\frac{1-z^{-1}}{z^{-1}T_s}\right)^2}{\left(\frac{1-z^{-1}}{z^{-1}T_s}\right)^2 + h^2\omega_1^2} = \frac{(1-z^{-1})^2}{(1-z^{-1})^2 + z^{-2}h^2\omega_1^2 T_s^2} = \frac{1-2z^{-1}+z^{-2}}{1-2z^{-1}+z^{-2}(h^2\omega_1^2 T_s^2+1)}. \tag{A.6}$$

### A.1.4 Backward Euler

Discretization of  $R_{1_h}(s)$  with the backward Euler method yields

$$R_{1_h}^{\text{b}}(z) = \frac{\frac{1-z^{-1}}{T_s}}{\left(\frac{1-z^{-1}}{T_s}\right)^2 + h^2\omega_1^2} = \frac{(1-z^{-1})T_s}{(1-z^{-1})^2 + h^2\omega_1^2 T_s^2} = T_s \frac{1-z^{-1}}{(h^2\omega_1^2 T_s^2+1) - 2z^{-1}+z^{-2}}. \tag{A.7}$$

Discretization of  $R_{2_h}(s)$  with the backward Euler method yields

$$R_{2_h}^b(z) = \frac{\left(\frac{1-z^{-1}}{T_s}\right)^2}{\left(\frac{1-z^{-1}}{T_s}\right)^2 + h^2\omega_1^2} = \frac{(1-z^{-1})^2}{(1-z^{-1})^2 + h^2\omega_1^2 T_s^2} = \frac{1-2z^{-1}+z^{-2}}{(h^2\omega_1^2 T_s^2 + 1) - 2z^{-1} + z^{-2}}. \quad (\text{A.8})$$

### A.1.5 Tustin

Discretization of  $R_{1_h}(s)$  with the Tustin method yields

$$\begin{aligned} R_{1_h}^t(z) &= \frac{\frac{2}{T_s} \frac{1-z^{-1}}{1+z^{-1}}}{\left(\frac{2}{T_s} \frac{1-z^{-1}}{1+z^{-1}}\right)^2 + h^2\omega_1^2} = \frac{2(1-z^{-1})(1+z^{-1})T_s}{4(1-z^{-1})^2 + (1+z^{-1})^2 h^2\omega_1^2 T_s^2} \\ &= 2T_s \frac{1-z^{-2}}{(h^2\omega_1^2 T_s^2 + 4) + z^{-1}(2h^2\omega_1^2 T_s^2 - 8) + z^{-2}(h^2\omega_1^2 T_s^2 + 4)}. \end{aligned} \quad (\text{A.9})$$

Discretization of  $R_{2_h}(s)$  with the Tustin method yields

$$\begin{aligned} R_{2_h}^t(z) &= \frac{\left(\frac{2}{T_s} \frac{1-z^{-1}}{1+z^{-1}}\right)^2}{\left(\frac{2}{T_s} \frac{1-z^{-1}}{1+z^{-1}}\right)^2 + h^2\omega_1^2} = \frac{4(1-z^{-1})^2}{4(1-z^{-1})^2 + (1+z^{-1})^2 h^2\omega_1^2 T_s^2} \\ &= 4 \frac{1-2z^{-1}+z^{-2}}{(h^2\omega_1^2 T_s^2 + 4) + z^{-1}(2h^2\omega_1^2 T_s^2 - 8) + z^{-2}(h^2\omega_1^2 T_s^2 + 4)}. \end{aligned} \quad (\text{A.10})$$

### A.1.6 Tustin with Prewarping

Discretization of  $R_{1_h}(s)$  with the Tustin with prewarping method yields

$$\begin{aligned} R_{1_h}^{\text{tp}}(z) &= \frac{\frac{h\omega_1}{\tan\left(\frac{h\omega_1 T_s}{2}\right)} \frac{1-z^{-1}}{1+z^{-1}}}{\left[\frac{h\omega_1}{\tan\left(\frac{h\omega_1 T_s}{2}\right)} \frac{1-z^{-1}}{1+z^{-1}}\right]^2 + h^2\omega_1^2} = \frac{1}{h\omega_1} \frac{\tan\left(\frac{h\omega_1 T_s}{2}\right) \frac{1-z^{-1}}{1+z^{-1}}}{\frac{(1-z^{-1})^2}{(1+z^{-1})^2} + \tan^2\left(\frac{h\omega_1 T_s}{2}\right)} \\ &= \frac{1}{h\omega_1} \frac{\sin\left(\frac{h\omega_1 T_s}{2}\right) \cos\left(\frac{h\omega_1 T_s}{2}\right) (1-z^{-1})(1+z^{-1})}{\cos^2\left(\frac{h\omega_1 T_s}{2}\right) (1-z^{-1})^2 + \sin^2\left(\frac{h\omega_1 T_s}{2}\right) (1+z^{-1})^2} \\ &= \frac{\sin(h\omega_1 T_s)}{2h\omega_1} \frac{(1-z^{-1})(1+z^{-1})}{\cos^2\left(\frac{h\omega_1 T_s}{2}\right) (1-2z^{-1}+z^{-2}) + \sin^2\left(\frac{h\omega_1 T_s}{2}\right) (1+2z^{-1}+z^{-2})} \\ &= \frac{\sin(h\omega_1 T_s)}{2h\omega_1} \frac{1-z^{-2}}{1-2z^{-1}\cos(h\omega_1 T_s) + z^{-2}}. \end{aligned} \quad (\text{A.11})$$

Discretization of  $R_{2_h}(s)$  with the Tustin with prewarping method yields

$$\begin{aligned}
R_{2_h}^{\text{tp}}(z) &= \frac{\left[ \frac{h\omega_1}{\tan\left(\frac{h\omega_1 T_s}{2}\right)} \frac{1-z^{-1}}{1+z^{-1}} \right]^2}{\left[ \frac{h\omega_1}{\tan\left(\frac{h\omega_1 T_s}{2}\right)} \frac{1-z^{-1}}{1+z^{-1}} \right]^2 + h^2 \omega_1^2} = \frac{\frac{(1-z^{-1})^2}{(1+z^{-1})^2}}{\frac{(1-z^{-1})^2}{(1+z^{-1})^2} + \tan^2\left(\frac{h\omega_1 T_s}{2}\right)} \\
&= \frac{\cos^2\left(\frac{h\omega_1 T_s}{2}\right) (1-z^{-1})^2}{\cos^2\left(\frac{h\omega_1 T_s}{2}\right) (1-z^{-1})^2 + \sin^2\left(\frac{h\omega_1 T_s}{2}\right) (1+z^{-1})^2} \\
&= \cos^2\left(\frac{h\omega_1 T_s}{2}\right) \frac{1-2z^{-1}+z^{-2}}{\cos^2\left(\frac{h\omega_1 T_s}{2}\right) (1-2z^{-1}+z^{-2}) + \sin^2\left(\frac{h\omega_1 T_s}{2}\right) (1+2z^{-1}+z^{-2})} \\
&= \cos^2\left(\frac{h\omega_1 T_s}{2}\right) \frac{1-2z^{-1}+z^{-2}}{1-2z^{-1}\cos(h\omega_1 T_s) + z^{-2}}.
\end{aligned} \tag{A.12}$$

### A.1.7 Zero-Pole Matching

The poles of  $R_{1_h}(s)$  are  $s = jh\omega_1$  and  $s = -jh\omega_1$ , and its zero is  $s = 0$ . Therefore, the poles of the discrete-time transfer function are  $z = e^{jh\omega_1 T_s}$  and  $z = e^{-jh\omega_1 T_s}$ , and its zero is  $z = e^0 = 1$ :

$$\begin{aligned}
R_{1_h}^{\text{zpm}}(z) &= K_d \frac{z-1}{(z-e^{jh\omega_1 T_s})(z-e^{-jh\omega_1 T_s})} \\
&= K_d \frac{z-1}{[z-\cos(h\omega_1 T_s) - j\sin(h\omega_1 T_s)][z-\cos(h\omega_1 T_s) + j\sin(h\omega_1 T_s)]} \\
&= K_d \frac{z-1}{[z-\cos(h\omega_1 T_s)]^2 - [j\sin(h\omega_1 T_s)]^2} \\
&= K_d \frac{z-1}{z^2 + \cos^2(h\omega_1 T_s) - 2z\cos(h\omega_1 T_s) + \sin^2(h\omega_1 T_s)} \\
&= K_d \frac{z^{-1} - z^{-2}}{1 - 2z^{-1}\cos(h\omega_1 T_s) + z^{-2}}.
\end{aligned} \tag{A.13}$$

The roots of  $R_{2_h}(s)$  are the same as those of  $R_{1_h}(s)$ , except for the fact that  $R_{2_h}(s)$  has an additional zero at the origin:

$$R_{2_h}^{\text{zpm}}(z) = (z-1)R_{1_h}^{\text{zpm}}(z) = K_d \frac{1-2z^{-1}+z^{-2}}{1-2z^{-1}\cos(h\omega_1 T_s) + z^{-2}}. \tag{A.14}$$

### A.1.8 Impulse Invariant

Discretization of  $R_{1_h}(s)$  with the impulse invariant method yields

$$R_{1_h}^{\text{imp}}(z) = T_s \mathcal{Z} \left\{ \mathcal{L}^{-1} \left[ \frac{s}{s^2 + h^2 \omega_1^2} \right] \right\} = T_s \mathcal{Z} [\cos(h\omega_1 t)] = T_s \frac{1-z^{-1}\cos(h\omega_1 T_s)}{1-2z^{-1}\cos(h\omega_1 T_s) + z^{-2}}. \tag{A.15}$$

Discretization of  $R_{2_h}(s)$  with the impulse invariant method yields

$$\begin{aligned} R_{2_h}^{\text{imp}}(z) &= T_s \mathcal{Z} \left\{ \mathcal{L}^{-1} \left[ \frac{s^2}{s^2 + h^2 \omega_1^2} \right] \right\} = T_s \mathcal{Z} [-h\omega_1 \sin(h\omega_1 t)] \\ &= -h\omega_1 T_s \frac{z^{-1} \sin(h\omega_1 T_s)}{1 - 2z^{-1} \cos(h\omega_1 T_s) + z^{-2}}. \end{aligned} \quad (\text{A.16})$$

### A.1.9 Forward Euler & Backward Euler

Application of Masons' gain formula [31] to the scheme that results from Fig. 1.22a (proportional-resonant (PR) controller) when the direct integrator is discretized with forward Euler, and the feedback one is discretized with backward Euler, yields

$$\begin{aligned} G_{\text{PR}_h}^{\text{f\&b}}(z) &= K_{\text{P}_h} + \frac{K_{\text{I}_h} \frac{z^{-1} T_s}{1-z^{-1}}}{1 + h^2 \omega_1^2 \frac{T_s}{1-z^{-1}} \frac{z^{-1} T_s}{1-z^{-1}}} = K_{\text{P}_h} + \frac{K_{\text{I}_h} T_s z^{-1} (1-z^{-1})}{(1-z^{-1})^2 + z^{-1} h^2 \omega_1^2 T_s^2} \\ &= K_{\text{P}_h} + \frac{K_{\text{I}_h} T_s (z^{-1} - z^{-2})}{1 + z^{-1} (h^2 \omega_1^2 T_s^2 - 2) + z^{-2}}. \end{aligned} \quad (\text{A.17})$$

Regarding Fig. 2.1 scheme (vector proportional-integral (VPI) controller), the following is obtained:

$$\begin{aligned} G_{\text{VPI}_h}^{\text{f\&b}}(z) &= \frac{K_{\text{P}_h} + K_{\text{I}_h} \frac{z^{-1} T_s}{1-z^{-1}}}{1 + h^2 \omega_1^2 \frac{T_s}{1-z^{-1}} \frac{z^{-1} T_s}{1-z^{-1}}} = \frac{K_{\text{P}_h} (1-z^{-1})^2 + K_{\text{I}_h} T_s z^{-1} (1-z^{-1})}{(1-z^{-1})^2 + z^{-1} h^2 \omega_1^2 T_s^2} \\ &= \frac{K_{\text{P}_h} + z^{-1} (K_{\text{I}_h} T_s - 2K_{\text{P}_h}) - z^{-2} (K_{\text{I}_h} T_s - K_{\text{P}_h})}{1 + z^{-1} (h^2 \omega_1^2 T_s^2 - 2) + z^{-2}}. \end{aligned} \quad (\text{A.18})$$

### A.1.10 Backward Euler & Backward Euler + Delay

Application of Masons' gain formula [31] to the scheme that results from Fig. 1.22a (PR controller) when both integrators are discretized with backward Euler, and a one step delay is added in the feedback line, yields

$$\begin{aligned} G_{\text{PR}_h}^{\text{b\&b}}(z) &= K_{\text{P}_h} + \frac{K_{\text{I}_h} \frac{T_s}{1-z^{-1}}}{1 + h^2 \omega_1^2 \frac{T_s}{1-z^{-1}} \frac{z^{-1} T_s}{1-z^{-1}}} = K_{\text{P}_h} + \frac{K_{\text{I}_h} T_s (1-z^{-1})}{(1-z^{-1})^2 + z^{-1} h^2 \omega_1^2 T_s^2} \\ &= K_{\text{P}_h} + \frac{K_{\text{I}_h} T_s (1-z^{-1})}{1 + z^{-1} (h^2 \omega_1^2 T_s^2 - 2) + z^{-2}}. \end{aligned} \quad (\text{A.19})$$

Regarding Fig. 2.1 scheme (VPI controller), the following is obtained:

$$\begin{aligned} G_{\text{VPI}_h}^{\text{b\&b}}(z) &= \frac{K_{\text{P}_h} + K_{\text{I}_h} \frac{T_s}{1-z^{-1}}}{1 + h^2 \omega_1^2 \frac{T_s}{1-z^{-1}} \frac{z^{-1} T_s}{1-z^{-1}}} = \frac{K_{\text{P}_h} (1-z^{-1})^2 + K_{\text{I}_h} T_s (1-z^{-1})}{(1-z^{-1})^2 + z^{-1} h^2 \omega_1^2 T_s^2} \\ &= \frac{(K_{\text{I}_h} T_s + K_{\text{P}_h}) - z^{-1} (K_{\text{I}_h} T_s + 2K_{\text{P}_h}) + z^{-2} K_{\text{P}_h}}{1 + z^{-1} (h^2 \omega_1^2 T_s^2 - 2) + z^{-2}}. \end{aligned} \quad (\text{A.20})$$

### A.1.11 Tustin & Tustin

Application of Masons' gain formula [31] to the scheme that results from Fig. 1.22a (PR controller) when both integrators are discretized with Tustin yields

$$\begin{aligned} G_{\text{PR}_h}^{\text{t\&t}}(z) &= K_{\text{P}_h} + \frac{K_{\text{I}_h} \frac{T_s}{2} \frac{1+z^{-1}}{1-z^{-1}}}{1 + h^2 \omega_1^2 \left( \frac{T_s}{2} \frac{1+z^{-1}}{1-z^{-1}} \right)^2} = K_{\text{P}_h} + \frac{2 K_{\text{I}_h} T_s (1+z^{-1})(1-z^{-1})}{4(1-z^{-1})^2 + h^2 \omega_1^2 T_s^2 (1+z^{-1})^2} \\ &= K_{\text{P}_h} + 2 K_{\text{I}_h} T_s \frac{1-z^{-2}}{(h^2 \omega_1^2 T_s^2 + 4) + z^{-1}(2h^2 \omega_1^2 T_s^2 - 8) + z^{-2}(h^2 \omega_1^2 T_s^2 + 4)}. \end{aligned} \quad (\text{A.21})$$

Regarding Fig. 2.1 scheme (VPI controller), the following is obtained:

$$\begin{aligned} G_{\text{VPI}_h}^{\text{t\&t}}(z) &= \frac{K_{\text{P}_h} + K_{\text{I}_h} \frac{T_s}{2} \frac{1+z^{-1}}{1-z^{-1}}}{1 + h^2 \omega_1^2 \left( \frac{T_s}{2} \frac{1+z^{-1}}{1-z^{-1}} \right)^2} = \frac{4 K_{\text{P}_h} (1-z^{-1})^2 + 2 K_{\text{I}_h} (1+z^{-1})(1-z^{-1})}{4(1-z^{-1})^2 + h^2 \omega_1^2 T_s^2 (1+z^{-1})^2} \\ &= \frac{4 K_{\text{P}_h} + 2 K_{\text{I}_h} - 8 z^{-1} K_{\text{P}_h} + z^{-2} (4 K_{\text{P}_h} - 2 K_{\text{I}_h})}{(h^2 \omega_1^2 T_s^2 + 4) + z^{-1}(2h^2 \omega_1^2 T_s^2 - 8) + z^{-2}(h^2 \omega_1^2 T_s^2 + 4)}. \end{aligned} \quad (\text{A.22})$$

## A.2 Discretization of Resonant Controllers with Delay Compensation

### A.2.1 Zero-Order Hold

Discretization of  $R_{1_h}^{\text{d}}(s)$  with the ZOH method yields

$$\begin{aligned} R_{1_h}^{\text{d,zoh}}(z) &= (1-z^{-1}) \mathcal{Z} \left\{ \mathcal{L}^{-1} \left[ \frac{R_{1_h}^{\text{d}}(s)}{s} \right] \right\} = (1-z^{-1}) \mathcal{Z} \left\{ \mathcal{L}^{-1} \left[ \frac{\cos(\phi'_h)}{s^2 + h^2 \omega_1^2} - \frac{h \omega_1 \sin(\phi'_h)}{s(s^2 + h^2 \omega_1^2)} \right] \right\} \\ &= (1-z^{-1}) \mathcal{Z} \left[ \frac{\cos(\phi'_h)}{h \omega_1} \sin(h \omega_1 t) - \frac{\sin(\phi'_h)}{h \omega_1} + \frac{\sin(\phi'_h)}{h \omega_1} \cos(h \omega_1 t) \right] \\ &= \frac{1-z^{-1}}{h \omega_1} \left[ \cos(\phi'_h) \frac{z^{-1} \sin(h \omega_1 T_s)}{1 - 2z^{-1} \cos(h \omega_1 T_s) + z^{-2}} - \frac{\sin(\phi'_h)}{1-z^{-1}} \right. \\ &\quad \left. + \sin(\phi'_h) \frac{1-z^{-1} \cos(h \omega_1 T_s)}{1 - 2z^{-1} \cos(h \omega_1 T_s) + z^{-2}} \right] \\ &= \frac{1}{h \omega_1} \left\{ \cos(\phi'_h) \frac{(z^{-1} - z^{-2}) \sin(h \omega_1 T_s)}{1 - 2z^{-1} \cos(h \omega_1 T_s) + z^{-2}} - \sin(\phi'_h) \frac{1 - 2z^{-1} \cos(h \omega_1 T_s) + z^{-2}}{1 - 2z^{-1} \cos(h \omega_1 T_s) + z^{-2}} \right. \\ &\quad \left. + \sin(\phi'_h) \frac{(1-z^{-1}) [1 - z^{-1} \cos(h \omega_1 T_s)]}{1 - 2z^{-1} \cos(h \omega_1 T_s) + z^{-2}} \right\} \\ &= \frac{z^{-1} [\sin(\phi'_h + h \omega_1 T_s) - \sin(\phi'_h)] + z^{-2} [\sin(\phi'_h - h \omega_1 T_s) - \sin(\phi'_h)]}{h \omega_1 [1 - 2z^{-1} \cos(h \omega_1 T_s) + z^{-2}]} \end{aligned} \quad (\text{A.23})$$

Discretization of  $R_{2h}^d(s)$  with the ZOH method yields

$$\begin{aligned}
R_{2h}^{\text{zoh}}(z) &= (1 - z^{-1}) \mathcal{Z} \left\{ \mathcal{L}^{-1} \left[ \frac{R_{2h}^d(s)}{s} \right] \right\} = (1 - z^{-1}) \mathcal{Z} \left\{ \mathcal{L}^{-1} \left[ \frac{s \cos(\phi'_h) - h\omega_1 \sin(\phi'_h)}{s^2 + h^2\omega_1^2} \right] \right\} \\
&= (1 - z^{-1}) \mathcal{Z} [\cos(\phi'_h) \cos(h\omega_1 t) - \sin(\phi'_h) \sin(h\omega_1 t)] \\
&= \cos(\phi'_h) \frac{(1 - z^{-1}) [1 - z^{-1} \cos(h\omega_1 T_s)]}{1 - 2z^{-1} \cos(h\omega_1 T_s) + z^{-2}} - \sin(\phi'_h) \frac{(z^{-1} - z^{-2}) \sin(h\omega_1 T_s)}{1 - 2z^{-1} \cos(h\omega_1 T_s) + z^{-2}} \\
&= \frac{(1 - z^{-1}) \cos(\phi'_h) - (z^{-1} - z^{-2}) \cos(\phi'_h - h\omega_1 T_s)}{1 - 2z^{-1} \cos(h\omega_1 T_s) + z^{-2}}.
\end{aligned} \tag{A.24}$$

## A.2.2 First-Order Hold

Discretization of  $R_{1h}^d(s)$  with the FOH method yields

$$\begin{aligned}
R_{1h}^{\text{foh}}(z) &= \frac{(1 - z^{-1})^2}{z^{-1} T_s} \mathcal{Z} \left\{ \mathcal{L}^{-1} \left[ \frac{R_{1h}^d(s)}{s^2} \right] \right\} \\
&= \frac{(1 - z^{-1})^2}{z^{-1} T_s} \mathcal{Z} \left\{ \mathcal{L}^{-1} \left[ \frac{\cos(\phi'_h)}{s(s^2 + h^2\omega_1^2)} - \frac{h\omega_1 \sin(\phi'_h)}{s^2(s^2 + h^2\omega_1^2)} \right] \right\} \\
&= \frac{(1 - z^{-1})^2}{z^{-1} T_s} \mathcal{Z} \left\{ \cos(\phi'_h) \left[ \frac{1}{h^2\omega_1^2} - \frac{1}{h^2\omega_1^2} \cos(h\omega_1 t) \right] \right. \\
&\quad \left. - \sin(\phi'_h) \left[ \frac{t}{h\omega_1} - \frac{1}{h^2\omega_1^2} \sin(h\omega_1 t) \right] \right\} \\
&= \frac{(1 - z^{-1})^2}{z^{-1} h^2\omega_1^2 T_s} \left\{ \cos(\phi'_h) \left[ \frac{1}{1 - z^{-1}} - \frac{1 - z^{-1} \cos(h\omega_1 T_s)}{1 - 2z^{-1} \cos(h\omega_1 T_s) + z^{-2}} \right] \right. \\
&\quad \left. - \sin(\phi'_h) \left[ \frac{z^{-1} h\omega_1}{(1 - z^{-1})^2} - \frac{z^{-1} \sin(h\omega_1 T_s)}{1 - 2z^{-1} \cos(h\omega_1 T_s) + z^{-2}} \right] \right\} \\
&= \frac{1}{h^2\omega_1^2 T_s} \left\{ \cos(\phi'_h) \left[ (z - 1) \frac{1 - 2z^{-1} \cos(h\omega_1 T_s) + z^{-2}}{1 - 2z^{-1} \cos(h\omega_1 T_s) + z^{-2}} \right. \right. \\
&\quad \left. \left. - (z - 2 + z^{-1}) \frac{1 - z^{-1} \cos(h\omega_1 T_s)}{1 - 2z^{-1} \cos(h\omega_1 T_s) + z^{-2}} \right] \right. \\
&\quad \left. - \sin(\phi'_h) \left[ h\omega_1 \frac{1 - 2z^{-1} \cos(h\omega_1 T_s) + z^{-2}}{1 - 2z^{-1} \cos(h\omega_1 T_s) + z^{-2}} - \frac{(1 - 2z^{-1} + z^{-2}) \sin(h\omega_1 T_s)}{1 - 2z^{-1} \cos(h\omega_1 T_s) + z^{-2}} \right] \right\} \\
&= \cos(\phi'_h) \frac{(1 - z^{-2}) [1 - \cos(h\omega_1 T_s)]}{h^2\omega_1^2 T_s [1 - 2z^{-1} \cos(h\omega_1 T_s) + z^{-2}]} \\
&\quad + \sin(\phi'_h) \frac{(1 + z^{-2}) [\sin(h\omega_1 T_s) - h\omega_1] + 2z^{-1} [h\omega_1 \cos(h\omega_1 T_s) - \sin(h\omega_1 T_s)]}{h^2\omega_1^2 T_s [1 - 2z^{-1} \cos(h\omega_1 T_s) + z^{-2}]}
\end{aligned} \tag{A.25}$$

Discretization of  $R_{2h}^d(s)$  with the FOH method yields

$$\begin{aligned}
R_{2h}^{\text{foh}}(z) &= \frac{(1-z^{-1})^2}{z^{-1}T_s} \mathcal{Z} \left\{ \mathcal{L}^{-1} \left[ \frac{R_{2h}^d(s)}{s^2} \right] \right\} \\
&= \frac{(1-z^{-1})^2}{z^{-1}T_s} \mathcal{Z} \left[ \mathcal{L}^{-1} \left( \frac{1}{s^2 + h^2\omega_1^2} \right) \right] = \frac{z-1}{T_s} R_{1h}^{\text{zoh}}(z) \\
&= \frac{[\sin(\phi'_h + h\omega_1 T_s) - \sin(\phi'_h)] - 2z^{-1} \sin(h\omega_1 T_s) \cos(\phi'_h)}{h\omega_1 T_s [1 - 2z^{-1} \cos(h\omega_1 T_s) + z^{-2}]} \\
&\quad + \frac{z^{-2} [\sin(h\omega_1 T_s - \phi'_h) + \sin(\phi'_h)]}{h\omega_1 T_s [1 - 2z^{-1} \cos(h\omega_1 T_s) + z^{-2}]} .
\end{aligned} \tag{A.26}$$

### A.2.3 Tustin with Prewarping

Discretization of  $R_{1h}^d(s)$  with the Tustin with prewarping method yields

$$\begin{aligned}
R_{1h}^{\text{tp}}(z) &= \frac{\frac{h\omega_1}{\tan\left(\frac{h\omega_1 T_s}{2}\right)} \frac{1-z^{-1}}{1+z^{-1}} \cos(\phi'_h) - h\omega_1 \sin(\phi'_h)}{\left[ \frac{h\omega_1}{\tan\left(\frac{h\omega_1 T_s}{2}\right)} \frac{1-z^{-1}}{1+z^{-1}} \right]^2 + h^2\omega_1^2} \\
&= \frac{h\omega_1 (1-z^{-1})(1+z^{-1}) \tan\left(\frac{h\omega_1 T_s}{2}\right) \cos(\phi'_h) - h\omega_1 (1+z^{-1})^2 \tan^2\left(\frac{h\omega_1 T_s}{2}\right) \sin(\phi'_h)}{h^2\omega_1^2 (1-z^{-1})^2 + h^2\omega_1^2 (1+z^{-1})^2 \tan^2\left(\frac{h\omega_1 T_s}{2}\right)} \\
&= \frac{1}{h\omega_1} \frac{(1-z^{-2}) \cos(\phi'_h) \sin\left(\frac{h\omega_1 T_s}{2}\right) \cos\left(\frac{h\omega_1 T_s}{2}\right) - (1+z^{-1})^2 \sin(\phi'_h) \sin^2\left(\frac{h\omega_1 T_s}{2}\right)}{(1-z^{-1})^2 \cos^2\left(\frac{h\omega_1 T_s}{2}\right) + (1+z^{-1})^2 \sin^2\left(\frac{h\omega_1 T_s}{2}\right)} \\
&= \frac{\frac{1}{2}(1-z^{-2}) \cos(\phi'_h) \sin(h\omega_1 T_s) - (1+2z^{-1}+z^{-2}) \sin(\phi'_h) \sin^2\left(\frac{h\omega_1 T_s}{2}\right)}{h\omega_1 [1 - 2z^{-1} \cos(h\omega_1 T_s) + z^{-2}]} .
\end{aligned} \tag{A.27}$$

Discretization of  $R_{2_h}^d(s)$  with the Tustin with prewarping method yields

$$\begin{aligned}
R_{2_h}^{\text{dtp}}(z) &= \frac{\left[ \frac{h\omega_1}{\tan\left(\frac{h\omega_1 T_s}{2}\right)} \frac{1-z^{-1}}{1+z^{-1}} \right]^2 \cos(\phi'_h) - h\omega_1 \frac{h\omega_1}{\tan\left(\frac{h\omega_1 T_s}{2}\right)} \frac{1-z^{-1}}{1+z^{-1}} \sin(\phi'_h)}{\left[ \frac{h\omega_1}{\tan\left(\frac{h\omega_1 T_s}{2}\right)} \frac{1-z^{-1}}{1+z^{-1}} \right]^2 + h^2 \omega_1^2} \\
&= \frac{(1-z^{-1})^2 \cos(\phi'_h) - (1-z^{-1})(1+z^{-1}) \tan\left(\frac{h\omega_1 T_s}{2}\right) \sin(\phi'_h)}{(1-z^{-1})^2 + (1+z^{-1})^2 \tan^2\left(\frac{h\omega_1 T_s}{2}\right)} \\
&= \frac{(1-2z^{-1}+z^{-2}) \cos(\phi'_h) \cos^2\left(\frac{h\omega_1 T_s}{2}\right) - (1-z^{-2}) \sin(\phi'_h) \sin\left(\frac{h\omega_1 T_s}{2}\right) \cos\left(\frac{h\omega_1 T_s}{2}\right)}{(1-2z^{-1}+z^{-2}) \cos^2\left(\frac{h\omega_1 T_s}{2}\right) + (1+2z^{-1}+z^{-2}) \sin^2\left(\frac{h\omega_1 T_s}{2}\right)} \\
&= \frac{\frac{1}{2}(-1+z^{-2}) \sin(\phi'_h) \sin(h\omega_1 T_s) + (1-2z^{-1}+z^{-2}) \cos(\phi'_h) \cos^2\left(\frac{h\omega_1 T_s}{2}\right)}{1-2z^{-1} \cos(h\omega_1 T_s) + z^{-2}}.
\end{aligned} \tag{A.28}$$

#### A.2.4 Zero Pole Matching

The poles of  $R_{1_h}^d(s)$  are  $s = jh\omega_1$  and  $s = -jh\omega_1$  [the same as for  $R_{1_h}(s)$ , in section §A.1.7], and its zero is  $s = h\omega_1 \tan(h\omega_1 T_s)$ . Therefore, the poles of the discrete-time transfer function are  $z = e^{jh\omega_1 T_s}$  and  $z = e^{-jh\omega_1 T_s}$ , and its zero is  $z = e^{\tan(\phi'_h) h\omega_1 T_s}$ .

$$\begin{aligned}
R_{1_h}^{\text{dzpm}}(z) &= K_d \frac{z - e^{\tan(\phi'_h) h\omega_1 T_s}}{(z - e^{jh\omega_1 T_s})(z - e^{-jh\omega_1 T_s})} \\
&= K_d \frac{z - e^{\tan(\phi'_h) h\omega_1 T_s}}{[z - \cos(h\omega_1 T_s) - j \sin(h\omega_1 T_s)][z - \cos(h\omega_1 T_s) + j \sin(h\omega_1 T_s)]} \\
&= K_d \frac{z - e^{\tan(\phi'_h) h\omega_1 T_s}}{[z - \cos(h\omega_1 T_s)]^2 - [j \sin(h\omega_1 T_s)]^2} \\
&= K_d \frac{z - e^{\tan(\phi'_h) h\omega_1 T_s}}{z^2 + \cos^2(h\omega_1 T_s) - 2z \cos(h\omega_1 T_s) + \sin^2(h\omega_1 T_s)} \\
&= K_d \frac{z^{-1} - z^{-2} e^{\tan(\phi'_h) h\omega_1 T_s}}{1 - 2z^{-1} \cos(h\omega_1 T_s) + z^{-2}}.
\end{aligned} \tag{A.29}$$

The roots of  $R_{2_h}^d(s)$  are the same as those of  $R_{1_h}^d(s)$ , except for the fact that  $R_{2_h}^d(s)$  has an additional zero (at the origin):

$$R_{2_h}^{\text{dzpm}}(z) = (z-1) R_{1_h}^{\text{dzpm}}(z) = K_d \frac{1-z^{-1} \left[ 1 + e^{\tan(\phi'_h) h\omega_1 T_s} \right] + z^{-2} e^{\tan(\phi'_h) h\omega_1 T_s}}{1 - 2z^{-1} \cos(h\omega_1 T_s) + z^{-2}}. \tag{A.30}$$

### A.2.5 Impulse Invariant

Discretization of  $R_{1_h}^d(s)$  with the impulse invariant method yields

$$\begin{aligned}
R_{1_h}^{\text{dimp}}(z) &= T_s \mathcal{Z} \left\{ \mathcal{L}^{-1} \left[ \frac{s \cos(\phi'_h) - h\omega_1 \sin(\phi'_h)}{s^2 + h^2\omega_1^2} \right] \right\} \\
&= T_s \mathcal{Z} [\cos(\phi'_h) \cos(h\omega_1 t) - \sin(\phi'_h) \sin(h\omega_1 t)] \\
&= T_s \left[ \cos(\phi'_h) \frac{1 - z^{-1} \cos(h\omega_1 T_s)}{1 - 2z^{-1} \cos(h\omega_1 T_s) + z^{-2}} - \sin(\phi'_h) \frac{z^{-1} \sin(h\omega_1 T_s)}{1 - 2z^{-1} \cos(h\omega_1 T_s) + z^{-2}} \right] \\
&= T_s \frac{\cos(\phi'_h) - z^{-1} [\cos(\phi'_h) \cos(h\omega_1 T_s) + \sin(\phi'_h) \sin(h\omega_1 T_s)]}{1 - 2z^{-1} \cos(h\omega_1 T_s) + z^{-2}} \\
&= T_s \frac{\cos(\phi'_h) - z^{-1} \cos(\phi'_h - h\omega_1 T_s)}{1 - 2z^{-1} \cos(h\omega_1 T_s) + z^{-2}}.
\end{aligned} \tag{A.31}$$

Discretization of  $R_{2_h}^d(s)$  with the impulse invariant method yields

$$\begin{aligned}
R_{2_h}^{\text{dimp}}(z) &= T_s \mathcal{Z} \left\{ \mathcal{L}^{-1} \left[ \frac{s^2 \cos(\phi'_h) - s h\omega_1 \sin(\phi'_h)}{s^2 + h^2\omega_1^2} \right] \right\} \\
&= T_s \mathcal{Z} [-h\omega_1 \cos(\phi'_h) \sin(h\omega_1 t) - h\omega_1 \sin(\phi'_h) \cos(h\omega_1 t)] \\
&= h\omega_1 T_s \left[ -\cos(\phi'_h) \frac{z^{-1} \sin(h\omega_1 T_s)}{1 - 2z^{-1} \cos(h\omega_1 T_s) + z^{-2}} - \sin(\phi'_h) \frac{1 - z^{-1} \cos(h\omega_1 T_s)}{1 - 2z^{-1} \cos(h\omega_1 T_s) + z^{-2}} \right] \\
&= h\omega_1 T_s \frac{-\sin(\phi'_h) + z^{-1} [\sin(\phi'_h) \cos(h\omega_1 T_s) - \cos(\phi'_h) \sin(h\omega_1 T_s)]}{1 - 2z^{-1} \cos(h\omega_1 T_s) + z^{-2}} \\
&= h\omega_1 T_s \frac{-\sin(\phi'_h) + z^{-1} \sin(\phi'_h - h\omega_1 T_s)}{1 - 2z^{-1} \cos(h\omega_1 T_s) + z^{-2}}.
\end{aligned} \tag{A.32}$$

### A.2.6 Forward Euler & Backward Euler

Application of Masons' gain formula [31] to the scheme that results from Fig. 2.7a [i.e.,  $R_{1_h}^d(s)$ ] when the direct integrator is discretized with forward Euler, and the feedback one is discretized with backward Euler, yields

$$\begin{aligned}
R_{1_h}^{\text{df&bb}}(z) &= \frac{\cos(\phi'_h) \frac{z^{-1} T_s}{1-z^{-1}} - h\omega_1 \sin(\phi'_h) \frac{T_s}{1-z^{-1}} \frac{z^{-1} T_s}{1-z^{-1}}}{1 + h^2 \omega_1^2 \frac{T_s}{1-z^{-1}} \frac{z^{-1} T_s}{1-z^{-1}}} \\
&= \frac{T_s \cos(\phi'_h) z^{-1} (1 - z^{-1}) - h\omega_1 T_s^2 \sin(\phi'_h) z^{-1}}{(1 - z^{-1})^2 + z^{-1} h^2 \omega_1^2 T_s^2} \\
&= T_s \frac{z^{-1} [\cos(\phi'_h) - h\omega_1 T_s \sin(\phi'_h)] - z^{-2} \cos(\phi'_h)}{1 + z^{-1} (h^2 \omega_1^2 T_s^2 - 2) + z^{-2}}.
\end{aligned} \tag{A.33}$$

Regarding Fig. 2.7b scheme [i.e.,  $R_{2h}^d(s)$ ], the following is obtained:

$$\begin{aligned}
 R_{2h}^{\text{df\&b}}(z) &= \frac{\cos(\phi'_h) - h\omega_1 \sin(\phi'_h) \frac{z^{-1}T_s}{1-z^{-1}}}{1 + h^2\omega_1^2 \frac{T_s}{1-z^{-1}} \frac{z^{-1}T_s}{1-z^{-1}}} = \frac{\cos(\phi'_h)(1-z^{-1})^2 - h\omega_1 T_s \sin(\phi'_h) z^{-1}(1-z^{-1})}{(1-z^{-1})^2 + z^{-1}h^2\omega_1^2 T_s^2} \\
 &= \frac{(1-2z^{-1}+z^{-2})\cos(\phi'_h) - (z^{-1}-z^{-2})h\omega_1 T_s \sin(\phi'_h)}{1+z^{-1}(h^2\omega_1^2 T_s^2-2)+z^{-2}}.
 \end{aligned}
 \tag{A.34}$$



## Appendix B

# Mathematical Development of Expressions for Chapter 3

### B.1 Phase of Plant Model at a Given Frequency

Applying the substitution  $z = e^{j\omega T_s}$  in (1.12) [i.e., in  $G_{PL}(z)$  expression] leads to

$$G_{PL}(e^{j\omega T_s}) = \frac{1 - \rho^{-1}}{R_F} \frac{e^{-2j\omega T_s}}{1 - e^{-j\omega T_s} \rho^{-1}} = \frac{1 - \rho^{-1}}{R_F} \frac{\cos(2\omega T_s) - j \sin(2\omega T_s)}{1 - [\cos(\omega T_s) - j \sin(\omega T_s)] \rho^{-1}}. \quad (\text{B.1})$$

Multiplication and division by the conjugate of the denominator gives

$$G_{PL}(e^{j\omega T_s}) = \frac{1 - \rho^{-1}}{R_F} \frac{\cos(2\omega T_s) - \cos(\omega T_s) \rho^{-1}}{1 + \rho^{-2} - 2 \cos(\omega T_s) \rho^{-1}} + j \frac{1 - \rho^{-1}}{R_F} \frac{\sin(\omega T_s) \rho^{-1} - \sin(2\omega T_s)}{1 + \rho^{-2} - 2 \cos(\omega T_s) \rho^{-1}}. \quad (\text{B.2})$$

The inverse tangent of the imaginary part of (B.2) divided by its real part, gives the phase of the plant model at a certain frequency  $\omega$ :

$$\angle G_{PL}(e^{j\omega T_s}) = \arctan \left( \frac{\sin(\omega T_s) \rho^{-1} - \sin(2\omega T_s)}{\cos(2\omega T_s) - \cos(\omega T_s) \rho^{-1}} \right). \quad (\text{B.3})$$

Equation (3.13) is obtained by evaluation of (B.3) at  $\omega = \omega_\lambda$ .

### B.2 Slope of Plant Model Phase at a Given Frequency

To obtain (3.11), the partial derivative of (B.3) with respect to frequency should be developed:

$$\frac{\partial \angle G_{PL}(z)}{\partial \omega}(\omega) = \frac{\partial \angle G_{PL}(e^{j\omega T_s})}{\partial \omega}(\omega) = \frac{\frac{\partial}{\partial \omega} \left[ \frac{\sin(\omega T_s) \rho^{-1} - \sin(2\omega T_s)}{\cos(2\omega T_s) - \cos(\omega T_s) \rho^{-1}} \right]}{1 + \left[ \frac{\sin(\omega T_s) \rho^{-1} - \sin(2\omega T_s)}{\cos(2\omega T_s) - \cos(\omega T_s) \rho^{-1}} \right]^2} \quad (\text{B.4})$$

where

$$\begin{aligned}
\frac{\partial}{\partial \omega} \left[ \frac{\sin(\omega T_s) \rho^{-1} - \sin(2\omega T_s)}{\cos(2\omega T_s) - \cos(\omega T_s) \rho^{-1}} \right] &= \\
&= \frac{[T_s \cos(\omega T_s) \rho^{-1} - 2T_s \cos(2\omega T_s)] [\cos(2\omega T_s) - \cos(\omega T_s) \rho^{-1}]}{[\cos(2\omega T_s) - \cos(\omega T_s) \rho^{-1}]^2} \\
&\quad - \frac{[\sin(\omega T_s) \rho^{-1} - \sin(2\omega T_s)] [-2T_s \sin(2\omega T_s) + T_s \sin(\omega T_s) \rho^{-1}]}{[\cos(2\omega T_s) - \cos(\omega T_s) \rho^{-1}]^2} \\
&= \frac{-2 [\cos^2(\omega T_s) + \sin^2(\omega T_s)]}{[\cos(2\omega T_s) - \cos(\omega T_s) \rho^{-1}]^2} + \frac{-\rho^{-2} [\cos^2(2\omega T_s) + \sin^2(2\omega T_s)]}{[\cos(2\omega T_s) - \cos(\omega T_s) \rho^{-1}]^2} \\
&\quad + \frac{3\rho^{-1} [\cos(\omega T_s) \cos(2\omega T_s) + \sin(\omega T_s) \sin(2\omega T_s)]}{[\cos(2\omega T_s) - \cos(\omega T_s) \rho^{-1}]^2} \\
&= \frac{-2 - \rho^{-2} + 3\rho^{-1} \cos(\omega T_s)}{[\cos(2\omega T_s) - \cos(\omega T_s) \rho^{-1}]^2}
\end{aligned} \tag{B.5}$$

Substitution of (B.5) back in (B.4) leads to

$$\begin{aligned}
\frac{\partial \angle G_{\text{PL}}(z)}{\partial \omega}(\omega) &= \frac{\frac{-2 - \rho^{-2} + 3\rho^{-1} \cos(\omega T_s)}{[\cos(2\omega T_s) - \cos(\omega T_s) \rho^{-1}]^2}}{1 + \left[ \frac{\sin(\omega T_s) \rho^{-1} - \sin(2\omega T_s)}{\cos(2\omega T_s) - \cos(\omega T_s) \rho^{-1}} \right]^2} \\
&= \frac{-2 - \rho^{-2} + 3\rho^{-1} \cos(\omega T_s)}{[\cos(2\omega T_s) - \cos(\omega T_s) \rho^{-1}]^2 + [\sin(\omega T_s) \rho^{-1} - \sin(2\omega T_s)]^2} \\
&= \frac{-2 - \rho^{-2} + 3\rho^{-1} \cos(\omega T_s)}{1 + \rho^{-2} - 2\rho^{-1} [\cos(\omega T_s) \cos(2\omega T_s) + \sin(\omega T_s) \sin(2\omega T_s)]} \\
&= -T_s \frac{2 + \rho^{-2} - 3\rho^{-1} \cos(\omega T_s)}{1 + \rho^{-2} - 2\rho^{-1} \cos(\omega T_s)}
\end{aligned} \tag{B.6}$$

Finally, evaluation of (B.6) at  $\omega = \omega_\lambda$  results in (3.11).

# Appendix C

## Mathematical Development of Expressions for Chapter 4

### C.1 $K_{P_T}$ Expression as a Function of $\eta_P$

The aim is to obtain a closed-form expression to calculate which  $K_{P_T}$  should be employed in order to achieve a certain sensitivity peak  $1/\eta_P$  for the system  $G_C(z) G_{PL}(z)$  when proportional-resonant (PR) controllers are employed [i.e., the sensitivity peak of  $K_{P_T} G_{PL}(z)$ ]. First of all, the frequency  $\omega_\eta$ , at which  $|D(z)|$  has its global minimum  $\eta_P$ , should be found. This frequency satisfies the following two constraints:

$$\frac{\partial |D(e^{j\omega T_s})|}{\partial \omega}(\omega_\eta) = 0 \quad (C.1)$$

$$\frac{\partial^2 |D(e^{j\omega T_s})|}{\partial \omega^2}(\omega_\eta) > 0. \quad (C.2)$$

Consequently, the first step is to develop an expression of  $D(z)$  as a function of  $\omega$  [i.e.,  $D(e^{j\omega T_s})$ ], and then to calculate the first and second partial derivatives of its magnitude (modulus) with respect to  $\omega$ . From (4.3), the following is obtained:

$$D(e^{j\omega T_s}) = 1 + K_{P_T} G_{PL}(e^{j\omega T_s}). \quad (C.3)$$

Substitution of (B.2) in (C.3) yields

$$\begin{aligned} D(e^{j\omega T_s}) = & \frac{1 + \rho^{-2} - 2\cos(\omega T_s)\rho^{-1} + K_{P_T} \frac{1-\rho^{-1}}{R_F} [\cos(2\omega T_s) - \cos(\omega T_s)\rho^{-1}]}{1 + \rho^{-2} - 2\cos(\omega T_s)\rho^{-1}} \\ & + j K_{P_T} \frac{1 - \rho^{-1}}{R_F} \frac{\sin(\omega T_s)\rho^{-1} - \sin(2\omega T_s)}{1 + \rho^{-2} - 2\cos(\omega T_s)\rho^{-1}}. \end{aligned} \quad (C.4)$$

By application of constraints (C.1) and (C.2) to

$$|D(e^{j\omega T_s})| = \sqrt{\{\Re\{D(e^{j\omega T_s})\}\}^2 + \{\Im\{D(e^{j\omega T_s})\}\}^2} \quad (C.5)$$

the general expression for  $\omega_\eta$  results in

$$\omega_\eta = T_s^{-1} \arctan \left( \frac{R_F^2 (-2 + 3\rho^{-2} - \rho^{-4}) + 2R_F A (1 + \rho^{-2}) + K_{PT} R_F (\rho^{-3} - \rho^{-2})}{R_F (1 + \rho^{-2}) - A} \right) \quad (\text{C.6})$$

where

$$A = \sqrt{R_F (1 - \rho^{-1}) [K_{PT} \rho^{-2} + R_F (1 + \rho^{-1})]}. \quad (\text{C.7})$$

Substitution of  $\omega_\eta$  in (C.5) gives

$$|D(e^{j\omega_\eta T_s})| = \eta_P \quad (\text{C.8})$$

and finally  $K_{PT}$  can be isolated from this equality giving rise to

$$K_{PT} = \frac{R_F}{1 - \rho^{-1}} \left( 1 - \rho^2 + \left\{ \frac{1}{6} \rho^{-1} + \frac{1}{3} \rho - \frac{1}{B} \left( \frac{1}{12} \rho^{-1} - \frac{2}{3} \rho + \frac{4}{3} \rho^3 \right) - \frac{B}{12} \rho^{-1} + j \frac{\sqrt{3}}{12} \left[ \frac{1}{B} (\rho^{-1} - 8\rho + 16\rho^3) - B \rho^{-1} \right] \right\}^2 \right) \quad (\text{C.9})$$

where

$$B = \left[ 1 + (54 \eta_P^2 - 12) \rho^2 + 48 \rho^4 - 64 \rho^6 + 6 \rho \eta_P \sqrt{3 + (81 \eta_P^2 - 36) \rho^2 + 144 \rho^4 - 192 \rho^6} \right]^{1/3}. \quad (\text{C.10})$$

Given the complexity of the operations involved, they are not shown here in full detail. They were carried out by execution of the Matlab script shown in Fig. C.1 (Matlab 7.1.0.246).

Note that (C.9) corresponds with the  $F_1$  function in (4.5). It should be also remarked that the  $j$  in (C.9) is always canceled with the imaginary components that result from the root square in (C.10), so  $K_{PT} \in \mathbb{R} \forall \eta_P \in (0, 1)$ .

The complexity of (C.9) is significantly reduced once  $T_s$ ,  $R_F$  and  $L_F$  are replaced with their particular values for a certain situation, leading to a much more simple equation of the form

$$K_{PT} = \lambda_1 - \left[ \lambda_2 - \frac{\lambda_3}{B} - \lambda_4 B + j \left( \frac{\lambda_5}{B} - \lambda_6 B \right) \right]^2 \quad (\text{C.11})$$

where

$$B = \left( 1 + \lambda_7 \eta_P^2 + \lambda_8 \eta_P \sqrt{\lambda_9 + \eta_P^2} \right)^{1/3} \quad (\text{C.12})$$

and  $\lambda_k \in \mathbb{R} \forall k \in \{1, 2, 3, \dots, 9\}$ .

```

1 clear
2
3 syms R L T K w eta %Symbolic variables:
4 %R is the ESR or the L filter
5 %L is the L filter inductance
6 %T is the sampling period
7 %K is the total proportional gain
8 %w is frequency
9 %eta is the minimum D(z) when only proportional gains are considered
10
11 %Real and imaginary part of D(z) in (C.3):
12 Re_D=(1+exp(-2*R*T/L)-2*cos(w*T)*exp(-R*T/L))+K*(1-exp(-R*T/L))/R*(cos(2*w*T)-cos(w*T)*exp(-R*T/L));
13 Im_D=K*(1-exp(-R*T/L))/R*(sin(w*T)*exp(-R*T/L)-sin(2*w*T));
14 mod_D=sqrt(Re_D^2+Im_D^2)/(1+exp(-2*R*T/L)-2*cos(w*T)*exp(-R*T/L)); %Evaluation of |D(z)|, i.e., (C.5)
15
16 first_deriv=diff(mod_D,w); %First partial derivative of |D(z)| with respect to w
17 w_extremes=solve(first_deriv,w); %Isolation of w from (C.1)
18 w_extremes=simple(w_extremes); %Simplification
19
20 second_deriv=diff(first_deriv,w); %Second partial derivative of |D(z)| with respect to w
21 second_deriv=simple(second_deriv); %Simplification
22
23 %Evaluation of constraint (C.2) in a particular case (specific values for parameters):
24 w_extremes0=subs(w_extremes,R,0.5);w_extremes0=subs(w_extremes0,T,1e-4);w_extremes0=subs(w_extremes0,L,5e-3);
25 w_extremes0=subs(w_extremes0,K,20);w_extremes0=double(w_extremes0);
26 second_deriv0=subs(second_deriv,R,0.5);second_deriv0=subs(second_deriv0,T,1e-4);
27 second_deriv0=subs(second_deriv0,L,5e-3);second_deriv0=subs(second_deriv0,K,20);
28 evaluation_second_deriv=double(subs(second_deriv0,w,w_extremes0)); %Evaluation of constraint (C.2) at w_extremes;
29 for i=1:size(w_extremes0,1)
30     if imag(w_extremes0(i))==0 & real(w_extremes0(i))>0 %Frequency should be real and positive
31         if evaluation_second_deriv(i)>0 %If w_extremes0(i) is a minimum
32             if w_extremes0(i)<0.8*pi/1e-4 %To assure that the frequency is not too close to the Nyquist limit
33                 index=i %Identification of the minimum extreme
34             end
35         end
36     end if
37 end
38 w_minimum=simple(w_extremes(index)); %Frequency at which |D(z)| is minimum
39 pretty(w_minimum) %Final solution for (C.6)
40
41 D_minimum=subs(mod_D,w,w_minimum); %Minimum of |D(z)|, obtained by evaluation of |D(z)| at w_minimum
42 D_minimum=simple(D_minimum); %Simplification
43 K_solution=solve(D_minimum-eta,K); %Isolation of K from (C.8)
44 K_solution=simple(K_solution); %Simplification
45 pretty(K_solution(3)) %Final solution for (C.9)

```

Figure C.1: Matlab script to obtain (C.6) and (C.9).

## C.2 $\phi'_h$ Expression for $\eta_h$ Maximization in PR Controllers

The  $\angle G_{\text{PL}}(e^{jh\omega_1 T_s})$  and  $\angle D(e^{jh\omega_1 T_s})$  terms in (4.16) are obtained in the following. Evaluation of (B.3) at  $\omega = h\omega_1$  gives

$$\angle G_{\text{PL}}(e^{jh\omega_1 T_s}) = \arctan \left( \frac{\sin(h\omega_1 T_s) \rho^{-1} - \sin(2h\omega_1 T_s)}{\cos(2h\omega_1 T_s) - \cos(h\omega_1 T_s) \rho^{-1}} \right). \quad (\text{C.13})$$

The inverse tangent of the imaginary part of (C.4) divided by its real part, and evaluated at  $\omega = h\omega_1$ , yields

$$\begin{aligned} \angle D(e^{jh\omega_1 T_s}) &= \\ &= \arctan \left( \frac{\sin(h\omega_1 T_s) \rho^{-1} - \sin(2h\omega_1 T_s)}{\frac{R_F}{K_{\text{PT}}(1-\rho^{-1})} [1 + \rho^{-2} - 2 \cos(h\omega_1 T_s) \rho^{-1}] + \cos(2h\omega_1 T_s) - \cos(h\omega_1 T_s) \rho^{-1}} \right). \end{aligned} \quad (\text{C.14})$$



# Appendix D

## Further Information About Testing Facilities

### D.1 dSPACE Platform

The dSPACE DS1004 is a rapid control prototyping system that can be mounted in a personal computer (PC). It is fully programmable from the Simulink block diagram environment. The dSPACE platform has been employed to implement the digital control for all the experimental results provided in this thesis. Fig. D.1 shows the block diagram of dSPACE DS1004. The main components and features of this board are the following.

- Master PowerPC MPC8240 running at 250 MHz.
  - 64-bit floating-point processor.
  - $2 \times 16$  KB cache, on-chip.
  - On-chip peripheral component interconnect (PCI) bridge (33 MHz).
- Slave digital signal processor (DSP) (Texas Instruments TMS320F240) running at 20 MHz for special input/output tasks.
  - 16-bit fixed-point processor.
  - Memory.
    - \*  $64\text{K} \times 16$  external code memory.
    - \*  $28\text{K} \times 16$  external data memory.
    - \*  $4\text{K} \times 16$  dual-port memory for communication.
    - \* 32 KB flash memory.
  - Input/output channels.
    - \* Ten pulsewidth modulation (PWM) outputs.
    - \* Four capture inputs.
    - \* One serial peripheral interface.
- Four general purpose timers.

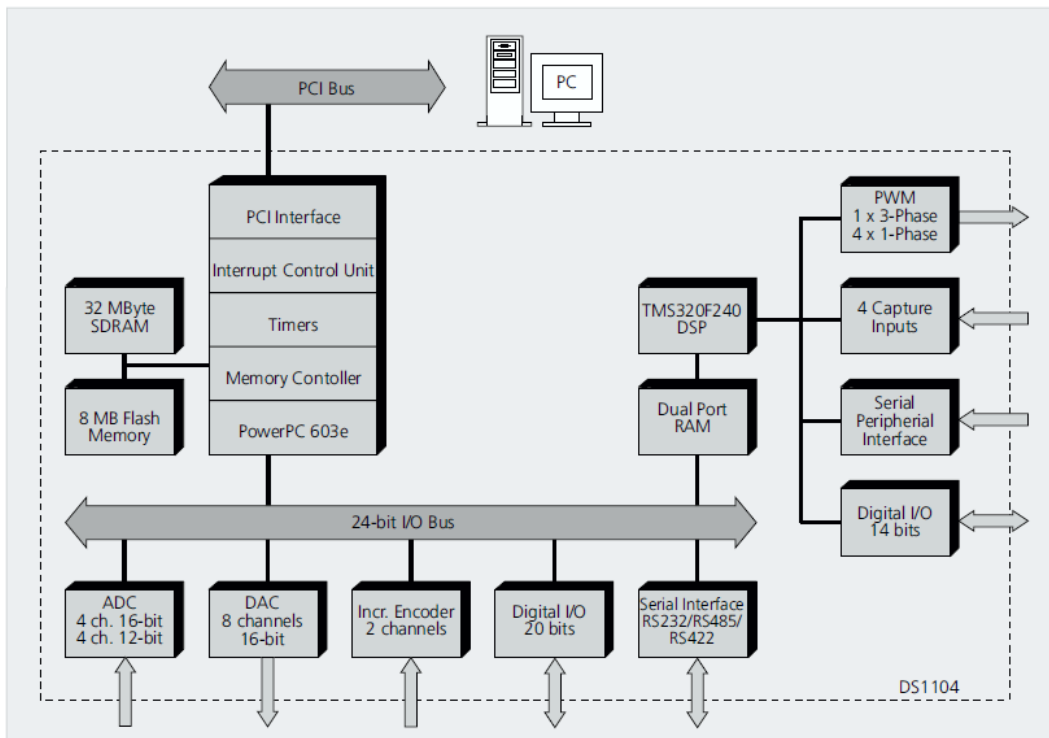


Figure D.1: Block diagram of dSPACE DS1004 platform.

- 8 MB flash memory as program memory.
- 32 MB global synchronous dynamic random memory (SDRAM) for data storage and data exchange with the host.
- Four 12-bit analog to digital converters (ADCs) and one 12-bit ADC with four multiplexed channels.
- Eight 16-bit analog output channels.
- Serial interface with RS232, RS422 and RS485 compatibility.
- Interrupt by host PC, slave DSP, serial interface, five timers, five ADCs, two incremental encoders and four external inputs (user interrupts).

## D.2 Voltage Source Converter

The converter employed for the experiments of this thesis is shown in Fig. D.2. The transistors are Semikron SKM200GB124D insulated-gate bipolar transistors (IGBTs). The driver is Semikron SKHI22A. The firing signals are sent to the driver by means of optocoupler circuits Agilent T1521 and R2521 (optical fiber) to avoid electrical interference.

The dc-bus consists of six capacitors of 2.2 mF each, connected as three parallel branches of two series-connected capacitors. In this manner, the total capacitance results in 3.3 mF.

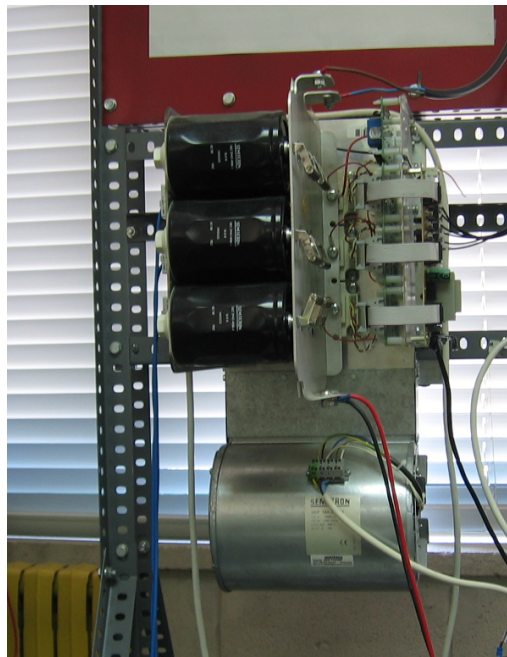


Figure D.2: Voltage source converter.

### D.3 Chroma Voltage Source

The voltage source Chroma 61501 (shown in Fig. D.3) has been employed in several tests (those of sections §2.7, §3.5 and §4.5.2) to supply the alternating voltage  $v_{ac}$ , which emulates, for example, the grid or the back-electromotive force of an electric machine (see section §1.2.2). It is able to supply a maximum power of 500 VA, with a voltage up to 300 V. It offers the possibility of adjusting the dc offset, the output impedance (emulated by means of a current feedback control circuit; in the range between  $0\ \Omega + 200\ \mu\text{H}$  to  $1\ \Omega + 1\ \text{mH}$ ), to simulate power line disturbance conditions such as voltage dips and interruptions, to synthesize harmonic distorted wave-shapes or to operate as a power amplifier of an external analog signal, among other functions. It provides measurements such as voltage root mean square (RMS), current RMS, frequency, true power, power factor and current crest factor.

The voltage output may be configured in two modes: in a range between 0 and 150 V, or between 0 and 300 V. In the former, the maximum current is 24 A in peak value and 4 A in RMS; in the latter, both values are halved. In both cases, the voltage resolution is 0.1 V. The maximum dc power is 250 W, which can be supplied with a combination of current up to 2 A and voltage up to 212 V, or with current up to 1 A and voltage up to 414 V. The frequency of the fundamental component can be set between 15 Hz and 1 kHz.

An external analog signal, generated in dSPACE, has been used in section §3.5.3.2 to perform a frequency transient.

### D.4 Kepco Bidirectional Power Supply

The bidirectional power source KEPCO BOP100-4D (shown in Fig. D.4) provides operation in the four quadrants, that is, it is able to supply or absorb power. It has been employed for the



Figure D.3: Chroma 61501 voltage source.



Figure D.4: Kepco BOP100-4D bidirectional power supply.



Figure D.5: HP 6035A power supply.

experimental tests of section §4.5.1, in which it supplies the voltage  $v_{ac}$  while absorbing a high-frequency current provided by the voltage source converter (VSC).

It is able to supply a maximum power of 400 W, with an output range of  $\pm 100$  V and  $\pm 4$  A. The output impedance values are  $500 \mu\Omega$  and  $500 \mu\text{F}$  for the series resistance and inductance, respectively, while the shunt resistance and capacitance are  $100 \text{ k}\Omega$  and  $0.1 \mu\text{F}$ .

## D.5 HP Power Supply for DC-Link

The power supply HP 6035A (shown in Fig. D.5) keeps constant the dc-link voltage during the tests of section §4.5.1, so that no fundamental current is required, and thus the high-frequency component can be clearly appreciated.

The maximum output voltage, current and power are 500 V, 5 A and 1050 W, respectively. To assure that the maximum power is not surpassed, its autoranging output adjusts the values in the combinations 500 V & 2 A, 350 V & 3 A and 200 V & 5 A. It offers programming accuracy of 0.25% in voltage and 0.3% in current, and a programming resolution of 125 mV and 1.25 mA. The output voltage ripple (in the range between 20 Hz and 20 MHz) is 160 mV peak-to-peak and 50 mV in RMS, while the current ripple is 50 mA in RMS. The transient response time is 5 ms with a step change of 10%. The dc floating voltage is between  $\pm 500$  V.

## D.6 Programmable Load

The programmable load Hoherl & Hackl ZSAC426 (shown in Fig. D.6) is employed in sections §2.7 and §3.5 to demand a distorted current. The operating ranges are 0 – 6 A, 0 – 260 V,



Figure D.6: Hocherl &amp; Hackl ZSAC426 programmable load.

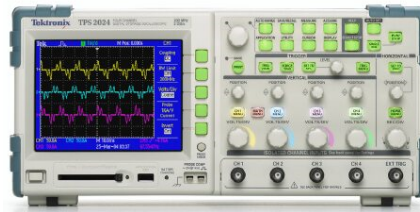


Figure D.7: Tektronix TPS2014 digital oscilloscope.

2 – 2000  $\Omega$  and 0 – 400 W. The nominal power value can be considered with ambient temperature up to 21°C, and a derating of  $-1.2\%/^{\circ}\text{C}$  should be taken into account for higher temperatures. The current accuracy is 0.5% of setting and 0.3% of range, while the resistance accuracy is 1.5% of setting and 0.5% of range. The frequency range of the fundamental component is between 40 Hz and 700 Hz. The current harmonic distortion for sinusoidal output at 50 Hz or 60 Hz is lower than 1%, and greater at higher frequencies. The input capacitance is 1.5  $\mu\text{F}/1400\text{ W}$ . It is able to provide proper functionality between operating temperatures between 5°C and 40°C. It can work as an amplifier of an external analog signal in the range 0 – 3.5 V or 0 – 7 V, with an accuracy of 0.5%  $\pm$  15 mV of setting and 2%  $\pm$  30 mV.

The frequency of the fundamental component of its current is automatically adjusted to match that of the voltage in its terminals. This property is used in the tests of section §3.5.3.2, in which a frequency transient is performed.

Additionally, it offers the possibility of being programmed by means of an interface, with 16 bit resolution in settings and 18 bit resolution in measurements. This is the procedure through which the harmonic currents have been programmed.

## D.7 Measurements

Measurements are done with the TPS2014 digital oscilloscope from Tektronix (shown in Fig. D.7). This is a digital oscilloscope with four fully isolated channels with 100 MHz bandwidth (1 GS/s). It is equipped with the TPS2PWR1 power measurement and analysis software, that allows, among others functions, to display harmonic spectrum of a waveform and to calculate the total harmonic distortion (THD) up to the 50th harmonic.

The current transducers for the input channels of the dSPACE platform are closed-loop (compensated) LEM transducers LA 55-P, based on Hall effect. The primary nominal RMS current is 50 A, and its measuring range is between  $\pm 70\text{ A}$ . The accuracy (with ambient temperature of 25°C and supply voltage of 15 V  $\pm$  5%) is 0.65%. The linearity error is less than 0.2%. In order to employ it for lower current values, five turns are used in the primary. Its offset current (at 25°C) is  $\pm 0.2\text{ mA}$ , its maximum residual current (after an overload of three times

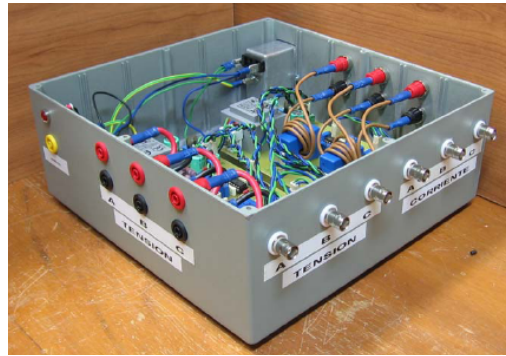


Figure D.8: Box including voltage and current sensors, as well as their conditioner circuits.

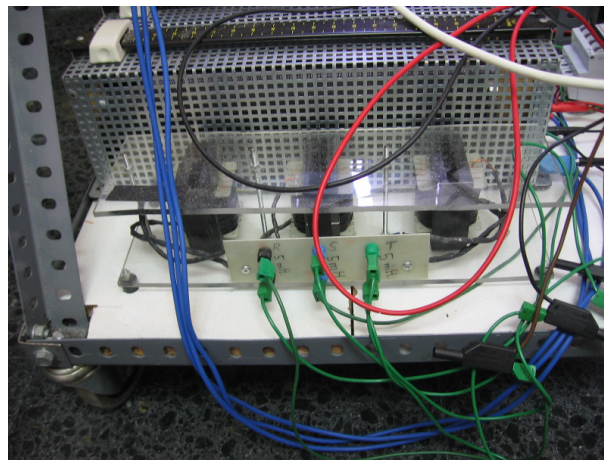


Figure D.9: Inductors.

the nominal primary current) is  $\pm 0.3$  mA, its maximum thermal drift is  $\pm 0.6$  mA, its reaction time (with 10% of the maximum primary current) is lower than 500 ns, its response time (with 90% of the maximum primary current) is lower than  $1 \mu\text{s}$  and the maximum current derivative accurately followed is  $200 \text{ A}/\mu\text{s}$ . The frequency bandwidth (-1 dB) is 200 kHz. The ambient operating temperature is between  $-25^\circ\text{C}$  and  $85^\circ\text{C}$ .

Each of the voltage transducers for the input channels of the dSPACE platform is based on a measuring resistor (with value selected depending on the range of voltages to measure in each case) and a closed-loop (compensated) LEM transducer LV 25-P. The primary nominal RMS current of the LEM sensor is  $\pm 10$  mA, and its measuring range is between  $\pm 14$  mA. The secondary nominal current is 25 mA. The accuracy (with ambient temperature of  $25^\circ\text{C}$  and supply voltage of  $15 \text{ V} \pm 5\%$ ) is 0.8%. The linearity error is less than 0.2%. Its offset current (at  $25^\circ\text{C}$ ) is  $\pm 0.15$  mA, its maximum variation with temperature is  $\pm 0.35$  mA and its response time (with 90% of the maximum primary current) is  $40 \mu\text{s}$ . The frequency bandwidth (-1 dB) is 200 kHz. The ambient operating temperature is between  $0^\circ\text{C}$  and  $70^\circ\text{C}$ .

Both current and voltage transducers, as well as their conditioner circuits, are placed inside the box shown in Fig. D.8.

## **D.8 Inductors**

The inductors (shown in Fig. D.9) employed in most of the experiments are made of EPCOS ferrite (type N27) cores E 70/33/32. The inductance and equivalent series resistance (ESR) have been measured with an inductance analyzer; their values are, respectively, 5 mH and 0.5  $\Omega$ .